Université catholique de Louvain
École Polytechnique de Louvain
Institute of Mechanics, Materials and Civil Engineering

MicroCT and contrast-enhanced microCT imaging to improve treatments for cardiovascular diseases

Lisa Leyssens
Biomedical Engineer

Thesis submitted in partial fulfillment
of the requirements for the degree of
docteure en sciences de l'ingénieur et technologie

Members of the jury:

Prof. Eric Deleersnijder (Chairperson)	UCLouvain
Prof. Greet Kerckhofs (Promotor)	UCLouvain
Prof. Pascal Jacques (Co-promotor)	UCLouvain
Prof. Sandrine Horman	UCLouvain
Prof. Laurent Delannay	UCLouvain
Prof. Jeremy Goldman	Michigan Technological University
Prof. Tríona Lally	Trinity College Dublin

March 2024
Louvain-la-Neuve, Belgium

Summary

Cardiovascular diseases are the leading cause of death and disability worldwide, with a significant impact on public health. Atherosclerosis is a chronic inflammatory disease, characterized by the buildup of plaque within the arterial walls causing blood vessel narrowing or blockage and is the primary cause of many cardiovascular diseases. Research for new or improved treatments is continuously ongoing to reduce the number of people facing disability. However, disease mechanisms and the native complex microstructure of vascular tissues are not yet well understood.

Classical 2D histology, the gold standard for microstructural imaging, has its limitations due to its two-dimensional scope, offering only a limited visualization of the intricate three-dimensional microstructure of tissues. In contrast, X-ray microfocus computed tomography (microCT) emerges as a powerful imaging technique that delivers three-dimensional insights of complex structures in a non-destructive way. Enhanced further by the integration of contrast-enhancing staining agents (CESAs), the application of microCT has broadened to soft tissue imaging. This technique, known as contrast-enhanced microCT (CECT), complements classical 2D histological analysis. The aim of this thesis is to optimize and apply X-ray based imaging to better understand the native microstructure of vascular tissues and to provide further insights into two different treatments for cardiovascular diseases: vascular synthetic grafts and biodegradable intravascular stents.

This manuscript opens with an overview of the cardiovascular system and its diseases, and highlights the limitations of current treatments. The second chapter outlines the problem statement, aim and objectives of this thesis. Chapter 3 provides a state-of-the-art on the current applications of *ex vivo* microCT-based techniques to characterize the cardiovascular system, providing several shortcomings regarding the microstructural analysis of the blood vessel wall, especially in terms of spatial resolution of current studies and the use of destructive CESAs. This highlights the fact that

the native 3D microstructure of the blood vessel wall is not well known and that many 3D representations found in the literature are based on 2D images.

Based on the state-of-the art, the fourth chapter of this thesis is dedicated to the optimization of CECT to image the native blood vessel wall, which is then applied to quantitatively assess and compare the microstructure of different types of blood vessels in different species. Different currently used synthetic vascular grafts, which are used to bypass blocked arteries, are also imaged using microCT and several structural parameters are assessed showing the gap that still exists in microstructure between native tissues and synthetic grafts and explaining the differences in functional behavior between both.

The following three chapters focus on the application of microCT-based techniques to study the behavior of potential candidate materials to be used as biodegradable intravascular stents, used to revascularize obstructed or blocked arteries. Chapter 5 starts with an outline of the advances in the development of biodegradable metallic stents. The next chapter is an *in vitro* study of the degradation behavior of candidate stent materials after static immersion tests using high-resolution microCT imaging to provide detailed 3D information on the surface properties, degradation rate, and degradation behavior of different metallic alloys. In chapter 7, these same materials are studied in a model of the rat abdominal aorta. In this case, by combining microCT and CECT, the *in vivo* behavior of these same materials is evaluated, such as the degradation rate and the degradation behavior in different locations of the implants, as well as the biocompatibility by studying the interactions between the implants and the surrounding tissue.

The advanced imaging techniques and image processing tools described in this thesis, provide a better description of the native blood vessel wall and its microstructural constituents and give insights into the development of optimized treatments for cardiovascular diseases.

Résumé

Les maladies cardiovasculaires sont la principale cause de décès dans le monde, avec un impact significatif sur la santé publique. L'athérosclérose est une maladie inflammatoire chronique caractérisée par l'accumulation de plaques dans les parois artérielles, ce qui entraîne le rétrécissement ou l'obstruction des vaisseaux sanguins et constitue la cause principale de nombreuses maladies cardiovasculaires. La recherche de nouveaux traitements cliniques est en cours afin de réduire le nombre de personnes souffrant d'un handicap. Cependant, les mécanismes de la maladie et la microstructure complexe des tissus vasculaires ne sont pas encore suffisament connus.

L'histologie classique en 2D, la technique de référence pour l'imagerie à l'échelle microscopique des tissues biologiques, a ses limites en raison de sa portée bidimensionnelle, n'offrant qu'une visualisation limitée de la microstructure tridimensionnelle complexe des tissus. En revanche, la micro-tomographie à rayons X (microCT) apparaît comme une technique d'imagerie puissante qui donne un aperçu tridimensionnel de structures complexes de manière non destructive. Améliorée par l'intégration d'agents amplifiant le contraste (AAC), l'application de la microCT s'est élargie à l'imagerie des tissus mous biologiques. Cette technique, connue sous le nom de microCT à contraste amélioré (MTCA), complète l'analyse histologique 2D classique. L'objectif de cette thèse est d'optimiser et d'appliquer l'imagerie à base de rayons X pour mieux comprendre la microstructure native des tissus vasculaires et d'évaluer deux différents traitements contre les maladies cardiovasculaires: les greffes vasculaires synthétiques et les stents intravasculaires biodégradables.

Ce manuscrit commence par une description du système cardiovasculaire et de ses maladies, et souligne les limites des traitements actuels. Le deuxième chapitre présente le but et les différents objectifs de cette thèse. Le chapitre 3 décrit l'état de l'art de l'utilisation actuelle des techniques d'imagerie basées sur la microCT en *ex vivo* pour caractériser le système

cardiovasculaire et en particulier les vaisseaux sanguins. Il met en avant les limitations des analyses faites actuellement, notamment, en ce qui concerne la faible résolution spatiale des techniques utilisées ainsi que le caractère destructif des AACs qui existent. Ceci met en évidence le fait que la microstructure 3D de la paroi des vaisseaux sanguins n'est pas bien connue et que de nombreuses représentations 3D trouvées dans la littérature sont basées sur des images 2D.

Sur base de cet état de l'art, le quatrième chapitre de cette thèse est consacré à l'optimisation de la MTCA pour l'imagerie *ex vivo* des vaisseaux sanguins de façon non destructive. La MTCA est ensuite utilisée pour évaluer de façon quantitative et comparer la microstructure de différents types de vaisseaux sanguins chez différentes espèces. Différentes greffes vasculaires synthétiques actuellement utilisées pour faire le pontage d'artères obstruées sont également imagées à l'aide de la microCT. Plusieurs paramètres structurels de ces greffes sont évalués pour montrer la différence au niveau de la microstructure entre les tissus natifs et les greffes synthétiques.

Les trois chapitres suivants concernent l'étude de métaux utilisés pour la fabrication de stents intravasculaires biodégradables. Les stents intravasculaires sont implantés chez les patients pour revasculariser les artères obstruées ou bloquées. Le chapitre 5 commence par un aperçu des progrès réalisés dans le développement des stents métalliques biodégradables. Le chapitre suivant est une étude *in vitro*, dans laquelle différents alliages métalliques sont étudiés au travers de tests d'immersion. Les alliages sont ensuite imagés grâce à la microCT pour fournir des informations 3D détaillées sur les propriétés de surface et la vitesse de dégradation de ceux-ci. Dans le chapitre 7, ces mêmes alliages métalliques sont étudiés dans un modèle d'aorte abdominale de rat. En combinant la microCT et la MTCA, le comportement *in vivo* de ces matériaux est déterminé, comme la vitesse et les phénomènes locaux de dégradation, ainsi que la biocompatibilité. Cette dernière peut être évaluée par l'étude des interactions entre l'implant et le tissu l'entourant.

Les techniques d'imagerie et les outils de traitement d'images décrits dans cette thèse, fournissent une meilleure description de la microstructure des vaisseaux sanguins et visent à améliorer le développement de traitements contre les maladies cardiovasculaires.

Acknowledgments

This manuscript marks the end of six years of research, an adventure that has been anything but an individual effort. Every interaction, collaboration, and shared moment have made it possible to achieve my goal. Therefore, I wish to start by extending my gratitude to everyone who has stood by me throughout this journey.

Om te beginnen wil ik mijn promotor, Greet Kerckhofs, bedanken voor de voortdurende steun gedurende de afgelopen zes jaar. Bedankt voor de vele meetings, de hoeveelheid tijd besteed aan het verbeteren van papers, abstracts, thesis hoofdstukken, de gezellige momenten op conferenties in NYC en Wenen, en de gesprekken over zowel wetenschappelijke als minder wetenschappelijke onderwerpen. Bedankt dat je mij deze kans hebt gegeven en dat je altijd in me hebt geloofd.

I would also like to thank the members of my jury for dedicating their time to review my work, taking interest in the topic, and helping me to improve this thesis with constructive discussions during the private defense and at other times.

Thank you also to Jeremy for the nice collaboration during my PhD years. Thank you for believing in my work and always being enthusiastic and positive about it. I always enjoyed the dinners at Grill Tov.

Next, I would like to mention all my colleagues in the ContrasT Team: Sarah, Arne, Camille, Tim, Delia, Gregory, Victor, Maïté, Lara, Walid, Pierre, Isabelle, and Kaveh. Thank you for the great collaborations and discussions, the numerous Teams meetings, the team buildings and the fun after-

work activities. This journey would not have been the same without your everyday support. Merci Camille d'avoir partagé pendant ces quelques années avec moi la vie de tous les jours, les moments fun et moins fun, merci pour toutes les discussions, ton soutien, tes bons conseils et merci de m'avoir toujours encouragée. C'était un privilège d'avoir pu partager cette expérience avec toi. Merci Delia pour les nombreuses discussions et moments passés ensemble, merci pour tes conseils et ton aide et d'avoir partagé ton expérience et ton expertise avec moi. Merci aussi à Maïté d'avoir été ma voisine ces dernières années, je garde de très bons souvenirs de nos échanges scientifiques et moins scientifiques, et de nos envies de biscuits ou de chocolat chaud dans le bureau. Thank you, Gregory, for sharing your passion for microCT imaging, and thank you for always being available night and day and weekends whenever needed. Bedankt Tim dat je altijd beschikbaar was als ik een vraag had en voor al de tijd die je hebt gestoken in het uitleggen van statistiek, diffusie, en POMs. Dankjewel Sarah en Arne voor de fijne gesprekken en jullie behulpzaamheid. Merci à Lara pour les discussions, les bons moments, et les nuits passées ensemble au synchrotron, merci Victor pour ton aide au niveau informatique et les chouettes discussions dans le train, merci Walid pour l'aide durant les longues heures passées sur les opérations des animaux au labo, merci Pierre pour ton aide au niveau expérimental, et merci Isabelle pour ces quelques derniers mois passés ensemble, pour les chouettes discussions et ton aide lors des nombreuses séances de TP.

Je voudrais aussi remercier mes collègues en MEED pour la bonne ambiance de travail, les chouettes moments à la cafet, les after-work, et les bonnes expériences partagées. Merci particulièrement à mes collègues de bureau, DJ Henri, toujours là (ou pas) pour mettre l'ambiance dans le bureau grâce à tes playlists "originales" et merci Louis pour les balles volantes, les blagues et les brainstormings de prénoms. Nos (ou vos) discussions de bureau de tous les jours ont rendu les journées plus fun.

Mama, Papa, Lex, en Thomas, bedankt voor jullie onvoorwaardelijke steun, zorgen, lieve woorden, en telefoontjes. Bedankt voor de zovele leuke momenten en vakanties samen. Ik kijk altijd uit naar de weekends dat we naar Behême komen en kom altijd vol energie terug naar huis na een weekendje samen. Thank you Joseph for always joining crazy family weekends and vacations, thank you for the encouragements, the fun memories, and thank you sharing my passion for whistling and funny ex-

pressions. Merci Clara pour ton enthousiasme, ta bonne humeur, ton aide, les chouettes discussions, et les vacancess qui m'ont permis de me changer les idées.

Merci aussi à tous mes amis, trop nombreux pour tous les citer, les copines d'enfance, les amis de l'unif, les cariocas et la team hockey, qui sont toujours là. Merci de m'avoir permis de me changer les idées en dehors du travail, merci pour vos encouragements, votre écoute et votre soutien.

Et enfin, Emilio, le plus grand des mercis te revient pour ton soutien inconditionnel. Merci d'avoir toujours cru en moi à chaque étape, de m'avoir encouragée, de m'avoir écoutée, conseillée, et d'avoir partagé avec moi au quotidien tous les beaux et moins beaux moments durant ces six dernières années.

List of publications and communications

Journal publications

- **Leyssens, Lisa**; Pestiaux, Camille; Kerckhofs, Greet. A Review of Ex Vivo X-ray Microfocus Computed Tomography-Based Characterization of the Cardiovascular System. *International Journal of Molecular Sciences*, Vol. 22, no.6, p.3263 (2021) `https://doi.org/10.3390/ijms22063263`

- Léger, Jean; **Leyssens, Lisa**; Kerckhofs, Greet; De Vleeschouwer, Christophe. Ensemble learning and test-time augmentation for the segmentation of mineralized cartilage versus bone in high-resolution microCT images. *Computers in Biology and Medicine*, Vol. 148, no.105932, p.- (2022) `https://doi.org/10.1016/j.compbiomed.2022.105932`

- Maes, Arne; Pestiaux, Camille; Marino, Alice; Balcaen, Tim; **Leyssens, Lisa**; Vangrunderbeeck, Sarah; Pyka, Grzegorz; De Borggraeve, Wim M.; Bertrand, Luc; Beauloye, Christophe; Horman, Sandrine; Wevers, Martine; Kerckhofs, Greet. Cryogenic contrast-enhanced microCT enables nondestructive 3D quantitative histopathology of cardiovascular tissues. *Nature Communications*, Vol. 13, no.6207, p.- (2022) `https://doi.org/10.1038/s41467-022-34048-4`

- **Leyssens, Lisa**; Balcaen, Tim; Pétré, Maïté; Béjar Ayllón, Natalia; El Aazmani, Walid; de Pierpont, Alix; Pyka, Grzegorz; Lacroix, Valérie; Kerckhofs, Greet. Non-destructive 3D characterization of the blood vessel wall microstructure in different species and blood vessel types

using contrast-enhanced microCT and comparison with synthetic vascular grafts. *Acta Biomaterilia*, Vol. 164, no.-, p.303-316 (2023) `https://doi.org/10.1016/j.actbio.2023.04.013`

- **Leyssens, Lisa**; Lapraille, Noémie; Pyka, Grzegorz; Jacques, Pascal J.; Horman, Sandrine; Goldman, Jeremy; Kerckhofs, Greet. Exploring the biodegradability of candidate metallic intravascular stent materials using X-ray microfocus computed tomography: an *in vitro* study. *Under revision in Journal of Biomedical Materials Research Part B: Applied Biomaterials*

- **Leyssens, Lisa**; El Aazmani, Walid; Balcaen, Tim; Jacques, Pascal J.; Horman, Sandrine; Goldman, Jeremy; Kerckhofs, Greet. MicroCT and contrast-enhanced microCT-based study of the degradation behavior and biocompatiblity of candidate metallic intravascular stent materials: in vivo study in an aortic rat model. *Submitted to Bioactive Materials*

Communications in conferences

- **Leyssens, Lisa**; Ryelandt, Sophie; Favache, Audrey; Kerckhofs, Greet. Nanoindentation of biological tissues: opportunities and challenges for the bone-tendon interface. *Indentation conference 2018* (Liège, Belgium, from 11/09/2018 to 14/09/2018), poster presentation

- **Leyssens, Lisa**; Ryelandt, Sophie; Favache, Audrey; Kerckhofs, Greet. Nanoindentation of biological tissues: opportunities and challenges for the bone-tendon interface. *European Society of Biomechanics conference 2019* (Vienna, Austria, from 07/07/2019 to 10/07/2019), poster presentation

- **Leyssens, Lisa**; Ryelandt, Sophie; Favache, Audrey; Kerckhofs, Greet. Advanced characterization of the 3D morphology and the mechanical properties of the enthesis: optimization study. *Computer Methods in Biomechanics and Biomedical Engineering, 2019* (New York, USA, from 14/08/2019 to 16/08/2019), poster presentation

- **Leyssens, Lisa**; Verhaegen, Carole; Horman, Sandrine; Jacques, Pascal J.; Kerckhofs, Greet. Optimization of contrast-enhanced micro-CT for characterization of the in vivo behavior of biodegradable metallic

intravascular stents. *Computer Methods in Biomechanics and Biomedical Engineering, 2019* (New York, USA, from 14/08/2019 to 16/08/2019), oral presentation

- **Leyssens, Lisa**; Béjar Ayllón, Natalia; Fehervary, Heleen; Lacroix, Valérie; Famaey, Nele; Kerckhofs, Greet. Arterial grafts: in depth characterization of structure and mechanical properties. *Belgian Society for Tissue Engineering symposium 2019* (Hasselt, Belgium, from 14/11/2019 to 15/11/2019), poster presentation

- **Leyssens, Lisa**; Pétré, Maïté; Kerckhofs, Greet. Optimization of microCT and CECT for Cardiovascular Applications. *Tomography for Scientific Advancement conference, 2021* (Online, from 01/09/2021 to 03/09/2021), oral presentation

- **Leyssens, Lisa**; Pétré, Maïté; Kerckhofs, Greet. Optimization of microCT and CECT for Cardiovascular Applications. *Computer Methods in Biomechanics and Biomedical Engineering, 2021* (Online, from 07/09/2021 to 09/09/2021), oral presentation

- **Leyssens, Lisa**; Pétré, Maïté; Kerckhofs, Greet. Screening of contrast-enhancing staining agents for 4D contrast-enhanced microCT of vascular tissues. *World Conference of Biomechanics, 2022* (Online, from 10/07/2022 to 14/07/2022), oral presentation

- **Leyssens, Lisa**; Pétré, Maïté; Kerckhofs, Greet. Optimization of contrast-enhanced microCT for vascular applications. *International Conference on Tomography of Materials and Structures, 2022* (Grenoble, France, from 27/06/2022 to 07/07/2022), oral presentation

- **Leyssens, Lisa**; Lapraille, Noémie; Pyka, Grzegorz; Jacques, Pascal J.; Horman, Sandrine; Goldman, Jeremy; Kerckhofs, Greet. Exploring the biodegradability and biocompatibility of candidate metallic intravascular stent materials using microCT and CECT. *Biometal conference, 2023* (Cetraro, Italy, from 21/08/2023 to 27/08/2023), special mention for outstanding oral presentation

Contents

Contents . . . . . **xi**

List of Figures . . . . . **xvii**

Abbreviations . . . . . **xx**

I Introduction

1 Context **3**
1.1 The cardiovascular system 3
1.2 Cardiovascular occlusive diseases 8
1.3 Treatments for cardiovascular occlusive diseases 11
1.3.1 Vascular grafts 11
1.3.2 Balloon angioplasty 13
1.3.3 Intravascular stents 14
1.3.4 Tissue-engineered vascular grafts 14
1.3.5 Clinical application 15

2 Problem statement, thesis aim and objectives **17**
2.1 Problem statement 17
2.2 Thesis aim and objectives 19
2.2.1 Objective 1 20
2.2.2 Objective 2 21
2.2.3 Objective 3 21
2.3 Thesis overview 22

II MicroCT-based imaging of native blood vessels and synthetic vascular grafts

3 A review of *ex vivo* microCT-based characterization of the cardiovascular system 27
3.1 Introduction 28
3.2 General description of microCT, CECT and PCCT 30
3.3 The heart 38
3.3.1 Anatomical and morphometric assessment of the whole heart . 38
3.3.2 Morphometrical analysis of the myocardium 42
3.3.3 Measurement of the calcifications in heart valves and assessment of the valve microstructure 45
3.4 The vasculature 47
3.4.1 Spatial distribution and morphometrics of the vascular tree . . 48
3.4.2 Microstructure of the vessel wall 53
3.5 Conclusions 57
3.6 Supplementary materials 58

4 Non-destructive 3D characterization of the blood vessel wall microstructure in different species and blood vessel types using CECT and comparison with synthetic vascular grafts 61
4.1 Introduction 62
4.2 Materials and methods 65
4.2.1 Animal age, sex and origin 65
4.2.2 Preparation of the blood vessels 66
4.2.3 Contrast-enhancing staining agents 66
4.2.4 Synthetic grafts 67
4.2.5 High-resolution microCT imaging 67
4.2.6 Classical 2D histological assessment 68
4.2.7 Image processing and analysis 68
4.2.8 Statistical analysis 68
4.2.9 Penetration rate and contrast enhancement study 69
4.2.10 CECT and paraffin embedding: volume comparison study . . . 71
4.2.11 Inter-species differences study 71
4.2.12 Comparison study between different types of blood vessels . . 72
4.2.13 Quantification of different structural parameters in different types of blood vessels. 72
4.2.14 Comparison between healthy and atherosclerotic human femoral artery: imaging and segmentation 73

4.2.15 Structural analysis of the synthetic grafts . . . 73
4.3 Results . . . 74
4.3.1 Screening of CESAs based on penetration rate and contrast enhancement . . . 74
4.3.2 Sample preparation for classical 2D histology causes tissue deformation . . . 74
4.3.3 Important differences in microstructure between the rat, porcine and human aorta and femoral artery . . . 76
4.3.4 Microstructural differences between the porcine aorta, femoral artery, and vena cava . . . 79
4.3.5 Quantification of structural parameters of different tissue constituents in different types of blood vessels . . . 79
4.3.6 CECT-based imaging allows to visualize and segment the different tissue constituents of an atherosclerotic human femoral artery . . . 81
4.3.7 The microstructure of different synthetic vascular grafts is highly variable and different compared to the native tissue . . . 83
4.4 Discussion . . . 83
4.5 Conclusion . . . 89
4.6 Supplementary materials . . . 90

III MicroCT-based imaging of metallic implants for biodegradable intravascular stents

5 Advancements in the development of biodegradable intravascular stent materials . . . **95**
5.1 Intravascular stents . . . 96
5.2 Biodegradable intravascular stents . . . 98
5.2.1 Magnesium-based biodegradable stents . . . 99
5.2.2 Iron-based biodegradable stents . . . 101
5.2.3 Zinc-based biodegradable stents . . . 102
5.2.4 Summary of the mechanical properties . . . 103
5.3 Reendothelialization . . . 105
5.3.1 In-stent restenosis . . . 106
5.3.2 Stent thrombosis . . . 106
5.4 Evaluation of stents in (pre)clinical conditions . . . 107
5.5 Summary . . . 109

6 MicroCT-based study of the *in vitro* degradation behavior of candidate metallic intravascular stent materials 111
6.1 Introduction 112
6.2 Materials and methods 115
6.2.1 Samples 115
6.2.2 In vitro static immersion 115
6.2.3 Inductively-coupled plasma - optical emission spectrometry (ICP-OES) 116
6.2.4 Corrosion rate based on ICP-OES 116
6.2.5 High-resolution microCT acquisition 117
6.2.6 Surface roughness analysis based on microCT 117
6.2.7 Corrosion behavior based on microCT 118
6.2.8 Scanning electron microscopy – energy dispersive X-ray spectroscopy (SEM-EDX) 119
6.2.9 Corrosion rate based on microCT 119
6.2.10 Statistical analysis 119
6.3 Results 120
6.3.1 Differences in corrosion behavior were visualized in full 3D and the corrosion products were identified. 120
6.3.2 The corrosion behavior of the different metal types was compared quantitatively using surface profile lines determined based on the microCT images. 122
6.3.3 Corrosion rate could be accurately determined by calculating the microCT-based volume loss of the wires. 124
6.3.4 Changes in surface roughness of the different metal types determined using the surface profile lines. 125
6.4 Discussion 126
6.5 Conclusion 131

7 MicroCT and CECT-based study of the *in vivo* degradation behavior and biocompatibility of candidate metallic intravascular stent materials 133
7.1 Introduction 134
7.2 Materials and methods 137
7.2.1 Animals 137
7.2.2 Implants 137
7.2.3 MicroCT acquisition of wires prior to implantation 138
7.2.4 Wire implantation 139
7.2.5 MicroCT acquisition of explants 140

7.2.6 CESA choice and staining time . . . 140
7.2.7 CECT acquisition of explants . . . 142
7.2.8 Classical 2D histology . . . 142
7.2.9 MicroCT and CECT datasets post-processing . . . 143
7.2.10 MicoCT and CECT image analysis . . . 143
7.2.11 Statistical analysis . . . 145
7.3 Results . . . 146
7.3.1 MicroCT allowed for determining the in vivo degradation behavior of the implants. . . . 146
7.3.2 Optimization of CECT imaging of the wires after implantation. 148
7.3.3 Combining microCT and CECT enabled computation of the regional in vivo implant degradation. . . . 148
7.3.4 The CECT images allowed the 3D structural characterization of the neointima and corrosion products. . . . 150
7.3.5 Neointima formation at the cellular level . . . 152
7.4 Discussion . . . 156
7.5 Conclusion . . . 161
7.6 Supplementary materials . . . 161

IV Discussion and conclusion

8 Overview, general discussion, and future perspectives . . . 167
8.1 Thesis overview, limitations, and potential improvements for each part . . . 167
8.1.1 Part I . . . 167
8.1.2 Part II . . . 168
8.1.3 Part III . . . 170
8.2 General discussion and future challenges . . . 175
8.2.1 Comparison of microCT-based imaging with other imaging techniques . . . 175
8.2.2 Optimization of microCT and CECT to improve treatments for cadiovascular diseases . . . 178
8.2.3 Future challenges of microCT-based techniques . . . 180

V Appendices

A Overview of the acquisition parameters of the Phoenix Nanotom M . . . 185

Bibliography **187**

List of Figures

1.1 Scheme of the circulatory system. 4
1.2 Idealized architecture of a healthy human elastic artery. 5
1.3 Structure of the vascular system. 7
1.4 Schematic view of atherosclerosis stages 10
1.5 Detailed scheme of atherosclerosis progression. 12
1.6 Surgical treatment options for artery narrowing or blockage caused by atherosclerosis. 13

2.1 Scheme presenting the structure of this thesis manuscript. . . . 23

3.1 Schematic representation of the published review. 31
3.2 Whole-heart CECT imaging. 41
3.3 Extraction of the fiber orientation in rat hearts based on PCCT. 44
3.4 MicroCT imaging of fresh calcified aortic valves from human patients that were explanted during aortic valve replacement. . 46
3.5 Microfil-perfused rat kidney vasculature in progressive ischemia/reperfusion (I/R)-induced renal injury. 49
3.6 Bone marrow vasculature of the tibial metaphysis stained with 1:2 Hf-WD POM. 51
3.7 Abdominal rat aorta stained with 1:2 Hf-WD POM. 53
3.8 Paraffin-embedded rat common carotid artery without CESA. Major arterial substructures are readily identifiable in the vessel wall. 55

4.1 CESA staining in function of time: Mono-WD POM and 1:2 Hf-WD POM. 75

4.2 Volume comparison of a piece of porcine aorta: fresh, fixed in FA, after 1:2 Hf-WD POM staining, and after paraffin embedding. 77
4.3 Differences in microstructure between the rat, porcine and human aorta. 78
4.4 Microstructural differences between the porcine aorta, femoral artery, and vena cava. 80
4.5 Quantitative structural parameters extracted from the media of the rat and porcine aortas. 82
4.6 Microstructural analysis of synthetic vascular grafts commercially available. 84

5.1 Ideal trade-off between mechanical integrity and degradation for a biodegradable stent. 99
5.2 Approximated stress-strain curves for currently investigated biodegradable stent materials 104
5.3 Possible outcomes for stent implantation. 107

6.1 Timeline for experiments 115
6.2 Output example of the in-house developed Matlab tool for 2D roughness analysis. 118
6.3 Visual comparison of different metal types (Co-Cr alloy, Fe, Zn, and Zn alloy) after immersion at different time points (1 day, 4 days, and 7 days). 121
6.4 Detection of corrosion products of wires after 7 days of static immersion. 122
6.5 Typical degradation behavior of Fe, Zn, and Zn alloy. 124
6.6 Comparison of the corrosion rate of the different metal types at different time points. 126
6.7 Comparison of the surface roughness of the different metal types at different time points. 127

7.1 Experimental workflow for microCT and CECT image acquisition and registration of both types of datasets. 138
7.2 MicroCT-based representations of the wires, diameter versus length graphs used to compute the percentage volume loss, and parameters that influence the percentage volume loss of the wires after explant collection. 147
7.3 Choice of CESA and optimization of staining time for CECT of the explants. 149

7.4 Comparison of percentage volume loss of the portion of the wires outside the lumen and inside the lumen, and degradation rate and behavior of the explanted wires, part only inside the lumen. 151
7.5 Segmentation of the neointima and the corrosion products from the CECT images and comparison of the structural parameters of the neointima and the corrosion products for all wires at 24 and 84 days. 153
7.6 Comparison between CECT and classical 2D histology imaging techniques for the explants. 155

Abbreviations

1:2 Hf-WD POM	1:2 Hafnium-substituted Wells-Dawson polyoxometalate.
AS	Aortic stenosis.
BHC	Beam hardening correction.
BMS	Bare metal stent.
BRS	Biodegradable stent.
CA	Contrast agent.
CABG	Coronary artery bypass surgery.
CAD	Coronary artery disease.
CCA	Casting contrast agent.
CECT	Contrast-enhanced computed tomography.
CESA	Contrast-enhancing staining agent.
CT	Computed tomography.
CVD	Cardiovascular disease.
CvD	Cerebrovascular disease.
DAPT	Dual antiplatelet therapy.
DES	Drug-eluting stent.
DT-MRI	Diffusion tensor magnetic resonance imaging.
DVT	Deep vein thrombosis.
EBSD	Electron backscatter diffraction.

EC	Endothelial cell.
ECM	Extracellular matrix.
EDX	Energy Dispersive X-ray Spectroscopy.
EEL	External elastic lamina.
FA	Formaldehyde.
ICP	Inductively-coupled plasma.
IEL	Internal elastic lamina.
ISR	In-stent restenosis.
LDL	Low density lipoprotein.
LV	Left ventricle.
microCT	X-ray microfocus computed tomography.
Mono-WD POM	Monolacunary Wells-Dawson polyoxometalate.
MRI	Magnetic resonance imaging.
OES	Optical emission spectrometry.
PAD	Peripheral arterial disease.
PAH	Pulmonary arterial hypertension.
PBS	Phosphate-buffered saline.
PCCT	Phase-contrast computed tomography.
PCI	Percutaneous coronary intervention.
PE	Pulmonary embolism.
PMA	Phosphomolybdic acid.
POM	Polyoxometalate.
PTA	Phosphotungstic acid.
ROI	Region of interest.
ROS	Reactive oxygen species.
RVE	Representative volume element.
SEM	Scanning electron microscopy.
SMC	Smooth muscle cell.
SPT	Sodium polytungstate.

ST	Stent thrombosis.
SVG	Saphenous vein graft.
TEM	Transmission electron microscopy.
TEVG	Tissue engineered vascular graft.
TWIP	Twinning-induced plasticity.
USI	Ultrasound imaging.
VEGF	Vascular endothelial growth factor.
VOI	Volume of interest.
XRD	X-ray diffraction.
Zr-POM	Zirconium-substituted Keggin polyoxometalate.

PART I
Introduction

1

Context

1.1 The cardiovascular system

The function of the cardiovascular system is to deliver oxygen and nutrients to the different organs of the body through the bloodstream, while eliminating their waste products. The cardiovascular system is constituted of the heart and its valves, the blood vessels and the blood. It is divided in two different circulatory systems: the pulmonary circulation and the systemic circulation. The loop that starts from the right side of the heart, travels through the lungs, and returns to the left side of the heart is referred to as the pulmonary circulation and is responsible for the reoxygenation of the blood. The loop that extends from the left side of the heart to the rest of the body and then goes back to the right side of the heart is known as the systemic circulation and is responsible for carrying the blood from the heart through the organs and tissues in the entire body [1, 2]. The vasculature consists of arteries, arterioles, capillaries, venules, and veins. Oxygenated blood is delivered through the arteries, which branch to form smaller arteries, and finally arterioles and capillaries. The capillaries then join together to form the venules, which in turn join to form veins and larger veins, which ultimately transport the deoxygenated blood back to the heart (Fig. 1.1) [2].

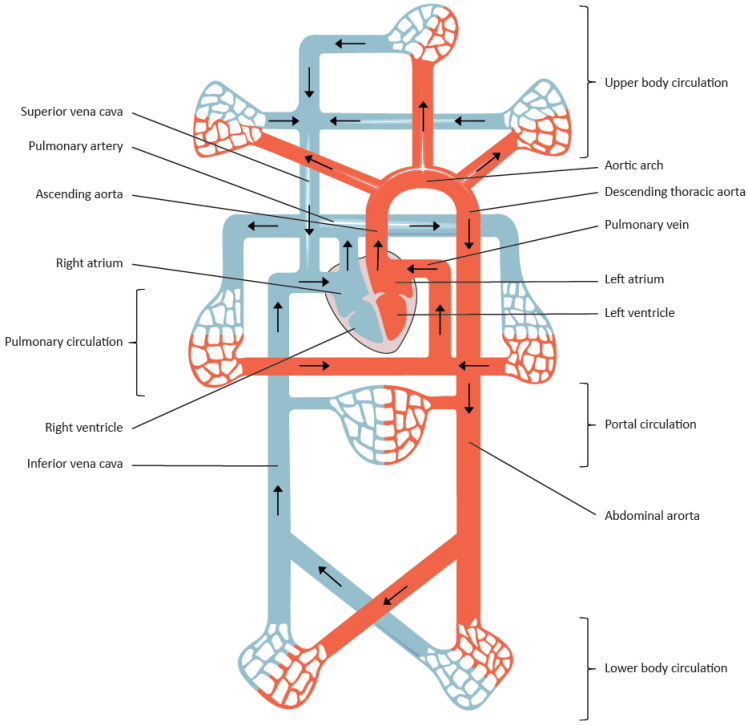


Fig. 1.1 Scheme of the circulatory system. Oxygenated blood is shown in red, deoxygenated blood in blue. Adapted from Servier Medical Art, licensed under a Creative Commons Attribution 3.0 Unported License [3].

Capillaries are thin-walled vessels composed a single layer of endothelial cells (ECs), while arteries and veins share a more complex structure. They are both made of three concentric layers: the tunica adventitia, the tunica media, and the tunica intima (Fig. 1.2).

- The tunica adventitia is the outermost layer composed mainly of fibroblasts, fibrocytes, extracellular matrix (ECM), and collagen fibers, primarily of type I. It is surrounded by loose connective tissue with no clearly defined outer boundary. Its role is to attach the vessel to the surrounding tissue and to provide shape and structural support to the vessel. This layer is the thickest layer in veins. It is separated from the tunica media by the external elastic lamina (EEL) in large arteries [4, 5].

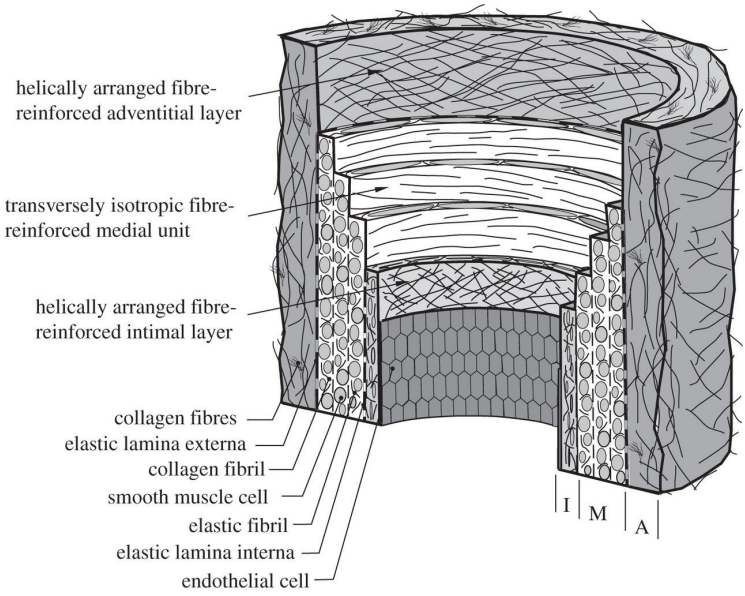


Fig. 1.2 Idealized architecture of a healthy human elastic artery, showing the three-layered microstructure (intima (I), media (M), and adventitia (A)). Used with permission of The Royal Society (U.K.), from [4]; permission conveyed through Copyright Clearance Center, Inc.

- The tunica media, or middle layer, is a complex three-dimensional (3D) network composed of elastin fibers, smooth muscle cells (SMCs) (present mainly in the muscular arteries and only in low amounts in the veins), and bundles of collagen fibrils of types I and III that help to maintain the structure and bind the media to the adjacent layers. The elastin fibers form fenestrated elastic lamellae, arranged concentrically, and separated by the SMCs and collagen fibrils [6]. This layer is the thickest layer in arteries and regulates the internal diameter of the vessel. It is separated from the tunica intima by the internal elastic lamina (IEL) in large arteries [4, 5, 7].

- The tunica intima, or innermost layer, is a very thin layer (only a few micrometers in thickness in a healthy human artery) composed of a single layer of ECs and a subendothelial layer of connective tissue (mainly collagen fibrils of types I and III). This layer constitutes the interface between the blood flow in the lumen and the rest of the vessel wall. It has an important role in ensuring a frictionless path to

allow blood to flow smoothly [4, 5]. It is essential that the endothelial layer keeps its integrity in order to regulate vascular permeability and protect the vessel against platelet deposition and thrombus formation. The vascular endothelium is also responsible for maintaining vascular tone by releasing vasodilating and vasoconstricting factors in a balanced way. Moreover, it plays a crucial role in regulating the migration and proliferation of vascular SMCs [8].

The microstructure of the different types of blood vessels varies based on their respective functions and locations within the body. Below is a brief description of each type of blood vessel and and its microstructure/function relationship (Fig. 1.3).

Arteries carry the blood from the heart to the different organs. They carry high-pressure blood and are therefore always under high pressure. To withstand this pressure, they contain an abundance of elastic tissue and a reduced amount of SMCs. The presence of elastic tissue enables these vessels to adapt their size and diameter. There are two main types of arteries: elastic arteries and muscular arteries. Elastic arteries are the ones closest to the heart (the aorta and the pulmonary arteries) and contain a lot of elastic tissue in the tunica media to allow them to maintain a relatively constant pressure gradient despite the constant pumping action of the heart. The muscular arteries are located further away from the heart (*i.e.* brachial artery, radial artery, femoral artery). They contain more SMCs in the tunica media and they distribute blood to smaller arteries and arterioles. The IEL and EEL are very promiment in muscular arteries while they are hardly distinguishable from the regular elastic laminae in elastic arteries [4, 11].

Arterioles provide blood to the organs and are mainly composed of SMCs. Their diameter and shape are influenced by the autonomic nervous system, allowing them to adjust in response to the specific nutrient and oxygen requirements of the surrounding tissue. The absence of substantial elastic tissue in their walls makes arterioles a key contributor to systemic vascular resistance. Arterioles have a length ranging from 8 to 60 micrometers and further subdivide into smaller vessels known as meta-arterioles [11].

Capillaries enable mass transfer between blood and the surrounding

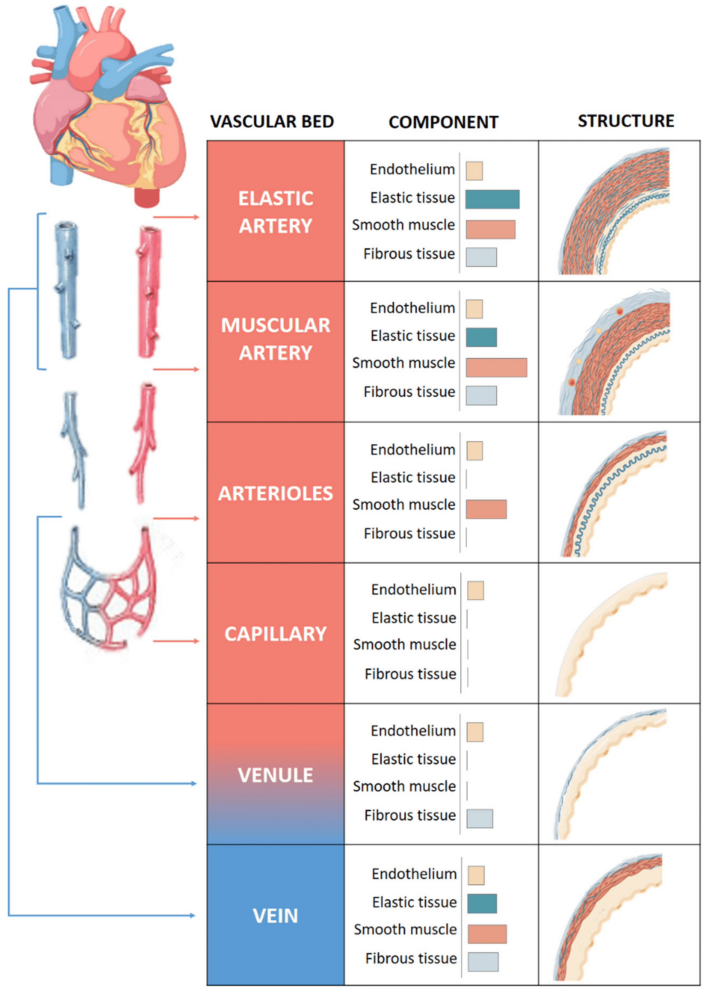


Fig. 1.3 Structure of the vascular system. Comparison of the microstructural composition of the walls of an elastic artery, muscular artery, arteriole, capillary, venule, and vein. Adapted from [9], licensed under a Creative Commons Attribution 4.0 License [10].

tissue. This efficiency in mass transfer is attributed to the extensive surface area of their walls and, in specific regions, the high permeability of the capillary wall structure. In the organs and through the capillaries, blood is deoxygenated and discharged of nutrients and recharged with carbon

dioxide [11].

Venules receive blood from the capillaries. They also participate in the exchange of oxygen and nutrients. Between the capillaries and venules, post-capillary sphincters, or bands of contractile mural cells that adjust blood flow, can be found. Venules have very thin walls and are susceptible to rupturing when exposed to excessive volume [11].

Veins carry the blood from the different organs back to the heart. Most of the blood pulses are damped in the capillaries and there is also a decrease in pressure. The blood flow is, therefore, at a lower pressure and pulsatility in the veins. This is why veins are thin-walled and less elastic. The second role of the veins is to maintain a reservoir of blood in case of blood loss. Additionally, veins have valves that prevent blood backflow [11].

It is important to note that the description of the microstructure of the blood vessel wall reported in this section is mainly based on what can be seen in classical histology and other microscopy-based techniques, which are often 2D-based techniques and/or are destructive to the sample. This information is then used to obtain 3D schematic representations. As a result, the complex 3D arrangement of the microstructural components is not well understood, making it more difficult to understand the development and progression of cardiovascular diseases (CVDs).

1.2 Cardiovascular occlusive diseases

Malfunctions of the cardiovascular system can lead to severe health complications and can be life-threatening. Indeed, the World Health Organization indicates that CVDs are responsible for 32% of all global deaths making them the leading cause of death worldwide. CVDs are a group of disorders that affect the heart and the blood vessels and they include: coronary artery disease (CAD), cerebrovascular disease (CvD), peripheral arterial disease (PAD), rheumatic heart disease, congenital heart disease, and deep vein thrombosis (DVT) and pulmonary embolism (PE) [12].

The mechanical properties of cardiovascular tissues that allow them to exert their specific function are closely tied to their microstructural composition. However, as described in the previous section, the microstructure of

blood vessels is complex with an intricate arrangement of mainly collagen and elastin fibers, and SMCs, organized in distinct layers, which are challenging to accurately describe in 3D. However, many CVDs are induced by alterations in this particular microstructure, especially the fibrous organization at a microscopic level. Alterations in the microstructure of the blood vessel wall often induce changes in the mechanical properties and can lead to serious complications.

In this manuscript, we will focus on CVDs that affect the blood vessels, and more specifically, cardiovascular occlusive diseases. Atherosclerosis, the predominant cause of cardiovascular occlusive diseases, arises from alterations in the typical signaling and functioning of ECs. It is a chronic inflammatory disease of the arteries and stands as the primary underlying cause behind many other CVDs [13]. The causes of atherosclerosis are often multifactorial. Risk factors include abnormal cholesterol levels, high blood pressure, smoking, diabetes mellitus, obesity, genetic factors, lifestyle habits, and an unhealthy diet. Atherosclerosis development is a complex event involving many cellular and molecular processes. It begins with endothelial dysfunction, which initiates the buildup of lipids within the arterial wall (Fig. 1.4). It is assumed lipids are retained in the intima by a matrix, such as proteoglycans. Subsequently, this lipid accumulation leads to chronic inflammation and eventually to the formation of fibrous plaques, which mature into complex atherosclerotic lesions that are susceptible to rupture or erode. Plaque rupture or erosion is responsible for life-threatening atherothrombosis [13, 14]. Atherosclerosis can affect most of the arteries in the body. The most common locations include the coronary arteries supplying the myocardium, the peripheral arteries in the legs, arms or pelvis (mainly the iliac arteries, and the femoropopliteal and tibial arteries), and the cerebral arteries. Critical atherosclerotic narrowing of the latter arteries leads to CAD, PAD, and CvD, respectively [15]. CAD is the most common one and is responsible for almost half of CVDs [16].

Cellular and molecular mechanisms of atherosclerosis

1. Endothelial dysfunction [13, 18, 19].

   In a healthy artery with high laminar shear stress, ECs are aligned in the direction of flow with low rates of proliferation and death (Fig. 1.5a). In regions where flow is disturbed (*e.g.*, in regions of arterial branching or curvature), ECs are poorly aligned and are in an ac-

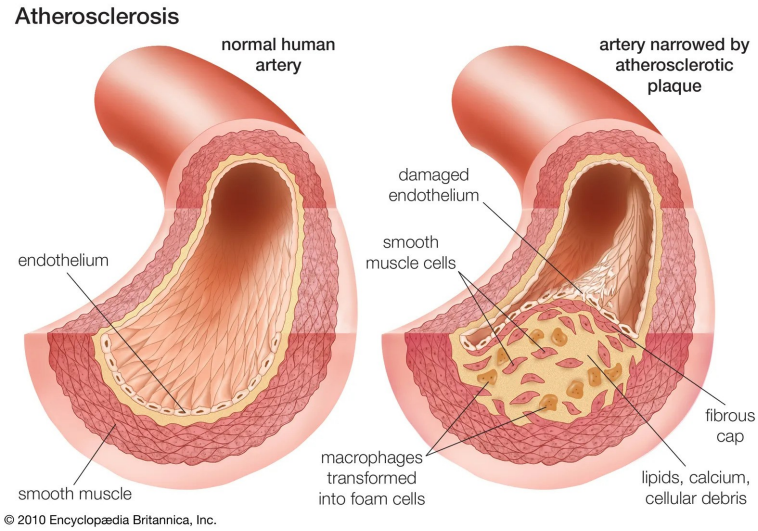


Fig. 1.4 Atherosclerosis stages with schematic view of (A) normal artery and (B) artery narrowed by atherosclerotic plaque [17]. By courtesy of Encyclopaedia Britannica, Inc., copyright © 2010 Encyclopaedia Britannica, Inc; used with permission.

tivated state. In these regions, an increased number of monocytes bind to the endothelium and migrate into the vessel wall (Fig. 1.5b).

2. Plaque formation [18, 20].

   Once in the intima, monocytes differentiate into macrophages, a highly phagocytic type of immune cell. These cells take up low density lipoproteins (LDLs), which carry cholesterol and triglycerides to the tissues. LDL-engorged macrophages are called foam cells. These cells are more activated and secrete cytokines and enzymes that alter the surrounding extracellular matrix and act on the SMCs. This also leads to thickening of the medial layer SMCs and the formation of a fibrous cap (Fig. 1.5c). These small fatty streaks can progress to larger and more inflamed lesions called atherosclerotic plaques, which expand towards the lumen leading to its narrowing (Fig. 1.5d). The rate at which this happens depends on the levels of blood plasma LDLs, oxidants from smoking, elevated blood glucose, and circulating inflammatory mediators. Plaques commonly consist of a central core composed of necrotic cells and fatty deposits containing cholesterol

crystals, foam cells, various immune cells, and SMCs. Later, foam cells undergo apoptosis, releasing their lipid content into the necrotic core of the lesion. The necrotic core of the growing atherosclerotic plaque undergoes calcification due to osteogenic differentiation of pluripotential pericyte-like cells located in the arterial intima.

3. Atherothrombosis [19, 21].

   Highly inflammatory plaques are vulnerable and may rupture. These are plaques that have a thin fibrous cap with low SMC density, and abundant LDL-enriched macrophages. Plaque rupture exposes highly prothrombotic elements to the blood and because prothrombotic factors are not balanced anymore by the anti-thrombotic factors of ECs, platelet activation, inflammation, and activation of the intrinsic pathway of coagulation are induced. These processes result in thrombus formation and eventually thrombosis.

1.3 Treatments for cardiovascular occlusive diseases

Atherosclerosis is extremely difficult to prevent because signs and symptoms only occur after severe narrowing or closure impedes the blood from flowing to different organs. However, before atherosclerosis is too severe, pharmacological treatments exist to improve the regulation of blood pressure and cholesterol levels. Statins are prescribed to reduce the LDLs in the blood by inhibiting hydroxyméthylglutaryl-CoA (HMG-CoA) reductase, a rate-limiting enzyme in the synthesis of cholesterol. This treatment is commonly used as several clinical trials have demonstrated a decrease in major cardiovascular events with the intake of statins, although they are associated with several side-effects, such as muscle pain and injury or liver damage [22]. When risk factor modification, exercise therapy, or medication are ineffective, surgery is considered the gold standard treatment (Fig. 1.6).

1.3.1 Vascular grafts

Before 1978, the only surgical method of revascularization was bypass grafting, a procedure in which a bypass is attached above and below the narrowed area or blockage to create an alternative path for blood flow (Fig. 1.6A) [23]. It is generally a major surgery that requires an extensive recovery process and is typically applied in cases of progressed atherosclerosis

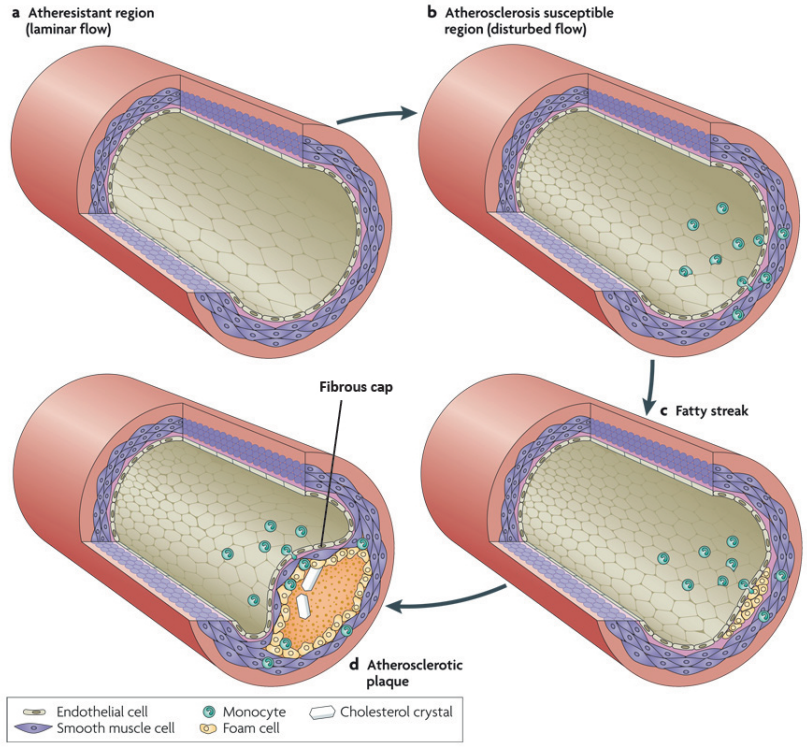


Fig. 1.5 Detailed scheme of atherosclerosis progression. (a) Normal flow in atheroresistant region with high laminar shear stress. (b) Atherosclerosis susceptible region with disturbed flow and accumulation of monocytes binding to the endothelium and going into the vessel wall. (c) Fatty streak formation. (d) Atherosclerotic plaque formation. Adapted from [18]. Reproduced with permission from Springer Nature.

in multiple coronary arteries or complex lesions in major vessels. However, surgical bypass grafting remains one of the most common surgical procedures, even with continuous current revolution of other surgical procedures. Vascular grafts are either autologous vessels or synthetic polymers. If possible, autologous conduits are preferred, however, synthetic conduits have to be used when the autologous vessels are unavailable, have inadequate size or are of poor quality. Saphenous vein grafts (SVG) are the preferred choice in 80% of bypass surgeries due to the ease of harvesting and handling, the reduced complexity of vein grafting (compared with multiple arterial grafting), and the often unavailability of arterial grafts due to

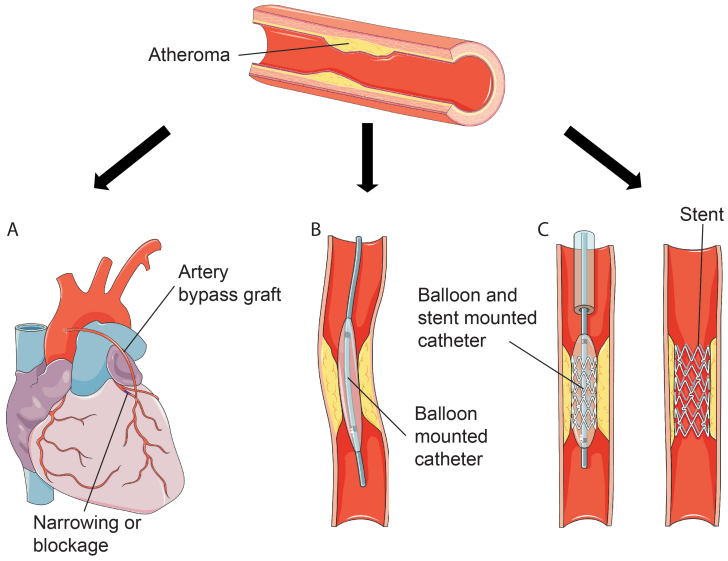


Fig. 1.6 Surgical treatment options for artery narrowing or blockage caused by atherosclerosis. (A) Coronary artery bypass graft. (B) Balloon angioplasty. (C) Stent placement using a stent mounted on a balloon and catheter for stent inflation and placement. Adapted from Servier Medical Art, licensed under a Creative Commons Attribution 3.0 Unported License [3].

previous usage or these being diseased themselves [24]. Synthetic grafts, such as polyethylene terephtalate (PET) from Dacron or expanded polytetrafluoroethylene (ePTFE) from Gore-Tex, demonstrate promising results, especially in arteries with medium-sized diameter (6-8 mm). However, mainly in smaller-caliber vessels, results have not been satisfactory due to thrombus formation, poor patency and biocompatibility, and a mismatch in compliance between the graft and the native vessels [25, 26].

1.3.2 Balloon angioplasty

In 1978, the first balloon angioplasty procedure was performed. Balloon angioplasty consists in the insertion of a balloon and catheter in the vessel. The balloon is inflated to compress the plaque to effectively reopen the vessel lumen (Fig. 1.6B). More specifically, the surgeon inserts a special needle, called a trocar, in the patient's leg or arm. Then, a catheter is guided to the problematic area in the body. Once the restricted area is well identified, the balloon mounted on a thin wire is inserted in the

catheter and brought precisely in the most narrow part of the vessel. The balloon is then briefly inflated, compressing the plaque deposits against the wall of the artery. The artery is stretched resulting in an enlargement of the lumen. However, this sometimes results in uncontrolled application of pressure and although this technique was a considerable breakthrough in the field of cardiovascular treatments, the procedure is associated with 1% risk of acute vessel dissection and 30-50% risk of restenosis in the coronary arteries [27].

1.3.3 Intravascular stents

To mitigate the side-effects of balloon angioplasty, stent placement was developed. A stent is a small mesh tube that remains in the vessel to provide mechanical support to the vessel wall. A stent is either self-expanding (slow radial expansion) or is inserted using a balloon catheter (Fig. 1.6C) [28]. The first human stent was implanted by *Sigwart et al.* in 1986 [29]. In later years, the results from a number of clinical trials consistently demonstrated that stent placement led to reduced restenosis rates in comparison to balloon angioplasty [14]. The early success of stent placement procedures paved the way for their extensive use in interventional cardiology and stent placement has become one of the gold standard treatment strategies. Nonetheless, there are still many issues caused by the continued presence of the stent within the vessel, with the risk of late target lesion failure and late or very late thrombosis.

1.3.4 Tissue-engineered vascular grafts

A tissue-engineered vascular graft (TEVG) aims to create a material that integrates with native tissue to restore, maintain, or improve physiological function with three interdependent components: cells, a scaffold, and signals (*e.g.* growth factors, biomechanical stimulation, etc.) [24]. The first real tissue engineered blood vessel constructed *in vitro* was reported by *Weinberg and Bell* in 1986 and consisted of collagen gel tubes and cultures of vascular cells from bovine origin, such as ECs, SMCs, and fibroblasts from the adventitia [30]. An ideal TEVG should be designed with a scaffold that shapes the graft and with an adhesive matrix consisting mainly of fibrin and vascular cells. It should have high strength to prevent rupture and facilitate manipulation and be of adequate size to replace the host tissue [25]. Some clinical results from arteriovenous access and pediatric reconstructive surgery for cavopulmonary grafting (oxygen-poor blood coming from

the vena cavae is directed directly to the pulmonary artery instead of going through the heart chambers) are promising and show that TEVGs are moving from laboratory-based academic research to clinical applications but further confirmation of graft efficacy, safety, and long-term function are still required, and need to be assessed in additional controlled studies to push them to direct clinical applicability [31]. There is still a lack of comprehensive understanding on the various biological and biophysical factors that influence the development of engineered tissues during *in vitro* incubation and remodeling after *in vivo* implantation, particularly, on how cells establish, maintain, remodel or repair the ECM, which ultimately determines the overall integrity of the graft and the environment to which they react [24]. More recently, computational-experimental paired approaches (*in silico* combined with *in vitro* or *in vivo*) have been investigated to optimize the design of new frameworks to describe and predict bio-chemo-mechanical phenomena relevant to TEVG growth, development, and integration. *In silico* models are useful to identify key regulating parameters, predict behavior, and minimize variability, increase quality, and optimize the design process [32].

1.3.5 Clinical application

In the University hospital of Saint-Luc in Brussels[1], around 60% of patients who suffer from atherosclerosis are treated with endovascular techniques. Out of this, around 30% of patients are treated with balloon angioplasty and 70% are implanted with an intravascular stent. The choice depends on the location and the morphology of the lesions.

Vascular grafts are employed in around 40% of cases, with around 65% being synthetic grafts (around half of the grafts used are Dacron and the other half are Gore-Tex), and the remaining 35% being autologous grafts. The primary patency of suprapopliteal (above the knee) synthetic grafts is 70% and of infrapopliteal (below the knee) synthetic grafts is 40% after 5 years. Grafts are mostly used to treat the coronary and the femoral arteries. Dacron is mostly chosen when above the knee (higher femoropopliteal intervention) and Gore-Tex when below the knee (lower femoropopliteal intervention) because Gore-Tex has heparin-coated grafts, which are more favorable against thrombosis.

[1] Personal communication with Prof. Valérie Lacroix

2

Problem statement, thesis aim and objectives

2.1 Problem statement

Treatments for cardiovascular occlusive diseases, such as the ones mentioned in chapter 1, remain a prominent and ongoing research topic as they continuously reduce the number of people that face disability. Nevertheless, CVDs still remain a major public health issue emphasizing the need to focus on prevention. A better understanding of the microstructure of healthy and diseased vessels will allow to better understand the mechanisms underlying diseases. Examining and monitoring microstructural alterations can offer insights into the stage of development of a disease and can inform on strategies to target specific aspects of vascular pathology. However, the native blood vessel wall microstructure is still not fully understood because there is a lack of methods that allow high-resolution structural quantitative analysis of large tissue sections in 3D. For now, the analysis of the microstructure is in many cases based on qualitative observations. Because of the complex 3D organization of cardiovascular tissues, the use of non-destructive 3D imaging techniques is crucial. X-ray microfocus computed tomography (microCT) is a 3D imaging technique that has recently been recognized as a valuable method to image the structure and

microstructure of complex materials in a non-destructive way [33].

Prior to becoming a standard imaging technique for biological tissues, microCT still faces several challenges due to the restricted ability of X-rays to differentiate different soft tissue constituents [33, 34]. Several techniques exist to improve the discrimination of soft tissues. One approach is to use microCT in phase contrast mode to enhance the interfaces between soft tissue constituents. It is then referred to as phase-contrast computed tomography (PCCT) [35]. This, however, requires a highly coherent synchrotron X-ray source or a specialized laboratory-based system. Alternatively, to be able to image biological samples with bench-top devices and with enough discrimination between the soft tissue constituents, microCT can be combined with contrast-enhancing staining agents (CESAs). It is then referred to as contrast-enhanced computed tomography (CECT) [36, 37]. In this case, the X-ray attenuating properties of the different constituents are increased by immersion of the biological sample in a staining solution containing heavy atom elements. Although several CESAs have been tested to image complex biological samples, the exact binding mechanisms are still poorly understood and many CESAs are destructive to biological samples, causing for instance an important tissue shrinkage [38]. Therefore, in a first step, the optimization of CECT for imaging in a non-destructive way and in 3D the microstructure of native and diseased blood vessels is required. Visualization of elastin, one of the main components that contribute to the mechanical behavior and which is intricately organized within the layers of vascular tissue, is crucial to better understand the functional behavior of different blood vessels and, hence, to improve treatment outcomes. For this, the optimal CESA as well as imaging protocol for CECT need to be identified.

Once optimized for healthy and diseased blood vessels, microCT and CECT can be used to assess and optimize different treatment options for cardiovascular occlusive diseases. Synthetic vascular grafting and intravascular stenting are two of the major surgical treatments. As mentioned in chapter 1, in the university hospital of Saint-Luc in Brussels, approximately 26% of patients are treated with a synthetic vascular graft and around 42% of patients are implanted with a stent in case of severe artery narrowing or blockage[1]. However, these clinical procedures still fail for many patients.

[1]Personal communication with Prof. Valérie Lacroix

The current challenges with vascular grafts originate from concerns surrounding biocompatibility, the mismatch in compliance between synthetic grafts and healthy tissue, and the fact that the same grafts are used to bypass many types of blood vessels, highlighting the need to further research and improve current treatments. More in-depth *ex vivo* characterization of the 3D microstructure of (i) different types of healthy blood vessels and (ii) currently used synthetic grafts at high resolution is essential to better understand the reasons behind the gap in functional behavior between both.

Permanent intravascular stents, although widely used, induce late-stage complications, such as thrombosis, inflammation, and stent fracture, highlighting the need for improved alternatives. Biodegradable stents are being investigated to mitigate these long-term effects but the ideal material that satisfies the criteria of appropriate mechanical behavior, degradation rate, and biocompatibility has not yet been found. *In vitro* evaluation of new biodegradable stent materials still often involves 2D techniques, such as scanning electron microscopy (SEM), which do not allow visualization and assessment of the degradation behavior of the full material. The same accounts for the *in vivo* evaluation of candidate materials in host tissue, for which it is important to study the interactions between the stent and the host in full 3D. This evaluation is often still done using classical 2D histology.

To conclude, it is clear that non-destructive 3D characterization is essential. Despite the remaining challenges associated with microCT and CECT, these techniques represent promising candidates to image in full 3D the microstructure of complex biological tissues (*i.e.*, to perform X-ray-based 3D histology) as well as to help improve disease treatments.

2.2 Thesis aim and objectives

Based on the context given in the previous section, we highlighted the need for non-destructive, high-resolution *ex vivo* 3D imaging and characterization of vascular tissues to improve our understanding of the microstructure of native tissues, the effect of changes in microstructure due to diseases, as well as to improve current treatment options, such as synthetic grafts and vascular stents.

MicroCT is a valuable 3D imaging technique used for visualizing mate-

rials that have sufficient X-ray attenuating properties. Therefore, microCT was optimized and used to visualize and characterize two types of synthetic materials: (i) different currently used synthetic vascular grafts and (ii) candidate metallic stent materials for intravascular stents. Since microCT is unable to image and distinguish different biological soft tissues due to their low X-ray attenuating properties, CECT imaging was optimized for the visualization and characterization of (i) different types of native vascular tissues and (ii) native rat aortas implanted with different metallic stent materials. In this context, this thesis has been subdivided in three main objectives.

2.2.1 Objective 1

Development and optimization of *ex vivo* microCT and CECT to evaluate the blood vessel wall of different types of blood vessels in different species and comparison with synthetic vascular grafts.
The first objective is dedicated to the optimization of *ex vivo* microCT-based techniques to gain insights into the 3D microstructure of native blood vessels with the aim, in the future, to improve current treatments for vascular diseases, such as vascular grafts. A comparative study of two different CESAs (Monolacunary and 1:2 Hafnium-substituted Wells-Dawson polyoxometalate) is performed based on staining time and contrast enhancement for imaging of the healthy porcine aorta. After optimization of CECT, differences between the blood vessels of different species (rat, porcine, and human) as well as between different blood vessel types (elastic artery, muscular artery, and vena cava, *i.e.*, aorta, femoral artery, and vena cava, respectively) in the porcine model are investigated. These differences are important to consider when studying microstructure with the aim of improving treatments for cardiovascular diseases. Indeed, large differences in the microstructure of different types of blood vessels show that the same treatment cannot be applied to every type of blood vessel and that results may vary depending on the animal model chosen. We also show the possibility to extract 3D quantitative information from the rat and porcine aortic wall, potentially to be used for computational modeling or for future design optimization of graft materials. Finally, a structural comparison with existing synthetic vascular grafts is made. This information aims at better understanding the *in vivo* functioning of native blood vessels and to improve current disease treatments.

2.2.2 Objective 2

Development and optimization of *ex vivo* microCT to evaluate the degradation behavior of candidate stent materials *in vitro*.
The second objective focuses on the optimization of *ex vivo* microCT-based techniques to study the *in vitro* behavior of candidate materials to be used as metallic biodegradable intravascular stents. MicroCT is used to evaluate the degradation mode, degradation rate, and material surface properties in 3D and at high resolution of large regions of interest of metallic implants. Three candidate biodegradable stent materials are evaluated in the form of wires, which simulate a single stent strut: pure iron, pure zinc, and a quinary zinc alloy (Zn-Ag-Cu-Mn-Zr). These metals are compared to a reference currently used permanent cobalt-chromium alloy. To validate the degradation mode and degradation rate evaluated with microCT, SEM and inductively-coupled plasma (ICP) are included. The aims of this study is to gain insights into the essential surface and corrosion properties of different biodegradable metals in a non-destructive way. This initial screening phase is crucial in evaluating their potential as suitable materials prior to going to *in vivo* animal studies.

2.2.3 Objective 3

Development and optimization of *ex vivo* microCT and CECT to evaluate the *in vivo* degradation behavior and biocompatiblity of candidate stent materials.
The third objective focuses on the optimization of *ex vivo* microCT-based techniques to study the *in vivo* behavior of candidate materials to be used as metallic biodegradable intravascular stents. The same four metals as those assessed in the previous objective (Co-Cr alloy, Fe, Zn, and the quinary Zn alloy) are implanted in the rat abdominal aorta, also in the form of wires. Rats are sacrificed, and after collection, explants are imaged with microCT to evaluate the degradation rate and behavior of the metals. Explants are also stained and imaged with CECT to visualize the interactions between the metals and the surrounding host tissue and to characterize the morphometrics of the neointimal tissue. The *in vivo* evaluation of these materials in 3D and in a non-destructive way helps to gain a better understanding of their biological integration and aims at improving the development of new biodegradable implants.

2.3 Thesis overview

The structure of this manuscript is detailed in Fig. 2.1. After a description of the cardiovascular system and cardiovascular occlusive diseases and their treatments in the introduction (Part I, chapter 1), Part II focuses on the microCT-based imaging of native blood vessels and synthetic vascular grafts and is divided in two chapters. The first one, chapter 3, presents the state-of-the-art on the current *ex vivo* X-ray-based imaging techniques used to characterize the cardiovascular system. The second one, chapter 4, describes our study in which microCT-based techniques are used to visualize and quantify structural parameters of the blood vessel wall constituents in native blood vessels and currently used synthetic vascular grafts. Part III is subdivided in three chapters. Chapter 5 gives an overview of the literature on the advancements that have been made regarding the development of biodegradable intravascular stents. Chapter 6 presents our study in which microCT imaging was used to characterize the degradation behavior of different candidate materials for intravascular stents using *in vitro* immersion tests. Chapter 7 covers our study in which microCT-based imaging techniques were used to analyze the degradation behavior and the biocompatibility of different candidate materials for intravascular stents in an *in vivo* study in a rat animal model. Part IV, chapter 8, concludes this manuscript with a general discussion and some future perspectives.

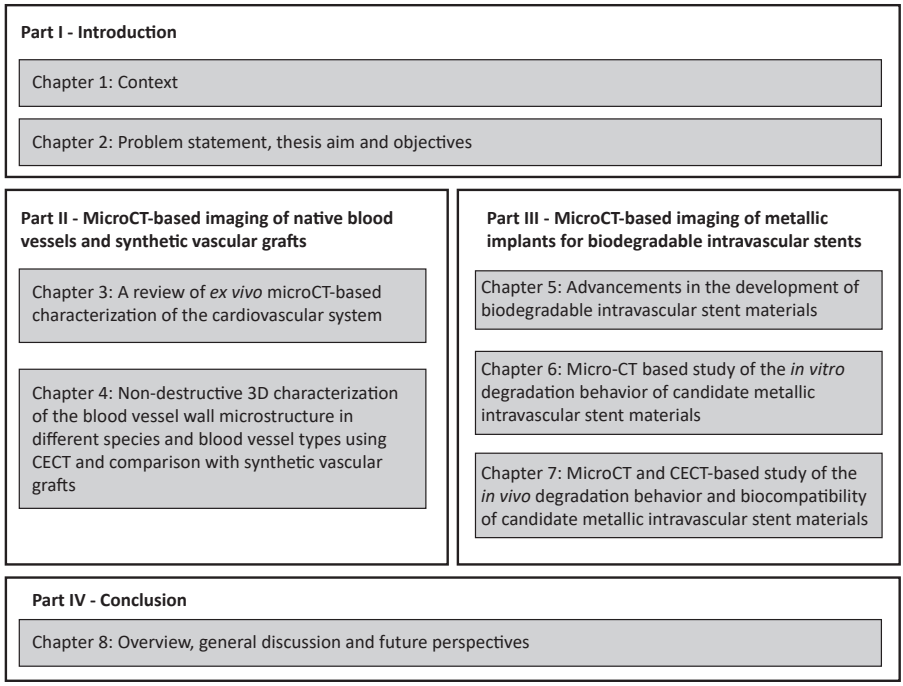


Fig. 2.1 Scheme presenting the structure of this thesis manuscript.

PART II
MicroCT-based imaging of native blood vessels and synthetic vascular grafts

3

A review of *ex vivo* microCT-based characterization of the cardiovascular system

Publication

A review of *ex vivo* X-ray microfocus computed tomography-based characterization of the cardiovascular system.

Leyssens, L.; Pestiaux, C. Kerckhofs, G. *International Journal of Molecular Sciences* 2021, 22, 3263. https://doi.org/10.3390/ijms22063263

Positioning in the context of this PhD thesis

This thesis focuses on the assessment of X-ray-based technical advancements for investigating healthy cardiovascular tissues and treatments for cardiovascular diseases. The purpose of this chapter is to present the cur-

rent state of the art regarding X-ray-based imaging techniques (mainly microCT, PCCT and CECT) to visualize and analyze the structure of cardiovascular tissues in a non-destructive way. The advantages of *ex vivo* microCT, CECT and PCCT for quantitative 3D imaging of the heart (the entire heart, the myocardium, and the heart valves) and the vasculature (the vascular tree and the microstructure of the vessel wall) are discussed in healthy and diseased state. Finally, this chapter highlights the remaining challenges, mainly with regard to the spatial resolution, the lack of quantitative data, and the contrasting methods for cardiovascular soft tissue imaging. This literature review has been accepted for a publication, in which L. Leyssens was joint first author and focused on the section related to the vasculature.

3.1 Introduction

Cardiovascular diseases are the number one cause of death worldwide, especially since their main risk factors such as obesity, a poorly balanced diet and high blood pressure are on the rise. Deaths due to diseases of the cardiovascular system represented 35.7% of all deaths in Europe in 2016 [39]. Ischemic heart disease (usually referred to as a heart attack), cerebrovascular disease (stroke) and atherosclerosis are among the most common cardiovascular diseases. Congenital cardiovascular defects affect 8% of births in Europe each year [40], and only 40% of fatal malformations are detected before death. The early diagnosis of heart malformations could, therefore, save a substantial number of lives. Valvular diseases concern more than 10% of the people over the age of 75 [41], the aortic and mitral valves being the most affected ones. In addition to primary cardiovascular diseases, external conditions can affect the cardiovascular system, such as Marfan syndrome [42], kidney disease [43–46], tumors [47–49] and many others.

Unfortunately, the exact causes of many cardiovascular diseases are still not fully understood. The current treatments continuously decrease the number of people that face disability, reduced quality of life and premature death. Nevertheless, cardiovascular diseases still remain a major public health issue. As the structures and microstructures of tissues play a crucial role in their proper functioning, improving the understanding of alterations in the structural properties of the cardiovascular substructures due to diseases is crucial to better understand the diseases or to further improve their treatments.

Nowadays, several *in vivo* imaging techniques exist to visualize the cardiovascular system and improve the understanding of its diseases by assessing its anatomy and functional behavior. Ultrasound imaging (USI), nuclear imaging, magnetic resonance imaging (MRI) and X-ray computed tomography (CT) are the most popular clinical in vivo imaging techniques [50].We can distinguish between structural imaging (CT and MRI) and functional imaging (USI, nuclear imaging and MRI). Structural imaging allows visualizing the spatial distribution and organization of the different substructures in an organ, while functional imaging enables the detection of changes in physiological activities. The current *in vivo* imaging devices are, however, limited in their attainable spatial and contrast resolution. The maximum spatial resolution for small animal *in vivo* imaging is obtained with microscopic MRI (microMRI) and X-ray microfocus CT (microCT) and is still limited to 25 µm [51] and to 10 µm [52], respectively. The resolution is mainly driven by the size of the sample, the restricted radiation dose and the fast acquisition time.

Ex vivo imaging is more suited to perform high-resolution imaging and a microstructural analysis of the heart and the vasculature. To that end, histology is still the gold standard. It enables the *ex vivo* assessment of the (micro)structure and composition of the cardiovascular system at both the tissue and cellular levels by providing 2D sections of the tissue with a resolution around 0.25 µm [53]. However, it results in the destruction of the sample, preventing further analysis, and the 3D reconstruction of the tissue requires image stacking and is highly labor-intensive. Moreover, it renders an anisotropic resolution; it is prone to artefacts and the sample preparation (fixation, embedding and cutting) can potentially alter the structural organization of the tissue [54–56]. Episcopic microscopy has already reduced some of the drawbacks of standard histology by automatically aligning the images of paraffin-embedded samples during sectioning, making the 3D reconstruction easier, but it does not prevent the destruction of the sample and still renders an anisotropic resolution [57]. Coupling optical microscopy imaging techniques such as fluorescence, two-photon and harmonic microscopy with advanced postprocessing techniques has also proven its effectiveness [58–60], especially in terms of resolution by allowing cellular-level imaging. However, the extraction of quantitative data is highly labor-intensive and is still limited. *Ex vivo* microMRI has also demonstrated promising results, especially in terms of soft tissue ima-

ging with a resolution going up to 20 µm [61–63]. To visualize fibrous structures, for example, to define myocardiocyte orientation, diffusion tensor MRI (DT-MRI) has been used [64–66]. However, in both cases, a high magnetic field and long scan times are required to achieve sufficiently high spatial resolution for a microstructural analysis of the tissues, which strongly increases the cost of the experiments. In combination with the appropriate contrast-enhancing techniques, microCT has the advantages of MRI (*i.e.*, 3D imaging in a nondestructive manner) while keeping the scan time much lower [67] and obtaining even better spatial resolution (<1 µm) [38]. Hence, in this review, we decided to describe the use of *ex vivo* microCT-based imaging techniques for the characterization of the cardiovascular system. We discuss the potential of microCT to visualize and quantitatively describe the structure and microstructure of healthy and diseased cardiovascular tissues. We show that this technique allows to visualize in full 3D the tissue microstructure and the spatial distribution of the tissue substructures (*e.g.*, collagen, elastin and myocardial fibers). In addition, microCT can provide morphometrical information, which is a quantitative analysis of the tissue characteristics, such as volume, diameter, density, length and spatial distribution.

The structure of this review is presented in Fig. 3.1. Hereafter, we provide a general description of the microCT-based techniques and a summary table of the contrasting agents used for analyzing the cardiovascular system. An overview of the microCT-based imaging of the heart and the vasculature are given in Sections 3.3 and 3.4, respectively. We finish with a brief conclusion on the current limitations and future perspectives.

3.2 General description of microCT, CECT and PCCT

MicroCT has two different imaging modes: absorption and phase contrast. In absorption mode, most often, benchtop devices are used with a polychromatic X-ray source. Images are generated based on the attenuation of the X-rays by the material. With phase-contrast microCT (PCCT) synchrotron is generally used in which the X-ray beam has a large spatial coherence. It allows computing the phase shift due to the interaction of the beam with the electrons in the material [69]. Imaging using phase contrast, as opposed to absorption contrast, is a powerful method to investigate low absorbing materials and to distinguish tissues with very similar X-ray attenuation but different electron densities [70–72]. However, access to a

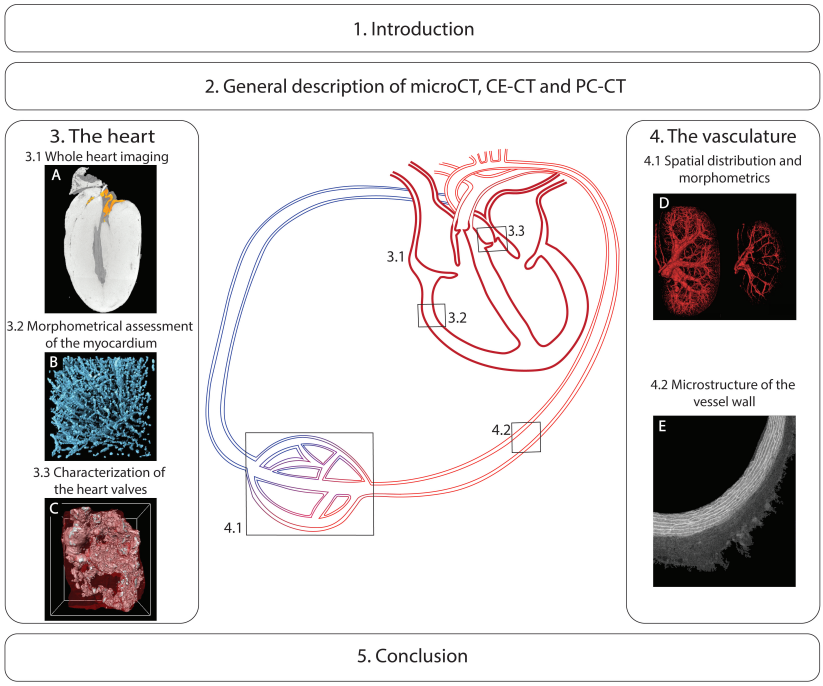


Fig. 3.1 Schematic representation of the published review. Section 3.2 corresponds to a general description of X-ray microfocus computed tomography (microCT), contrast-enhanced microCT (CECT) and phase-contrast microCT (PCCT). Section 3.3 describes the use of microCT for imaging the heart with three different parts: (A) the whole heart, (B) the morphometrical assessment of the myocardium (adapted from Reference [68]) and (C) the heart valves. Section 3.4 focuses on (D) the spatial distribution and morphometrics of the vasculature (adapted from Reference [43]) and (E) the vessel wall microstructure. The conclusion mentions the current limitations and future perspectives.

synchrotron is not always guaranteed, and, thus, for routine imaging, absorption mode imaging with benchtop devices is still most often used.

X-rays are highly attenuated by dense materials, such as calcified tissues. However, in absorption mode, there is a need to use contrasting agents composed of atoms of high atomic numbers to stain and, thus, differentiate the low absorbing (soft) tissues. Combining microCT with contrast agents (CAs) is further referred to as contrast-enhanced microCT (CECT). Two types of contrasting agents can be used: casting contrast agents (CCAs) or contrast-enhancing staining agents (CESAs). A CCA fills up the blood vessels or the heart, usually by perfusion, allowing for the visualization and measurement of the volume and the identification of the spatial distribution of the structure [45, 73]. CCAs are useful to obtain an overall view of the anatomy, but they also present some disadvantages. The perfusion pressure is important and needs to be carefully monitored. Too-high pressures can lead to tissue damage, whereas too-low pressures might result in incomplete filling of the desired vessels. Viscosity is also an important factor to consider for reaching the smaller capillaries and for keeping the perfusion pressure low [74–76]. Alternatively, the tissue can be stained through passive diffusion by immersion in a solution containing a CESA. During diffusion, the CESA interacts with the tissue, rendering it X-ray-attenuating, which enables the characterization of its microstructure [38]. Unfortunately, knowledge about the interaction mechanisms between the CESA and the tissue is often lacking. Additionally, some CESAs are known to be destructive, altering the native structure of the tissue [38, 77]. Finally, both the concentration of the CESA and the staining time need to be adapted for each tissue type.

Table 3.1 provides a summary of the three main microCT based imaging techniques for biological tissues. In Table 3.2, an overview is given of the different CAs that have been used for CECT imaging of the cardiovascular system.

Table 3.1 Pros and cons of X-ray microfocus computed tomography (microCT)-based imaging techniques for biological tissues.

Technique		Pros	Cons
MicroCT without contrast- or phase-enhancement	Attenuation of the X-rays by the tissues	• High contrast between dense and soft tissues, for example, allowing the detection of calcifications in the cardiovascular system • Readily available	• No differentiation between distinct soft tissues
Contrast-enhanced microCT (CECT)	Attenuation of the X-rays by the tissues and the CAs	• Good distinction between soft tissues • Readily available	• Need for nondestructive CAs • Staining mechanisms of CESAs not fully understood, needs optimization to find component-specific agents • Difficult to control the perfusion pressure in order for the CCA to reach all the capillaries
Phase-contrast microCT (PCCT)	Phase shift at interfaces between different tissue constituents	• No need for CAs • Good distinction between soft tissues	• Complex computation of phase shift • Not readily available • Often requires dehydration of the tissue

Table 3.2 Summary table for contrast agents used in CECT imaging of the cardiovascular system with their composition, characteristics and references.

Casting Contrast agents (CCAs)			
Contrast agent	**Composition**	**Characteristics**	**References**
Microfil	Lead-containing radiopaque silicone rubber	• Time-based hardening (polymerization) of a cast in the luminal space of cardiovascular structures for qualitative volumetric analysis • High viscosity not always allowing complete vascular filling	[43, 45–50, 73, 75, 78–84]
µAngiofil	Angiofil (liquid radiocontrast agent based on iodine), Orasol Blue dye, polyurethans resin, hardener	• Time-based hardening (polymerization) of a cast in the luminal space of the vasculature for quantitative volumetric analysis • Lower viscosity than Microfil allowing more complete vascular filling	[85–87]
Barium sulfate	$BaSO_4$	• Temperature-based gelation of a cast in the luminal space of the vasculature for quantitative volumetric analysis • Higher viscosity than Microfil and µAngiofil, sometimes leading to inconsistent vascular filling	[49, 73, 75, 80, 88–90]

Table 3.2 (continued)

Contrast-enhancing staining agents (CESAs)			
Contrast agent	**Composition**	**Characteristics**	**References**
Lugol's iodine	I_3K (often referred to as I_2KI)	• Specifically stains unsaturated lipids through covalent interactions: stains muscle, fat and connective tissue • Used for cardiac tissue resulting in a good delineation of the ventricular myocardium and identification of fiber bundles • Tissue shrinkage is observed	[77, 91–107]
Osmium tetroxide	OsO_4	• Specifically stains unsaturated lipids through covalent interactions • Used to highlight lipid-rich plaques in the artery wall • Tissue shrinkage is observed and the compound is very toxic	[108, 109]
Sodium Polytungstate (SPT) (also referred to as sodium metatungstate)	$H_2Na_6O_{40}W_{12}$	• Specifically stains elastic fibers • Has been used for visualization of elastic fibers in blood vessels during tensile and circumferential loading tests to observe mechanisms of damage • No tissue shrinkage observed	[110, 111]

Table 3.2 (continued)

Modified Verhoeff's stain (Tri-element stain with iodine, aluminium, and iron)	56% v/v aluminium hematoxylin, 2.2% w/v $FeCl_3 \bullet 6H_2O$, 0.6% w/v KI and 0.3% w/v I_2	• Specifically stains elastic fibers and endothelial cells • Was used in whole-body perfusion for staining of the vessel wall • Inert and no known toxic properties	[112]
Phosphotungstic acid (PTA) *Keggin POM*	$H_3PW_{12}O_{40}$	• Specifically stains fibrin, collagen, fibers of connective tissue and blood • Used for observation of the collageneous structures of the vein walls and whole-heart imaging (fiber structure of the atrium, ventricles, myocardium and vessel walls) • Tissue shrinkage is observed (one of the strongest acids among the POMs)	[99, 105, 113]
Phosphomolybdic acid (PMA) *Keggin POM*	$H_3PMo_{12}O_{40}$	• Specifically stains collageneous components and blood • Used for observation of the collageneous structures of vein walls • Tissue shrinkage is observed (even more than for PTA)	[99]

Table 3.2 (continued)

Zirconium-substituted Keggin POM (Zr-POM) *Keggin POM*	$(Et_2NH_2)_{10}[Zr(PW_{11}O_{39})_2]$	–	• Specifically stains muscle, connective tissue and blood, fat tissue is not stained and thus can be differentiated from stained tissues • Used for visualization of the vascular structure in the placenta (Zr-POM), kidney and bone marrow and its vasculature (1:2 Hf-WD POM and Mono-WD POM), the heart and the blood vessel wall layers (1:2 Hf-WD POM) • Less tissue deformation than Lugol's iodine, PTA, PMA and OsO_4	[114]
1:2 Hafnium-substituted Wells-Dawson POM (1:2 Hf-WD POM) *Wells-Dawson POM*	$K_{15}H[Hf(\alpha_2 P_2W_{17}O_{61})_2]\bullet 19H_2O$	–		[115, 116]
Monolacunary-Wells-Dawson POM (Mono-WD POM) *Wells-Dawson POM*	$\alpha_2 K_{10}P_2W_{17}O_{61}\bullet 20H_2O$	–		[116]

3.3 The heart

The heart is the central organ that pumps the blood through the vessels to bring nutrients and oxygen to the rest of the body. In this section, we distinguish three categories of studies: (i) studies about the visualization of the overall morphology of the whole heart and changes due to a disease or a malformation, with the aim of validating the imaging protocol, (ii) studies on the morphometrical analysis of the fibers in the myocardium and (iii) studies dedicated to characterizing the heart valves.

3.3.1 Anatomical and morphometric assessment of the whole heart

The heart is a complex and highly heterogeneous organ. Imaging the whole heart in full 3D gives important insights into cardiac diseases that structurally alter the heart. CECT and PCCT imaging have been applied on small samples to visualize cardiac diseases or malformations in animal models, to investigate the human fetus heart in case of intrauterine death and to provide quantitative information such as a chamber's volume or mass.

The integrity of the septum and the valves, the position of the chambers and the connection of the main vessels of the heart have been evaluated using both CECT [77, 97, 101, 103, 108] and PCCT [68, 117] to investigate cardiac diseases or malformations. Anatomical defects associated with complex cardiac diseases, such as intrauterine growth restriction and tetralogy of Fallot, were revealed in animal models. The complete 3D visualization of the whole heart allowed the visual inspection of the heart morphology at different stages of embryogenesis, with or without genetic alterations. For instance, *Kim et al.* were able to distinguish subjects with and without congenital heart defects, such as ventricular septal defects, persistent truncus arteriosus and aortic arch anomalies, in a group of mice [103]. *Degenhardt et al.* successfully applied CECT to detect a previously unappreciated cardiac venous connection in the rodent model they studied [77]. Moreover, *Midgett* and colleagues used CECT to identify the wrong positioning of the main vessels, ventricular septal defects and tetralogy of Fallot after changing either the inflow or outflow tracts of the heart in chick embryos. They concluded that the distinct abnormalities were correlated to the degree of hemodynamic alteration. They highlighted that altered blood flow can lead to congenital heart defects and that genetic alteration

is not the only possible cause [97]. CECT is, thus, able to provide important information about the developmental processes for various cardiac diseases. Where the studies mentioned above are based on CECT using Lugol's iodine, *Gonzalez-Tendero et al.* applied PCCT without any CESA to image the hearts of rabbits after intrauterine growth restriction and compare them with the control samples. Although this imaging technique did not require any staining, a dehydration step was necessary, which induced tissue shrinkage [117].

A particular application, for which CECT has shown its greatest potential, is the 3D anatomical analysis of the human fetus heart in the case of unexplained intrauterine death. The nondestructive visualization of the heart chambers, heart valves and main vessels provided by CECT imaging using Lugol's iodine staining allows researchers to make the same diagnosis as the standard autopsy or to obtain a final diagnosis when the autopsy cannot determine the cause of death [96, 102, 104]. This is particularly true for challenging specimens, on which a standard autopsy is usually precluded because of size restrictions or changes in the soft tissues (maceration). These conditions can increase the complexity of the autopsy by creating artificial structural changes and lead to a wrong diagnosis. In this regard, CECT offers a valuable alternative diagnostic tool to visualize the anatomical structures. Moreover, from an ethical point of view, the use of a nondestructive evaluation technique is more accepted by parents. As a proof of concept and to avoid using CESAs, several groups also applied PCCT to human hearts from fetuses and infants, and they demonstrated detailed visualizations of the cardiac anatomical features [118–120]. *Garcia-Canadilla et al.* were able to characterize the complex congenital heart disease of a mid-gestation fetus through the identification of right-sided heart (wrong orientation of the heart), atrioventricular septal defect and wrong connection of the vessels [120].

In the previous paragraphs, we presented the anatomical description of cardiac malformations in animal models and human fetuses. In addition to this, CECT in combination with a CCA can be used to determine the volume of the heart chambers and the blood vessels. *Butcher et al.* perfused Microfil in the blood vessels and the heart cavities of chicks at various embryonic stages [84]. They were able to quantify the volumetric variations and to illustrate the changes in the shapes of the atrioventricular valves and septa during development. Nevertheless, their perfusion tech-

nique requires a lot of fine-tuning and is not robust. Moreover, instead of staining the tissue itself, the cavities in the tissue are filled and, thus, visualized. If they are too small or if their walls have collapsed, the cavities could potentially be neglected. Therefore, staining the tissue with a CESA might be more accurate, since it improves the contrast of the soft tissues in a sample and helps to identify its microstructure. Lugol's iodine was used on mouse hearts by *Merchant et al.* and *Doost et al.* to measure the thickness of the compact myocardium and the mass of the left ventricle, respectively [98, 106]. Although many studies have been carried out to optimize the staining of cardiac tissues with Lugol's iodine [77, 95, 100, 107, 121], this CESA is still known to cause tissue shrinkage, and hence, morphometric measurements can be biased. *Dullin et al.* proposed phosphotungstic acid (PTA) as a CESA for volume measurement, even though it is also known to introduce tissue shrinkage [113]. To reduce tissue deformation, PCCT imaging is a solution, because no contrasting agent is required to visualize the soft tissue. However, the sample often needs to be dehydrated during the preparation. Our own data shows that one of the solutions to avoid tissue shrinkage is the use of CECT with a less destructive CESA, such as Hafnium-substituted Wells-Dawson polyoxometalate (1:2 Hf-WD POM) [115, 116]. Fig. 3.2 illustrates the application of the successive staining of 1:2 Hf-WD POM (Fig. 3.2 A-E, K) and isotonic Lugol's iodine (Fig. 3.2F-J, L) on a mouse heart. The heart was then sectioned and stained with Masson's trichrome for comparison (Fig. 3.2M,N). For both CESAs, the valves can be segmented, as shown in the 3D renderings (Fig. 3.2A, F). The connection of the chambers and the large vessels can be highlighted (red arrows), and the heart valves can be visualized (*). By the comparison between Fig. 3.2C,H, it can be seen that the thickness of the myocardium is highly reduced after staining with isotonic Lugol's iodine, indicating pronounced tissue shrinkage.

As described in this section, both CECT and PCCT are valuable tools to complement the standard histology for the anatomical evaluation and morphometrical assessment of the heart. Nevertheless, they are still limited to small samples, and the preparation should still be improved to preserve the native anatomy of the tissue, for example, by using nondestructive CESAs such as 1:2 Hf-WD POM.

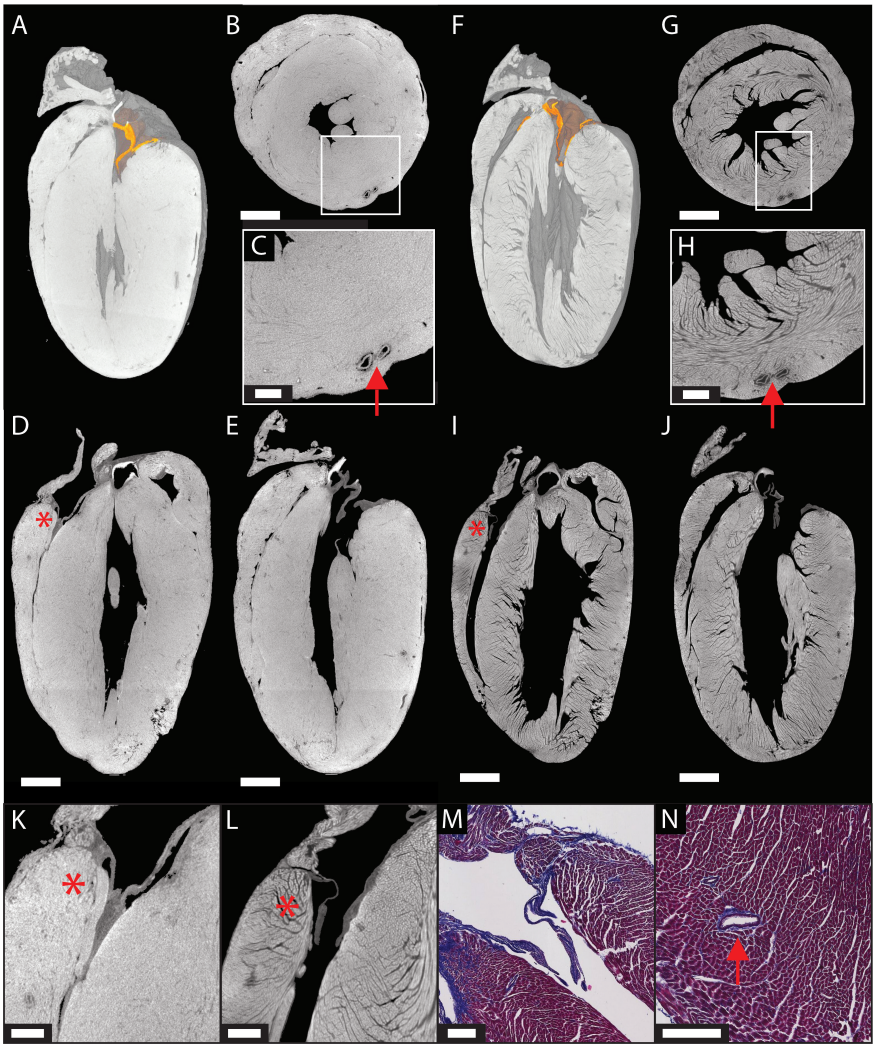


Fig. 3.2 Whole-heart CECT imaging (Supplementary materials, section 3.6). Mouse heart stained with 3.5 % (wt/v) 1:2 Hafnium-substituted Wells-Dawson polyoxometalate (1:2 Hf-WD POM) (A-D, K), rinsed in phosphate-buffered saline (PBS) and then stained with 3.5% isotonic Lugol's iodine (E-H, J). (A,F) 3D renderings with the heart valves in orange and (B-E, G-J) orthogonal slices. (K,L) A zoom-in on the tricuspid valve after 1:2 Hf-WD POM and isotonic Lugol's iodine staining, respectively. (M, N) Classical 2D histology sections of the same sample and within the same region as CECT with Masson's trichrome staining. Arrows indicate blood vessels, and * indicate the tricuspid valve. Scalebars are 1 mm (A, B, D-G, I, J), 0.3 mm (C, H, K, L) and 0.2 mm (M, N).

3.3.2 Morphometrical analysis of the myocardium

The proper functioning of the heart depends, among other things, on the complex organization of its myofibers. Since the action potential propagation is prescribed by the microstructure and the precise orientation of the cardiomyocytes, the myocardium has often been investigated using a broad variety of techniques [122]. Both CECT and PCCT have been widely applied to image the ventricle microstructure, since the anisotropic 3D orientation of the fibers can be scarcely extracted by the histological analysis [123]. This section presents studies dedicated to the optimization of the sample preparation for proper CECT or PCCT imaging, the development of the mathematical algorithm allowing to quantify the fiber orientation and the application of the techniques to diseased samples.

The optimization of the sample preparation is crucial to obtain accurate quantitative information about the myofiber orientation. Indeed, the resolution and contrast should be high enough to visualize the cardiomyocytes. *Mirea et al.* demonstrated that cardiomyocytes could be automatically segmented from images of human heart samples obtained by PCCT at a resolution of 3.5 µm [124]. *Reichardt et al.* optimized the heart preparation for PCCT by comparing five protocols: paraffin or liquid ethanol embedding, Lugol's iodine staining, PTA staining and the evaporation-of-solvent method. Among the CESAs they used, they concluded that PTA was more specific to connective tissue than Lugol's iodine and had a similar signal-to-noise ratio. They demonstrated that the heart muscle network could be reconstructed even without any CESA, and in this case, the evaporation-of-solvent method provided the best contrast. The approach involved dehydration in ethanol and the removal of lipids by immersion in xylene, which was then evaporated. Even though *Reichardt* and colleagues did not observe any effect of this procedure on the structure of the heart, it might still have altered the native structural properties of the tissue [125]. With CECT, *Stephenson et al.* reported that the cardiac conduction system could be distinguished from the myocardium itself based on differential staining of Lugol's iodine in the conduction system and in the contractile myocardium [92]. Finally, when optimizing the preparation protocols, several research groups mentioned the importance of imaging such a complex organ with a multiscale approach, either by focusing on a region of interest (ROI) [68, 126–128] or by combining several imaging modalities [108].

Once a good imaging protocol has been determined, the algorithm for fiber orientation extraction should be validated. It should be robust in order to eliminate the presence of other anatomical structures, such as blood vessels or fat. Such algorithms provide, in most cases, the helical angle, defined as the longitudinal orientation of the myocytes with respect to the long axis of the ventricular cavity. Two methods have mainly been developed: using the Fourier domain [127–129] or a structure tensor approach [91, 93, 125, 126, 130]. In their work, *Reichardt et al.* compared the two approaches and obtained similar results. However, using the local 3D Fourier-transform, they quantified the degree of alignment and the local thickness of single muscle fiber bundles [125]. These approaches have been used to characterize cardiac malformations [68, 101, 117, 120]. *Garcia-Canadilla et al.* applied PCCT on a fetus heart suffering from complex heart disease and compared this with a control heart. They demonstrated that the transmural variation of the helical angle of the myocyte fibers was smooth, even in the diseased heart. Nevertheless, among the cardiomyocytes, the thickness of the circumferential layer was larger in the case of congenital heart disease, and the right ventricle was particularly disorganized [120]. *Matos* and colleagues applied a structure tensor analysis after CECT imaging to better characterize the disarray associated with hypertrophic cardiomyopathy in cats. They quantified the helical angle, fractional anisotropy and myocardial disarray index and concluded that CECT was appropriate to quantify the myocardial disorganization and fibrosis with a resolution of 16 to 24 µm [101]. As it was done for muscle fibers, *Dejea et al.* extracted the orientation of collagen fibers in various samples taken from the left ventricle of rat hearts, imaged by PCCT at a resolution of 0.65 µm [68]. As they applied their strategy to healthy rodents (WKY rats) and two models of cardiovascular diseases (namely, SHR- (spontaneous hypertensive rat) and ISO (isoproterenol)-treated rats to mimic myocardial infarction), they reported that it could assess the remodeling induced in the ventricles in the case of pathologies (Fig. 3.3). Indeed, in addition to providing the detailed morphology of the whole heart, they were able to quantify the amount of extracellular collagen matrix by calculating the fraction of collagen with respect to the total cellular area. This allowed a precise quantification of the collagen amount in different subvolumes of the ventricles and led to the localization of scar tissue on the myocardial infarction models.

The extraction of the myofiber orientation is a challenging task regard-

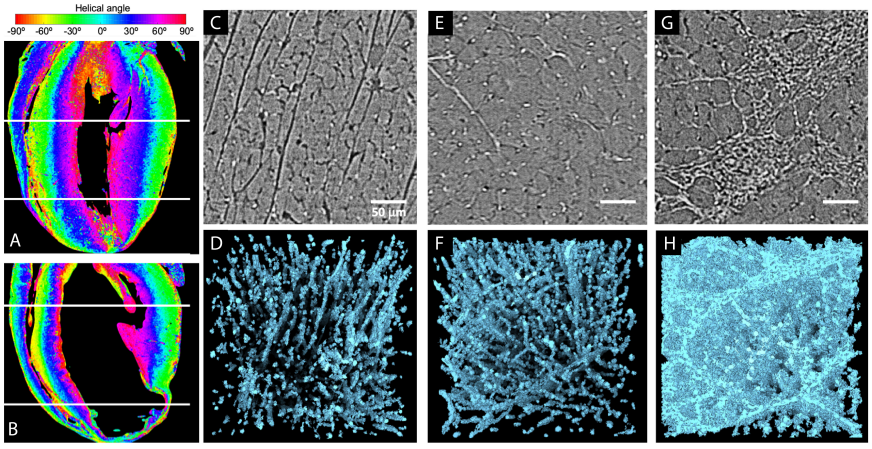


Fig. 3.3 Extraction of the fiber orientation in rat hearts based on PCCT. First column: quantification of the orientation of myocyte aggregates in (A) WKY and (B) LAD hearts: ventricular helical angle maps in four chamber views. White dashed lines were used for additional illustrations. Last three columns: collagen segmentation in high-resolution images. (C-G) Representative PCCT image slices from subvolumes in the left ventricular septum of the WKY, SHR and ISO hearts, respectively. (D-H) 3D rendering of collagen segmentation in the same subvolumes, visually showing the increase in density and change in shape and distribution around the tissue. Scar tissues can be seen in the ISO specimen. ISO: isoproterenol-treated rats, LAD: left anterior descending artery ligation model, SHR: spontaneous hypertensive rat and WKY: Wistar Kyoto rat model (adapted from and with kind permission from Reference [68], licensed under the Creative Commons Attribution 4.0 International License [10]).

ing the imaging protocols (*i.e.*, contrast and spatial resolution) and post-processing (*i.e.*, segmentation and accurate measurements of the fiber orientation). Several studies have been conducted to develop and validate the mathematical methods after using CECT or PCCT. It enables to compute the orientation of other fibrous components, such as collagen fibers. Computational models of the whole heart already exist, including models of cardiac diseases [131, 132]. Nevertheless, microCT imaging is often restricted to subvolumes of the ventricle or requires the combination of several individual scans to maintain a sufficient resolution.

3.3.3 Measurement of the calcifications in heart valves and assessment of the valve microstructure

Calcific aortic stenosis (AS) is a degenerative valve disease in which microCT is particularly appropriate for the diagnosis, since it allows a clear visualization of the calcified tissues without the need of a CESA. Moreover, histology is not routinely performed on calcified valves, because decalcification is required [133]. Where an *in vivo* clinical CT is used on patients to identify and quantify calcifications in soft tissues, an *ex vivo* microCT analysis of the leaflets of a stenotic aortic valve provides a much more precise measurement of the relative volume of calcification. Indeed, *ex vivo* imaging is not subject to artefacts related to movement and reduces the risk of misidentifying valvular calcification from vessel calcification due to their *in vivo* proximity. Additionally, microCT allows detailed visualization of the spatial distribution of the calcifications, and it enables the quantification of the diameters of calcification particles, the calcification volume fraction and the proportion of low- and high-density calcifications (Fig. 3.4 - own data). The amount of calcification in explanted aortic valves can vary highly (Fig. 3.4 E). Based on the accurate quantification of tissue calcification using *ex vivo* microCT, several correlations were demonstrated between the extent of the calcifications and various biomedical parameters such as the hemodynamic measurements, biological indices and changes at the protein level [134–138], indicating a clear correlation between the relative amount of calcification and the disease severity. *Mazur et al.* demonstrated that the calcification process is correlated with an increase in the expression of genes involved in osteoblastogenesis. This was particularly true in the calcified portion of the valve but not in the remaining soft section, and this difference was more pronounced in tricuspid than in bicuspid aortic valves [136]. The precise characterization of calcification

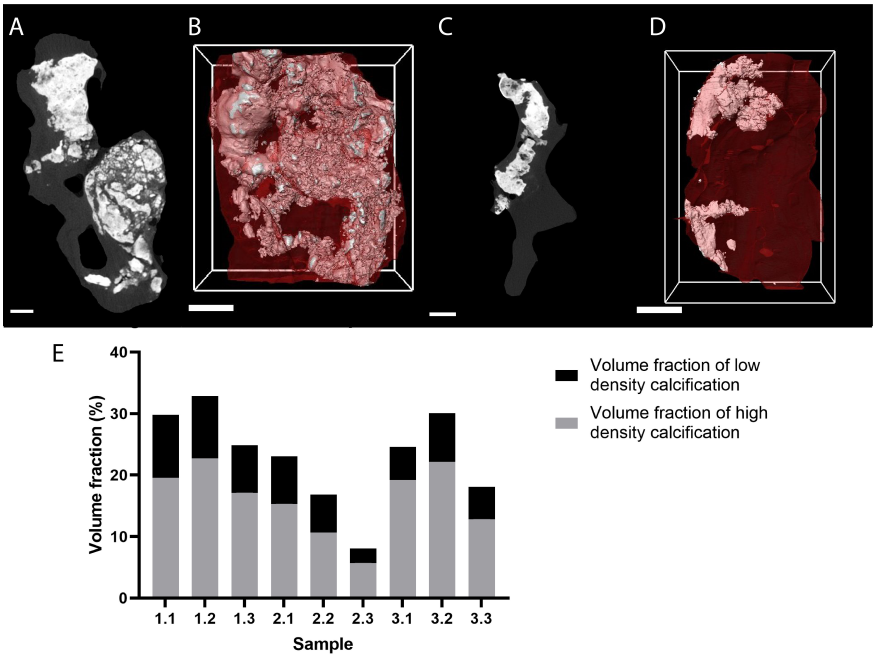


Fig. 3.4 MicroCT imaging of fresh calcified aortic valves (n=3) from human patients that were explanted during aortic valve replacement (Supplementary materials, section 3.6). (A,C) Cross-sectional 2D microCT image (no contrast enhancement) of samples 1.2 and 2.3, respectively, after the region of interest (ROI) selection. (B,D) 3D rendering of samples 1.2 and 2.3, respectively; calcifications are white and soft tissue red. (E) Volume fraction of the calcifications in the entire valve. Semiautomatic segmentation of the soft tissue and the different densities of calcification were done based on greyscale differences. Scalebars represent 1 mm.

makes high-resolution microCT a valuable tool for uncovering the pathological mechanisms behind the process of calcification. Nevertheless, since the valve is only explanted when heart valve replacement is performed, studies at earlier stages of the disease are still lacking to obtain more information about the onset of AS.

As described in the section dedicated to whole-heart imaging, heart valves could be identified on whole-heart images obtained with both CECT and PCCT, and their integrities have been evaluated [68, 84, 93, 95, 102–104, 108, 117]. However, the resolution of these images remains relatively low compared to the sizes of the valves, and the valve positioning could

not be described accurately. In order to visualize the substructures of the valves (*i.e.*, leaflets and chordae tendineae), advanced techniques have been implemented. *Pierce et al.* showed that the soft tissue of the bovine mitral valve can be tracked by fiducial markers to avoid using invasive techniques and CESAs [139]. Fiducial markers were placed on the surfaces of heart valves, and their motions were recorded by microCT. *Toma et al.* optimized the sample preparation by showing that a fixation with glutaraldehyde reduced the surface tension and provided more details about the chordae tree [140]. In addition to imaging, a heart simulator was added to this set-up by *Bloodworth et al.* to mimic the position of the valve in either healthy, diseased (mitral regurgitation) or repaired states of the heart. They were able to reproduce and image the complex structural remodeling of the mitral valve [141]. They highlighted the importance of a subject-specific description of the mitral valve geometry as input for the computational models.

This section described the potential of microCT to visualize and quantify the calcifications in stenotic aortic valves and the challenge for imaging the soft tissues of the valve. Indeed, microCT has never been able to reveal the spatial arrangement of the microstructural components of the valve (namely, collagen, elastin and proteoglycans). As a solution, CECT could be a valuable tool to study the healthy states of heart valves in three dimensions but, also, the remodeling of their microstructures in an unprecedented way.

3.4 The vasculature

The vascular system, a complex network extending from the heart, carries nutrients and oxygen to all our tissues. Here, we highlight the different applications in which microCT imaging is beneficial to study the vasculature. We distinguished two categories: (i) studies in which CECT imaging provides a general overview of the spatial distribution of the vasculature of an organ or organism, and (ii) studies that focus on the characterization of the vessel wall microstructure using CECT or PCCT. In the first category, the main objectives are (i) to show the feasibility of the technique, (ii) to study the spatial organization of the vasculature and vascular development and (iii) to evaluate the effect of a pathology on the vessel morphometrics. When imaging the vessel wall microstructure, the goals are (i) to study the microstructure of the different vessel wall layers in healthy ani-

mals, (ii) to evaluate mechanical properties and mechanisms of the rupture of the vessel wall and (iii) to identify the effects of a pathology on the vessel walls in diseased animals.

3.4.1 Spatial distribution and morphometrics of the vascular tree

As opposed to 2D techniques, microCT allows studying 3D parameters such as variations in the vessel diameter, tortuosity and branching in a nondestructive way. CCAs are most often used for vascular tree imaging, and thus, CECT is favored. Among the existing CCAs, Microfil and barium sulphate ($BaSO_4$) are the most common (Table 3.1). µAngiofil [85–87] has also been used as a newly emerging polymerizing CCA. All three of these CCAs allow to create vascular casts for 3D imaging and skeletonization of the vasculature. As these CCAs need to be perfused through the vasculature, in many cases, the perfusion technique first needs to be validated [49, 81, 88, 142]. Then, the imaging technique also needs validation, which is commonly done by comparing it to standard histomorphometry [47, 80, 86, 112] and by evaluating the number of vessels filled with the CCA. Some studies go further by analyzing the effect of a disease on angiogenesis, vascular development, vessel remodeling and vessel morphometrics based on a vascular tree analysis. The vascular organization of the heart [78, 83, 105, 143], kidneys [43–46], lungs [47, 89], hind limbs [75, 86] and bones [48, 80, 90, 115] have been thoroughly studied and will be briefly discussed below.

The heart is one of the most commonly studied organs using CECT vascular imaging. The highly heterogeneous nature of its vasculature due to asymmetric branching and different spatial scales makes it a complex structure difficult to study with standard 2D imaging techniques. CECT imaging using Microfil has been used to investigate age-related alterations of the coronary circulation by quantifying the vessel volume, since it is hypothesized that these alterations could play a role in left ventricular (LV) fibrosis and LV dysfunction [83]. Using Microfil, the vasa vasorum growth in the coronary arteries of newborn pigs was investigated by examining the 3D branching characteristics [78]. Although less common, CESAs have recently also been used to study the coronary vasculature. *Dunmore-Buyze et al.* compared PTA and Lugol's iodine to demonstrate the feasibility of imaging mouse heart vasculature using a perfusion approach. Instead of creating a vascular cast, they perfused the mouse with the CESA, staining the tissue itself, and then excised the heart and embedded it in paraffin wax

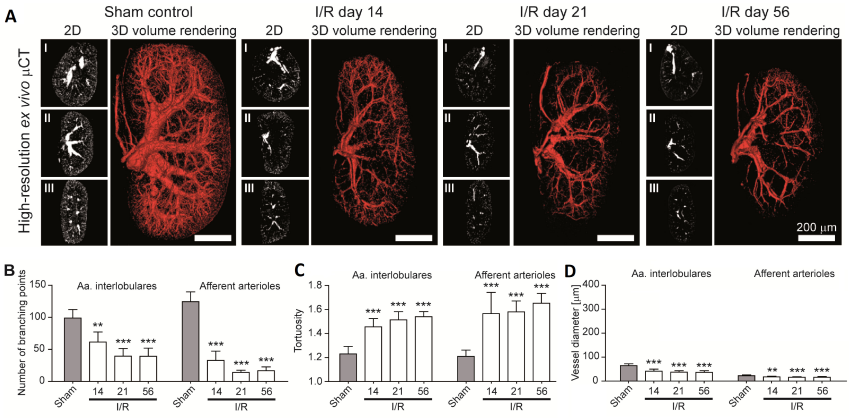


Fig. 3.5 Microfil-perfused rat kidney vasculature in progressive ischemia/reperfusion (I/R)-induced renal injury. (A) Representative CECT renderings of the sham control and I/R at days 14, 21 and 56 (2D cross-sectional images in the transversal (I), coronal (II) and sagittal (III) planes, as well as 3D volume renderings). CECT-based quantification of (B) the vascular branching points, (C) mean vessel tortuosity and (D) mean vessel diameter in the sham control and I/R at days 14, 21 and 56 for the 4th- (Aa. interlobulares) and 5th (afferent arterioles)-order branching points. Progressive rarefaction of the functional vessels and continuous shrinkage of the fibrotic kidneys, as well as an increased vessel tortuosity over time, can be seen. Scalebars are 200 µm. ** $p < 0.01$; *** $p < 0.001$ (adapted from and with kind permission from [43]).

for imaging. The quantitative analysis indicated no significant differences in vessel wall enhancement itself between the two CESAs but indicated a superior delineation of the vessel wall for PTA-perfused hearts due to a larger relative difference between the myocardium and vessel walls [105].

Studying the kidney's vascular organization is of strong interest, because renal diseases are often associated with alterations in the microvasculature. Different animal models have been developed for the study of kidney diseases with Microfil-based casts [44, 45]. This allowed to assess the changes in vessel morphometrics and the vascular volume fraction. In the frame of progressive kidney disease, *Ehling et al.* studied three different animal models, of which ischemia/reperfusion (I/R) was one. They found a reduction in the vessel diameter and vessel branching and an increase in vessel tortuosity for the preglomerular arteries in all their models. Fig. 3.5A shows 3D volume renderings for a sham control and 14, 21 and 56 days after I/R. Quantitative data was obtained for a number of the branching points (Fig. 3.5B), tortuosity (Fig. 3.5C) and vessel diameter (Fig. 3.5D) and is shown for the smallest vessels (Aa. interlobulares and afferent arterioles are the fourth and fifth-order branching points, respectively, in the kidney) [43].

The lungs are also particularly interesting to study using CECT imaging because of the complexity and fragile nature of their microvasculature, making the imaging quite challenging. Indeed, achieving consistent lung perfusion with CCAs is not trivial. A protocol has been proposed for lung perfusion in normal rats and pulmonary arterial hypertension (PAH) rats, comparing several perfusion techniques with $BaSO_4$ as the CCA to quantify the variabilities in the vessel volume and diameter. This study showed vascular loss in the PAH animal model [89]. $BaSO_4$, however, had a higher viscosity than Microfil, which means it had more difficulty in reaching the smaller capillaries. Microfil was used by *Savai et al.* to study the lungs in a mouse model of lung cancer to identify tumor angiogenesis. They evaluated a treatment with bevacizumab (humanized monoclonar antibody against vascular endothelial growth factor) in the lung tumor model, and, using CECT, they identified a reduced lung tumor angiogenesis and reduced lung tumor volume in bevacizumab-treated animals [47].

CECT imaging can also be applied to study the hindlimb vasculature,

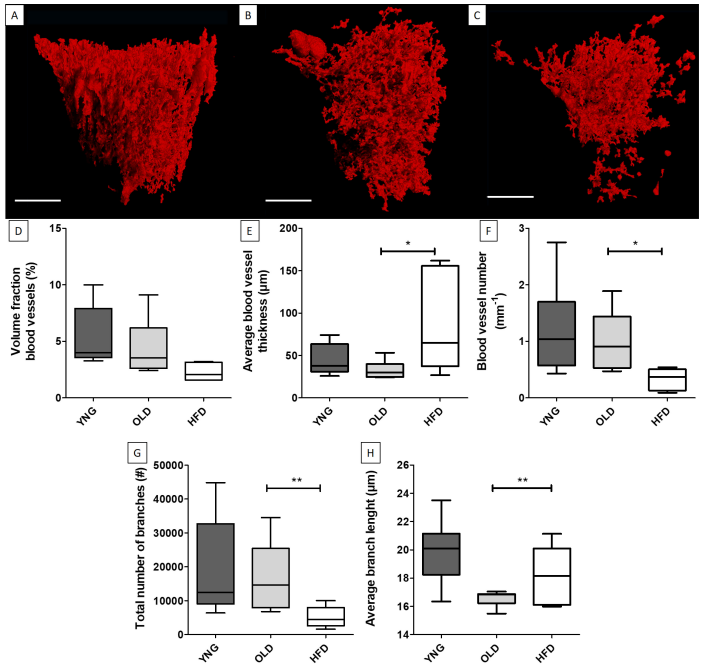


Fig. 3.6 Bone marrow vasculature of the tibial metaphysis stained with 1:2 Hf-WD POM. (A) Young (YNG), (B) old and (C) high-fat diet mice (HFD). Scalebars represent 250 µm. Quantification of the (D) volume fraction of the blood vessels in the medular open volume, (E) average blood vessel thickness, (F) blood vessel density, (G) total number of branches and (H) average branch length. * $p < 0.05$; ** $p < 0.01$ (adapted from and with kind permission from [115] with permission from Elsevier).

allowing for a rapid estimation of its vascular volume and vessel size distribution. This is especially useful in evaluating angiogenesis. Vascular density in the mouse hindlimb has been quantitatively evaluated following hindlimb ischemia using Microfil [75] and after the cell-based delivery of a vascular endothelial growth factor (VEGF) dose using µAngiofil [86].

The vasculature of the bone and bone marrow have also been studied quantitatively. *Nyangoga et al.* performed a quantitative analysis of the vascular volume, distribution and vessel diameter in rat femur bone metastasis, and they evidenced tumor angiogenesis using Microfil [48]. Although Microfil is popular for imaging the vasculature in soft tissues, it has been

shown that $BaSO_4$ is more reliable than Microfil for the imaging and quantification of the bone vasculature in decalcified samples, as it provides a better continuity and morphology of the blood vessels [80]. *Qiu et al.* visualized human intraosseous arteries using $BaSO_4$ and the measured artery area, volume and length [90]. *Kerckhofs et al.* showed that the bone marrow vasculature can be visualized and quantified for the blood vessel number, thickness distribution, volume fraction, number of branches and mean branch length using a CESA instead of a CCA. They incubated the tissue in 1:2 Hf-WD POM, and they compared the different parameters for young (YNG—8 weeks old), old (OLD—30 weeks old) and high-fat diet (HFD)-induced obese mice (30 weeks old) in the tibial metaphyseal bone marrow vasculature (Fig. 3.6) [115]. They found that aging and the HFD had a significant impact on the 3D spatial organization and branching of the vasculature, something that is difficult to obtain via standard 2D histology. More recently, *de Bournonville* and colleagues showed that Monolacunary WD-POM (Mono-WD POM) also allows visualizing bone marrow and kidney blood vessels with a lower synthesis time at lower costs [116].

Finally, the brain is an organ that is less commonly studied with CECT imaging. High variations in the extent of CCA filling are often seen due to the complexity of its vascular network, conferring different images of the vasculature for different subjects. For this reason, studies have mainly focused on developing new perfusion and imaging methods of the cerebrovascular system [82, 87, 144, 145]. *Ghanavati* and colleagues developed a new surgical procedure for perfusing Microfil through the left ventricle to achieve a uniform perfusion of the blood vessels in the brain [82].

The range of applications for vascular imaging is broad because of the wide range of organs and related pathologies that can be studied. Many other organs that have not been mentioned yet have been investigated, such as the spinal cord [146], the placenta [49, 73, 79, 114, 147], the larynx, spleen, mandible and liver [88]. Whole-body specimens were also imaged [81, 112] using *ex vivo* CECT in order to visualize the entire vasculature. For the latter, the spatial distribution could only be assessed qualitatively because of an insufficient spatial image resolution when imaging the whole body. Vascular casting is still the most popular imaging technique for CECT imaging of the vascular tree, even though the difficulty of perfusing correctly all the desired vessels remains. To avoid this problem, a few innovative CESAs have been developed, such as 1:2 Hf-WD POM

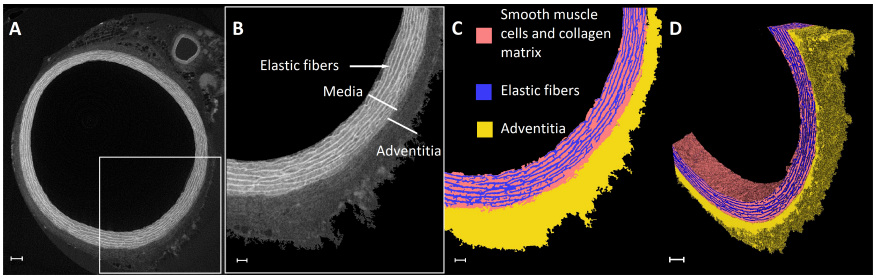


Fig. 3.7 Abdominal rat aorta stained with 1:2 Hf-WD POM (Supplementary materials, section 3.6). (A) 2D CECT ortho-slice, (B) ROI selection and segmentation of aortic wall from background with an indication of the substructures, (C) segmentation of the media and adventitia and elastic fibers on a 2D ROI ortho-slice and (D) a 3D view of the segmentation on the ROI of the aortic wall. Scalebars are 100 µm (A,D) and 50 µm (B,C).

[115], Zr-POM [114], and a new tri-element stain composed of iodine, aluminum and iron [112], which allows staining of the tissue itself instead of creating a cast. For all the previously mentioned studies, the spatial resolution was often limited to tens of microns to several microns, depending on the sample. Some alternative imaging techniques exist that can go down to the nanometer scale, such as scanning electron microscopy (SEM) [148] or fluorescence-based optical microscopy [149]. However, these techniques often necessitate labor-intensive tissue preparation and post-processing.

3.4.2 Microstructure of the vessel wall

For imaging the microstructure of the blood vessels, CESAs are mostly employed, because the vessel wall and, thus, the tissue itself should be visualized, rather than the lumen space. In order to better understand and treat vascular diseases, it is important to first be able to distinguish the healthy substructures of the different vessel wall layers and their compositions. PTA and phosphomolybdic acid (PMA) are well-known CESAs used for vessel wall imaging, because they are described to bind to the collagenous components of soft tissues [99]. *Nierenberger et al.* compared PTA, PMA and Lugol's iodine for the visualization of the 3D architecture of the collagen fibers in porcine iliac vein walls. They were able to distinguish the intimal and adventitial layers of the vessel wall and to identify the volume fraction of collagen in each layer. A higher contrast was obtained with PTA

and PMA compared with Lugol's iodine. However, as PTA, PMA and Lugol's iodine are known to cause tissue shrinkage due to their high acidity, we used the previously mentioned nondestructive 1:2 Hf-WD POM [116] on a fixed abdominal rat aorta. Using this CESA enabled us to distinguish, in 3D, the medial and adventitial layers and to segment the elastic fibers in the media without affecting the original aortic structure (Fig. 3.7). *Walton et al.* were able to visualize and segment the adventitia and the media and to highlight the respective structures using absorption microCT in combination with phase-contrast enhancement, induced by both the specimen preparation (differential dehydration of the tissue components and paraffin embedding) and instrumentation (use of thin scintillators instead of a flat panel detector). They highlighted the collagen and the elastic fibers in the adventitia and the media, respectively, and were able to segment the layers based on grayscale differences (Fig. 3.8). This technique allowed 3D virtual dissection of the medial and adventitial layers and of the elastic lamellae and interlamellar regions in the media without the need to use a CESA [150].

Some studies have aimed at performing mechanical testing in combination with CECT to observe the mechanisms of damage in the vessel walls. This is further referred to as 4D CECT. *Helfenstein-Didier et al.* used *in situ* tensile testing in a microCT device to analyze dissection, one of the damage mechanisms in large arteries. They used sodium polytungstate (SPT) as the CESA and stained the non-fixed samples in solution for 24 h after showing that this CESA did not have a significant effect on the mechanical properties of the tissue of interest [110]. *Brunet* and colleagues then used the same CESA to investigate the aortic dissection using a tension–inflation testing device inside a microCT system [111].

The effect of different pathologies on the vessel wall microstructure has also been studied. Atherosclerosis is one of the leading causes of death and disability globally and can lead to serious health risks, such as myocardial infarction [151]. It affects the vascular system by creating a build-up of plaques on the insides of artery walls. Highlighting the accumulation of plaques and characterizing their compositions and their temporal and spatial developments, as well as their mechanical properties, will help to better understand this disease. As plaques are often distributed in a heterogeneous way throughout the vasculature, 3D techniques such as microCT imaging are crucial. Calcified plaques are significantly denser than the soft

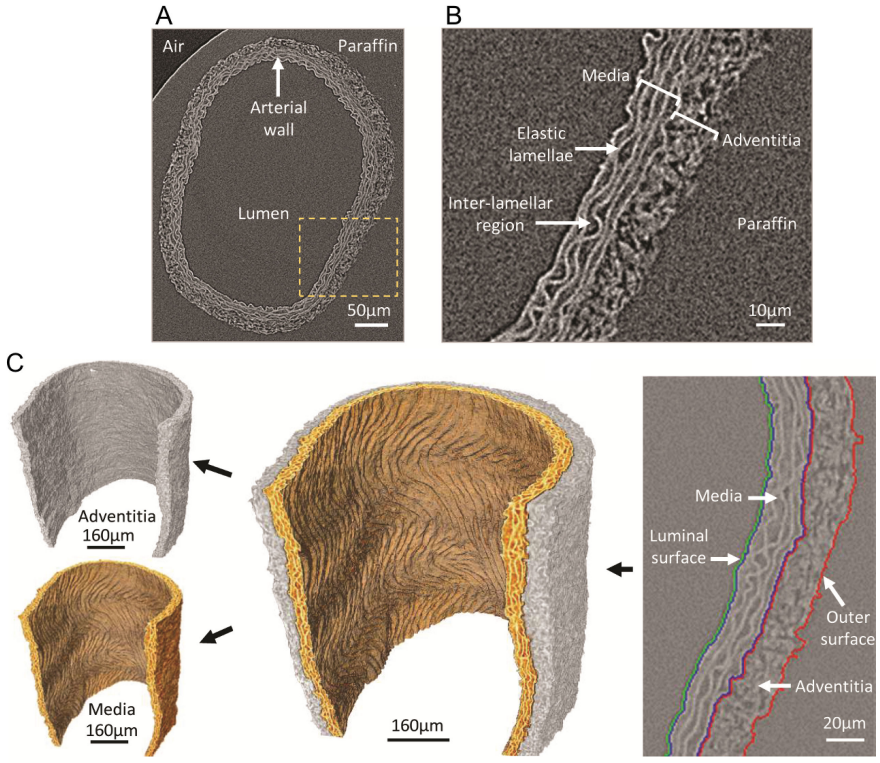


Fig. 3.8 Paraffin-embedded rat common carotid artery without CESA. Major arterial substructures are readily identifiable in the vessel wall. (A) Virtual slice extracted from an X-ray tomogram of an intact rat common carotid artery (yellow box indicates the magnified region in panel (B). (B) Major arterial substructures. (C) Rendering showing the output of the segmentation process that enables the medial and adventitial layers to be virtually dissected (adapted from and with kind permission from [150] — licensed under the Creative Commons Attribution 4.0 International License [10]).

tissues in which they grow, so in order to visualize them, CESAs are not always required. *Postnov et al.* used microCT to evaluate and quantify rat vascular ectopic calcifications due to adenine-induced chronic renal failure. They computed the volume and density of the calcified units [152]. However, not only the calcifications themselves but, also, the vessel wall layers, which contain the plaques, are important to visualize and identify the onsets of calcifications. To improve soft tissue contrasts, *Holme et al.* used a combination of benchtop and synchrotron-based microCT to design a protocol for highlighting plaques in atherosclerotic human coronary arteries and differentiating between plaques, muscle and fat tissue without the need of a CESA [153]. The mechanical properties of plaques have been derived by correlating microCT-based calcification volume fraction measurements of calcified human carotid plaques with circumferential loading tests [154]. Only a few studies are available where CECT was used to assess the soft tissues in atherosclerotic blood vessels. *Pai et al.* used OsO_4 as the CESA for visualizing lipid-rich plaques. Despite its high toxicity, OsO_4 is popular for this application, because it preferentially binds to lipids [109]. Using an iodine-based CESA, *Self et al.* demonstrated that CECT allows the visualization of the vessel wall layers together with the plaque size and morphology and calcium phosphate deposition [155]. *Borland* and colleagues recently reviewed the use of microCT and CECT for analyzing vascular calcifications in animal models. They included a variety of animal models that can be used, the different CAs and the sample preparation techniques [156].

Other pathologies that have been under investigation include aortic dissection and Marfan syndrome. Using propagation-based, synchrotron PCCT, *Logghe et al.* investigated aortic medial ruptures in BAPN/AngII-infused mice, which is an animal model for aortic dissection. They attained a spatial resolution of 1.625 µm and segmented the medial elastic lamellae in order to define the locations of the ruptures [69]. *López-Guimet et al.* used synchrotron PCCT at a 1.1-µm spatial resolution to examine aortic wall remodeling in aging mice and mice with Marfan syndrome. They evaluated the 3D microstructures of large, unstained samples and found that Marfan syndrome could be viewed as an accelerated aging process characterized by an increased variation in the aortic diameter, medial thickness and cross-sectional area [42]. The advantage of using PCCT is that there is no need for the use of a CESA. However, it must be noted that the samples have to be dehydrated, causing a possible alteration in the original tissue

structure [110].

The microstructure of the vessel wall is complex and challenging to image. Many research groups have already shown the potential of microCT to visualize the vessel wall substructures in healthy and pathological cases approaching spatial resolutions in the order of 1 µm. However, more efforts are still required, for example, in terms of the quantification of the fiber orientation and detection of the spatial distribution of specific proteins. The use of 4D CECT also still needs optimization in terms of the CESA selection and set-up to mimic more accurately the *in vivo* environment.

3.5 Conclusions

Cardiovascular imaging is crucial to better understand diseases, because it allows to acquire more knowledge on the structural and microstructural properties of the heart and the vasculature. In this review, we focused on *ex vivo* microCT-based imaging for the characterization of the cardiovascular system. We discussed a variety of applications for which microCT imaging can be used, but we have also highlighted some shortcomings, mainly in terms of spatial resolution and contrasting methods. Overview imaging allows studying the integrity and spatial organization of both the heart and the vasculature. Imaging at very high spatial resolutions allows in-depth characterization of the different substructures: the orientation of the myocyte and collagen fibers in the ventricle, the integrity of the cardiac valves in the heart and the microstructure of the vessel walls for the vasculature. These advances pave the way to a better understanding of diseases causing structural changes of the cardiovascular system. However, very high-resolution imaging is still limited to small samples in *ex vivo* conditions, where the exposure time is not limited as it is *in vivo*. In terms of the contrasting methods, CESAs have started to emerge quickly, but they are often harmful to the tissue. Some more recent CESAs are being developed that are nondestructive, but their staining mechanisms are still not well-known and need further investigation. Other contrasting methods such as PCCT exist, but the equipment needed for this is often not readily available for use because of its high cost. Additionally, dehydration of the samples is often required in this case, altering the native structure of the tissue. In the future, we anticipate that there will be more progress in this field, particularly thanks to the technological improvements of the machines and to

the development of more tissue- or molecule-specific CAs. Based on these advances, a better knowledge of the structure and microstructure of the cardiovascular system will be acquired. This will trigger the development of more robust 3D computational models and provide input for improving the current treatments of cardiovascular diseases.

3.6 Supplementary materials

Materials and Methods for our own data:

Fig. 3.2: The mouse heart was explanted immediately after death. It was flushed with phosphate buffered saline (PBS) to remove the blood and fixed for 24 h in 4% formaldehyde (FA) at 4 °C. It was rinsed in PBS for 24 h and stained with 3.5% (wt/v) 1:2 Hf-WD POM powder in PBS at room temperature for 10 days. It was scanned with a Phoenix Nanotom M (GE Measurement and Control Solutions, Wunstorf, Germany) by three vertical consecutive scans with a voltage of 60 kV, a current of 165 µA, an isotropic voxel size of 2.37 µm, averaging 3, skip 1 and an exposure time of 500 ms. It was then rinsed in PBS for 10 days, stained with isotonic Lugol's iodine at room temperature for 4 days and scanned again with the same parameters. The homemade isotonic Lugol's iodine was made of 0.65% (wt/v) I_2 and 1.29% (wt/v) KI and diluted in PBS 1:1. The heart was then rinsed in PBS and processed for histology. The tissue was cut in 5-µm sections using a microtome (Leica Biosystems, Wetzlar, Germany), and the sections were stained with Masson's trichrome for comparison with CECT. The valves were manually segmented, and the 3D renderings were created using Avizo software (Thermo Fischer Scientific, Waltham, MA, USA).

Fig. 3.4: Aortic valve cusps were explanted from patients during heart valve replacement. They were frozen and stored at -80 °C. Prior to microCT imaging, they were thawed and wrapped in parafilm to prevent dehydration. MicroCT imaging was done with a Phoenix Nanotom M (GE Measurement and Control Solutions, Wunstorf, Germany) using a 0.5-mm aluminum filter, a voltage of 80 kV, a current of 400 µA, an isotropic voxel size between 10 and 14 µm and an exposure time of 500 ms. We scanned using fast scan mode. The images were postprocessed using CTAn (Bruker MicroCT, Kontich, Belgium) based on the ROI selection and semiautomatic thresholding and segmentation. Calcifications of low density were defined by gray values between 120 and 189 and calcifications of high density by gray values between 190 and 255. The 3D renderings were made using Avizo software (Thermo Fischer Scientific).

Fig. 3.7: A piece of the abdominal rat aorta was collected and fixed in 4% formaldehyde for 48 h at 4 °C and stained with 3.5% (wt/v) 1:2 Hf-WD POM powder in PBS at room temperature for 48 h. It was then scanned with a Phoenix Nanotom M (GE Measurement and Control Solutions, Wunstorf, Germany) with a voltage of 60 kV, a current of 70 µA, an isotropic voxel size of 1.1 µm, averaging 3, skip 1 and an exposure time of 500 ms. An ROI was selected and was then segmented manually based on grayscale values using Avizo software (Thermo Fischer Scientific).

4

Non-destructive 3D characterization of the blood vessel wall microstructure in different species and blood vessel types using CECT and comparison with synthetic vascular grafts

Publication

Non-destructive 3D characterization of the blood vessel wall microstructure in different species and blood vessel types using contrast-enhanced microCT and comparison with synthetic vascular grafts.

Leyssens, L.; Balcaen, T.; Pétré, M.; Béjar Ayllón, N.; El Aazmani, W.; de Pierpont, A.; Pyka, G.; Lacroix, V.; Kerckhofs, G. *Acta Biomaterialia*, 2023, 164, 303–316. https://doi.org/10.1016/j.actbio.2023.04.013

Positioning in the context of this PhD thesis

Synthetic vascular grafts, used as treatment in case of vascular occlusion, still often fail clinically, potentially because of a mismatch in mechanical behavior between the native blood vessel and the graft. To better understand the causes of this mismatch, this chapter is dedicated to the microstructural characterization of the blood vessel wall of different types of native blood vessels (aorta, femoral artery, vena cava) in different species (rat, porcine, human) using CECT. Additionally, the microstructure of different blood vessels is compared to currently clinically used synthetic vascular grafts. The objective of this part is first to demonstrate the ability of CECT to allow the visualization in 3D and at high resolution of the native blood vessel wall and to quantify structural parameters of its constituents. Secondly, this part also demonstrates that the outcomes of vascular treatments are predominantly influenced by the specific blood vessel and animal species that are being studied, highlighting the importance of adapting treatments to each vessel type. This research work has been accepted for a publication, in which L. Leyssens was first author.

4.1 Introduction

Vascular diseases are a major cause of death and disability. The most common forms of diseases of the arteries include atherosclerosis [152, 157], aneurysm [158, 159], stiffening of the wall due to aging [160, 161], and dissection [162–164]. Venous diseases, such as chronic venous insufficiency and varicose veins, are also prevalent [165–167], causing venous wall injuries and inflammation with significant physical and psychological im-

pact. To treat complications, proper surgical actions must be undertaken. In the case of vessel calcification and occlusion, one of the most common vascular pathologies, different options exist, such as bypass surgery. Bypasses are made using autologous vessels or prosthetic vascular conduits also known as vascular grafts. For the latter, elastic polymers have often been used with the aim of matching the elastic behavior of the host arteries. Although polymer-based synthetic bypass grafts, such as Dacron [168–171] and Gore-Tex [172, 173], are clinically used, complications that affect their performance still remain, such as mechanical failure and progressive dilation [174–176]. It is often hypothesized that this is due to a mismatch in compliance between the graft and the native vessel and due to biocompatibility issues [26, 177–180].

Another potential reason for clinical complication is that animal models are often used to study cardiovascular diseases and their treatments. However, the microstructure and composition of the blood vessels might vary from one species to the other. Through classical 2D histological studies, structural differences have already been observed between human and porcine aortic tissues [181]. Moreover, disease treatments are often not adapted from one blood vessel type to the other. Structural differences between the porcine aorta and vena cava have been studied through classical 2D histology and multiphoton imaging, showing important differences in elastin and collagen content and orientation of these fibers, leading to differences in mechanical properties [182]. For the study of vascular diseases or disease treatment options, differences in vessel microstructure should be considered.

For better understanding and treating vascular diseases or for obtaining better tissue models, there is a need to better characterize the microstructure and mechanical properties of diseased tissues [183, 184] but also to visualize and quantify the structural properties of healthy tissue in 3D at high resolution on *ex vivo* harvested samples. This could lead to a better understanding of the link between microstructure and proper functioning of the vessel and of the influence of disease on the microstructure, and this information is important to improve the design of vascular grafts.

Blood vessels are typically described as being composed of three main layers: the tunica intima (single layer of endothelial cells), the tunica media (contains mainly elastic lamellae, collagen fibers, and smooth muscle

cells (SMCs)), and the tunica adventitia (composed mainly of fibrous connective tissue, such as collagen fibers). Different types of arteries can be distinguished. The largest arteries in the body are highly elastic, as they contain a lot of elastin and collagen in their tunica media, conferring them pulse-smoothing properties. The medium-sized vessels or muscular arteries have a larger quantity of SMCs to contract and expand in order to supply blood to the peripheral system. Veins and venules are thinner and are composed of lower amounts of SMCs and elastin, since they transport low-pressure blood [11].

2D histological sectioning techniques are still the gold standard for microscopical tissue visualization, but they are not well suited for 3D visualization. Scanning electron microscopy [185, 186], confocal laser microscopy [187, 188], and multiphoton microscopy [182, 189] have shown their potential to produce high-resolution, 3D images, but they only allow visualization of small tissue volumes. Light sheet fluorescence microscopy allows fast imaging of larger tissues but at lower resolution [190–192]. X-ray microfocus computed tomography (microCT) has proven to provide high-resolution, 3D microstructural information of larger and complex materials. To visualize the different soft tissue constituents in the vessel wall, synchrotron phase-enhancement is often required [42, 69, 193, 194]. However, access to synchrotron equipment is limited and costly. Lab-based absorption microCT is more readily available and can be used to visualize the different low X-ray-attenuating soft tissues using contrast-enhancing staining agents (CESAs). This technique is then referred to contrast-enhanced microCT (CECT). CECT has been applied for imaging vascular tissues, but many limitations are still present today in terms of spatial resolution and the invasive character of the CESAs being used [195]. *Butters et al.* [107] and *Balint et al.* [196] have investigated the diffusion kinetics of different CESAs in biological tissues, such as Lugol's iodine solution (I_2KI), phosphotungstic acid (PTA), and phosphomolybdic acid (PMA). These CESAs are commonly used for CECT of the cardiovascular system [99, 105, 155, 197]. However, they have shown to be destructive [77, 100, 197, 198]. Iodine will participate in multiple chemical reactions with the tissue, and as a consequence of these reaction mechanisms, protons are released in the solution acidifying the staining solution [198]. PTA and PMA are considered very acidic compounds [198] and will harm the tissue by inducing extensive tissue shrinkage, resulting in an altered microstructure. In previous studies, our group has shown the potential of Monolacunary and 1:2

Hafnium-substituted Wells-Dawson polyoxometalates (Mono-WD POM and 1:2 Hf-WD POM, respectively) for non-destructive staining of kidney and soft skeletal tissues [116, 199]. Mono-WD POM and 1:2 Hf-WD POM are synthesized as the salt of the acid and, hence, they are not acidifying the solution, causing less tissue shrinkage. However, these POMs have never been used for imaging blood vessels. In this study, we assessed the penetration rate and the contrast enhancement in the porcine aorta by Mono-WD POM and 1:2 Hf-WD POM. Providing superior contrast enhancement, 1:2 Hf-WD POM was used as CESA for the remainder of the experiments, in which a comparison was made between different species (rat, porcine, and human) for two vessel types (aorta and femoral artery) and between different porcine vessel types (aorta, femoral artery, and vena cava). We additionally quantified the 3D thickness of the different vessel layers, as well as different structural parameters of the elastic lamellae in the porcine aorta. We showed the potential of CECT to image an atherosclerotic human femoral artery. Finally, we performed a structural characterization of different currently clinically used synthetic vascular grafts to assess their differences with native tissue.

4.2 Materials and methods

4.2.1 Animal age, sex and origin

Porcine aortas were obtained from the slaughterhouse (RIMA Vleesgroothandel, Mechelen, Belgium and WestVlees, Staden, Belgium). The rat aortas and femoral arteries were gathered from waste material from a study at the CARD department (UCLouvain) approved by local authorities (Comité d'éthique facultaire pour l'expérimentation animale, 2016/UCL/MD/027 and 2021/UCL/MD/012) and performed in accordance with the Guide for the Care and Use of Laboratory Animals, published by the US National Institutes of Health (NIH Publication, revised 2011). The human aortas were remaining material from body donations (UCLouvain Biothèque, notification number BB190051). The porcine femoral arteries were obtained from Landrace pigs autopsied during ongoing experiments at the Department of Cardiac Surgery of KU Leuven (ECD 026/2019). The human femoral arteries were donated by the European Homograft Bank (donor bank). An end-stage atherosclerotic human femoral artery was obtained from an amputated patient (EC Research S number: S62776).

4.2.2 Preparation of the blood vessels

For each type of healthy blood vessel, only three samples were harvested, due to time constraints and limited sample availability. All the biological tissues were fixed using 4% formaldehyde (FA) in phosphate-buffered saline (10 mM, pH = 7.4) (PBS), for 48 h at 4°C on a shaker plate to improve CESA diffusion. The porcine and human aortas and the porcine vena cavas were cut in square shaped samples of 1 × 1 cm. The orientation of the samples (circumferential vs. axial direction, luminal vs. adventitial side, proximal vs. distal side) was referenced by cutting a small triangle from the upper right corner of each piece of tissue. For the rat aortas and the rat, porcine, and human femoral arteries (healthy and diseased), the entire circumference of the sample was kept and a piece of 0.5 cm (rat femoral artery) or 1 cm (for all the others) in length was used. For the CECT and classical 2D histology comparison study, a smaller piece of porcine aorta of 0.5 × 0.8 cm was cut. For the different aortas, the samples were always dissected from the descending thoracic aorta.

4.2.3 Contrast-enhancing staining agents

The Monolacunary Wells-Dawson POM $\alpha_2 - K_{10}P_2W_{17}O_{61}\bullet 20H_2O$ ($\alpha_2 - P_2W_{17}$ or Mono-WD POM) and 1:2 Hafnium(IV)-substituted Wells-Dawson POM $K_{16}[Hf(\alpha_2 - P_2W_{17}O_{61})_2]\bullet 19H_2O$ ($\alpha_2 - Hf - P_2W_{17}$ or 1:2 Hf-WD POM) were synthesized as described in literature [200, 201]. For the penetration rate and contrast enhancement study, samples were stained either with Mono-WD POM or with 1:2 Hf-WD POM. For all the other studies, Hf-WD POM was used. Staining solutions (pH = 7.32) were prepared by dissolving 35.0 mg/mL (3.5%) POM in PBS. For the Mono-WD POM, 3 mg/mL of lithium chloride (LiCl) was added as previously described [116, 202]. Samples were immersed in separate tubes, containing 5 mL of staining solution each. This ensured that the volume of CESA solution was at least 20 times the volume of the samples. Staining time was different for all the samples depending on their size. For the penetration rate study, different staining times were applied (0, 3, 6, 9, 24, 48, 72, 168, 240, 360 h). For the contrast enhancement study, porcine aortas were stained 15 days with 1:2 Hf-WD POM and 48 h with Mono-WD POM + LiCl. For the CECT and classical 2D histology comparison, the porcine aorta was stained 7 days. The rat aortas, rat femoral arteries, and porcine vena cavas were stained for 48 h. The porcine and human femoral arteries (healthy and diseased) were stained for 7 days. The human aortas were stained for 12 days. Bi-

ological samples were removed from their staining solution and wrapped in parafilm in their wet state to avoid dehydration or degradation during acquisition. They were placed and attached in a dedicated sample holder to avoid any movement during CECT acquisition.

4.2.4 Synthetic grafts

Three different synthetic grafts were purchased: Dacron (DuPont, USA), Gore-Tex (Gore, USA), and Vectra (Thoratec laboratories corporation, USA). Dacron (polyethylene terephthalate, PET) and GoreTex (expanded polytetrafluoroethylene, ePTFE) are used in a surgical procedure to bypass a diseased blood vessel, while Vectra (three-layered polyetherurethaneurea with non-porous layer under the luminal surface) is a specialty graft for creating vascular access in hemodialysis [203]. The grafts were cut in square-shaped pieces of 1 × 1 cm. The synthetic grafts were not stained, they were placed and attached in a dedicated sample holder to avoid movement during microCT acquisition.

4.2.5 High-resolution microCT imaging

MicroCT datasets were acquired using a Phoenix NanoTom M (GE Measurement and Control Solutions, Germany) equipped with a 180-kV/15W energy micro/nanofocus X-ray tube. The detector area is 2400 × 3072 pixels (height x width). A diamond-coated tungsten target was used for all scans. The biological samples were stained with a CESA and then imaged with microCT (referred to as CECT). The synthetic grafts were imaged with microCT (no staining). An overview of the microCT and CECT acquisition parameters is given in Table 4.1. The expected resolution is two to three time the voxel size [33]. The microCT and CECT datasets were reconstructed with the Datos|x software (GE Measurement and Control Solutions) and exported as XY slices (.tiff). A beam hardening correction (BHC) of 6 was applied for biological tissues and 7 for the synthetic graft materials. BHC goes on a scale from 0 (no correction applied) to 10 (very strong correction applied). Three different filters were applied: inline median (projections are filtered during reconstruction using a 3 × 3 median filter which reduces the noise in the volume), ROI-CT (increases the resolution of the CT dataset for a selected ROI of the object), and filter volume (volume is filtered in slices after reconstruction using the Unsharp Masking Filter). For the penetration rate and contrastenhancement study, samples were imaged together with a reference material (aluminum oxide bead

(Al_2O_3)) for gray value normalization. In all the other cases, the reference materials were air and parafilm.

4.2.6 Classical 2D histological assessment

One previously CESA-stained and CECT-imaged biological sample of each kind was washed in PBS for at least 1 day to remove residual staining solution of the surface of the sample, and was then embedded in paraffin. The embedding protocol goes as follows: samples were placed in successive baths: formalin solution (37 °C, 45 min), ethanol 70% (37 °C, 30 min), ethanol 90% (37 °C, 45 min), isopropyl alcohol (4 baths, 37 °C, 30 min, 45 min, 1 h, 1 h), toluene (3 baths, 37 °C, 45 min, 1 h, 1 h), paraffin (4 baths, 58 °C, 30 min, 1 h, 1 h, 1 h). Samples were then embedded in paraffin in a cassette and cooled down for the paraffin to harden. Sections with a thickness of 5 µm were cut using a microtome and stained with Verhoeff's stain. Histological sections were imaged using a SNC400 Slice Scanner (Leica Microsystems, Germany).

4.2.7 Image processing and analysis

For each acquired dataset, an in-house developed Matlab (Mathworks, Natick, USA) script was used to convert the 16-bitslices (.tiff) to 8-bit slices (.bmp), while simultaneously adapting the grayscale histograms of the datasets to normalize them to each other [199, 204]. Then, all the datasets were segmented using the *Magic Wand* and *Watershed* segmentation tools in the Avizo software (Thermo Fischer Scientific, Massachusetts, USA) to remove the background. All 3D renderings were generated in Avizo.

4.2.8 Statistical analysis

GraphPad Prism 9 (GraphPad Software, California, USA) was used for the statistical analysis and data visualization. Normality and homoscedasticity of the residuals were checked before doing each statistical test. To ensure that normality and homoscedasticity were met, a logarithmic (Log10) transformation of the data was sometimes necessary. When a comparison was made between two groups, a two-sided *t*-test was performed. The Welch's correction was applied in case of unequal variances. A nonparametric test was performed in case the distribution was not normal. When more than two groups were compared, a one-way ANOVA was applied, followed by a Tukey's multiple comparisons test. Welch's correction was

applied in case of unequal variances, followed by a Dunnett's T3 multiples comparisons test. A mixed-effects analysis was performed when n = 3 with repeated measures, followed by a Bonferroni's multiple comparisons test. The Geisser-Greenhouse correction was applied in case of unequal variances, followed by a Tukey's multiple comparisons test. P-values below 0.05 were considered to be significant; ns $p > 0.05$, $* p \leq 0.05$, $** p \leq 0.01$, $*** p \leq 0.001$, $**** p \leq 0.0001$. For the distribution graphs (Fig. 4.5), p-values were calculated based on the difference between the mean of the distributions. All the statistical tests were verified after consultation with a statistician. In the bar graphs, the mean value of the different samples is indicated by the height of the bars and individual values are also represented. Error bars represent the standard deviation.

4.2.9 Penetration rate and contrast enhancement study

The datasets of the same samples (number of samples (n) = 2 for both Mono-WD POM and 1:2 Hf-WD POM) but different time points were registered to each other (Avizo registration wizard). A volume of interest (VOI) of 400 slices was selected for each dataset. One registered slice from each dataset for each time point was then selected and the grayscale values along a line through the sample were computed using Dataviewer (Bruker Micro-CT, Kontich, Belgium). As the adventitia (loose connective tissue) has a variable thickness and is stained rapidly (fully stained after 3 h for all samples), it was not considered in the grayscale value measurements. A point at $x = 0$ mm was defined at the location where the tunica media starts (on the side of the adventitia). The remaining segment was discretized into smaller segments of 86 µm (10 pixels). The gray value for each small segment was the mean value of all the values from the segment. The grayscale for three different locations inside the tissue was stored: 14.5 pixels (0.0985 mm approximated to 0.1 mm), 44.5 pixels (0.3025 mm $\sim$ 0.3 mm), and 74.5 pixels (0.5066 mm $\sim$ 0.5 mm). The experimental data was fit to an exponential plateau equation (Eq. 4.1).

Table 4.1 MicroCT and CECT acquisition parameters for all types of samples.

	Porcine aorta (Fig. 4.1A-D)	Porcine aorta (Fig. 4.1E-F, Fig. 4.3, Fig. 4.4, Fig. 4.5, suppl. Video 4.1)	Porcine aorta (Fig. 4.2)	Rat aorta (Fig. 4.3 and Fig. 4.5)	Human aorta (Fig. 4.3)	Porcine femoral artery (Suppl. Fig. 4.1, Fig. 4.4, Suppl. Video 4.1)	Rat femoral artery (Suppl. Fig. 4.1)	Human femoral artery (Suppl. Fig. 4.1)	Porcine vena cava (Fig. 4.4, Suppl. Video 4.1)	Atherosclerotic human femoral artery (Video 4.1)	Synthetic grafts (Fig. 4.6)
Isotropic voxel size (µm)	8.6	2.75-2.8	4/1.68	1.12	1.5-2	1.75-2.5	1	2.72-3.11	2.75	2.5	3
Source voltage (kV)	80	70	60/90	70	70	80	70	60-80	80	120	50
Tube current (µA)	450	168	281/78	60	90-120	90	60	160-190	140	80	250
Exposure time (ms)	500	750	500	500	500	500	500	500	500	500	500
Mode	0	0	0	0	0	0	0	0	0	0	0
Number of images	1800	2400	2400	2400	2400	2400	2400	2400	2400	2400	2400
Average	1	3	1/3	3	2-3	3	2	1	1	3	1
Skip	0	1	0/1	1	1	1	1	0	0	1	0
Fast scan mode	YES	NO	YES/NO	NO	NO	NO	NO	YES	YES	NO	YES
Scan time (min)	15	129	32/86	89	60-129	89	69	20	20	86	20

$$I = I_{max} - (I_{max} - I_0)e^{-kt} \tag{4.1}$$

where I_0 is the mean of all gray values at $t = 0$, I_{max} is the mean gray value at the latest time point, and k is found by minimizing the sum of squared values between the curve and the experimental data. Finally, a saturation level of $\frac{I}{I_{max}} = 99\%$ was defined, which allowed to compute the staining time necessary for each position inside the tissue. This data was fit to an exponential equation (Eq. 4.2).

$$t = Ae^{cx} \tag{4.2}$$

where t is the staining time, x is the location inside the tissue and A and c are constants that have been fitted to minimize the sum of squared values between the curve and the experimental data. On high-resolution CECT images of smaller pieces of porcine aorta (n = 3), the contrast difference between the elastic lamellae and the background (mainly collagen and SMCs) was determined by calculating the grayscale difference between peaks and valleys of grayscale lines drawn perpendicular to the orientation of the elastic lamellae on 2D slices (in-house developed Python code). Three lines were drawn on 16 slices for each dataset (n = 3 per condition).

4.2.10 CECT and paraffin embedding: volume comparison study

Three fresh pieces of porcine aorta were imaged at low resolution (4 µm voxel size), then fixed in 4% FA and imaged again at low resolution (4 µm). The pieces were stained in 1:2 Hf-WD POM and imaged at low resolution (4 µm) and high resolution (1.68 µm). They were then embedded in paraffin and imaged again at low (4 µm) and high resolution (1.68 µm). The low-resolution imaging allowed to visualize the entire samples and compute their volume to make a comparison between fresh, fixed, stained, and embedded tissue volumes. The high-resolution datasets only allowed to visualize a small VOI in the sample and were registered to each other to allow a one-on-one visual comparison between stained and embedded tissue (n = 3).

4.2.11 Inter-species differences study

For the three types of aortas and the three types of femoral arteries, the adventitia and the media were segmented from each other using the Avizo software (*Magic Wand* and *Watershed* segmentation tools). The thickness

distribution of each layer (media and adventitia) was computed using the 3D analysis in CTAn (Bruker MicroCT, Kontich, Belgium), which uses a sphere-fitting algorithm [205] on binarized images. We chose to remove all thicknesses below 1% in the frequency thickness distribution. The mean and standard deviation of the thickness of the media and the adventitia were then computed for all samples and normalized to the full vessel thickness. Thickness of the media and adventitia were compared between each other for each vessel type. The full thickness of each vessel was also computed and compared between species (n = 3 per sample type).

4.2.12 Comparison study between different types of blood vessels

Avizo was used to generate a video comparing the microstructure of the porcine aorta, femoral artery, and vena cava in 3D. The thickness of the media and adventitia of the vena cava were computed in 3D with CTAn in the same way as for the femoral arteries and the aortas. For each type of porcine blood vessel (aorta, femoral artery, and vena cava), the thickness of each layer was normalized to the thickness of the entire wall and was plotted to compare the relative thickness of each layer (n = 3 per sample type).

4.2.13 Quantification of different structural parameters in different types of blood vessels.

In the rat and in the porcine aortas, three VOIs of 250 × 54 × 60 pixels (approximately 280 × 60 × 67 µm) and 150 × 150 × 150 pixels (420 × 420 × 420 µm), respectively, were selected on each side (intima and adventitia) of the medial layer of each aorta (n = 3 samples). Each VOI was filtered using the following filters, available in Avizo: median filter (interpretation 3D, neighborhood 6, iterations 3), deblur (sharpening factor 5), median filter (interpretation 3D, neighborhood 6, iterations 3), deblur (sharpening factor 5), and Gaussian filter (interpretation 3D, kernel type separable, standard deviation 1, kernel size factor 2). The elastic lamellae were segmented using the *Magic Wand* tool (Avizo). The following parameters were computed for the elastic lamellae using the 3D thickness analysis (CTAn): thickness distribution (µm), separation (or distance between elastic lamellae) distribution (µm), and connectivity density (connectivity, determined by calculating the Euler characteristic, divided by sample volume in μm^{-3} [206]). The volume fraction (volume of elastic lamellae over total VOI volume) and the tortuosity of the elastic lamellae inside a VOI were computed

using Tau factor, a Matlab tool developed by *Cooper et al.* [207]. The tool computes the tortuosity by assessing diffusive tortuosity, which refers to the diffusive transport of a fluid through a porous material. The tortuosity factor τ accounts for the effect of the geometric complexity of the pathways and the volume fraction of the conductive phase on the diffusion process. A higher τ indicates a more complex or elongated pathway, which reduces the effective diffusivity (Eq. 4.3).

$$D^{eff} = D\frac{\epsilon}{\tau} \tag{4.3}$$

where ϵ is the volume fraction of the conductive phase; D is the intrinsic diffusivity of the conductive phase; and D^{eff} is the effective diffusivity through a porous volume where the second phase is insulating. When given a binary 3D volume of the media containing elastic lamellae as input, the script simulates flow through the elastic lamellae in a chosen direction. It compares the steady-state diffusive flow through the network of sheets with that in a fully dense control volume of the same size. The tortuosity of the elastic lamellae was computed in the circumferential direction.

4.2.14 Comparison between healthy and atherosclerotic human femoral artery: imaging and segmentation

The different tissue constituents of an atherosclerotic human femoral artery were segmented with Avizo using the *Magic Wand* and *Watershed* segmentation tools. A video was generated in Avizo to compare the healthy and the atherosclerotic human femoral arteries.

4.2.15 Structural analysis of the synthetic grafts

For the evaluation of the structural parameters (fiber thickness, fiber separation, and fiber volume fraction), images were filtered (Gaussian filter, 3D space, squared kernel with radius 3) and binarized using manual thresholding, and structural parameters were computed with the 3D analysis tool (CTAn) (n = 5 for Dacron and n = 6 for Gore-Tex and Vectra). The fiber thickness is the average thickness of the material present between the pores (µm). The fiber separation is the average size of the pores (µm). The volume fraction in the volume of the object (fibers) divided by the total volume of the graft (%).

4.3 Results

4.3.1 Screening of CESAs based on penetration rate and contrast enhancement

To select the optimal CESA for blood vessel staining and the visualization of the blood vessel wall microstructure, the penetration rate and contrast enhancement of both Mono-WD POM and 1:2 Hf-WD POM were compared using porcine aorta samples. Visual comparison showed that the penetration is faster for Mono-WD POM than for 1:2 Hf-WD POM (Fig. 4.1A). After 48 h, the tissue was fully stained with Mono-WD POM, while it was only fully stained with 1:2 Hf-WD POM after 15 days (Fig. 4.1B-D).1:2 Hf-WD POM staining resulted in a higher final gray value than Mono-WD POM staining, confirmed by the different plateau level of the normalized gray value. High resolution images (2.75–2.8 µm voxel size) were then used to compare the microstructure of the same tissue with both CESAs (Fig. 4.1E–F). From these images, we assume more POM is present in the elastic lamellae when staining with 1:2 Hf-WD POM compared to Mono-WD POM (Fig. 4.1E–F). This was confirmed by measuring the difference in contrast between the elastin sheets and the background for both CESAs (Fig. 4.1H). Classical 2D histological sections colored with Verhoeff's stain confirmed that the bright areas in the CECT images are the elastic lamellae (Fig. 4.1G). Because of the higher contrast between the elastic lamellae and the background (*i.e.* SMCs and collagen) for 1:2 Hf-WD POM staining compared to Mono-WD POM, this CESA was selected for the remainder of the experiments, despite its slower penetration through the tissue.

4.3.2 Sample preparation for classical 2D histology causes tissue deformation

Classical 2D histology is still the reference in the field and is often used to validate CECT-based acquired images. To evaluate the influence of sample preparation and image acquisition of both techniques on tissue integrity, the volumes of different pieces of porcine aorta were computed at different stages of the sample preparation (Fig. 4.2). The fixation of the tissue in 4% FA induced a shrinkage of 18.5% $\pm$ 4.0% compared to the fresh state (Fig. 4.2B), while the staining with 1:2 Hf-WD POM caused an increase in volume of 17.9% $\pm$ 3.9% (Fig. 4.2C) compared to the fixed state. Subsequent embedding in paraffin for classical 2D histology caused a decrease in volume of the tissue of 45.3% $\pm$ 3.1% compared to the fresh state and of 43.0% $\pm$ 3.1% compared to the stained state (Fig. 4.2D). It shows that

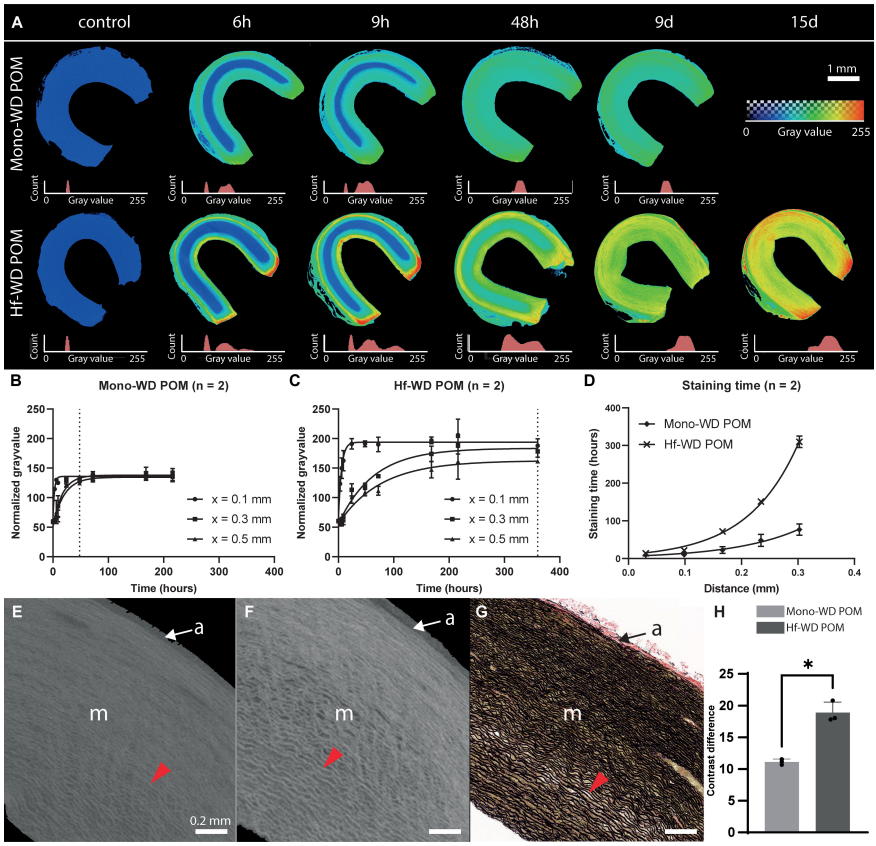


Fig. 4.1 **CESA staining in function of time: Mono-WD POM and 1:2 Hf-WD POM.** (A) CECT-based cross-sections for a few selected time points, the color-legend scalebar goes from 0 to 255 of gray values and the gray value histogram is shown below in red. (B-C) Normalized gray value in function of time for different locations (x) inside the tissue and fitted with an exponential decay curve for (B) Mono-WD POM and (C) 1:2 Hf-WD POM. Dotted vertical line represents full staining of the tissue. (D) Staining time needed for the CESA to reach a certain distance inside the tissue. Comparison of high-resolution CECT-based cross-section of porcine aorta stained with (E) Mono-WD POM and (F) 1:2 Hf-WD POM and comparison with (G) classical 2D histological analysis with Verhoeff's stain, a = adventitia, m = media, red arrowhead = elastic lamella. (H) Contrast difference between elastic lamellae and background (SMCs and collagen) for Mono-WD POM and 1:2 Hf-WD POM-stained samples. Scalebar = 1 mm for (A) and 0.2 mm for (E-G), number of samples (n) = 2 (B-D) and n = 3 (H), $* p \leq 0.05$.

validation of CECT using classical 2D histological sections is possible only in a visual manner, but not quantitatively.

4.3.3 Important differences in microstructure between the rat, porcine and human aorta and femoral artery

The difficulty in obtaining human tissue often leads to the use of animal models, which are then extrapolated to humans. However, differences between species are an important factor to consider when studying diseases or treatment options. Here, rat, porcine, and human aortas and femoral arteries were compared visually and using layer thickness measurements to show the differences in microstructure and size of the arteries among these species (Fig. 4.3 and Suppl. Fig. 4.1). For all species, there is a heterogeneous arrangement of the elastic lamellae present in the medial layer of the aorta, although this is much less present for the rat aorta (Fig. 4.3A). Close to the intima, the sheets are less densely packed and more wavy while close to the adventitia, the sheets are densely packed to each other and less wavy. The porcine and human aorta have a similar thickness, while the rat aorta is significantly thinner than both. However, the normalized thickness of the adventitia and the media compared to the full vessel thickness is similar for all species. The media is the thickest layer, with approximately 82% of full vessel thickness on average for all species (Fig. 4.3B). Contrary to the aorta, for the femoral artery, there are clear visual differences in microstructure between the porcine and human samples (Suppl. Fig. 4.1). In the porcine femoral artery, the external elastic lamina (EEL) is a thick layer of connected sheets ($\sim$ 131 µm) and we defined it to be part of the media where most of the elastin is located. In the human and rat femoral arteries, the EEL is composed of only one (rat) or a few (human) elastic lamellae. The variation in full vessel thickness between all three species is larger for the femoral artery with an increasing thickness going from rat (average thickness = 81.48 µm) to porcine (average thickness = 671.37 µm) to human (average thickness = 1328.73 µm). The difference in normalized thickness between media and adventitia is highly variable among species. The average media thickness is 47.97%, 85.88%, and 69.60% of full vessel thickness for the rat, porcine, and human femoral artery, respectively (Suppl. Fig. 4.1).

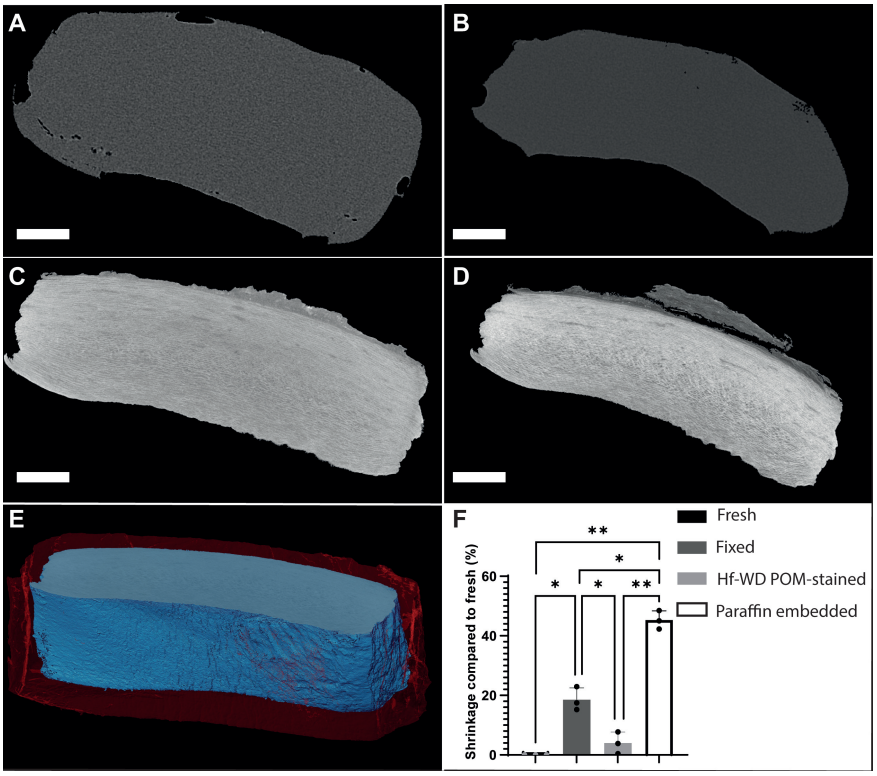


Fig. 4.2 **Volume comparison of a piece of porcine aorta: fresh, fixed in FA, after 1:2 Hf-WD POM staining, and after paraffin embedding.** CECT-based sections of porcine aorta (A) fresh, (B) after fixation in FA, (C) after staining with 1:2 Hf-WD POM and (D) after embedding in paraffin. (E) Overlay of CECT-based volumes after 1:2 Hf-WD POM staining (red translucent) and after embedding in paraffin (blue). (F) Volume comparison between fresh, fixed, after 1:2 Hf-WD POM staining, and paraffin embedding. Scalebars = 500 µm, n = 3, $*$ $p \leq 0.05$, $**$ $p \leq 0.01$, ns $p > 0.05$.

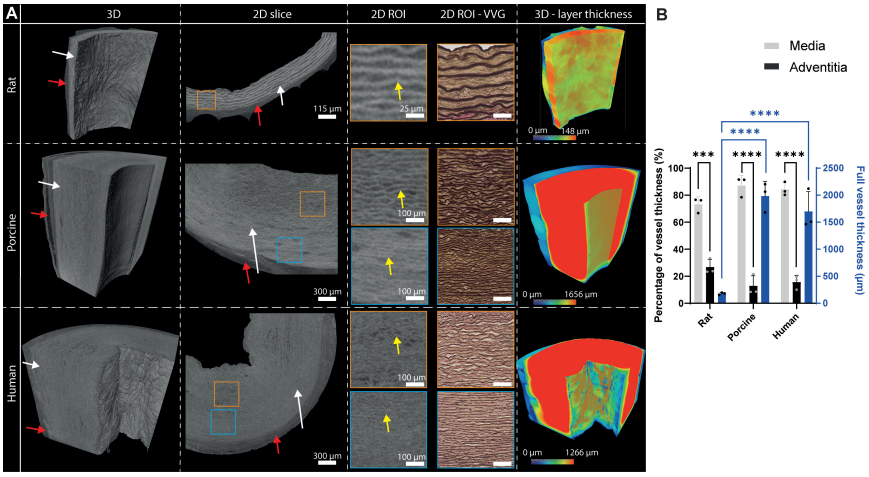


Fig. 4.3 **Differences in microstructure between the rat, porcine and human aorta.** (A) Comparison of CECT-based high-resolution images of the rat, porcine, and human aorta stained with 1:2 Hf-WD POM, showing a 3D representation in the first column, a 2D slice in the second column, a comparison with classical 2D histology with Verhoeff's stain (VVG) on a small ROI in the third column and the results of the layer thickness measurements in the last column, the color-legend scalebar represents the thickness for each vessel layer. (B) Comparison between the normalized media and adventitia thickness for the three species (left Y-axis) and comparison of the full vessel thickness between the three species (right Y-axis). White arrow = media, red arrow = adventitia; yellow arrow = elastic lamella, n = 3, $***\ p \leq 0.001$, $****\ p \leq 0.0001$, ns $p > 0.05$.

4.3.4 Microstructural differences between the porcine aorta, femoral artery, and vena cava

Differences in the microstructure of the different types of blood vessels in the porcine animal model were found: aorta (elastic artery), femoral artery (muscular artery), and vena cava (vein). This shows that treatment options may need to be adapted according to the blood vessel type for optimized treatment. For this reason, it is important to understand the 3D arrangement of the blood vessel wall constituents as can be obtained from CECT-based high-resolution images (Fig. 4.4). The relative thickness of each layer (media and adventitia) varies according to the function of the blood vessel and hence the blood vessel type (Suppl. Video 4.1). The aorta has the thickest medial layer relative to its full thickness with elastic lamellae throughout because it needs to be able to stretch during ventricular contraction and subsequently return to its original shape (average total vessel wall thickness of 1984 µm measured) (Fig. 4.4A). The femoral artery has a thinner medial layer. As it is a muscular artery and is responsible for distributing the blood to the lower limbs, it is less subjected to the heart contractions and high-pressure changes and needs fewer elastic lamellae throughout its media. It has a prominent internal elastic lamina (IEL) and EEL (average total vessel wall thickness of 671 µm measured) (Fig. 4.4B). The vena cava is characterized by its thin medial layer compared to its thick adventitia. It is the largest vein in the body and is responsible for bringing the deoxygenated blood back to the heart and is not subjected to high blood pressures (average total vessel wall thickness of 1668 µm measured) (Fig. 4.4C).

4.3.5 Quantification of structural parameters of different tissue constituents in different types of blood vessels

To better understand the 3D blood vessel wall microstructure, it is important to be able to quantify the structural parameters of its constituents. This information can be used as input for the design of optimized treatments, such as vascular grafts. In the rat and porcine aorta, the elastic lamellae in the media can be segmented to visualize their 3D arrangement and quantify their structural parameters (Fig. 4.5). VOIs at the intimal and at the adventitial side of the media were selected (Fig. 4.5A,B) to show the differences in thickness distribution (Fig. 4.5C,H), average separation (Fig. 4.5D,I), tortuosity (Fig. 4.5E,J), volume fraction (Fig. 4.5F,K), and connectivity density (Fig. 4.5G,L) of the elastic lamellae depending on their lo-

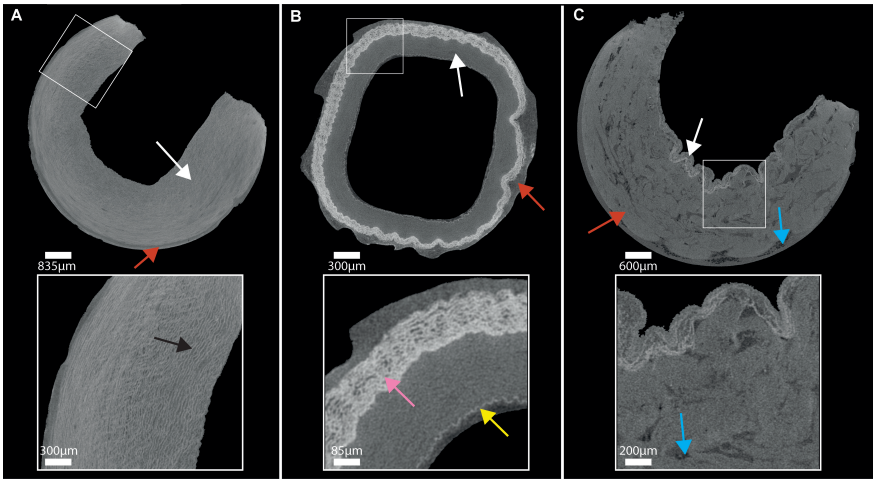


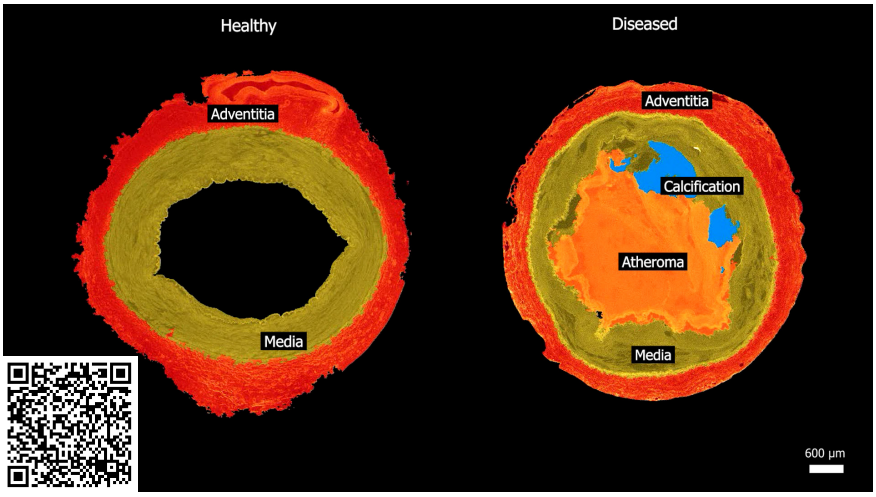
Fig. 4.4 **Microstructural differences between the porcine aorta, femoral artery, and vena cava.** CECT-based representations of the porcine (A) aorta, (B) femoral artery, and (C) vena cava. Red arrow = adventitia, white arrow = media, yellow arrow = internal elastic lamina, pink arrow = external elastic lamina, black arrow = elastic lamella, blue arrow = adipocytes.

cation in the media. In the rat aorta, the elastic lamellae are homogeneous throughout the media. No significant differences are observed between the adventitial and intimal sides of the media for any of the structural parameters characterizing the elastic lamellae. In the porcine aorta, on the intimal side of the media, the elastic lamellae are thinner (difference in average thickness is significant with $p = 0.0377$ *) with a larger, although not significant, distance between them. The spread of the thickness distribution of the elastic lamellae is similar at the adventitial and intimal sides, indicating that the variation in thickness is the same throughout the media. It is important to note that the thicker sheets at the adventitial side can be partly explained by the fact that they are so close together (in some cases touching each other) that multiple sheets are sometimes detected as one. The larger spread of the separation distribution at the intimal side than at the adventitial side is explained by the higher variation in distance between elastic lamellae, and hence the higher tortuosity of the sheets. Additionally, their volume fraction is lower on the intimal than on the adventitial side of the media. The latter is not significant, but the variation on the tortuosity factor is much higher on the adventitial side. The connectivity density of the elastic lamellae is larger on the intimal side than on the adventitial side

of the media, although not significantly. The elastic lamellae in the porcine aorta are approximately three times thicker than in the rat aorta. The elastic lamellae of the rat aorta are on average more wavy (higher tortuosity factor) and hence, their volume fraction is lower. It can also be observed that the average connectivity density of the elastic lamellae is lower in the rat aorta. This structural information is important because the elastic lamellae are a key constituent for assessing the mechanical behavior of the aorta.

4.3.6 CECT-based imaging allows to visualize and segment the different tissue constituents of an atherosclerotic human femoral artery

Using CECT, it is also possible to visualize and segment the tissue constituents of diseased blood vessels, such as atherosclerotic arteries (Video 4.1). A visual comparison was made between a healthy and an atherosclerotic human femoral artery. In both vessels, the media and the adventitia were segmented. In the diseased vessel, the atheroma and the calcified regions of the vessel were located and segmented.



Video 4.1: Segmentation of a healthy and diseased human femoral artery. CECT- based 3D representations of a (left) healthy and (right) an end-stage atherosclerotic human femoral artery. Segmentation of the different vessel layers (media and adventitia) in both vessels, and segmentation of the atheroma and calcified regions in the diseased blood vessel.

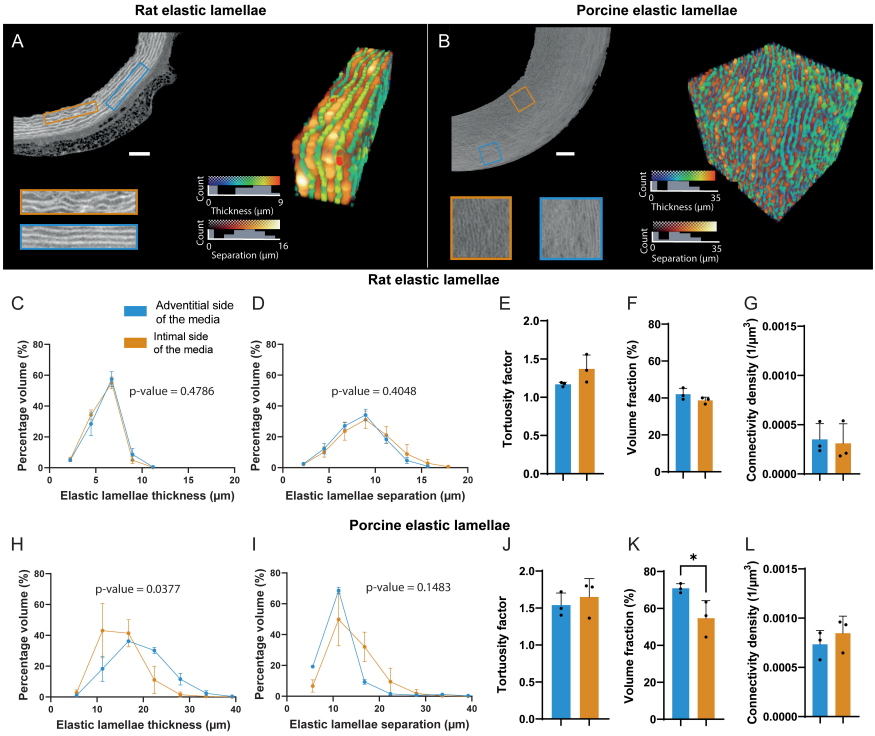


Fig. 4.5 **Quantitative structural parameters extracted from the media of the rat and porcine aortas.** Visual differences between an ROI selected in the media, close to the intima (orange) and close to the adventitia (blue) and representative VOI with thickness and separation (distance between elastic lamellae) of the elastic lamellae represented with a color scalebar for the (A) rat aorta and (B) porcine aorta. Quantitative parameters of the elastic lamellae computed on VOIs close to the intima (orange) or close to the adventitia (blue) (each datapoint represents the average of three selected VOIs): (C,H) thickness distribution, (D,I) separation distribution, (E,J) tortuosity factor, (F,K) volume fraction, and (G,L) connectivity density. Scalebar = 100 μm for (A) and 400 μm for (B), n = 3, $*$ $p \leq 0.05$, ns $p > 0.05$, p-values given for graphs C, D, H, and I are for the comparison between mean values of the distributions.

4.3.7 The microstructure of different synthetic vascular grafts is highly variable and different compared to the native tissue

When the function of a blood vessel is compromised by disease and needs to be replaced, arterial bypass surgery can be performed. Currently used synthetic vascular grafts still lack in biocompatibility and appropriate compliance. We compared the microstructure of several currently used synthetic grafts (Fig. 4.6). Dacron and Gore-Tex are both composed of a single layer with homogeneous properties (Fig. 4.6A). The microstructure of Dacron and Gore-Tex described here does not match that of the native tissue, which is usually composed of three layers having a heterogeneous composition. Vectra does contain three self-bonded microporous layers: an inner layer (foam), a self-sealing middle layer or sheet, and an outer layer (foam), containing a coiled wire (Fig. 4.6A). These layers still have a homogeneous microstructure, not resembling that of the native tissue. The 3D visualization of the microstructure of the grafts with CECT is useful to compare them with native tissue and shows that their microstructure is very different. Some important structural parameters of these vascular grafts were determined: fiber thickness (Fig. 4.6B), separation (Fig. 4.6C) and volume fraction (Fig. 4.6D). Dacron has the thickest fibers, with an average volume fraction of around 72.46 %. Gore-Tex has the smallest pores, with an average volume fraction of around 77.77 %. Vectra only has an average volume fraction of 25.02 %. These parameters are interesting to compare synthetic grafts between them, but it remains difficult to compare them to native tissue. In native tissue, collagen fibers and elastic sheets are present, for example, and it is not always trivial or relevant to compare the fibers of the grafts to these constituents.

4.4 Discussion

Cardiovascular occlusive diseases are commonly treated with the help of synthetic vascular grafts [208–210]. However, the latter still fail in many cases because their functional properties are not optimized to match with those of the native tissue. The mismatch in compliance and caliber, and the stress concentration at the interface between graft and native tissue lead to abnormal shear stresses at the vessel wall, still creating a gap in functional behavior between both [179]. Since 'form follows function' and vice versa [211], the microstructure of the current synthetic vascular grafts might not be appropriate to match their functional properties with those of the native

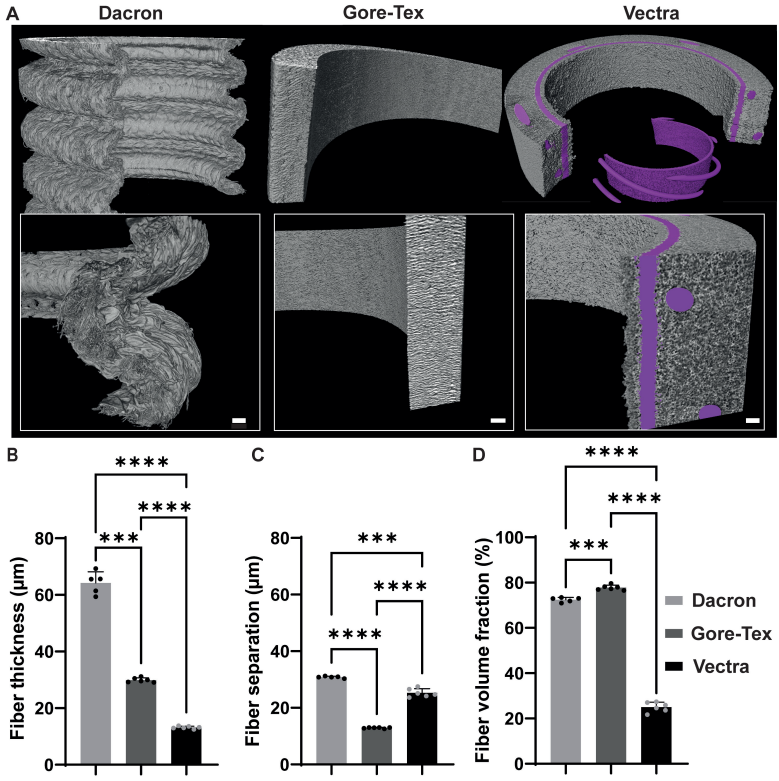


Fig. 4.6 **Microstructural analysis of synthetic vascular grafts commercially available.** CECT-based 3D representations of (A) Dacron, Gore-Tex, and Vectra and comparison of fiber (B) thickness, (C) separation, and (D) volume faction. Scalebars = 200 µm, n = 5 (Dacron), n = 6 (Gore-Tex and Vectra), $***$ $p \leq 0.001$, $****$ $p \leq 0.0001$.

tissue. Native vessels are composed of different functional layers, which themselves also have an inhomogeneous structure. As an example, in the porcine model, the medial layer, one of the three main layers of the aorta, contains elastic lamellae with varying waviness and thickness from one side to the other, as shown in our study (Fig. 4.5). Additionally, often the same synthetic grafts with only a difference in diameter are used for the different types of blood vessels, which have a different microstructure. All this makes the microstructural comparison and matching of the functional properties of synthetic vascular grafts with native tissue challenging. We were able, in this study, to determine the microstructural properties, such as the fiber thickness, the fiber separation and the fiber volume fraction of the most common clinically used synthetic grafts. Dacron and Gore-Tex are currently clinically used as vascular conduits, but they both have a homogeneous microstructure throughout, explaining some of the many issues that remain in terms of biocompatibility. Vectra is currently not used as a bypass graft for diseased vessels, but rather as an arteriovenous graft to optimize hemodialysis, by increasing pressure and blood flow through the vein. Its microstructure is not yet optimal, but its layered structure provides insights for the design of new materials that more accurately replicate the functional behavior of the artery. Although the comparison between grafts and native tissue, based on structural parameters, is challenging, the 3D microCT-based images of the grafts and the 3D CECT-based images of the native tissue are helpful to further optimize the design of grafts. New innovative methodologies involving vascular tissue engineering have been explored to mitigate the poor patency rates of synthetic grafts, especially for small-caliber grafts. They involve the vascular cell seeding of polymeric scaffolds [212–214]. However, efforts are still required to obtain ideal mechanical and biological performance.

To improve treatment options, microstructural knowledge on current synthetic grafts as well as of native tissue is crucial. In the literature, experimental evaluation of pathologies and their treatments is mostly done on one selected blood vessel type in one animal. Only few studies report microstructural differences between blood vessels in different species or differences between types of blood vessels [181, 182]. As porcine animal models are often used to study human heart valve-related diseases, under the assumption that these tissues are similar, some groups have investigated porcine and/or human aortic tissues, focusing on the ascending aorta and heart valves [181, 215]. According to their results, care should

be taken when using porcine animal models to study human diseases. However, their microstructural analysis is based on classical 2D histological techniques only. In the current study, we investigated microstructural differences between three species (rat, porcine, human) and between three porcine blood vessel types (aorta, femoral artery, vena cava). The tunica media and tunica adventitia were segmented for all blood vessels. The tunica intima is composed of a single layer of endothelial cells and could not be readily visualized at the spatial resolutions we imaged. Visual differences between the rat, porcine, and human aortas and femoral arteries were found mainly in terms of spatial arrangement, shape of the elastic lamellae and microstructural arrangement of the external elastic lamina. The ratio in thickness between the media and adventitia is similar for all species in the aorta (elastic artery) with a thicker media compared to the adventitia, containing much more elastic tissue than the media of the femoral artery (muscular artery) to allow it to maintain a relatively constant pressure gradient despite the pumping action of the heart [11]. In the femoral artery, the thickness ratio between media and adventitia is highly variable among species, but the media contains much more SMCs and less elastic tissue. In terms of full vessel thickness, the rat aorta is significantly thinner than the porcine and human aorta and the rat femoral artery is significantly thinner than the porcine and human femoral artery. Between the aorta, femoral artery, and vena cava, differences mainly were detected concerning the relative thickness of the different layers and their content in elastic lamellae versus collagen and SMCs. Additionally, when computing different structural parameters of the elastic lamellae in the media of the rat and porcine aortas, it was shown that the variation throughout the media is very different for both species. In the rat aorta, the elastic lamellae are much more homogeneous throughout the medial layer than for the porcine aorta. In the current literature, parameters such as breaks in the elastic lamellae are often counted manually on classical 2D histological slices [216–218] or shown visually in scanning electron microscopy images [219]. In phase-contrast or synchrotron microCT, some parameters have been quantified such as, waviness [220], and volume fraction [42]. However, to detect breaks in the elastin, manual annotations are often still required [69]. The advantage of CECT is that after segmentation of the elastic lamellae, structural parameters can be computed automatically and in 3D. However, it remains non-trivial to quantify change in the structure of the elastic lamellae. In this study, we have mainly imaged small tissue sections to obtain high resolution images. However, it is also possible to

image the entire circumference of the different blood vessels. This is sometimes at the cost of a loss in resolution, however, this is necessary to study pathological specimens, such as aneurysms or atherosclerotic plaque, as shown in Video 4.1. Indeed, for CECT imaging to be widely used, it is important to show that it is possible to apply the technique to diseased heterogeneous blood vessels. We showed the possibility to image and segment an end-stage atherosclerotic human femoral artery. After segmentation, it is possible to obtain quantitative information such as volume of calcified tissue and volume of the atheroma. It also allows studying where onsets of calcifications are occurring and how the microstructural constituents, such as the internal and external elastic lamina are affected by the disease. This is important for better understanding the pathogenesis of atherosclerosis, which is still not fully understood [221].

A limitation of our study is that we focused on the imaging of elastin as constituent because we did not achieve sufficient resolution to image the collagen fibers. However, collagen fibers and their orientation have an important impact on the mechanical behavior and are thus an important wall constituent. Moreover, due to time constraints and limited sample availability, only three biological samples per group were assessed. More samples should be imaged in the future. The goal was to show a proof of concept for the quantitative assessment of blood vessel wall structural properties using CECT-based imaging.

To validate CECT data, often classical 2D histology is used [69, 113, 155]. For visual and qualitative validation, this might be appropriate. However, in this study, we found evidence that classical 2D histology cannot be used to validate the thickness measurements of the different wall layers nor for the structural analysis of the tissue constituents. Our analysis showed a shrinkage of the tissue due to fixation in 4% FA of around 18.5 %. This shrinkage can be explained due to the cross-linking of the proteins in the tissue [222–225]. The staining with 1:2 Hf-WD POM caused consistent swelling of the tissues of around 17.9 %. Swelling was also observed upon staining with Mono-WD POM (data not shown). We hypothesize that this is caused by osmotic effects [226]. This means that when POMs and other ions enter the tissue, this seems to be accompanied by an osmotically-driven flow of water molecules in the tissue, leading to swelling. When we then prepare the tissue for sectioning for classical 2D histology (embedding in paraffin), a more significant decrease in volume of around 43 %

compared to the 1:2 Hf-WD POM-stained tissue was found. We have also seen that the sectioning and colorimetric staining after paraffin embedding can cause additional damage/changes to the microstructure of the tissue (disruption of the adventitial layer of the wall in the aorta and femoral artery, data not shown). Both the substantial tissue shrinkage as well as the potential tissue disintegration with classical 2D histology show the benefit of using CECT for conservation of the tissue integrity for quantitative microstructural characterization, provided that the appropriate CESA is used that does not cause any tissue deformation.

We evaluated in this study the use of two polyoxometalates (POMs), Mono-WD POM and 1:2 Hf-WD POM, for CECT imaging of the vascular tissues. 1:2 Hf-WD POM and Mono-WD POM are both negatively charged while tropoelastin, elastin's subunit, is likely to be positively charged at physiological pH. On the contrary, the other proteins present in the blood vessel wall (mainly collagen and fibrillin) are likely to have a negative net charge at physiological pH (net charge at pH = 7.4 determined with Expasy [227] and ClustalW). The POMs are thus more likely to interact with elastin compared to the other proteins.

Concerning their diffusion kinetics, we found that both for Mono-WD POM and 1:2 Hf-WD POM, there is an exponential increase in staining time with distance. This means that the penetration speed is non-linear and decreases over time until it stabilizes, when the tissue is fully stained. This suggests that the diffusion process is limited by the tissue's capacity to accommodate the CESAs evenly across its depth. This is further evidenced by the observation of clear diffusion fronts in the imaging data, indicating areas where the CESAs have penetrated compared to those they have not yet reached, rather than a smooth gradient of staining (Fig. 4.1A). This could be due to the following reasons. (i) The resolution of our imaging technique is limited. This limitation could result in the appearance of more abrupt diffusion fronts than might actually be the case if observed at a higher resolution. (ii) The gray value, which represents the intensity of staining, decreases with tissue depth before reaching a plateau. This suggests that the tissue composition and structure, such as the presence of elastic lamellae with higher gray values, play a significant role in the diffusion process. Elastic lamellae, being denser and possibly having different affinities for the CESAs, could hinder smooth diffusion. Additionally, fenestrations or openings within these sheets may not allow for unobstructed

diffusion of the CESAs, further complicating the staining process. Hence, the relationship between staining time and distance, influenced by these factors, highlights the complexity of tissue staining with CESAs. It highlights the need for a detailed understanding of both the diffusion dynamics of the CESAs (*i.e.*, their chemical interactions with the tissue microstructural components) and the microstructural characteristics and composition of the tissue being stained.

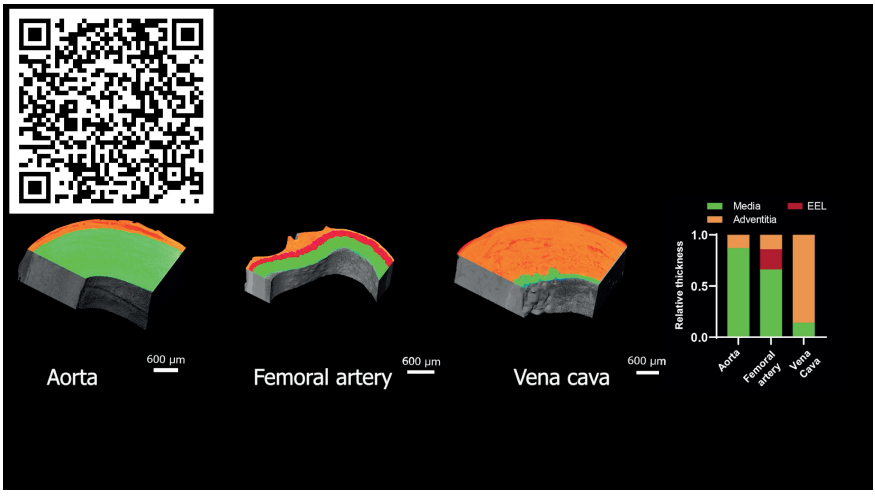
We found that, even though staining time and therefore sample preparation time is reduced using Mono-WD POM, 1:2 Hf-WD POM allowed a better visualization of the microstructure of the blood vessel wall, allowing the distinction of the individual elastic lamellae mostly present in the medial layer of the aorta. It must be noted that the Mono-WD POM and 1:2 Hf-WD POM concentrations used in this study lead to a molar concentration of Mono-WD POM that is approximately twice as high as that of 1:2 Hf-WD POM. This should be considered when comparing staining times. However, we assume that at the same molar concentration, the Mono-WD POM will still penetrate the tissue faster compared to the 1:2 Hf-WD POM given that it reaches the plateau four times faster on average. Independently of the staining time, the specificity, and hence the binding mechanisms of 1:2 Hf-WD POM are different from those of Mono-WD POM. The slow diffusion of the 1:2 Hf-WD POM most likely comes from a stronger POM-protein interaction for this compound [228]. 1:2 Hf-WD POM has one Lewis acidic Hafnium atom that has oxidation state + IV, which should improve interaction with proteins, such as elastin [228]. This is not the case for Mono-WD POM. Ongoing research in our group is currently focusing on better understanding the link between the interactions and the diffusion of the CESAs.

4.5 Conclusion

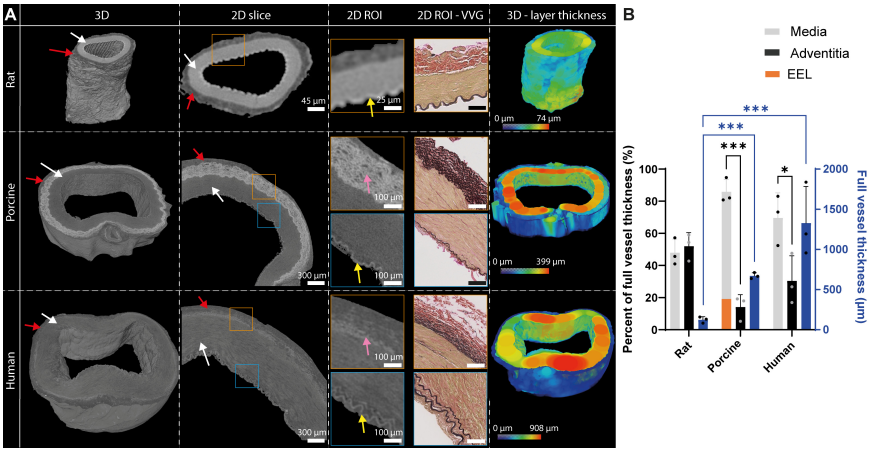
Cardiovascular diseases are still a major cause of death and to enhance our treatment strategies, improved knowledge on the native tissue microstructure of the blood vessels could be useful. Indeed, we emphasized the gap that still remains between existing vascular replacement grafts and the native vascular tissue. We have shown that 1:2 Hf-WD POM CECT combined with advanced image processing and analysis provides a way to visualize the 3D microstructure and quantify the structural parameters of the native blood vessel wall and synthetic grafts. We showed that this

technique is advantageous compared to classical 2D histology for structural analysis, which induces tissue deformation during sample preparation and can thus not be used to extract quantitative data. Moreover, CECT allows avoiding paraffinization and tissue degradation and provides 3D information instead of only 2D. We indicated the differences that exist in the microstructure of the blood vessels of different species to highlight the importance of carefully choosing an animal model when studying a disease or disease treatment. In the porcine model, the differences between blood vessels were also highlighted to show that disease treatments should also consider blood vessel type. From the CECT-based representations of the blood vessels, we extracted quantitative information, such as thickness, separation, volume fraction, and tortuosity of the elastin sheets of the aorta. This information leads to a better understanding of the native blood vessel wall. It is important knowledge to further improve the current disease treatments, such as providing input for new and optimized design of synthetic vascular grafts.

4.6 Supplementary materials



Suppl. Video 4.1: Differences in layer thickness between the porcine aorta, femoral artery, and vena cava. 3D CECT-based representations of porcine aorta, femoral artery, and vena cava and graph representing the relative thickness of the media and adventitia for the three types of blood vessels. n=3.



Suppl. Fig. 4.1: Differences in microstructure between the rat, porcine and human femoral artery. (A) Comparison of CECT-based high-resolution images of the rat, porcine, and human femoral artery stained with 1:2 Hf-WD POM, showing a 3D representation in the first column, a 2D slice in the second column, a comparison with classical 2D histology with Verhoeff's stain (VVG) on a small ROI in the third column, and the results of the layer thickness measurements in the last column. (B) Comparison between the normalized media and adventitia thickness for the three species (left Y-axis) and comparison of the full vessel thickness between the three species (right Y-axis). White arrow = media, red arrow = adventitia, yellow arrow = internal elastic lamina, pink arrow = external elastic lamina, n = 3, $*$ $p \leq 0.05$, $***$ $p \leq 0.001$, ns $p > 0.05$.

PART III
MicroCT-based imaging of metallic implants for biodegradable intravascular stents

5

Advancements in the development of biodegradable intravascular stent materials

Positioning in the context of this PhD thesis

In chapter 1, a series of treatments for cardiovascular occlusive diseases were presented. After studying different synthetic vascular grafts in the previous chapter, the next three chapters focus on intravascular stenting. Stent placement has become one of the gold standard treatment strategies for vessel revascularization. However, there are still issues related to the permanent presence of a foreign body within the artery, which is associated with the risk of late-stent thrombosis (ST), chronic inflammation or stent-strut fracture [229, 230]. In this chapter, different requirements for stent success, the different generations of stent designs, and their respective properties will be discussed before presenting the results of our own studies on stent research in the two subsequent chapters. There, we explored the biodegradability and biocompatibility of candidate metallic intravascular stent materials using microCT and CECT. This chapter has

been written with the support of Noémie Lapraille within the frame of her master thesis.

5.1 Intravascular stents

To be successful in restoring the blood flow without causing any adverse effects, a stent has to fulfil a list of specific requirements:

A. Biocompatibility, reflected by [231]

- Low toxicity: Materials that are toxic to the body can cause local or systemic reactions. Using low-toxicity materials reduces the risk of allergic reactions and other complications that can arise from the body's response to foreign substances.
- Low restenosis: Excessive tissue growth should be prevented, as this may cause thickening of the vessel wall and re-narrowing of the artery.
- Low inflammation: Inflammation is part of the healing process, but if excessive, it can lead to complications. Reducing inflammation is key to promoting healing and reducing the risk of restensosis.
- Reendothelialization: This is crucial for integrating the stent into the blood vessel and restoring its natural function.
- No genotoxicity: No alterations in DNA or chromosomal structure or other DNA or gene damage which could result in permanent changes in cell function and ultimately in carcinogenesis.
- Low oxidative stress: Oxidative stress may be caused by an imbalance between the production of reactive oxygen species (ROS) during stent implantation and the body's ability to neutralize them, which may lead to cell damage and tissue injury.
- Low platelet aggregation: Platelet aggregation is a normal part of the healing process to prevent bleeding, but if excessive it can lead to the formation of a blood clot and lead to ST.
- Complete and functional endothelium recovery to prevent neoatherosclerosis.

B. Appropriate mechanical properties [229, 232]

- High elastic modulus to prevent recoil (elastic recoil on expansion < 4% [233])
- High tensile properties after expansion to provide radial strength and allow the use of thinner struts (> 300 MPa [233])
- Low yield strength to allow stent expansion at low inflation pressures ($\sim$ 200 MPa [234])
- High ductility to allow plastic deformation during expansion without cracking (elongation to failure > 15-18% [233])

C. Radio-opaque to be visible by the surgeon using X-ray-based techniques [27]

D. Be deliverable at the lesion site in non-deployed state (*i.e.* passing through tortuosity and calcified sites without being damaged or dislodged from the balloon) [27]

The first generation of stents, which appeared in the 1980s, were called bare metal stents (BMS), and were manufactured using inert corrosion resistant materials, such as stainless steel, cobalt-chromium alloys, and shape memory nickel-titanium alloys [235]. However, the long-term use of permanent stents has been associated with many drawbacks including chronic inflammation, late-stage thrombosis, and stent-strut fracture [233]. While ISR rates were reduced compared to the stenosis rates observed in balloon angioplasty where no stent was applied, it was reported that 25% of cases following BMS placement still involved ISR [14]. The second generation of stents, introduced around 2002-2003, known as drug-eluting stents (DES) were coated with antiproliferative drugs to prevent ISR. DES are constituted of a metallic backbone (stainless steel, cobalt-chromium, or nickel-titanium) and coated with a polymer to control drug elution rate. The polymer was permanent (poly(ethylene-co-vinyl acetate) (PEVA) or poly(styrene-b-isobutylene-b-styrene) (SIBS)) in the first generations of DES and biodegradable in the later generations (poly(L)-lactic acid (PLLA), poly (D,L)-lactic acid (PDLLA), or polycaprolactone (PCL)). The later generations of DES stents yielded excellent early and mid-term results, however, due to the continued presence of the stent in the blood vessel and the decreasing effect of the released drug, late stage thrombosis was not eliminated [14, 236]. Moreover, to prevent ST, DES stent implantation always has to be accompanied by anti-coagulants and dual antiplatelet therapy (DAPT) [237].

5.2 Biodegradable intravascular stents

To mitigate the side effects and limitations of permanent BMS and DES, biodegradable stents have been investigated for the past two decades [238]. Many benefits are attributed to biodegradable stents. They do not require prolonged DAPT, decreasing the risk of bleeding, especially in older patients. When they disappear, vessel treatment is possible, which also makes it easier to reach the peripheral branching blood vessels that were initially blocked by the stent. Additionally, as the artery is not permanently caged, late positive remodeling is possible to widen or adapt in response to physiological changes. Finally, the absorption of the stent could potentially lead to a full recovery of the endothelial function (Table 5.1) [239].

Table 5.1 Comparison between the three main types of stents: bare-metal stents (BMS), drug-eluting stents (DES), and biodegradable stents (BRS). CABG = coronary artery bypass surgery, PCI = percutaneous coronary intervention. Adapted from [239], licensed under the Creative Commons Attribution license [3]

	BMS	**DES**	**BRS**
Radial support	Permanent	Permanent	Transient
Need for prolonged double antiplatelet therapy	No	Yes	No
Late ST	Yes	Yes	No
Expansive remodeling possible	No	No	Yes
Permanently close off side branches	Yes	Yes	No
Facilited reintervention in the treated segment (CABG or PCI)	No	No	Yes
Potential recovery of the endothelial function	No	No	Yes

Biodegradable stents are expected to meet the same criteria as BMS and DES, with the added necessity of considering specific requirements related to their degradation behavior (*i.e.* their corrosion rate and the biocompatibility of their byproducts). A biodegradable stent is required to last for 6 to 12 months to allow vessel remodeling and should fully disappear within 12 to 24 months (Fig. 5.1) [233, 240]. To this day, two classes of biomaterials have been considered for biodegradable stents: polymers and metals. Polymers

are associated with serious limitations linked to their insufficient mechanical properties [21] as well as their biocompatibility (vascular toxicity and local inflammation) [241, 242]. Additionally, they are not radio-opaque, making their placement difficult using angiography. Hence, metals with high mechanical strength, high ductility, and adequate biocompatibility are of interest for use as biodegradable intravascular stents [235]. Three main classes of metals have been identified as candidate materials owing to their favorable biocorrosion properties: magnesium (Mg), iron (Fe), and zinc (Zn).

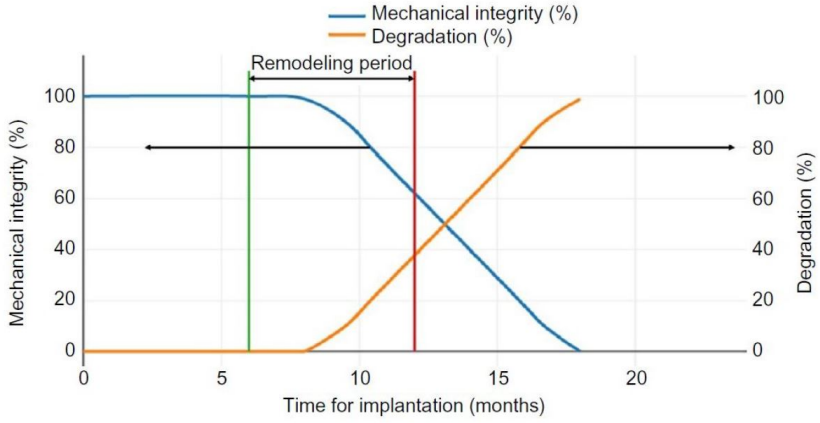


Fig. 5.1 Ideal trade-off between mechanical integrity and degradation for a biodegradable stent. Reprinted from [243], Copyright 2018, with permission from Elsevier.

5.2.1 Magnesium-based biodegradable stents

Mg has been considered for biodegradable implants because of its essential functions in the body. Mg is involved in over 600 enzymatic reactions having a role in energy metabolism, protein synthesis, DNA and RNA synthesis and stabilization of mitochondrial membranes. It also has a role in the maintenance of several physiological functions, such as cardiac excitability, muscle contractions, and normal blood pressure [244].

The degradation of Mg in aqueous environment produces hydroxide ions and hydrogen gas and can be decomposed in an anodic (5.1) and a

cathodic (5.2) reaction. The hydroxide ions can significantly increase the local pH, which may cause adverse effects on local cell function. The hydrogen gas evolution can lead to the formation of gas cavities in the tissue or bloodstream, which can be harmful to cells. Next, Mg^{2+} and OH^- react to form magnesium hydroxide, as described in reaction 5.3, which is a degradation layer that forms on the surface of the magnesium stent and only provides limited protection from subsequent degradation because of its loose and porous microstructure [245].

Anodic reaction:

$$Mg \longrightarrow Mg^{2+} + 2\,e^- \tag{5.1}$$

Cathodic reaction:

$$2\,H_2O + 2\,e^- \longrightarrow H_2 + 2\,OH^- \tag{5.2}$$

Chemical reaction with $Mg(OH)_2$ formation:

$$2\,Mg^{2+} + 2\,OH^- \longrightarrow Mg(OH)_2 \tag{5.3}$$

Pure Mg exhibits poor mechanical properties. As cast Mg has a yield strength of 20 MPa, tensile strength of 86 MPa, and elongation to failure of 13 % [246]. Strategies to improve the mechanical properties of pure Mg include alloying and heat treatment. Although these strategies considerably improve the mechanical properties of pure Mg, the latter has a high negative standard corrosion potential equal to -2.73V, which implies rapid metal corrosion and by extension, mechanical loss [229].

Mg-based biodegradable stents are the first degradable metallic stents that have been used in the clinics. AMS, DREAMS, and Magmaris from Biotronik (Berlin, Germany) have been involved in many clinical investigations. Magmaris, their last generation DES biodegradable stent, seems to present a good safety profile but its radial strength and corrosion are still too low inducing vessel recoil. Hence, its use is limited to short and less calcified lesions in situations where the patient stands to benefit significantly from the complete absorption of the stent (young and otherwise healthy patients) [235, 236].

Recent new strategies to improve the performance of pure Mg and

obtain materials with improved strength, ductility, and corrosion performance include alloying with Ca, Mn, Zn, Sn, Al, Zr, Sr, as well as rare earth elements, new manufacturing techniques (*e.g.*, flat sheet precursors combined with convectional laser cutting, selective laser melting), and coatings (*e.g.*, PLLA, PLGA, drug reservoirs) that control the degradation kinetics and improve interactions between the stent and tissue [235].

5.2.2 Iron-based biodegradable stents

Fe is essential for human life. It plays a crucial role in the formation of various metalloproteins, including hemoglobin, myoglobin, cytochromes, and ferritin. These proteins are involved in vital processes, such as oxygen transport and storage, electron transfer, and enzymatic catalysis. Additionally, iron is important in oxygen sensing mechanisms and is indirectly involved in DNA synthesis [244]. When iron corrodes in the presence of physiological fluids, it undergoes a reaction with water and oxygen to produce rust (reactions 5.4 to 5.6).

Anodic reaction:

$$\mathrm{Fe} \longrightarrow \mathrm{Fe}^{2+} + 2\,\mathrm{e}^{-} \tag{5.4}$$

Cathodic reaction:

$$2\,\mathrm{H_2O} + \mathrm{O_2} + 4\,\mathrm{e}^{-} \longrightarrow 4\,\mathrm{OH}^{-} \tag{5.5}$$

Chemical reaction with $\mathrm{Fe(OH)_2}$ formation:

$$\mathrm{Fe}^{2+} + 2\,\mathrm{OH}^{-} \longrightarrow \mathrm{Fe(OH)_2} \tag{5.6}$$

Additional byproducts of Fe corrosion in a physiological pH environment include the coordination compounds of iron oxides ($\mathrm{FeO \cdot Fe_2O_3}$). Given that the human body also contains sodium, chloride, carbon, and phosphorous, other byproducts include iron carbonates, iron phosphates, and iron chlorides [247].

Fe is an attractive material because of its superior mechanical properties compared to Mg. Indeed, 99.9% purity Armco Fe has a yield strength of 250 MPa, tensile strength of 300 MPa, and elongation to failure of 37.5 % [246]. However, the standard corrosion potential of Fe is -0.44V, meaning a corrosion rate that is very slow for biodegradable stent material appli-

cations [229]. The greatest challenge with Fe-based biodegradable stents is to develop processing techniques and alloys that increase the corrosion rate while maintaining optimal biocompatibility and mechanical properties. Over the past decade, there has been a growing interest in nitrided Fe stents because of their improved corrosion rate and mechanical properties compared to pure Fe [235]. IBS from Lifetech Scientific (Shenzhen, China) is the first Fe-based biodegradable stent that went to preclinical testing. It is a nitrided Fe stent coated with PDLLA and sirolimus. One disadvantage of IBS is that, despite its good biocompatibility, appropriate degradation rate, and good mechanical properties, the corrosion products stay in the vessel in the long term due to slow clearance [248]. However, a first in-human evaluation of this stent was published in 2023 after a 3-year follow-up study and showed promising results in terms of safety and effectiveness [249].

Continued research to improve the corrosion rate of Fe has included alloying. Different elements have been considered for binary systems, such as Mn, Co, Al, W, Sn, B, C, S, Pd, and Pt, as well as ternary systems, such as Fe-Mn-Pd and Fe-Mn-C [246, 247]. Fe-Mn alloys have attracted special attention due to their enhanced mechanical properties, with some of them classified as twinning-induced plasticity (TWIP) steels [230]. TWIP refers to the occurrence of mechanical twinning as a plastic deformation mechanism [250]. Fe-Mn TWIP steels are characterized by a high strain hardening, large uniform elongation (50 % to over 60 %) and high ultimate tensile strength levels (800 to over 1000 MPa). Due to their remarkable mechanical characteristics, TWIP steels have found extensive applications in the automotive, shipbuilding, and oil and gas sectors [251]. *Verhaegen et al.* have pointed out that they could also be promising candidates for novel bioresorbable stents owing to their mechanical properties, biocompatibility, and appropriate corrosion rate if correctly alloyed [230]. However, some concerns have been raised regarding increased inflammatory reactions that have been observed in Fe alloys compared to pure Fe. The local biocompatibility of Fe-based stents should be studied more in-depth to study the local effects of Fe corrosion products on neighboring tissue and cells [248].

5.2.3 Zinc-based biodegradable stents

Zn has only been first introduced as candidate material for biodegradable stents in 2013 [233]. Zn is also a vital element for basic biological function.

It is involved in nucleic acid metabolism, signal transduction, apoptosis regulation, and gene expression in addition to interacting with various organic ligands [233]. Reactions 5.7, 5.8, and 5.9 describe the degradation process of pure Zn.

Anodic reaction:

$$\mathrm{Zn} \longrightarrow \mathrm{Zn}^{2+} + 2\,\mathrm{e}^{-} \tag{5.7}$$

Cathodic reaction:

$$\mathrm{O_2} + 2\,\mathrm{H_2O} + 4\,\mathrm{e}^{-} \longrightarrow 4\,\mathrm{OH}^{-} \tag{5.8}$$

Chemical reaction with $\mathrm{Zn(OH)_2}$ formation:

$$2\,\mathrm{Zn}^{2+} + 4\,\mathrm{OH}^{-} \longrightarrow 2\,\mathrm{Zn(OH)_2} \tag{5.9}$$

Pure Zn stents were implanted for the first time in a rabbit abdominal aorta model in 2017 by *Yang et al.* [252]. However, pure Zn has a much too low tensile strength ($\sim$ 120 MPa) [240]. Regarding biodegradation, the standard corrosion potential of Zn is -0.76V, which lies between Fe and Mg and presents a good trade-off between these two elements [229]. The challenge is to develop a material with suitable mechanical properties without sacrificing the appropriate corrosion and biocompatibility characteristics. Alloying with various elements, such as Mg, Ca, Cu, Mn, and Sr, has been considered for this purpose [253]. Some elements that have been used to improve the properties of Mg have also been alloyed with Zn, such as Al, with favorable mechanical properties (Bowen-2017). *Oliver et al.* have investigated a promising quinary Zn-Ag-Mn-Zr-Cu alloy with inflammation resistant properties [254].

5.2.4 Summary of the mechanical properties

To summarize the mechanical properties of the different materials that have been described in this section as (candidate) stent materials, Table 5.2 and Fig. 5.2 compare the yield strength, ultimate tensile strength, elastic modulus, and elongation at fracture of these materials.

It is important to note that the mechanical properties of metals, which

Table 5.2 Mechanical properties (yield strength, ultimate tensile strength, elastic modulus, and elongation at fracture) of different currently investigated biodegradable stent materials and comparison with biostable 316 L stainless steel (SS) and a Co-Cr alloy

Material	Composition	Yield strength (MPa)	Ultimate tensile strength (MPa)	Elastic modulus (GPa)	Elongation at failure (%)	Reference
Polymer	Poly-L-lactic acid (PLLA)	70	50	2.8-4	5-10	[240]
Pure Mg, as cast	Mg	20 20	86 86	/ 41	13 13	[246] [240]
Pure Zn	Zn	/ / 75-160 /	100-150 120 / /	78-121 / / /	/ / / 10-15	[255] [240] [256] [257]
316L SS	Fe, Cr, Ni, Mo, Si, P, S	190 190	490 490	/ 193	40 40	[246] [240]
Co-Cr alloy ASTM F90	Co, Cr, W, Ni, Fe, Mo, Si, C	310	860	190	20	[246]
Pure Fe	Fe	150 120-150	210 180-210	/ 211	40 /	[246] [258]

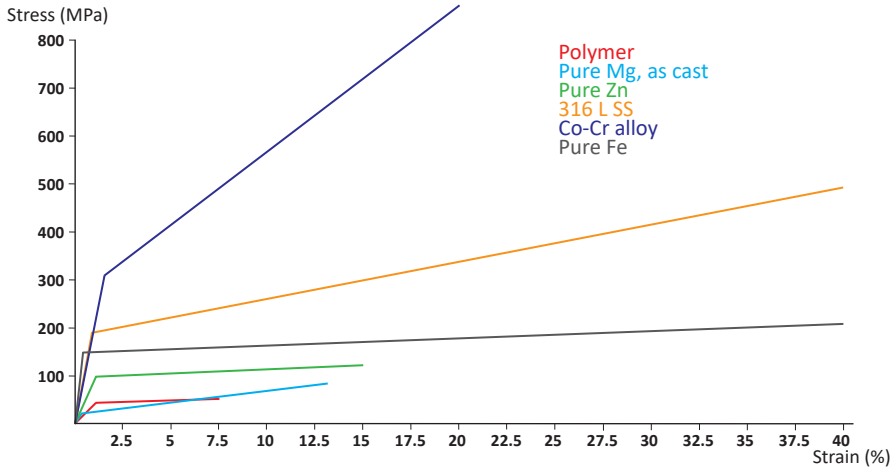


Fig. 5.2 Corresponding approximated stress-strain curves for currently investigated biodegradable stent materials compared with biostable 316 L stainless steel (SS) and a Co-Cr alloy

determine their ability to provide support to the vessel wall, are closely linked to their corrosion behavior. This link is based not only on the chemical composition of the metals but also on their microstructure, including the arrangement of grains, phases, and the presence of defects such as dislocations and voids. The mechanical integrity of a metal, determined by these factors, directly impacts its corrosion behavior. For example, certain

elements within an alloy slow down or accelerate corrosion and have an impact on corrosion behavior. Similarly, specific microstructural features can either offer paths of resistance or become sites of weakness where corrosion initiates.

5.3 Reendothelialization

Stent implantation induces mechanical vascular injury due to the stretching of the vessel wall. This induces activation, damage, or denudation of the ECs. Reendothelialization is an important part of the wound healing process during which stent struts are covered by neointimal tissue lined by newly formed ECs. Rapid endothelialization is essential to ensure safety of the device. Indeed, the anti-thrombotic and anti-adhesive properties of ECs prevent the recruitment and adhesion of platelets and leukocytes to the stented area [259].

The stent design and composition are of the main factors that influence stent endothelialization and endothelial cell recovery following a stenting procedure [260]. However, many other factors influence endothelialization.

- Stent design: The geometry and strut thickness can affect cell migration and attachment.
- Stent material composition: The material itself and its degradation products should be non-toxic and promote EC growth.
- Surface roughness: Increased surface roughness due to corrosion can potentially enhance endothelial cell adhesion and proliferation, which is beneficial for the healing process around a stent. However, excessive roughness or irregular corrosion products could potentially lead to adverse effects.
- Stent coating: A stent coating can release drugs or other bioactive substances that can inhibit excessive cell proliferation or promote endothelial cell growth.
- Mechanical stress: The mechanical stress imposed by the stent on the vessel wall can influence cell migration and proliferation. A stent that better adapts to the movements of the vessel is likely to support healthier recovery.

- Patient-specific factors: Individual patient factors, such as underlying health conditions, medication use, and genetic predispositions can affect the rate of reendothelialization.

Two different processes can occur because of impaired reendothelialization: ISR or ST (Fig. 5.3).

5.3.1 In-stent restenosis

ISR is a frequent late-stage event associated with morbidity corresponding to progressive lumen narrowing due to neointimal hyperplasia. When reendothelialization is impaired, platelet activation and adhesion causes fibrin to accumulate at the injury site. Activated platelets express adhesion molecules, leading to the recruitment of inflammatory cells. The recruitment of platelets and leukocytes releases growth factors and cytokines, which stimulate SMC proliferation, migration, and the deposition of ECM proteins within the arterial intima, contributing to ISR [260].

5.3.2 Stent thrombosis

ST can be an early (acute/subacute) or a late-stage event. It is less frequent than ISR, but it is life-threatening because it involves sudden lumen narrowing due to the formation of a thrombus in the arterial lumen.

Early thrombosis is often related to technical issues during implantation (significant residual stenosis, stent underexpansion, residual thrombus within the treated segment) or treatment of complex lesions (long lesions, small vessels, bifurcations with multiple stents). It is initiated by the loss of ECs due to mechanical injury resulting in thrombus formation or the presence of a thrombogenic biomaterial in the blood resulting in adsorption of plasma proteins to the surface [261].

Late ST is more complex and is related to incomplete stent endothelialization related to antiproliferative drugs on DES [262], stent underexpansion [262], thick struts [262], inappropriate polymer type [263], penetration of the necrotic core of the atherosclerotic plaque by the stent strut [264], or neoatherosclerosis [265]. A delayed reendothelialization process leads to the lack of antithrombotic molecules originating from ECs and extended exposure of subendothelial matrix proteins to blood. This situation ultimately leads to the development of a thrombus, as described in the part on

atherothrombosis in chapter 1, section 1.2. Even when endothelialization is complete, other events may cause late ST, such as stent fracture.

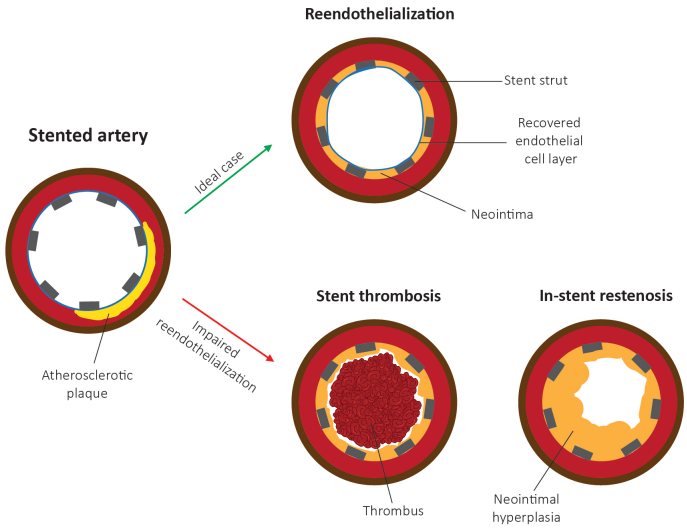


Fig. 5.3 Possible outcomes for stent implantation. In the ideal case of healthy reendothelialization, the stent struts are encapsulated by neointimal tissue and a newly endothelial cell layer has formed. In case of impaired reendothelialization, stent thrombosis (sudden lumen narrowing) or in-stent restenosis (progressive lumen narrowing) may occur.

5.4 Evaluation of stents in (pre)clinical conditions

Clinical or preclinical evaluation of stent outcomes in patients can be performed with several techniques or diagnostic tools to evaluate the efficacy and safety of the stent.

- Angiography is an X-ray based imaging technique used for stent placement. It involves the insertion of a catheter into the blood vessel. A contrast dye is injected through the catheter and X-ray images are taken as the dye moves through the blood vessels. It allows to visualize the arteries and to identify the degree of stenosis prior to and after stent placement [266].
- Optical coherence tomography (OCT) is an imaging technique that uses near-infrared light to provide high-resolution images of the ar-

teries and to assess stent apposition, stent strut coverage, and the presence of ST [236].

- Intravascular ultrasound (IVUS) is an imaging technique that uses an ultrasound probe inserted into the arteries to provide information on stent deployment, apposition, and the presence of ST or ISR [267].

- Coronary computed tomography angiography (CCTA) is a noninvasive X-ray based 3D imaging technique that is combined with a contrast-agent injected intravenously to visualize the presence of ISR and other stent complications [268].

- Biomarkers derived from blood sampling, such as erythrocyte sedimentation rate, highly sensitive C-reactive protein, neutrophil to lymphocyte ratio, and platelet to lymphocyte ratio can help predict ISR rates [269].

- Functional assessment includes different physiological measurements to assess functional changes in the arteries, such as Doppler flow wire, whichs allows to measure coronary artery flow velocity [270].

There exist several primary endpoints, or evaluation metrics, to assess the safety and efficacy of stents in preclinical and clinical conditions. The choice of the specific primary endpoint varies depending on the stent type, specific patient population, and the study design. Below is a list of primary endpoints that are commonly used to assess stent performance [236, 266, 271–274].

- ST is classified in different types according to the timing (acute - 0 to 24 hours after stent implantation, subacute - 24 hours to 30 days after implantation, late - 30 days to 1 year after implantation, or very late - more than 1 year after implantation) and to the level of certainty of the diagnosis (definite, probable, and possible).

- ISR is the degree of artery narrowing at the site of the stent compared to the reference vessel diameter. It is expressed as a percentage of the reference vessel diameter.

- Target lesion revascularization (TLR) is a measure of revascularization post-stenting.

- Target lesion failure (TLF) is a combination of cardiac death, target vessel-related myocardial infarction, and need for clinically driven TLR.
- Device-oriented composite endpoint (DOCE) is a device-centered endpoint caused by cardiac death, target-vessel myocardial infarction, or need for TLR.
- Major adverse cardiac events (MACE) is caused by all-cause mortality, target-vessel myocardial infarction, or need for TLR.
- Patient-oriented composite endpoint (POCE) is a patient-centered endpoint that is a caused by of all-cause mortality, myocardial infarction, or revascularization.

Methods for *in vitro* or *ex vivo* evaluation of stents and stent materials are given in the next two chapters.

5.5 Summary

The number of stents that are implanted in the clinic annually is rising, yet the importance of developing new and improved solutions is emphasized by the remaining challenges related to ISR, ST, and long-term biocompatibility issues. Many efforts have been made to improve current permanent intravascular stents. Biodegradable stents are considered as good candidates because they limit the risk of ISR, thrombosis, and inflammation by staying in place only during the required time for the vessel to heal and thereafter, gradually disappear. Polymer biodegradable stents have been introduced in the clinics but without optimal results due to their insufficient mechanical properties. The introduction of metallic stents was a major step in the advancement of biodegradable stents. Investigating different alloys, surface treatments, and manufacturing methods for metallic biodegradable stents is essential to understand how these factors impact corrosion properties and, subsequently, the biological response. More in-depth analysis will offer insights into the development of new stents with enhanced clinical outcomes.

6

MicroCT-based study of the *in vitro* degradation behavior of candidate metallic intravascular stent materials

Publication

Exploring the biodegradability of candidate metallic intravascular stent materials using X-ray microfocus computed tomography: an *in vitro* study.

Leyssens, L.; Lapraille, N.; Pyka, G.; Jacques, P. J.; Horman, S.; Goldman, J.; Kerckhofs G. *Manuscript under revision in Journal of Biomedical Materials Research Part B: Applied Biomaterials*

Positioning in the context of this PhD thesis

In vitro testing for evaluating degradation mode and rate of candidate biodegradable metals to be used as intravascular stents is crucial before going

to *in vivo* animal models. In this study, microCT is proven to be a key added-value to visualize degradation mode and to evaluate degradation rate and material surface properties in 3D and at high resolution of large regions of interest. The *in vitro* degradation behavior of three candidate biodegradable stent materials is evaluated and compared to a reference biostable alloy. This study provides a detailed microCT-based structural characterization of the *in vitro* corrosion behavior of different candidate stent materials in 3D in a non-destructive way. The aim is to provide insights for the development of more effective biodegradable materials for use as intravascular stents. This work has been submitted for a publication, in which L. Leyssens is first author.

6.1 Introduction

Cardiovascular diseases (CVDs) are the leading cause of death globally. Atherosclerosis is the primary cause of coronary heart disease, ischemic stroke, and peripheral artery diseases [275] and causes narrowing and possibly obstruction of the arteries. The gold standard treatment for narrowed arteries is vascular stenting. Until recently, stent technology was based on permanent stents. Cobalt-chromium (Co-Cr) is one of the standard materials used for permanent metallic frameworks [29]. However, permanent stents are associated with long-term complications due to late stage thrombosis, stent strut fracture, chronic inflammation, and in-stent restenosis [229, 230]. During the last two decades, biodegradable polymers and metals have been studied in an effort to replace permanent stents [240, 242]. A stent is required to last for 6 to 12 months during arterial remodeling and healing to provide mechanical support, and after that, the presence of the stent within the blood vessel is not necessary anymore [276]. Polymer-based bioresorbable scaffolds have been investigated, but their poor mechanical properties (low ultimate tensile strength), inability to expand completely with balloon dilatation, their higher delayed thrombogenicity, and the fact that they are not radiopaque have shifted focus to their metallic counterparts [230, 240].

Iron (Fe) and magnesium (Mg) alloys have been reported to be suitable materials for biodegradable stents owing to their good biocompatibility and mechanical properties [277–284]. However, Mg alloys have a degradation rate that is too high, which is also associated with the evolution of hydrogen gas (H_2). The latter is a big concern due to the release

of H_2 bubbles, which may block the blood stream [285, 286]. Fe has a reasonable degradation rate (although considered too slow for a biodegradable stent) and appropriate mechanical properties, but some concerns have been raised related to the stability of the corrosion product [240]. A third class of metallic alloys based on zinc (Zn) has been introduced in 2013, and it appears to have an appropriate degradation rate and good biocompatibility [240, 287]. However, pure Zn still lacks of mechanical strength and undergoes strain softening [229], thus requiring adequate alloying [254]. As a result, the optimal alloy with suitable mechanical properties, proper corrosion rate and behavior, and appropriate biocompatibility still needs to be found. Attempts at alloying pure Zn have been undertaken [229, 254, 288]. However, the addition of elements and their varied concentrations can have strong effects on corrosion and biocompatibility characteristics.

In vitro corrosion test methods are a first screening step to determine if a material is potentially appropriate to be used for biodegradable stents and to learn about the effects of metallurgical modifications on corrosion properties. They do not require complicated surgeries and sacrificing animals, and some methods are well accepted to evaluate the degradation rate and surface properties of candidate alloys. To determine the corrosion rate, currently used techniques include mass loss measurements, pH monitoring, potentiodynamic polarization, electrochemical impedance spectroscopy, and released ion concentration evaluation using inductively-coupled plasma (ICP) [289]. However, these techniques often do not provide information on degradation mechanisms (mass loss), require pH change which is normally avoided for *in vitro* tests (pH monitoring), are destructive to the surface (potentiodynamic polarization), or only provide overall corrosion behavior information as opposed to local information (mass loss, pH monitoring, potentiodynamic polarization, ICP) [289]. Beyond the corrosion rate, the surface properties of candidate stent materials are important because they are a determinant of thrombogenicity and tissue reaction, *i.e.* the nature of the metal surface is crucial to blood compatibility. A stent needs to have an athrombogenic surface to enhance biocompatibility. A smooth surface can help prevent the activation and aggregation of platelets, which is recognized as a part of the thrombosis process [290]. Previous studies with animal models have shown that metallic surface treatment using electrochemical polishing decreased not only thrombogenicity but also neointimal hyperplasia [291]. Surface properties can be determined at high resolution (up to the nm-scale) with techniques such as scanning electron mi-

croscopy (SEM), scanning probe microscopy, and profilometry for small surface areas [292].

Our aim was to perform a detailed evaluation of the degradation behavior and surface roughness properties of four different metals: a Co-Cr alloy (biostable reference), pure Fe, pure Zn, and a Zn-Ag-Cu-Mn-Zr alloy. The quinary Zn alloy is an advanced and newly developed alloy that has improved mechanical properties compared to pure Zn and was shown to have inflammation-resistant properties compared to other Zn alloys [254]. X-ray microfocus computed tomography (microCT) has been used in the past to visualize corrosion products and to evaluate the *in vitro* and *in vivo* degradation rate of different metals using the volume loss method. However, this has been done at low resolution (from 6 µm and up to several tens of µm voxel size) [241, 252, 293–296]. We have used high-resolution microCT imaging (1 µm voxel size) for improved accuracy of the corrosion rate measurements and have registered the volume of the wires before and after degradation. Then, we further optimized microCT-based post-processing tools to study not only the degradation rate, but also the surface properties of the different metals, by improving an in-house developed Matlab routine that detects the surface profile and allows to compute the roughness parameters of both straight and curved wires. The surface properties provided information about the roughness but also offered valuable insights into the corrosion behavior, distinguishing between homogeneous and heterogeneous corrosion patterns by investigating the peaks and valleys, and the total and average roughness of the surface profile. Wires were used to mimic a single stent strut, as a simplified and low-cost alternative to full stents [297]. 3D microCT images were acquired prior to and after *in vitro* immersion tests at three different time points. The microCT images allowed to obtain a detailed comparison of the degradation rate through the volume loss method, the changes in surface roughness over time, as well as the degradation behavior of the four metals. Results obtained with the volume loss method were validated by measuring the released ion concentration through ICP. The degradation behavior observed in the microCT images was compared with SEM. SEM was also combined with energy dispersive X-ray spectroscopy (EDX) to identify the nature of the corrosion products. The combination of these techniques for the same samples was possible thanks to the non-destructive character of microCT. This study gives initial insights into the degradation behavior of different metals, providing essential information before going to *in vivo* studies in animals.

6.2 Materials and methods

6.2.1 Samples

Four types of wires were purchased. The cobalt-chromium alloy (40Co-20Cr-15Fe-15Ni-7Mo-2Mn-C-Be (wt %)) wire of diameter 0.25 mm (ref. CO125140), the high purity iron (Fe 99.99+ wt %) wire of diameter 0.25 mm (ref. FE005141), and the high purity zinc (Zn 99.99+ wt %) wire of diameter 0.25 mm (ref. ZN00-WR-000115) were purchased at GoodFellow Corporation (Oakdale, PA, USA). The quinary zinc alloy (Zn-4Ag-0.8Cu-0.6Mn-0.15Zr (wt %)) was developed by Dr. Jaroslaw W. Drelich [254] and drawn to 0.25 mm diameter wire by Fort Wayne Metals (Fort Wayne, IN, USA). Fig. 6.1 illustrates the experimental steps.

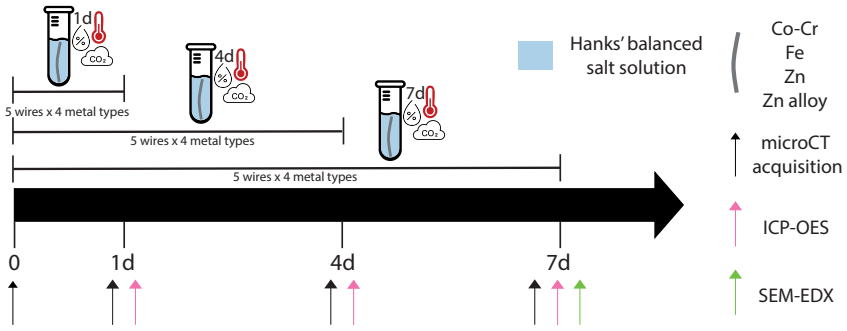


Fig. 6.1 **Timeline for experiments.** Co-Cr, Fe, Zn, and Zn alloy wires were immersed in Hanks' balanced salt solution at physiological conditions (37 °C and 5 vol.% CO_2) for 1, 4, or 7 days (5 wires x 4 metal types x 3 time points). MicroCT acquisition of the wires was performed at time points 0, 1, 4, and 7 days. ICP-OES was performed after 1, 4, and 7 days. SEM-EDX was performed after 7 days.

6.2.2 *In vitro* static immersion

Fifteen 20 mm-long wires of each metal or metallic alloy were cut, washed with Milli-Q water and dried with compressed air. They were washed again with ethanol. The immersion tests were done in a Hanks' balanced salt solution. They were carried out according to the ASTM G31-72 standard [298]. The solution was prepared with 9.5 g of balanced Hanks' salts (H1387, Sigma-Aldrich) and 0.35 g of $NaHCO_3$ in 0.85 L of distilled water. Using a pH meter (WTW pH 330), the pH of the solution was adjusted to 7.4 by the addition of HCl 1 M or NaOH 1 M. Distilled water was then

Table 6.1 Ionic concentrations determined for each metal type using ICP.

Metal type	Elements for which concentration was detected
Co-Cr alloy	Co, Cr
Pure Fe	Fe
Pure Zn	Zn
Quinary Zn alloy	Zn, Ag, Cu, Mn, Zr

added to reach 1 L of solution. Before immersing each wire in the solution, the pH was once again measured to verify its stability. Containers were stored statically in an incubator (Binder CB 170) at 37 °C and 5 vol.% CO_2. Each container was filled with 33 mL of Hanks' solution (according to the standard). The upper part of each wire was attached to the container cap with a piece of sewing thread to suspend the wire in the solution. Incubation times were 1, 4, or 7 days. The solution was replaced after 48 h for the longer time points to maintain constant pH throughout the duration of incubation. After incubation, wires were rinsed with distilled water and ethanol to remove non-adherent corrosion precipitates on the surface. Both the remaining Hanks' solution and the rinsing liquid were kept. N = 5 per time point and per metal type.

6.2.3 Inductively-coupled plasma - optical emission spectrometry (ICP-OES)

ICP-OES (Agilent Technologies 5100) was performed to determine the ion concentration in the Hanks' solution and rinsing liquid after wire immersion. Concentrations of the different elements were measured in $mg \cdot L^{-1}$. The detection limit of the ICP-OES system was 0.05 $mg \cdot L^{-1}$ for Ag and Cr and 0.01 $mg \cdot L^{-1}$ for the other elements. The elements for which the concentration has been determined are listed in Table 6.1 for each metal type.

6.2.4 Corrosion rate based on ICP-OES

The corrosion rate was determined using the ion-release concentration:

$$CR = \frac{cV}{\rho A t}$$

CR is the corrosion rate (mm·year^{-1} or mmpy), ρ is the metal density (mg·mm^{-3}), c is the released ion concentration (mg · L^{-1}), V is the initial solution volume (L), A is the exposed surface area (mm^2), and t is the exposure time (years).

6.2.5 High-resolution microCT acquisition

The lower 2 mm of each wire was imaged with microCT (Phoenix NanoTom M, GE Measurement and Control Solutions, Germany) prior to (time point 0) and after immersion. The NanoTom M is equipped with a 180-kV/15W energy micro/nanofocus X-ray tube and a diamond-coated tungsten target was used for all acquisitions. Images were acquired at a 1 µm isotropic voxel size, with a source voltage of 100 kV and a tube current of 42 µA. The exposure time was 500 ms. Imaging was done in mode 0, 2400 projections were acquired with averaging 1 and skip 0. All acquisitions took 20 min in fast scan mode. A copper filter of 0.1 mm thickness was placed between the source and the sample. The microCT datasets were reconstructed with the Datos|x software (GE Measurement and Control Solutions). A beam hardening correction (BHC) of 6 was applied. BHC goes on a scale from 0 (no correction applied) to 10 (very strong correction applied). Three different post-processing filters were applied in the reconstruction software: inline median (projections are filtered during reconstruction using a 3x3 median filter which reduces the noise in the volume), ROI-CT filter (increases the resolution of the CT dataset for a selected ROI of the object), and filter volume (volume is filtered in slices after reconstruction using the Unsharp Masking Filter, enhancing object edges). Slices were exported as 16-bit XY slices (.tiff) and then converted to 8-bit (.bmp) images, while simultaneously adapting the grayscale histograms of the datasets to normalize them to each other using an in-house developed Matlab routine [204].

6.2.6 Surface roughness analysis based on microCT

Two longitudinal cross-sections (YZ and XZ slices) of each acquired microCT dataset of the wires after immersion were exported using Dataviewer (Bruker MicroCT, Kontich, Belgium). The same was repeated for three microCT datasets of each type of wire before immersion (time point 0). Using an in-house developed Matlab routine described in [299] and extended for non-straight surfaces (Fig. 6.2), the 2D surface roughness was determined for each section on both edges of the wire cross-sections (resulting in 4

surface profile lines per wire). The following roughness parameters were determined: R_a (average roughness (µm) over the evaluated length), R_t (total roughness (µm), the vertical distance between the lowest and highest points over the evaluated length), and R_{ku} (Kurtosis or a measure of the sharpness of the roughness profile, $R_{ku} < 3$ for a bumpy surface and $R_{ku} > 3$ for a spiky surface).

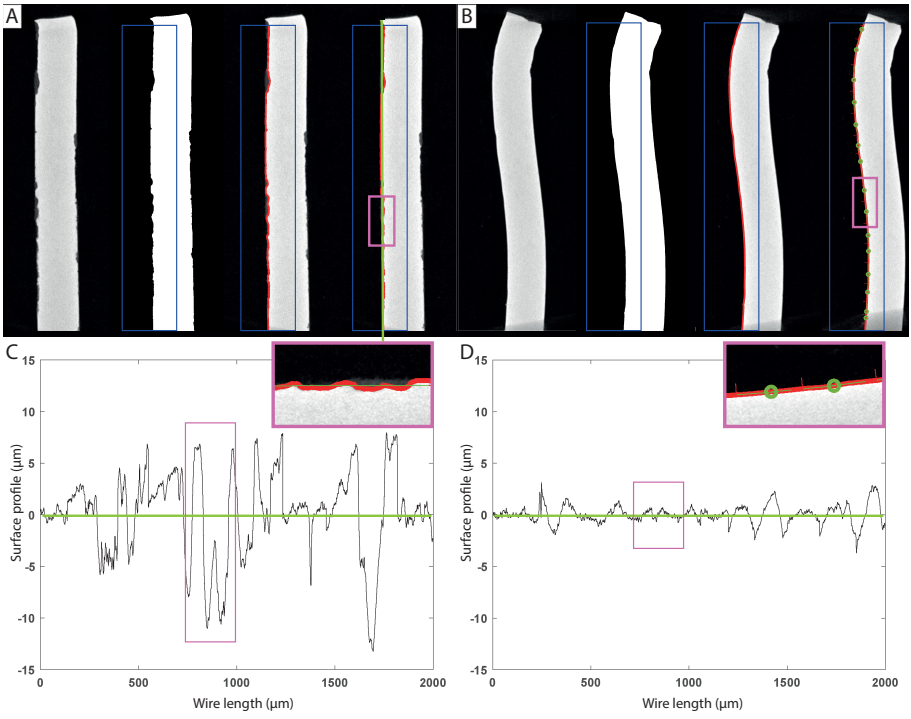


Fig. 6.2 **Output example of the in-house developed Matlab tool for 2D roughness analysis.** (A-B) For two different wires: original microCT-based longitudinal cross-section, binarized section with ROI selection (blue box), surface detection inside ROI indicated by red line, and baseline detection inside ROI indicated by green line/dots. (C-D) Surface profile over wire length, baseline is indicated in green. In (A,C) a linear baseline for a straight wire was used and in (B,D) a spline baseline (piecewise polynomial function between green dots) for curved wire was used.

6.2.7 Corrosion behavior based on microCT

The profile lines of each wire used for the surface roughness analysis were used to determine the corrosion behavior: homogeneous versus heteroge-

neous and pitting versus surface corrosion, only after the 4 day-time point, at which most variation is observed between metal types. This was done by computing the mean of peaks (µm), mean of valleys (µm), coefficient of variation (mean/standard deviation) (%) of peaks, and coefficient of variation (%) of valleys for the surface profile lines of each wire (4 profiles per wire).

6.2.8 Scanning electron microscopy – energy dispersive X-ray spectroscopy (SEM-EDX)

SEM (Ultra 55 FEG SEM, Zeiss, Germany) was performed on the 7-day samples to confirm the degradation behavior observed in the microCT images. Images of the surface of the wires were obtained with a voltage of 30 kV (N = 1 per material). Other wires of the same time point were embedded in epoxy resin and polished to 1 µm grain size for obtaining cross-sectional images with a voltage of 15 kV (N = 1 per material). EDX (Bruker QUANTAX, Germany) was performed on the latter to analyze the chemical composition of the degradation products.

6.2.9 Corrosion rate based on microCT

The Avizo software (Thermo Fischer Scientific, Massachusetts, USA) was used to register microCT datasets of the wires prior to and after immersion to each other using the *Image Registration Wizard* tool. Datasets were binarized using the *Auto thresholding* tool. Datasets were then cropped to remove the extremities of the wires to obtain equal length of the pieces of wire imaged prior to and after immersion. Finally, the *Label Analysis* tool was used to compute the area and volume of each piece of wire. The volume loss due to immersion of each piece of wire was computed. The CR was determined using the volume-loss method:

$$CR = \frac{\Delta V}{At}$$

CR is the corrosion rate (mm·year^{-1} or mmpy), ΔV is the volume loss (mm^3), A is the exposed surface area (mm^2), and t is the exposure time (years).

6.2.10 Statistical analysis

GraphPad prism 9 (GraphPad Software, California, USA) was used for the statistical analysis and data visualization. Normality and homoscedasticity

of the residuals were checked. When more than two different groups were compared, a one-way ANOVA was applied, followed by Šidák's multiple comparisons test. A Kruskal-Wallis test was applied when normal distribution could not be assumed, followed by Dunn's multiple comparisons test. When the effect of two independent variables (*i.e.*, material type and time) on one third variable (*i.e.*, corrosion rate or roughness) was investigated, a two-way ANOVA was applied, followed by Šidák's multiple comparisons test. When data was not normally distributed, a Kruskal-Wallis test was performed to investigate the effect of each variable separately, followed by Dunn's multiple comparisons test. P-values below 0.05 were considered to be significant; not significant (no star) $p > 0.05$, * $p \leq 0.05$, ** $p \leq 0.01$, *** $p \leq 0.001$, **** $p \leq 0.0001$. In the bar graphs, the mean value of the different samples is indicated by the height of the bars and individual values are also represented. Error bars represent the standard deviation.

6.3 Results

6.3.1 Differences in corrosion behavior were visualized in full 3D and the corrosion products were identified.

Visual differences in corrosion behavior between Co-Cr, Fe, Zn, and the quinary Zn alloy were observed 1, 4, and 7 days after immersion on 3D microCT-based representations of the wires and on 2D cross-sections (Figs. 6.3 and 6.4). As expected, the Co-Cr alloy is stable and does not degrade over time. For the biodegradable metals, the corrosion products were segmented from the microCT images (represented in orange in Figs. 6.3 and 6.4). The corrosion products form an oxide layer on the surface of the wire as confirmed by the EDX analysis of the surface of Fe and Zn (Fig. 6.4), which is why they have lower X-ray attenuation and appear with lower gray values than the original metal in the microCT images. They can also be observed in Video 6.1, showing microCT-based transversal cross-sections over the full length of each wire type. For Fe, after 1 day, there were almost no structural changes compared to the control wire. Over time, the wire degraded slowly and homogeneously (Fig. 6.3). The degradation of Fe was wide and shallow (Fig. 6.4). For pure Zn and the Zn alloy, there was almost no structural change after 1 day of immersion (Fig. 6.3). Thereafter, degradation of the wires increased, with local deep pitting corrosion for Zn (Fig. 6.3). For the Zn alloy, the corrosion was more homogeneous along the length of the wire, even though there were re-

gions that were much less corroded than others (Fig. 6.3). SEM images showed that the corrosion occurred preferentially in the darker phase (Zn phase), which means that the alloy phase (lighter phase where Ag is mostly present) slowed down the corrosion (magnified regions of the Zn alloy in Fig. 6.4). Hence, the alloying has produced deficiencies, as this led to the formation of deep dendrites.

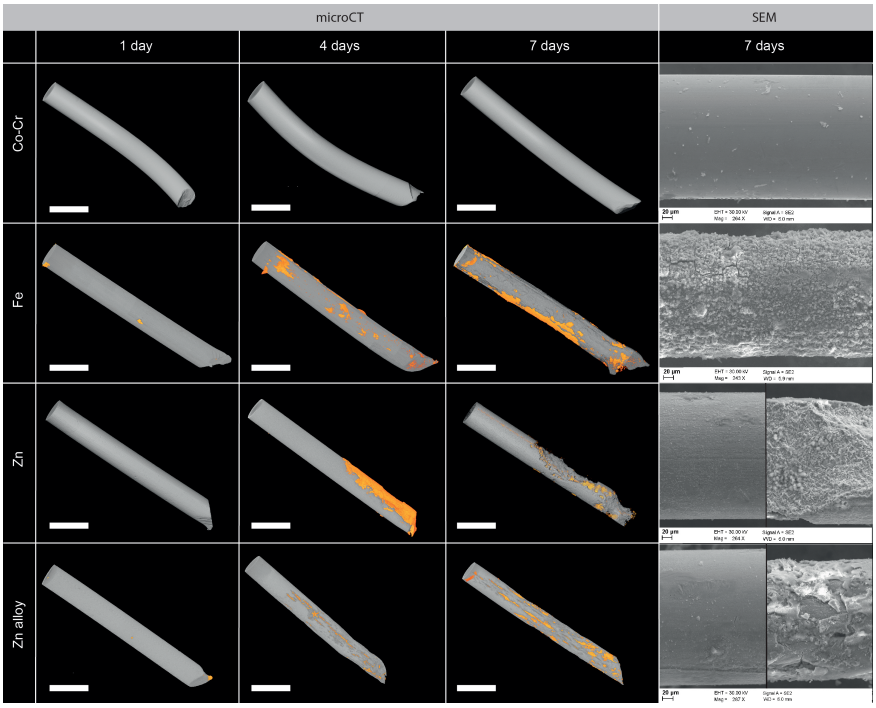


Fig. 6.3 **Visual comparison of different metal types (Co-Cr alloy, Fe, Zn, and Zn alloy) after immersion at different time points (1 day, 4 days, and 7 days).** A representative microCT-based 3D rendering is given for each time point and a SEM image of the wire surface is given for the latest time point. Corrosion products are represented in orange in the microCT renderings, scalebars = 400 µm for microCT and 20 µm for SEM.

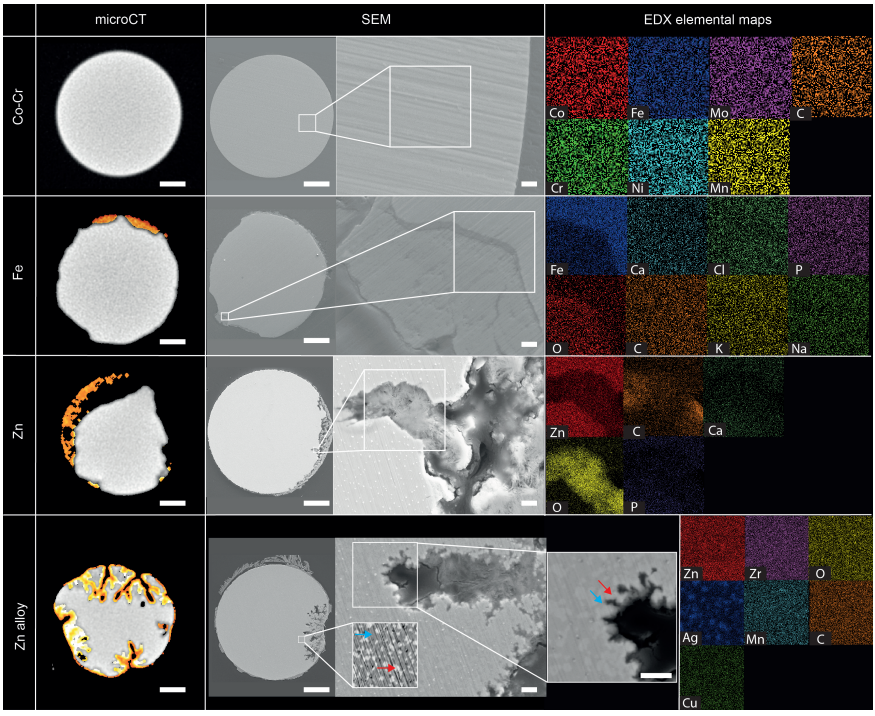
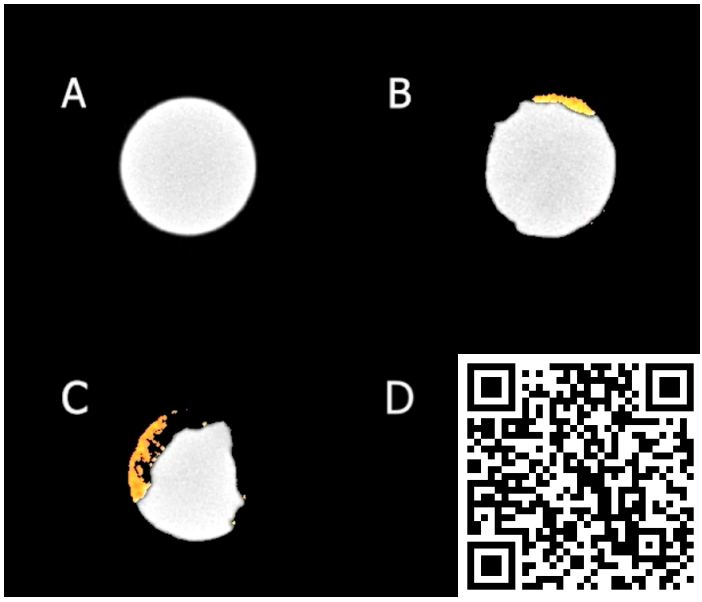


Fig. 6.4 Detection of corrosion products of wires after 7 days of static immersion. Co-Cr alloy, Fe, Zn, and Zn alloy transversal cross-sections imaged with microCT and SEM, and EDX elemental maps of corroded and non-corroded regions. Corrosion products are represented in orange in microCT cross-sections. Red arrow = light phase (alloy), blue arrow = dark phase (Zn). Scalebars = 50 µm for cross-sections, scalebars = 2 µm for magnified regions.

6.3.2 The corrosion behavior of the different metal types was compared quantitatively using surface profile lines determined based on the microCT images.

The fundamental added value of microCT is that it permits the assessment of a large 3D volume, rather than just a 2D cross-section or a small region of the wire surface. This enables a determination of whether the corrosion is homogeneous or heterogeneous across the length of the wire (Fig. 6.5). The variation in the surface profile was measured (Fig. 6.5D). The Co-Cr alloy, used as a biostable control, showed no significant degradation or change in surface properties, as demonstrated in Figs. 6.3 and 6.4, supporting its role as a stable benchmark. Based on our measurements of



Video 6.1: MicroCT-based transversal cross-sections of the wires over their full length. (A) Co-Cr alloy, (B) Fe, (C) Zn, and (D) Zn alloy transversal cross-sections over the length of the wire after 7 days of immersion. Corrosion products are highlighted in orange.

the surface profile from the images, we concluded that pure Fe undergoes superficial degradation, characterized by low average values for the peaks and valleys, indicating that the corrosion is predominantly at the surface (Fig. 6.5A,E). Pure Zn exhibits a more pronounced degradation pattern, characterized by higher peaks and deeper valleys, along with significant variation between samples, suggesting that the corrosion of pure Zn is less uniform across different samples (Fig. 6.5B,E). For some of the Zn wires, no degradation was visible on the part of the wire that was imaged. The Zn alloy has mean values of peaks and valleys in between Fe and Zn, indicating a corrosion behavior that is more uniform than pure Zn but more pronounced than the superficial degradation of Fe (Fig. 6.5C,E). However, no significant differences between any of the metal types were observed due to the variations between wires of the same metal type and due to the limited number of samples analyzed. The coefficient of variation of peaks and valleys is similar for all three materials, suggesting a consistent relative variability in the surface degradation patterns despite some differences in

mean values (Fig. 6.5F).

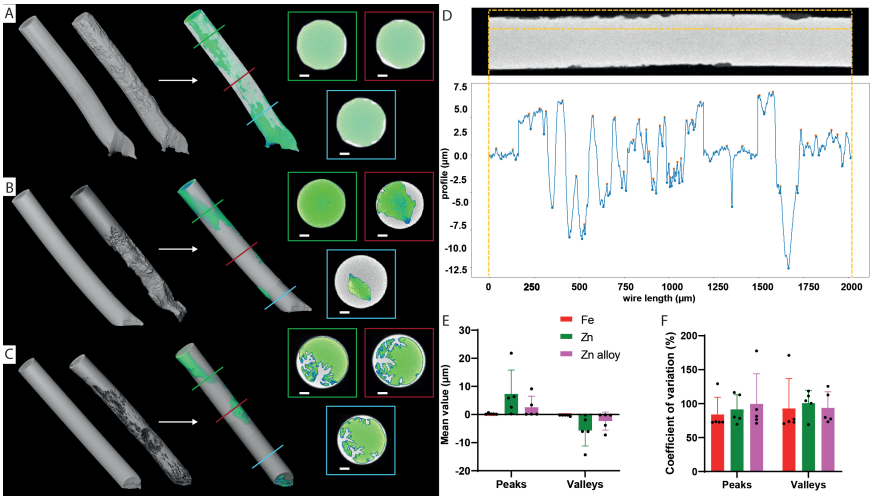


Fig. 6.5 **Typical degradation behavior of Fe, Zn, and Zn alloy.** Illustration of degradation behavior of (A) Fe, (B) Zn, (C) Zn alloy with on the left the two grey 3D images representing the wire at time point 0 and after immersion and on the right the superposition of both wires in 3D and a selection of 2D cross-sections (gray represents the wire at time point 0 and green represents the wire after immersion). (D) Typical wire longitudinal cross-section with corresponding surface profile with peaks represented with orange dots and valleys with blue dots, only peaks above 0 and valleys below 0 were considered, (E) mean value of the peaks and of the valleys of the surface profile for all metal types, (F) coefficient of variation of the peaks and valleys of the surface profile for all metal types. Scalebars = 50 µm, $p > 0.05$ (ns), $n = 5$.

6.3.3 Corrosion rate could be accurately determined by calculating the microCT-based volume loss of the wires.

The corrosion rate was computed based on the volume loss using the microCT-based 3D datasets and this was related to the measured ion concentration in solution (Fig. 6.6). Although the absolute corrosion rates obtained from both methods are not the same, the trends are similar (Fig. 6.6A-F). The two methods are in agreement, as shown by the Bland-Altman plot (Fig. 6.6G). This plot compares corrosion rate measurements from microCT and ICP, showing their agreement. The bias (black dotted line at 0.01938) indicates a small average difference between methods. The limits of agreement (red dotted lines at ± 0.91277) outline where 95% of the differ-

ences lie, reflecting the consistency between the methods. A random scatter of points around the bias line suggests uniform agreement across measurements. The ion released concentration of Co-Cr in solution was below the detection limit, and hence the corrosion rate was set to 0 (Fig. 6.6A-C). The volume loss of the Co-Cr wires was small, and inaccuracies in the segmentation and registration of the datasets led to some variations and negative values of corrosion rate (Fig. 6.6D-F). The corrosion rate stayed constant over time for Fe and remained below 0.3 mmpy for both measuring methods (Fig. 6.6A,D). For Zn and Zn alloy, there was an increase in corrosion rate at 4 days (Fig. 6.6B,C,E,F). The spread of the degradation rate was higher for Zn than for the Zn alloy because of the large variations in degradation from one sample to the other, due to heterogeneous corrosion. When comparing the metal types to each other for each time point, using the volume loss method, no significant differences were observed due to large variations, but the highest degradation rate was observed for pure Zn at 4 days (Fig. 6.6H).

6.3.4 Changes in surface roughness of the different metal types determined using the surface profile lines.

Apart from using the surface profile lines to assess the corrosion behavior homogeneity, we also investigated the surface roughness. The surface roughness of a stent is a key factor in determining biocompatibility. Average and total roughness measurements showed that the largest differences between metal types occurred at the 4-day time point, with a larger average and total roughness for Zn compared to the other metal types (Fig. 6.7A-B). After 7 days, there were no more significant differences between metal types, but large variations between wires of the same material were observed. The increase in roughness was not significant compared to the control samples for all metal types, except for the total roughness of the Zn alloy after 7 days (Fig. 6.7D-I). However, an increase in the average and total roughness of Fe appeared after 7 days (Fig. 6.7D,E), while the roughness of pure Zn increased after 4 days and decreased again after 7 days (Fig. 6.7F,G). To have a better idea of the sharpness of the surface of the wires, kurtosis was also evaluated (Fig. 6.7C). The mean value for kurtosis is above 3 for all materials and all time points, indicating that the roughness distribution has many high peaks and low valleys and is thus irregular. At 4 and 7 days the mean kurtosis value for Zn is higher than for Co-Cr, although not significant, with large variations between the Zn

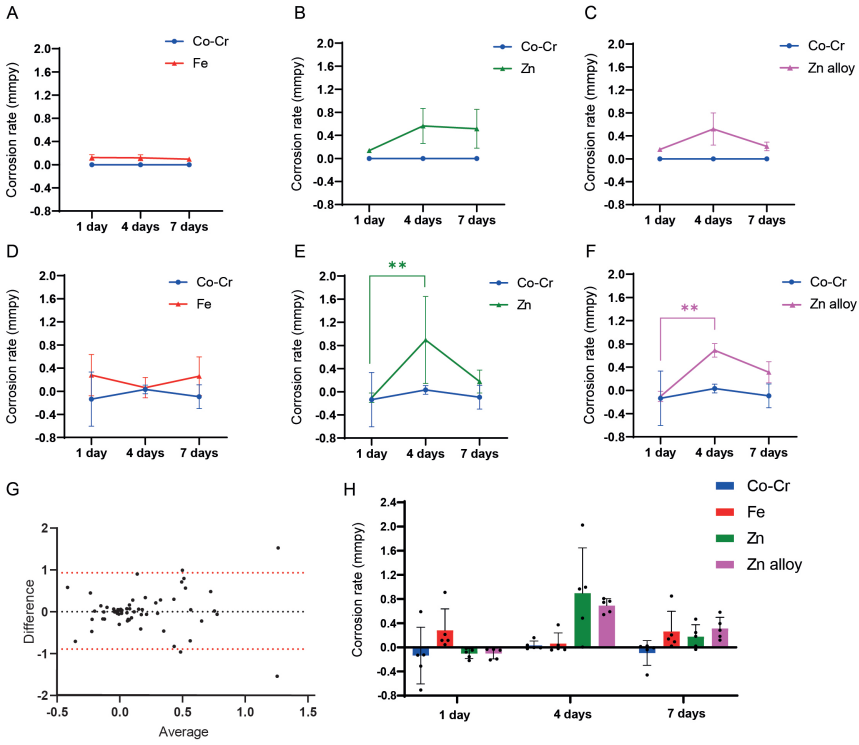


Fig. 6.6 Comparison of the corrosion rate of the different metal types at different time points. Corrosion rate evaluated using the ion-released concentration based on ICP-OES comparing Co-Cr with (A) Fe, (B) Zn, and (C) Zn alloy. Corrosion rate evaluated using the volume loss method based on microCT comparing Co-Cr with (D) Fe, (E) Zn, and (F) Zn alloy. (G) Bland-Altman plot comparing both methods (ICP- and microCT-based corrosion rate) with bias = 0.01938. (H) Comparison between Co-Cr, Fe, Zn, and Zn alloy of the corrosion rate at different time points using the volume loss method, ns $p > 0.05$, * $p \leq 0.05$, ** $p \leq 0.01$, $n = 5$.

wires, indicating a surface that is sharper than for the other materials.

6.4 Discussion

When developing new biodegradable alloys for intravascular stent applications, there are several targets in terms of corrosion rate, corrosion behavior, and surface properties. The degradation rate of Fe-based materials is considered to be too low, while Mg-based alloys have a degradation rate

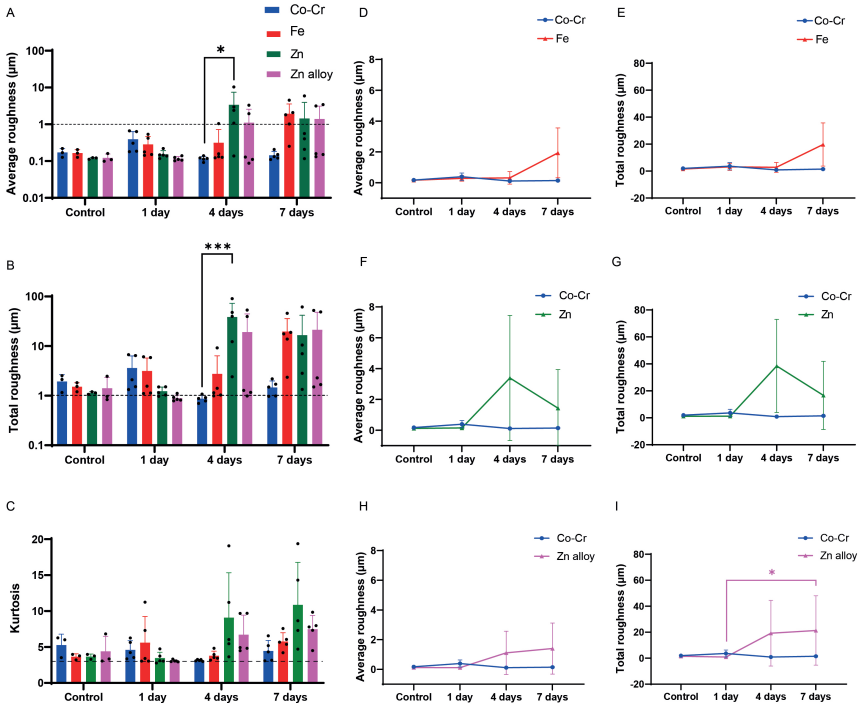


Fig. 6.7 **Comparison of the surface roughness of the different metal types at different time points.** MicroCT-based (A) average roughness (R_a), (B) total roughness (R_t) with Y-axis in base 10 logarithmic scale, and (C) Kurtosis (R_{ku}) for Co-Cr, Fe, Zn, and Zn alloy for the control samples and after 1 day, 4 days, and 7 days of immersion. Significant differences between metal types per time point are indicated on the bar graphs. The dotted line at Y = 1 µm in (A) and (B) represents the limit of the roughness detected because the images were acquired at 1 µm voxel size. The dotted line at R_{ku} = 3 in (C) represents the limit between a bumpy (Rku < 3) or spiky (R_{ku} > 3) surface. Comparison of the average roughness (R_a) between Co-Cr and (D) Fe, (F) Zn, and (H) Zn alloy and comparison of the total roughness (R_t) between Co-Cr and (E) Fe, (G) Zn, and (I) Zn alloy showing significant differences between time points for the same material, ns $p > 0.05$, * $p \leq 0.05$, ** $p \leq 0.01$, *** $p \leq 0.001$, n = 5.

that is too high [297]. Zn is a newcomer within the biodegradable metals and has a corrosion rate that is higher than that of Fe and lower than that of Mg, being a good compromise between both [300]. However, the mechanical strength of Zn needs to be enhanced and this can be done through alloying. The challenge is to find the optimal elemental composition with-

out compromising its positive qualities in terms of biocompatibility and degradation rate. That is why *in vitro* screening studies of different metal types are crucial.

The present study aimed at establishing a method to evaluate the corrosion behavior and surface properties in a more detailed and accurate 3D manner than existing techniques, such as mass loss measurements or polarization experiments. We used high-resolution microCT imaging with a voxel size of 1 µm. This level of detail in the imaging process allowed for a more detailed evaluation of the corrosion rate across different metal types and the 3D imaging provided information on the implant as a whole as opposed to only 2D sections or small regions of interest, as in the case with SEM imaging [233, 301]. We improved an existing surface roughness measurement tool to compute the roughness parameters relative to an adaptable baseline for both straight and curved wire geometries. The surface roughness parameters of the implants can be used to explain the corrosion behavior in a more quantitative way and provide more information on the biocompatibility of the materials. We complemented our results with two already well-established techniques: ICP-OES and SEM-EDX. The corrosion rate computed through the ion loss concentration based on ICP measurements allowed us to validate our volume-loss microCT-based technique. SEM-EDX allowed us to compare the corrosion behavior observed in our microCT images, and it enabled the chemical identification of corrosion products. The latter is not possible with standard microCT. The microCT images allowed to differentiate between the base metal and the corrosion product layer. This differentiation was crucial as it allowed to exclude the corrosion products from our corrosion rate calculations, thereby improving the accuracy of our measurements. In the ICP-OES approach, as not all corrosion products were effectively removed from the metal surface prior to measurement of the ion released concentration, this potentially led to an underestimation of the actual corrosion rates. To address this challenge and improve the precision of corrosion rate assessments with ICP-OES in the future, it is important to fully remove the corrosion product layer, using, for example, chemical methods. In this case, it is important to remove all corrosion products without compromising the integrity of the underlying base material, highlighting the advantage of using microCT imaging to compute the corrosion rate.

In terms of corrosion behavior, the ideal material should degrade uni-

formly and at the surface. Pitting, the formation of dendrites, or any preferential corrosion should be avoided to prevent fragmentation and premature failure of the stent. The roughness parameters can be used to better assess and quantify the corrosion behavior. Indeed, we found that the surface roughness of the different metals was closely related to the corrosion behavior and rate. High variation in the roughness surface profile and in average and total roughness between samples also meant higher variations in corrosion rate. Considering that the Co-Cr was the biostable reference, our analysis confirmed that its average and total roughness, and its degradation rate were close to 0. The Fe wires, which had low average values of peaks and valleys in the surface profile and a low increase in roughness through time, also had the lowest corrosion rate and a low variability in corrosion rates across samples. This corrosion mode is believed to be ideal. The pure Zn had the highest variation in its surface profile (high peaks and high valleys) and high variation between samples for average and total roughness. It also exhibited the highest variation in corrosion rate across samples. This behavior indicates heterogeneous deep pitting corrosion and could promote the detachment of larger pieces of metal in the blood circulation if this occurs too quickly *in vivo*, which could lead to serious complications, such as embolism. Zn also presented a high value of kurtosis, indicating that the surface of the wires was sharp. As a smooth surface is believed to reduce platelet activation and aggregation, a sharp surface could potentially induce platelet activation, thrombosis, and neointimal proliferation [302]. The Zn-Ag-Cu-Mn-Zr alloy, which was in between Fe and Zn with regard to the mean values of the peaks and valleys in the surface profile also experienced an increase in average and total roughness that was between Fe and Zn and corrosion rate values between Fe and Zn, with less variation across samples than Zn. We did observe preferential corrosion in the alloy phase compared to the Zn phase. To solve this deficiency, a solution heat treatment could be applied to the metal to increase the dispersion of the second phase, as observed by *Guillory et al.* [303]. Such a treatment has also been shown to improve mechanical properties (tensile strength and ductility). Nevertheless, this novel Zn alloy, with superior mechanical properties and inflammation-resistant characteristics also showed improved corrosion behavior compared to pure Zn with more homogeneous corrosion and less pitting. The detailed 3D investigation of this alloy, which had not been done before, provides beneficial information on the corrosion behavior at high resolution, giving new insights for further investigation of new and improved Zn alloys. Understanding the

relationships between corrosion rate and surface roughness allows for a better interpretation of corrosion behavior and highlights the importance of controlling surface roughness in mitigating corrosion. Additionally, the roughness measurements provide information on the biocompatibility of the material. Increased surface roughness due to corrosion can potentially enhance endothelial cell adhesion and proliferation, which is beneficial for the healing process around a stent. However, excessive roughness or irregular corrosion products could potentially lead to adverse biological responses, including inflammation or thrombosis [290, 291].

We have also identified some limitations to our study. The microCT data offers valuable high-resolution 3D information on the corrosion behavior of the metals. However, it is limited by the fact that it cannot provide other crucial microstructural information, such as grain size, grain orientation, and electrochemical behavior. Such microstructural details are essential for a deeper understanding of the variations in corrosion behavior across different metal types. This limitation highlights the need for complementary analytical techniques, such as more in-depth SEM analysis or electron backscatter diffraction (EBSD) to better understand the underlying mechanisms driving corrosion processes. These techniques can be applied after microCT thanks to its non-destructive character. Moreover, as we decided to work on high-resolution microCT images (1 µm isotropic voxel size) to accurately measure the surface roughness and volume loss of the samples, we only acquired images of a small portion of each wire. This means that the ICP-based corrosion rate was computed on the entire wire, while the volume loss method corrosion rate was based on a small portion of each wire. However, the corrosion rate remained similar, meaning that the smaller portion of wire represented the behavior of the entire wire relatively well. Additionally, the same location was assessed in each wire (the lower 2 mm of each wire) to balance out any effects of location on the wires. In the future, however, it would be interesting to image and compute the volume loss of multiple areas of interest for each wire. Additionally, we found that comparing the absolute corrosion rate values obtained here with those from other studies in the literature remains challenging, as the rates from *in vitro* immersion tests reported vary significantly based on specific experimental conditions (immersion solution used, static versus dynamic conditions, time points examined, method use for computing the corrosion rate) [253, 287, 304–307]. In our case, we have performed static immersion tests because it has been shown in the past that

dynamic immersion testing (solution agitation or shaking) fails to replicate accurately the *in vivo* behavior. Indeed, the presence of blood flow tends to slow down the degradation process by forming a protective passivation layer, composed of corrosion products, on the metal surface, thereby mitigating rapid degradation [297]. This is in contrast with dynamic immersion testing, which has been observed to accelerate degradation rates, differing from the natural *in vivo* environment [305]. However, dynamic immersion testing might have allowed to minimize localized effects, such as pH changes. Finally, we did not do a follow-up study of the same wires over time because different wires were used for each time point. However, this could be easily done in the future as microCT is a non-invasive technique.

In the future, the same microCT-based technique can be applied to acquire images of explanted wires that have been implanted in an animal model, such as in [254, 297, 308–310]. In these studies, classical 2D histological cross-sections were obtained to evaluate biocompatibility and interactions between the tissue and the metallic implant. However, only limited cross-sections were available per sample due to the labor-intensive technique and the requirement of special cutting methods to section the metal. With 3D microCT, the location of interest can be readily selected, and further analysis can provide more insights into important properties, such as homogeneous versus heterogeneous corrosion behavior. The biocompatibility could also be assessed by measuring the volume of the neointimal growth that surrounds the wire or implant.

6.5 Conclusion

Overall, this study provides insights into the corrosion behavior of biodegradable metallic alloys for intravascular stent applications and proposes an optimized microCT-based technique for evaluating corrosion rate, behavior, and surface properties from *in vitro* immersion tests. The results could potentially inform and accelerate the development of more effective biodegradable materials for use in medical devices.

7

MicroCT and CECT-based study of the *in vivo* degradation behavior and biocompatibility of candidate metallic intravascular stent materials

Publication

MicroCT and contrast-enhanced microCT to study the *in vivo* degradation behavior and biocompatibility of candidate metallic intravascular stent materials.

Leyssens, L.; El Aazmani, W.; Balcaen, T.; Jacques, P. J.; Horman, S.; Goldman, J.; Kerckhofs, G. *Manuscript submitted to Bioactive Materials*

Positioning in the context of this PhD thesis

In this chapter, the same metallic alloys as in chapter 6 are investigated in an *in vivo* study. The materials are implanted in the rat aorta and collected after sacrificing the animals at different time points. MicroCT and CECT are combined to evaluate the volume loss of the wires in different locations (outside the lumen, inside the lumen, and inside the lumen and encapsulated by neointima), to compute their degradation rate, the structural parameters of the neointima, the lumen obstruction index, and the volume of the corrosion products. This study shows the power of combining microCT and CECT to provide 3D, high-resolution information in a non-destructive way on the *in vivo* degradation properties and the biocompatibility of candidate stent materials. It demonstrates the potential of these imaging techniques to provide essential information for the development of improved biodegradable stents, designed to treat occluded or blocked vessels. This work will be submitted for a publication, in which L. Leyssens is first author.

7.1 Introduction

Cardiovascular diseases (CVDs) are the leading cause of death worldwide. This high mortality rate is significantly influenced by atherosclerosis, a major underlying cause of many cardiovascular conditions, characterized by a buildup of plaque in the arterial wall [12]. Angioplasty in combination with stent deployment and implantation is one of the most frequently performed interventions to treat atherosclerotic arteries and revascularize occluded vessels [311]. Biodegradable stents have been studied for the last two decades to replace permanent stents. The latter are associated with long-term complications, such as chronic inflammation and late-stage thrombosis, which may lead to neointimal proliferation and ISR [229, 240, 311]. Metallic biodegradable stents are popular owing to their good mechanical properties and radiopacity, in contrast to polymeric stents. However, the ideal material that meets all the criteria in terms of mechanical properties, degradation behavior and rate, and biocompatibility has not yet been found [235].

Several iron- (Fe) and zinc- (Zn) based alloys have been developed and tested for their potential application as degradable biomaterials. Fe and its alloys are highly promising stent materials owing to their outstanding

mechanical properties and biocompatibility, and have undergone extensive *in vitro* and *in vivo* studies. The primary focus currently is on enhancing the degradation rate of Fe, which is too low, without compromising the favorable biocompatibility and mechanical properties. This could be achieved by alloying, optimizing the manufacturing process, or adding coatings [236]. In more recent years, Zn has gained attention as a potential material for biodegradable stents [233, 240, 287, 295, 308, 311, 312]. Zn-based alloys demonstrate promising *in vivo* degradation behavior and biocompatibility. However, there is a need for further optimization of their elemental composition and processing route to enhance their mechanical strength [236]. Additionally, there is a need for improved 3D methods to characterize and evaluate the behavior and performance of these materials both *in vitro* and *in vivo* to better understand and predict long-term outcomes and to improve their design.

In vitro experiments that simulate the *in vivo* environment of biodegradable stents for evaluating their degradation behavior are important. They allow a first selection of materials without requiring the sacrifice of animals or the implementation of complicated and expensive surgeries. However, the complex interactions between blood, proteins, local and blood-borne cells, and the stent with its degradation products, along with the shear stress of blood flow and vasomotion all play an important role in the degradation behavior, mechanical strength, and biocompatibility of stents. These conditions can be difficult to replicate *in vitro* [236]. Presently, the *in vivo* corrosion behavior of Fe, Zn, and their alloys has been studied in different animal models including the mouse, rat, rabbit, dog, and pig [231, 247, 313]. Recently, different metallic alloys have been tested in a rat abdominal aorta model [241, 283, 297, 301, 308, 311]. The rat model has been shown to be advantageous because requirements for space and care are low compared to other animals (pigs, rabbits, dogs, primates) and it allows for evaluating the degradation behavior, biocompatibility, and systemic toxicity *in vivo* [236]. A simplified and low-cost *in vivo* model was developed by *Pierson et al.* in 2011, which consists of implanting a metallic wire into the lumen of the rat abdominal aorta. The wire penetrates the aorta, advances through the lumen, and penetrates the aorta again, leaving a segment of the wire within the lumen of the artery in contact with the endothelium [297]. In several follow-up studies, the same group has evaluated the *in vivo* degradation behavior and biocompatibility of different Zn-based alloys in the rat abdominal aorta [229, 254, 303, 308–310].

Promising results have been obtained from these studies regarding the development of new Zn alloys.

To investigate toxicity, thrombosis, and inflammation of candidate stent materials using *in vivo* animal models, endpoint classical 2D histological evaluation, histomorphometry, and histopathology techniques are typically employed [283, 284, 295, 301, 311, 312, 314–317]. Scanning electron microscopy (SEM) has been used to evaluate the reduction in cross-sectional area to determine the degradation rate and combined with energy dispersive spectroscopy (EDX) and Raman spectroscopy to analyze the composition of the corrosion products [241, 294, 295, 301, 317]. The degradation rate has also been assessed through the measurement of the mass loss after removing the tissue surrounding the metallic implant [318, 319].

However, many of the methods used for evaluating the *in vivo* stent behavior are destructive to the sample, and they only allow for evaluating a small region or a single slice, which is generally not representative of the entire sample. Furthermore, sectioning for classical 2D histology is often challenging due to the presence of the metal implant, complicating the use of conventional methods for sectioning soft tissues. The role of more advanced 3D characterization methods becomes essential to gain a deeper understanding of the *in vivo* degradation behavior and biocompatibility performance of newly developed materials. X-ray microfocus computed tomography (microCT) is a non-destructive technique that is advantageous to study the behavior of candidate stent materials because it allows for visualizing the full sample in 3D and at high-resolution [241, 252, 253, 293–295, 314]. In these studies, microCT has primarily been employed to calculate the degradation rate by quantifying the volume loss of metallic explants or to visualize the corrosion products.

In a previous study, we have used microCT-based processing tools not only for volume loss measurements to determine the degradation rate, but also to assess degradation behavior by evaluating the surface properties of different materials following *in vitro* immersion tests [320]. Four different metals were evaluated: a cobalt-chromium (Co-Cr) alloy (biostable reference), pure Fe, pure Zn, and a recently developed advanced quinary Zn-Ag-Cu-Mn-Zr alloy [254].

In the present work, we evaluated the same four metals (Co-Cr alloy,

Fe, Zn, and the quinary Zn alloy) in an *in vivo* degradation study. The four types of wires were implanted in the rat abdominal aorta following the model introduced by *Pierson et al.* [297]. Rats were sacrificed and after collection, explants were imaged with microCT. However, microCT alone only allowed the visualization of the metallic implant, which is a high X-ray-attenuating material. To visualize the soft tissue surrounding the metal, microCT needs to be combined with contrast-enhancing staining agents (CESAs) containing high-atomic number elements, which can diffuse into the low X-ray attenuating tissues, a technique referred to as contrast-enhanced microCT (CECT) [38, 195]. Explants were stained and then imaged with CECT to visualize the interaction between the implants and the surrounding tissue. We then non-destructively evaluated the degradation rate, the degradation behavior, and the neointimal tissue formation of candidate stent material explants in 3D.

7.2 Materials and methods

7.2.1 Animals

40 8-week-old female Wistar rats were purchased from Janvier Labs (Le Genest-Saint-Isle, France) for the animal experiments. Animals were housed in the animal facility for 11 days prior to the start of the experiments. They were fed a standard diet throughout the entire duration of the experiments. Animal procedures and protocols were approved by local authorities (Comité d'éthique facultaire pour l'expérimentation animale, 2021/UCL/MD/071) and performed in accordance with the Guide for the Care and Use of Laboratory Animals, published by the US National Institutes of Health (NIH Publication, revised 2011).

7.2.2 Implants

The cobalt-chromium alloy (40Co-20Cr-15Fe-15Ni-7Mo-2Mn-C-Be (wt %)) wire of diameter 0.25 mm (ref. CO125140), the high purity iron (Fe 99.99+ wt %) wire of diameter 0.25 mm (ref. FE005141), and the high purity zinc wire (Zn 99.99+ wt %) wire of diameter 0.25 mm (ref. ZN00-WR-000115) were purchased at GoodFellow Corporation (Oakdale, PA, USA). The quinary zinc alloy (Zn-4Ag-0.8Cu-0.6Mn-0.15Zr (wt %)) developed by Dr. Jaroslaw W. Drelich [254] was drawn to 0.25 mm diameter wire by Fort Wayne Metals (Fort Wayne, IN, USA).

7.2.3 MicroCT acquisition of wires prior to implantation

The different experimental steps are represented in Fig. 7.1. Wires of ∼ 12 mm in length were cut for the four metal types (40 Co-Cr wires, 20 Fe wires, 40 Zn wires, and 20 Zn alloy wires). MicroCT datasets were acquired for 6 random wires of each metal type with the Phoenix NanoTom M (Waygate Technologies, Baker Hughes Digital Solutions GmbH, Germany) equipped with a 180-kV/15W energy micro/nanofocus X-ray tube. A diamond-coated tungsten target was used for all acquisitions. The acquisition parameters are listed in Table 7.1 (*MicroCT of wires at time point 0*). A beam hardening correction (BHC) of 9 was applied. BHC operates on a scale from 0 (no correction applied) to 10 (very strong correction applied). Three different post-processing filters were applied in the reconstruction software: inline median (projections are filtered during reconstruction using a 3x3 median filter which reduces the noise in the volume), ROI-CT filter (increases the resolution of the CT dataset for a selected ROI of the object), and filter volume (volume is filtered in slices after reconstruction using the Unsharp Masking Filter, enhancing object edges). Slices were exported as 16-bit XY slices (.tiff).

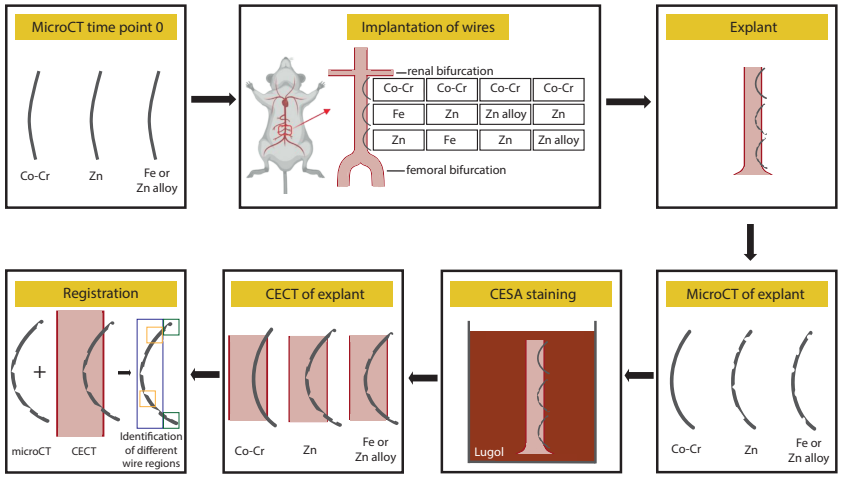


Fig. 7.1 Experimental workflow for microCT and CECT image acquisition and registration of both types of datasets.

7.2.4 Wire implantation

After microCT imaging, for each wire, one of the tips was sharpened with pliers to help with later implantation. Each wire was washed in acetone for 2 minutes and rinsed in PBS and then placed in EtOH 70% for a few minutes for sterilization. The Wistar rats were anesthetized with isoflurane in oxygen gas, their lower abdomen was opened, and the aorta was dissected from the vena cava. The aorta was clamped between the renal and the femoral bifurcations. Three wires were implanted per rat to minimize the number of animals needed, complying with the 3R (Replacement, Reduction and Refinement) policy, following the surgical procedure described previously [310] with 3 to 4 mm of the wire inside the lumen and the remaining length of the wire exteriorized from the aorta on both sides (Suppl. Fig. 7.1). Each rat was implanted either with a Co-Cr, Fe, and Zn wire or a Co-Cr, Zn alloy, and Zn wire. The Co-Cr wire was always implanted closest to the renal bifurcation. The Fe and Zn wires and the Zn alloy and Zn wires were implanted closest to the femoral bifurcation and their order was inversed in half of the rats (Fig. 7.1, Implantation of wires). Each wire was secured with a suture thread at both extremities to the surrounding connective tissue to prevent dislocation. The lower abdomen was closed with suture thread (muscle) and staples (skin). Each rat was injected with 80 µL of Buprenorfine hydrochloride (Temgesic 0.3 mg/mL) before waking up for pain management.

After 7, 24, or 84 days, the rats were euthanized using a large concentration of isoflurane in oxygen gas. One rat died for unknown reasons before sample collection could be done. This resulted in 12 arteries collected after 7 days, 12 arteries collected after 24 days, and 15 arteries collected after 84 days. While the heart was still beating, the rats were perfused with phosphate buffered saline (PBS) to remove all the blood from the circulatory system. This was done by injecting PBS through the left ventricle with a needle and collecting blood at the right auricle. The aorta implanted with the three wires was then collected and placed in 4% formaldehyde (FA) at 4°C for 5 hours for fixation. The samples were rinsed in PBS, fast frozen in isopentane at -80°C and placed in the -80°C freezer until further processing. This conservation method was selected based on our own previous results [199].

7.2.5 MicroCT acquisition of explants

Samples were thawed for 5 min prior to microCT imaging. Three microCT datasets of each explanted artery (one for each wire) were acquired using the NanoTom M. The acquisition parameters are listed in Table 7.1 (*MicroCT of explants*). The distance between the X-ray source and the sample was adjusted according to the length of each individual sample to ensure the entire sample could be captured within the field of view. As a result, the voxel size varies among the samples, but stayed within the range of 3.5-6 µm. All datasets were reconstructed with the Datos | x software. A BHC of 9 was applied. Three different post-processing filters were applied in the reconstruction software: inline median, ROI-CT filter, and filter volume. Slices were exported as 16-bit XY slices (.tiff). After microCT imaging of the explants, samples were again fast frozen in isopentane at-80°C and placed in the -80°C freezer until further processing. The microCT datasets were used to compute the evolution of diameter of the wires over their entire length, their volume loss, and the degradation mode and rate of the wires. This was done to ensure that these measurements were not influenced by any further degradation of the wires that could have occurred during the next processing and imaging steps, which include staining of the samples in a CESA solution and CECT imaging.

7.2.6 CESA choice and staining time

Four different CESAs were considered for staining the rat aorta explants: Hexabrix (Hexabrix 320, Guerbet, Princeton, New Jersey, USA) (20 V/V % in PBS), 1:2 Hafnium-substituted Wells-Dawson polyoxometalate (1:2 Hf-WD POM) (35 mg/mL in PBS) synthesized as described in [200, 201], CA4+ (24 mg/mL in PBS), and buffered Lugol's iodine-based solution, I_2KI (Lugol's iodine). The Lugol's iodine solution was prepared by mixing isotonic Lugol's iodine (3.24 g I_2 + 6.48 g KI in 250 mL MilliQ water) with a 266 mM phosphate buffer (pH = 7.16, 63.1 mM KH_2PO_4 + 202.9 mM Na_2HPO_4) in a 1:1 ratio as described in [121]. A native healthy explanted abdominal rat aorta without wire, which was fixed in 4% FA for 5 hours and rinsed in PBS, was cut in four pieces. Each piece was stained in 2 mL of one of the four CESA solutions for 24 h on a shaker plate at room temperature to ensure complete staining. A CECT dataset of each piece of aorta was then acquired. Acquisition parameters are mentioned in Table 7.2 (*CECT of healthy rat aorta*). The two most promising CESAs were selected based on visual comparison of the contrast enhancement of the rat aortic wall.

Table 7.1 MicroCT and CECT acquisition parameters for the wires and explants

	MicroCT of wires at time point 0	MicroCT of explants	CECT of explants
Tube voltage (kV)	100	100	90
Tube current (µA)	210	148-253	163-281
Filter	0.1 mm Cu	0.1 mm Cu	0.25 mm Cu
Exposure time (ms)	500	500	500
Number of projections	2400	2400	2400
Acquisition time (min)	20	20	20
Averaging	1	1	1
Skip	0	0	0
Fast scan mode	Yes	Yes	Yes
Voxel size (µm)	5	3.5-6	3.5-6
CESA	/	/	Lugol

Then, two wires of each of the biodegradable metal types (Fe, Zn, and Zn alloy) were placed each in a piece of porcine aorta obtained from the slaughterhouse (one part of the wire inside the tissue and one part sticking out of the tissue to simulate the rat aorta explants). Three samples (one with each type of wire) were placed each in 5 mL of 1:2 Hf-WD POM solution, and the three other samples were placed in 5 mL of Lugol's iodine solution for 17 h at room temperature on a shaker plate. After 17 h, CECT datasets of each sample were acquired. Acquisition parameters are mentioned in Table 7.2 (*CECT of wire in porcine aorta*). This allowed for determining which CESA interacted with the metallic wires the least.

To optimize the staining time, one rat aorta explant was thawed and placed in 5 mL of Lugol's iodine solution at room temperature on a shaker plate. CECT datasets were acquired at different time points after staining (1 h, 2 h, 4 h, 6 h, 8 h, 10 h, 12 h, 14 h, 17 h) with the acquisition parameters mentioned in Table 7.2 (*CECT of explant*). Staining time should be long enough so that the CESA fully diffuses through the tissue, but as short as possible so that the interaction with the metallic wires is as low as possible to prevent any potential further degradation of the metal.

Table 7.2 MicroCT and CECT acquisition parameters for the choice of CESA and optimization of staining time for CECT

	CECT of healthy rat aorta	**CECT of wire in porcine aorta**	**CECT of explant**
Tube voltage (kV)	70	90	90
Tube current (µA)	100	234	234
Filter	/	0.25 mm Cu	0.25 mm Cu
Exposure time (ms)	500	500	500
Number of projections	2400	2400	2400
Acquisition time (min)	20	20	20
Averaging	1	1	1
Skip	0	0	0
Fast scan mode	Yes	Yes	Yes
Voxel size (µm)	1.667	5	5
CESA	CA4+, Hexabrix, Hf-WD POM, Lugol	Hf-WD POM, Lugol	Lugol

7.2.7 CECT acquisition of explants

Two samples from the 84-day time point, one implanted with Co-Cr, Fe, Zn and one implanted with Co-Cr, Zn, Zn alloy, were kept for classical 2D histology. Based on our investigation to determine the appropriate CESA and staining time, all other samples were thawed and stained during 17 h in 5 mL of Lugol's iodine solution on a shaker plate at room temperature. CECT acquisition was performed for each wire using the same voxel size as for the microCT acquisitions prior to staining. The CECT acquisition parameters are listed in Table 7.1 (*CECT of explants*). All datasets were reconstructed with the Datos | x software. A BHC of 9 was applied. Three different post-processing filters were applied in the reconstruction software: inline median, ROI-CT filter, and filter volume. Slices were exported as 16-bit XY slices (.tiff).

7.2.8 Classical 2D histology

Classical 2D histological analysis was performed by LLS Rowiak LaserLabSolution GmbH (Hannover, Germany). Samples were embedded in

methylmethacrylate, sectioned with a lasermicrotome, and stained with hematoxylin and eosin (H&E). This was done on 6 different explants, containing three wires each, from the 84-day time point only. Two sections per wire were cut in two different regions of interest: at both artery penetration points, with the implant inside the lumen having just fully passed the internal elastic lamina.

7.2.9 MicroCT and CECT datasets post-processing

The 16-bit XY slices (.tiff) were converted to 8-bit (.bmp) images, while simultaneously adapting the grayscale histograms of the datasets to normalize them to each other using an in-house developed Matlab routine [204]. For the microCT images, the grayscale values of the wires and of the background were used for normalization to ensure that all the wires had the same gray value (meaning that the gray values were independent of the X-ray attenuation). For the CECT images, the parafilm, in which the samples were wrapped for imaging, and the background were used as reference materials for normalization. The rest of the steps were performed using Avizo (Thermo Fischer Scientific, Massachusetts, USA). Each CECT acquired explanted wire was registered with its corresponding previously acquired microCT explanted wire, using the *Image Registration Wizard* module and adapting manually when necessary. Different locations of the wires were determined manually in the CECT datasets (wire outside the lumen, wire inside the lumen, and wire inside the lumen and encapsulated by neointima). This information was translated to the microCT datasets.

7.2.10 MicoCT and CECT image analysis

Diameter versus length

The microCT datasets of the wires were segmented from the background using the same threshold value for all wires. The *Cylinder Correlation* module (cylinder length of 174.332 µm, angular sampling of 5°, mask cylinder radius of 132.158 µm, outer cylinder radius of 120.144 µm, inner cylinder radius of 0 µm, bright on dark for the contrast of the signal to be detected) followed by the *Trace Correlation Lines* module (minimum seed correlation of 68, minimum continuation of 45, direction coefficient of 0.3, minimum distance of 240.288 µm, minimum length of 174.332 µm, search cone length of 80 µm, search cone angle of 37°, and minimum step size of 10) were applied to each binarized wire to identify and trace the centerline of each wire. The *Thickness Map* module (boundary voxels averaged) was applied

to each binarized wire to obtain a 3D thickness map of each wire. The *ThicknessToFiberRadius* module, which takes as input the result from the *Trace Correlation Lines* module and the thickness map of each wire, was then applied to compute the diameter at different locations defined by the *Trace Correlation Lines* module along the length of each wire.

Percentage volume loss

The volume of each wire was computed using its length and the diameter computed by the *Thickness Map* module. This volume was compared to the volume of a perfect cylinder of the same length and with a diameter equal to the maximum diameter of the degraded wire (there was always at least one region where the wire showed no degradation). Comparing these two volumes allowed for computing the percentage volume loss of each wire. The percentage volume loss was calculated in the same way for the portion of wire located outside the lumen, the portion inside the lumen, and the portion inside the lumen that was encapsulated by neointima. The portion of the wire inside the lumen was used for the calculating the degradation rate, assessing the wire diameter during degradation, and neointima and corrosion product segmentation.

Degradation rate

The degradation rate of each wire was computed based on its volume loss using the following formula:

$$CR = \frac{\Delta V}{At}$$

CR is the corrosion rate (mm·year^{-1} or mmpy), ΔV is the volume loss of the wire inside the lumen (mm^3), A is the exposed surface area (mm^2) computed as $2\pi rL$ (r (mm) is the initial wire radius and L (mm) is the evaluated wire length), and t is the exposure time (years).

Wire diameter rate of change and maximal diameter range

The average rate of change in diameter along the wire was computed based on the graphs of the diameter versus the length. The interval chosen to compute the average rate of change was the distance between two positions along the wire chosen by the *Trace Correlation Lines* module, and for which the diameter was computed by the *ThicknessToFiberRadius* module. The maximum range of the diameter (maximum diameter – minimum diameter) for each wire was also computed.

Neointima and corrosion products segmentation in the CECT datasets

Using the *Magic Wand*, *Watershed*, and *Brush* tools from Avizo, the neointimal tissue, the wire, the aorta, and the corrosion products were segmented from the CECT datasets. The 3D analysis tool in CTAn (Bruker MicroCT, Kontich, Belgium) was used to compute the thickness distribution, volume, and surface area of the neointima from the binarized slices, of each segmented volume individually, that were exported from Avizo. The total volume and the peak thickness of the combination of the wire and neointima were computed in the same way for each dataset using CTAn. The binarized slices of the aorta were used to compute the lumen perimeter of each aorta in CTAn by using *Path* from the *Measure* tool and manually drawing the internal perimeter of the aorta on five different slices and taking the average. From the mean internal perimeter of each aorta, a mean cross-sectional area of the lumen was computed. The volume of a perfect cylinder with the same cross-sectional area and the same length as the aorta was computed to obtain the lumen volume. The wire and neointima volume were divided by the lumen volume to obtain a lumen obstruction index, expressed in percentage. The binarized slices of the corrosion products were also processed with CTAn. First, a *Despeckle* step was applied (remove white speckles less than 4 pixels in size in 2D space) to remove the border of the wire which remained in the slices of the corrosion products. Then, the volume of the corrosion products was computed using the 3D analysis tool. Avizo was used to make 2D and 3D visual representations of the segmentation of the wire, neointima, corrosion products, and aorta of the explants at the three different time points (7, 24, and 84 days).

7.2.11 Statistical analysis

GraphPad prism 9.5.1 (GraphPad Software, California, USA) was used for the statistical analysis and data visualization. Normality and homoscedasticity of the residuals were checked. To ensure the normality and homoscedasticity assumptions, a logarithmic transformation of the data was sometimes necessary. When a comparison was made between two groups, a two-tailed Student's *t*-test was performed (paired or unpaired depending on whether the data were matched). When more than two different groups were compared, a one-way ANOVA was applied, followed by a Tukey's multiple comparison test. Welch's correction was applied in case of heterogeneity of variances. A Kruskal-Wallis test was applied when normal distribution could not be assumed. A two-way ANOVA was applied

when assessing the effect of two factors on one dependent variable. P-values below 0.05 were considered significant; not significant (no star) $p > 0.05$, * $p \leq 0.05$, ** $p \leq 0.01$, *** $p \leq 0.001$, **** $p \leq 0.0001$. In the bar graphs, the mean value of the different samples is indicated by the height of the bars and individual values are also represented. Error bars represent the standard deviation.

7.3 Results

7.3.1 MicroCT allowed for determining the in vivo degradation behavior of the implants.

The graphs of the diameter of each wire over the full length allow for visualizing the local loss in material of each wire (Fig. 7.2A). The representative graph of each type of wire after 84 days of implantation revealed that Co-Cr stayed intact, as expected. Fe showed low amounts of loss in diameter over its length, whereas both Zn and the Zn alloy demonstrated more and deeper pits. This information was reflected quantitatively in the percentage volume loss, computed for all wire types and time points (Fig. 7.2B). At the early time point (7 days), the volume loss of the Zn alloy was significantly larger than for the other metal types, indicating its rapid and early degradation. At the two later time points (24 and 84 days), the volume loss of both pure Zn and the Zn alloy was significantly higher compared to Co-Cr and Fe. The differences in volume loss between pure Zn and the Zn alloy were no longer significant at the later time points.

Among the implanted wires, there were three different parameters that varied: the wire metal type (Co-Cr, Fe, Zn, or Zn alloy), the implantation time (7, 24, or 84 d), and the order of implantation of the wires (Co-Cr – Fe – Zn, Co-Cr – Zn – Fe, Co-Cr – Zn alloy – Zn, or Co-Cr – Zn – Zn alloy) (Fig. 7.1, Implantation of wires). We created a least squares regression model to investigate which of these parameters had an effect on the percentage volume loss of the wires (Fig. 7.2C-E). We found that the metal type and the implantation time had a significant effect on the volume loss, as anticipated ($p < 0.0001$) (Fig. 7.2C,D). However, the order in which the wires were implanted in the aorta did not have a significant influence on their volume loss (Fig. 7.2E). Consequently, the wire implantation order was disregarded for evaluating the volume loss and degradation rate of the wires in the remainder of the study.

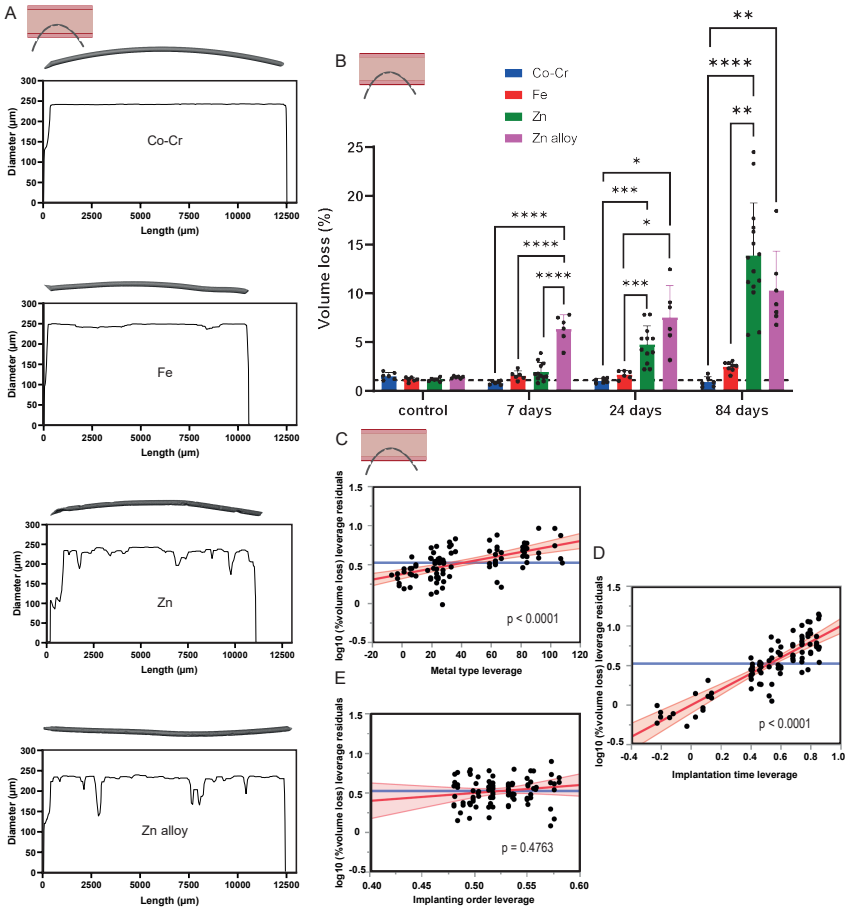


Fig. 7.2 MicroCT-based representations of the wires, diameter versus length graphs used to compute the percentage volume loss, and parameters that influence the percentage volume loss of the wires after explant collection. (A) Typical diameter versus length graphs of the different wire types at 84 days with corresponding 3D representation of each type of wire: Co-Cr, Fe, Zn, and Zn alloy. (B) Percentage volume loss of the wires computed over their full length for all materials and all time points. The control time point represents the volume loss of the wires prior to implantation. The dotted line indicates the threshold below which volume loss is considered insignificant (mean percentage volume loss of Co-Cr), * $p \leq 0.05$, ** $p \leq 0.01$, *** $p \leq 0.001$, **** $p \leq 0.0001$. (C-E) Least squares regression model showing which parameters influence the percentage volume loss of the wires. (C) Effect of metal type on the percentage volume loss (significant, $p < 0.0001$), (D) effect of the implantation time on the percentage volume loss (significant, $p < 0.0001$), (E) effect of the order of implantation of the wires on the percentage volume loss (not significant, $p = 0.4763$).

7.3.2 Optimization of CECT imaging of the wires after implantation.

Due to the limitation of microCT imaging to only allow visualization of the metallic implants, CECT imaging was performed to image also the soft tissues surrounding the wires and, therefore, to identify the portions of the metallic wires inside the aorta lumen, the portions encapsulated by neointima, and the portions extending outside of the lumen. The goal was to identify a CESA that offers optimal contrast enhancement of the different types of soft tissues while minimizing further degradation of the metallic wires. Essentially, the staining time should be long enough to allow the CESA to diffuse into the samples but as short as possible to limit further degradation of the wires during the staining process. Out of the four different CESAs tested in this study (*i.e.*, CA4+, Hexabrix, 1:2 Hf-WD POM, and Lugol's iodine) for the contrast enhancement of the rat aorta, 1:2 Hf-WD POM and Lugol's iodine gave the best visual results (Fig. 7.3A). The interactions between these two CESAs and the different biodegradable metal types (*i.e.* Fe, Zn, and Zn alloy) showed that the wires experienced less degradation when immersed in Lugol's iodine compared to 1:2 Hf-WD POM, evidenced by the fact that the wires maintained greater integrity when immersed in Lugol's iodine (Fig. 7.3B). Additionally, full staining of the soft tissue with 1:2 Hf-WD POM required more time than with Lugol's iodine, meaning that the sample would need to be exposed to the CESA longer when using 1:2 Hf-WD POM (data not shown). The time required to fully stain the explants with Lugol's iodine varied across samples, depending on the amount of adipocytes, muscle fibers, and connective tissue that were present around the aorta. We found that 17 hours was the shortest staining time possible to ensure full staining of all the samples with Lugol's iodine (Fig. 7.3C).

7.3.3 Combining microCT and CECT enabled computation of the regional *in vivo* implant degradation.

The degradation of the wires was not uniform along their length. By analyzing the CECT images of the explanted samples, distinct regions of the wires were identified: the segment within the lumen, the segment inside the lumen + encapsulated by neointima, and the segment outside the lumen embedded in other soft tissues (adipocytes, muscle fibers, and connective tissue, mainly). By registering these images with the microCT datasets, the *in vivo* degradation of the wires was calculated for each of these specific regions (Fig. 7.4A-B and Suppl. Fig. 7.2). For all materials and at

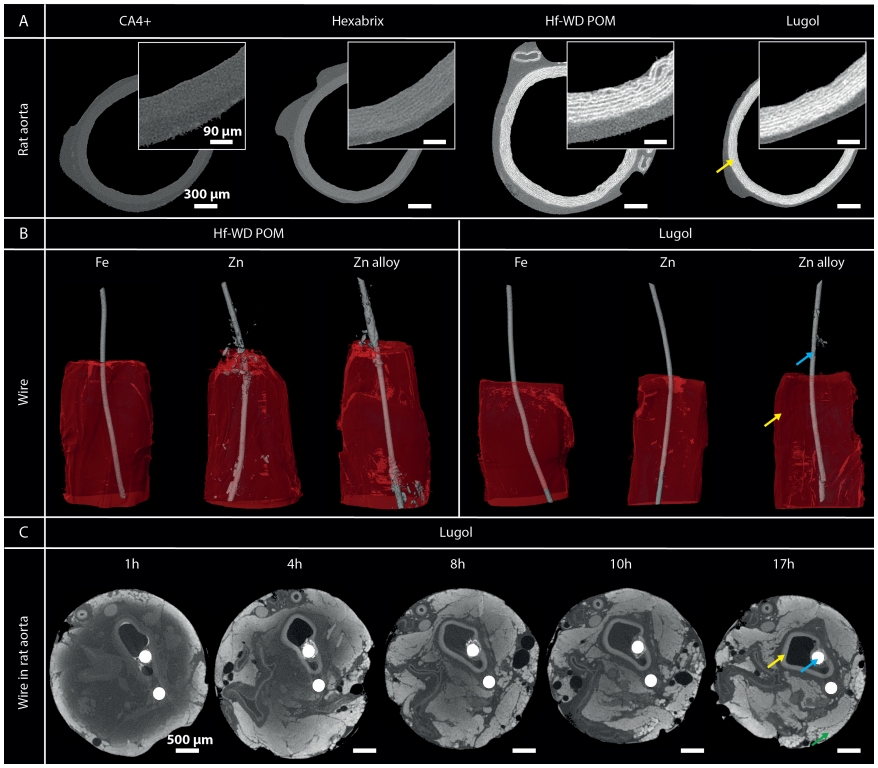


Fig. 7.3 Choice of CESA and optimization of staining time for CECT of the explants. (A) Normalized cross-sections of a rat aorta after staining with different CESAs (CA4+, Hexabrix, 1:2 Hf-WD POM, and Lugol's iodine) to compare their contrast enhancement. (B) 3D representations comparing 1:2 Hf-WD POM and Lugol's iodine for their interactions with the biodegradable wires of different metal types (Fe, Zn, and Zn alloy) placed inside a piece of porcine aorta (red). (C) Normalized cross-sections of a rat aorta explant, at different time points after staining with Lugol's iodine to optimize the staining time. Blue arrow = Zn alloy wire, yellow arrow = aorta, green arrow = adipocytes. Scalebar in A is 300 µm (overview image) and 90 µm (inset image) and scalebar in C is 500 µm.

every time point, the wire segments outside the lumen exhibited a greater volume loss compared to those inside the lumen. This difference was particularly significant at the 84-day time point for both Fe and Zn, with Zn exhibiting substantial degradation in the portions of the wires located outside the lumen (Fig. 7.4A). At the initial 7-day time point, the neointimal tissue was not discernible (Suppl. Fig. 7.2). At the 24 and 84-day time

points, for Fe, there was a greater volume loss for the portion of the wire encapsulated by neointimal tissue, although this was only significant at 24 days, as compared to the total volume loss of the wire portion situated within the lumen. The Zn and Zn alloy wires were fully encapsulated after 24 days, thus showing no difference between the portion of the wire in the lumen and the portion of the wire encapsulated by neointima in the lumen.

The assessment of the volume loss across the different materials was based on the percentage volume loss of the entire segment of the wires located within the lumen. Zn alloy had the highest percentage volume loss at all time points, followed by Zn, Fe, and CoCr (Fig. 7.4B). The portion inside the lumen was identified as the most biologically relevant for determining the degradation rate (Fig. 7.4C). The degradation rate decreased over time, from 7 to 84 days for all materials, and was initially much higher for the Zn alloy than for the other materials (Fig. 7.4C). The variation in degradation rate was high for Zn and Zn alloy because the volume loss was variable between samples for these materials, indicating inconsistent degradation behavior. From 7 to 84 days of implantation, the average degradation rate went from 0.23 to 0.03 mmpy for the Zn alloy, from 0.07 to 0.02 mmpy for pure Zn, and from 0.05 to 0.004 mmpy for Fe.

The homogeneous versus heterogeneous degradation behavior was described using the maximum range of the diameter and the variation of the diameter of the wires (Fig. 7.4D,E), based on the graphs from Fig. 7.2A. For the maximum range, there were no significant differences between materials at 7 days. At 24 days, the range was significantly higher for Zn and Zn alloy compared to Co-Cr and Fe. At 84 days, the maximum range for Zn was significantly higher than for all the other materials, while the variations for the Zn alloy were too large to detect any significant differences (Fig. 7.4D). The Zn alloy had the highest variation in diameter for all time points, which increased with time, although never significantly higher than Zn due to large variations observed between wires (Fig. 7.4E).

7.3.4 The CECT images allowed the 3D structural characterization of the neointima and corrosion products.

The evaluation of the morphometry of the neointima surrounding the wires gives insights into the biological performance of the implant. The neointimal tissue formation and corrosion products were assessed from the CECT

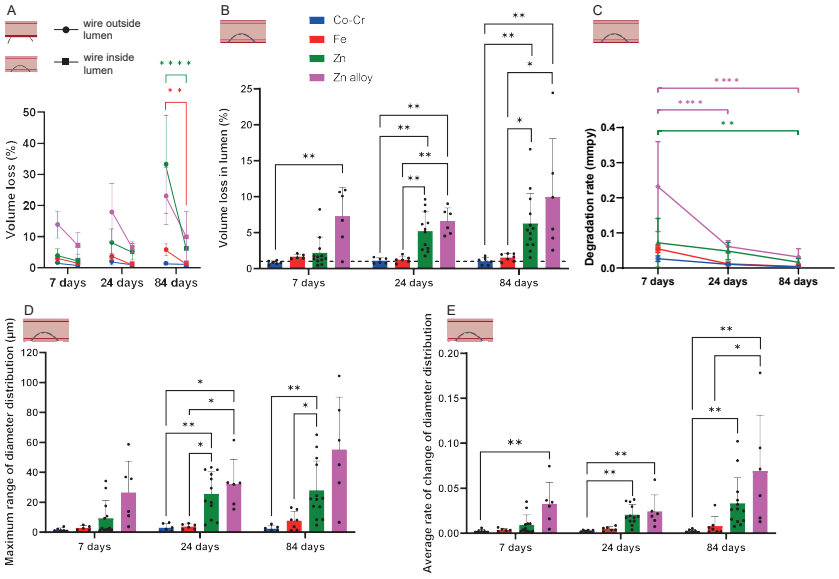


Fig. 7.4 Comparison of percentage volume loss of the portion of the wires outside the lumen and inside the lumen, and degradation rate and behavior of the explanted wires, part only inside the lumen. (A) Comparison between the percentage volume loss of portion of the wire outside the lumen (circle) and inside the lumen (square) for all materials and time points. (B) Percentage volume loss of the wires for the part of the wire that was inside the lumen of the aorta for all materials and time points. Dotted line indicates the threshold below which volume loss is considered insignificant (mean percentage volume loss of Co-Cr). (C) Degradation rate (mmpy), (D) maximum range of the diameter distribution (µm), and (E) average rate of change of the diameter distribution for all materials and time points, * $p \leq 0.05$, ** $p \leq 0.01$, *** $p \leq 0.001$, **** $p \leq 0.0001$.

images, and from this the lumen obstruction index was computed (Fig. 7.5). It is important to note that we found that the order of implantation of the metal types also did not have a significant effect on the lumen obstruction index (data not shown here). We verified that the corrosion products we identified were correctly segmented and could be differentiated from the neointimal tissue by comparing the microCT and CECT images of the same samples. An example is shown in Suppl. video 7.1. Video 7.1 illustrates the segmentation of the different components of the explants (aorta, wire, neointima, and corrosion products) and their spatial arrangement in a typical CECT dataset of a Zn alloy explant after 84 days of implantation.

Neointimal tissue formation was visible after 24 days and was negligible at 7 days of implantation (Fig. 7.5A). Co-Cr was the only material for which there was a significant increase in neointima formation between 24 and 84 days, with a significant increase in surface area, volume, and thickness of the neointimal tissue between these two time points (Fig. 7.5B-D). Neointimal tissue formation was less pronounced in the presence of Fe (lower surface area, volume, and thickness) than Co-Cr and no significant differences were observed between 24 and 84 days. In contrast, both pure Zn and the Zn alloy exhibited neointimal surface area, volume, and thickness values comparable to those of Co-Cr, but no significant differences were observed between the 24 and 84 days (Fig. 7.5B-D). The wire and the neointima were both considered to compute the peak thickness and the lumen obstruction index (Fig. 7.5E-F). For both parameters, Fe had lower values than the other materials. The average peak thickness of the wire and neointima in the Zn and the Zn alloy samples was not significantly higher than that of Co-Cr. The maximum peak thickness among all explants was 0.45 mm for Co-Cr, 0.28 mm for Fe, 0.55 mm for Zn, and 0.49 mm for Zn alloy. The maximum lumen obstruction index measured for Co-Cr was 20.64% and 22.34% at 24 and 84 days, respectively. These measurements were used as a reference, and the lumen obstruction index for the other materials was evaluated in comparison to these values. In the case of Fe, only 1 out of 7 explants at the 84-day time point showed a lumen obstruction index exceeding that of Co-Cr. For pure Zn, 6 out of 12 implants at 24 days and 4 out of 13 implants at 84 days surpassed the Co-Cr lumen obstruction index. For the Zn alloy, 2 out of 6 implants at both 24 and 84 days demonstrated a higher lumen obstruction index than that of Co-Cr. The corrosion products were absent or not visible for the Fe wires. They were only visible for the Zn and Zn alloy wires and only at time points 24 and 84 days. The assessment of their volume indicated no significant differences between both time points, but a significantly higher amount of corrosion products for the Zn alloy compared to pure Zn (Fig. 7.5G).

7.3.5 Neointima formation at the cellular level

The classical 2D histology sections of the samples allowed to validate what can be visualized in the CECT images (aorta, wire, and neointima) and provided additional details on the tissue in the explants at the cellular level (Fig. 7.6). Around the Co-Cr wires, the neointima appeared ideal, with cells uniformly distributed throughout the tissue (Fig. 7.6A). In contrast,

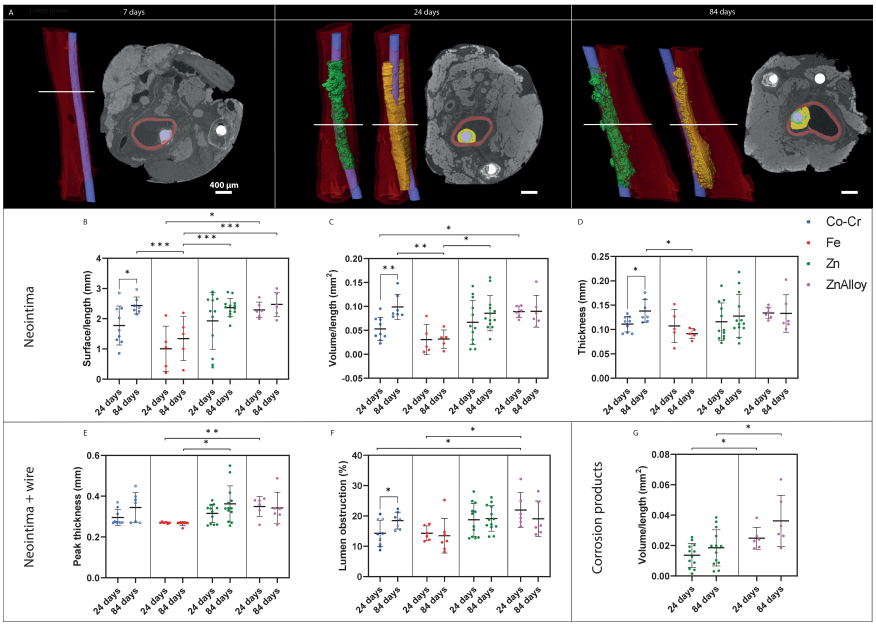
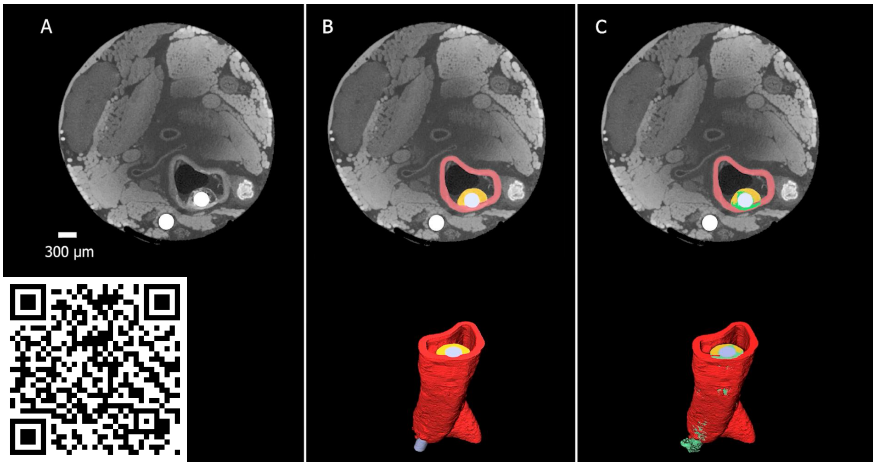


Fig. 7.5 Segmentation of the neointima and the corrosion products from the CECT images and comparison of the structural parameters of the neointima and the corrosion products for all wires at 24 and 84 days. (A) Visual representations of the corrosion products (green) and the neointima (yellow) surrounding the wire (light purple) inside the aorta (red) after 7, 24, and 84 days for representative Zn alloy wires. Comparison of (B) the surface area normalized by the length of the wires, (C) the volume normalized by the length of the wires, and (D) thickness of the neointima for all materials and the two last time points (24 and 84 days). Comparison of (E) the peak thickness of the neointima and wire combined and of (F) the lumen obstruction index for all four materials and the two last time points. (G) Comparison of the volume of the corrosion products normalized by the length of the wires for Zn and Zn alloy for the two last time points. Scalebars = 400 µm (A), * $p \leq 0.05$, ** $p \leq 0.01$, *** ≤ 0.001.

the Fe, Zn, and Zn alloy wires induced some acellular regions (Fig. 7.6B-D). Mild inflammation was also detected in specific areas around the Zn and Zn alloy wires (Fig. 7.6B,C), while Fe did not cause any inflammation (Fig. 7.6D). However, the Fe wires were not entirely covered by neointima. This suggests that the process of reendothelialization was not uniformly around the entire implants.



Video 7.1: CECT-based images of a Zn alloy explant, after 84 days of implantation. (A) The original grayscale slices, (B) the segmentation of the wire, the aorta, and the neointima, and (C) the segmentation of the wire, the aorta, the neointima, and the corrosion products. Red = aorta, light blue = wire, yellow = neointima, green = corrosion products. Scalebars = 300 µm.

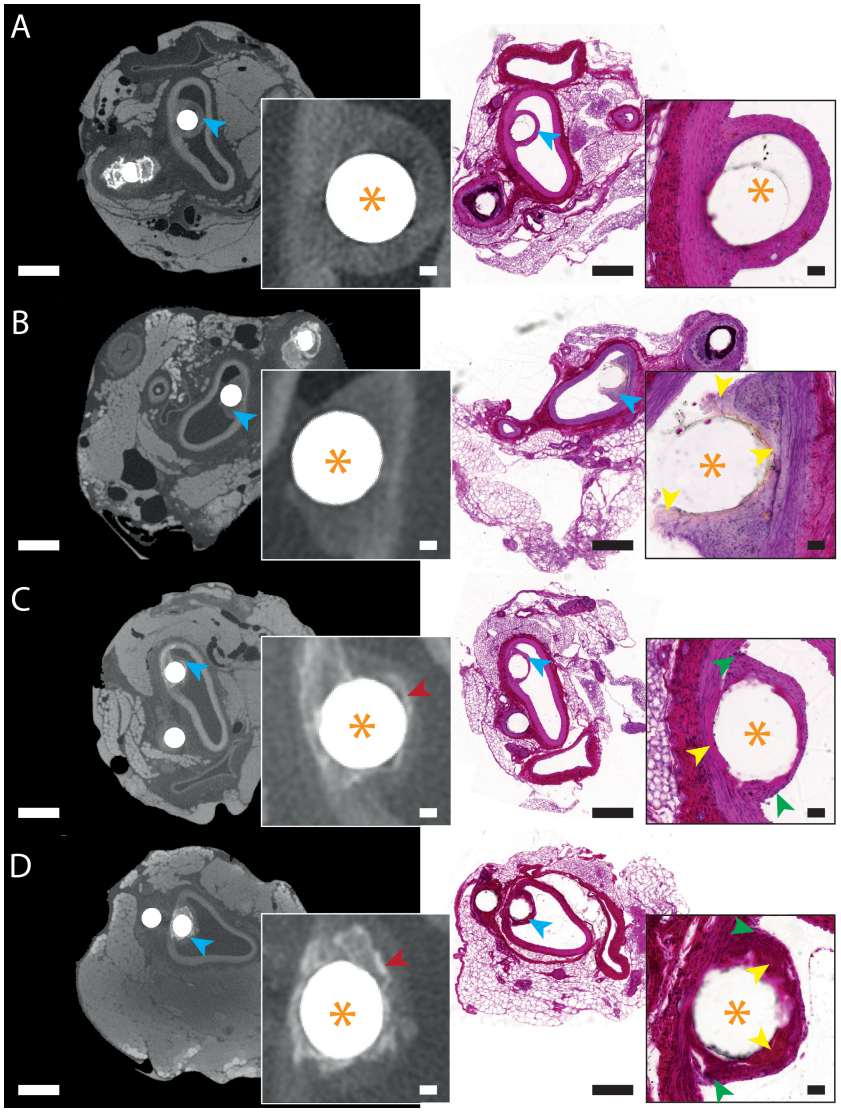


Fig. 7.6 Comparison between CECT and classical 2D histology imaging techniques for the explants. Representative CECT and classical 2D histology section for a (A) Co-Cr, (B) Fe, (C) Zn, and (D) Zn alloy wire. Blue arrow = neointima, red arrow = corrosion products, yellow arrow = acellular region, green arrow = mild inflammation, * = wire or wire location. Scalebars = 500 μm (entire sample cross-section) and 50 μm (zoom on neointima and wire).

7.4 Discussion

Biodegradable intravascular stents are advantageous compared to permanent stents with their ability to avoid long-term complications by disappearing from the body. Various biodegradable candidate materials have been investigated in the past two decades. However, the ideal material that provides sufficient mechanical support during arterial regeneration and then harmlessly degrades once its function has been served has not been discovered. Fe and Zn are candidates of high interest owing to their suitable biocompatibility. However, Fe corrodes too slowly according to benchmark standards [278, 282, 283] and Zn needs improved strength [240]. Hence, it is required to alloy these metals to improve their performance without affecting their biocompatibility. Many *in vitro* and *in vivo* experiments have been conducted and have yielded encouraging results and promising alloys, although the ideal alloy has not yet been found. More advanced characterization techniques, which allow 3D visualization and quantification of degradation behavior and host response, are required for a better understanding of the biological integration of the implant, improved implant designs, and hence better clinical outcomes in the future.

After implantation of candidate metals in animal models, analysis of the explants often involves techniques such as SEM or classical 2D histological analysis [241, 315] which only allow obtaining 2D local information on material behavior and biocompatibility. Due to the high variability that is often seen in candidate metal biodegradation behavior and biological responses, important information (such as the peak neointimal thickness or variability of the degradation behavior) can be misinterpreted from 2D analyses that make generalized conclusions from a limited number of cross-sections. Unfortunately, 3D image-based studies are still often rudimentary due to their insufficient resolution or inability to simultaneously detect both the metal implant and its surrounding tissue. X-ray based investigations can be done *in vivo*, using angiography, for instance. They allow for investigating properties such as luminal diameter [315] or implant volume loss [241] in real time, but only at very low resolution. Higher-resolution X-ray based studies have been conducted on explants to investigate the volume loss and the degradation products of metallic implants [241, 252, 293–295]. However, these studies did not allow for studying the interactions between the implant and the host tissue. In our study, we have combined microCT and contrast-enhanced microCT imaging to assess both

the degradation properties as well as the interactions between the implants and the soft tissue. These 3D imaging techniques can still be combined with classical 2D histology as they are non-destructive to the samples, in order to obtain information at the cellular level. Table 7.3 makes a comparison between microCT, CECT, and classical 2D histology and lists their pros and cons.

Table 7.3 Comparison between microCT, CECT, and classical 2D histology techniques for analysis of the explants

MicroCT	CECT	Classical 2D histology
- 3D technique with isotropic voxel size of ∼5 µm to allow visualization of full wire	- 3D techniques with isotropic voxel size ∼5 µm to allow visualization of full wire and soft tissue	- 2D technique with resolution of < 1 µm, gives local information
- CECT, classical 2D histology, and other techniques can still be performed afterwards	- Classical 2D histology and other techniques can still be performed afterwards	- End-stage technique
- Further degradation of the wire after explantation is very limited because microCT imaging was performed directly after explant collection	- Some degradation of the wire might have occurred during CESA staining for CECT imaging but limited thanks to the proper CESA selection and staining time optimization	- Degradation of the wire might have occurred during the preparation of the sample for classical 2D histology (methylmethacrylate embedding) - Cutting of the samples is challenging due to the presence of the metal and sometimes requires specific and expensive equipment

We showed that microCT allowed for obtaining a 3D visual representation and quantitative information on the volume loss of the implanted wires through the diameter versus length graphs. Visually, these graphs convey the homogeneous versus heterogeneous nature of the volume loss, volume loss at the surface versus in deeper regions, and the degree of vo-

lume loss. Using the data from these graphs, it is also possible to obtain quantitative information on the percentage volume loss of each wire.

Our analysis confirmed that the order of implantation of the wires did not have any effect on their percentage volume loss or on the lumen obstruction index. This means that the effects of degradation were local enough, and confirms that we could indeed implant three wires per animal without affecting the volume loss or tissue formation in the neighboring wires. This allows for reducing the number of animals required for such a study and significantly reduces the costs.

For the CECT imaging, CESA optimization was required to maximize the contrast enhancement of the different soft tissues while minimizing the effects of the staining on the degradation of the wires. 1:2 Hf-WD POM and Lugol's iodine presented the best contrast enhancement of the rat aorta, and they have been used in the past to stain cardiovascular tissues [77, 111, 199, 321]. However, because 1:2 Hf-WD POM is composed of metals in its highest oxidation state, it is known to engage in strong redox reactions causing a reduction of the POM with simultaneous oxidation of the metallic biodegradable wires. Also, we found that 1:2 Hf-WD POM required more time to fully diffuse into the tissue than Lugol's iodine. Therefore, we chose to use Lugol's iodine as CESA in our study. However, as Lugol's iodine solution is commonly known to cause tissue shrinkage due to acidification of the staining solution [198, 321], we decided to apply a Lugol's iodine solution buffered with a higher concentration of buffer ions, introduced by *Dawood et al*. Such a solution was shown to have a stable pH during the entire staining process, which prevents pH-induced tissue shrinkage. This solution is referred to as buffered Lugol's iodine solution [121].

Regardless, further degradation of the wires due to staining with buffered Lugol's iodine could not be totally excluded. For this reason, we decided to use the microCT datasets to compute the volume loss and hence, degradation rate of the implanted wires. Due to registration of the CECT with the microCT datasets, we could identify different interesting regions of the implanted metallic wires (portion of the wire inside and outside the lumen, and portion encapsulated by neointimal tissue). We showed that the percentage volume loss of the wires was higher for the portion of the wire outside the lumen than the one inside the lumen. From the portion of the

wires inside the lumen, we also showed that, for Fe, the portions that were encapsulated by neointimal tissue showed more volume loss than the ones that were exposed to the blood. This could partly be caused by blood contact tending to passivate the metal surface and thus reduce corrosion, as described [322]. This also illustrates the profound effects of the local environment of the implant on the degradation behavior. Indeed, the degradation rate differs in distinct locations within the same implant, depending on whether it is encapsulated by tissue or exposed to the blood flow. This finding has clear implications for biodegradable stents, given that the luminal side of a stent is exposed to blood while the abluminal side is exposed to the arterial tissue. Future work with the imaging approaches developed here could be used in large animal stent implantation studies to investigate the heterogeneity of stent biodegradation based upon exposure of the strut surfaces to the blood vs. arterial wall. Since a uniform biodegradation mode is desired, biodegradable stent designs may need to take this feature of highly localized environmental influences into account. For example, coatings can be applied locally to biodegradable implants to control their initial corrosion rate and prevent rapid degradation.

When comparing the different wire implants (focusing only on the portions inside the lumen), it was clear that Zn and Zn alloy exhibited the highest degradation rates, consistent with our *in vitro* study findings [320]. A precise comparison of degradation rates was challenging, as the degradation rate was found to vary considerably over time *in vivo* and only early time points were analyzed in the *in vitro* study. However, it was observed that the average degradation rates were lower *in vivo* than *in vitro* at the same 7-day time point. Additionally, the Zn alloy exhibited higher average corrosion rates compared to pure Zn both *in vivo* (0.23 vs. 0.07 mmpy) and in vitro (0.31 vs. 0.17 mmpy) at 7-days. A large variation between samples for Zn and Zn alloy was observed in both studies. This large variation could be explained by their very heterogeneous corrosion behavior, as shown by the large range and rate of change of their diameter compared to both the Co-Cr control and Fe wires. We also detected the formation of deep dendrites after corrosion of the Zn alloy wires, which was observed previously [320], confirming the consistent corrosion behavior of the materials *in vitro* and *in vivo*.

The neointima and the corrosion products were identified using the CECT images. To the best of our knowledge, this is the first time that the

neointimal tissue has been fully visualized in 3D. The 3D morphometric characterization of both the neointima and corrosion products provides a more comprehensive understanding of the biological integration of the implant by giving information on the explant as a whole as opposed to randomly selected 2D sections or smaller regions. It is important to note that the corrosion products are also visible on the microCT images (Suppl. Video 7.1), which validates the segmentation of the neointima (not visible in the microCT images) versus corrosion products in the CECT images. The average formation of neointimal tissue around the Zn and Zn alloy implants was similar, as was also observed previously [254], showing that the Zn alloy did not show worse behavior in terms of neointima formation compared to Zn. Nonetheless, at least one-third of the Zn and Zn alloy explants exhibited a lumen obstruction index higher than the maximum observed in Co-Cr implants, which was approximately 20% at 24 days and 22% at 84 days, with a maximum of 28% for Zn, and 32% for the Zn alloy. This might indicate a potential decrease in biocompatibility for the Zn and Zn alloy implants when compared to Co-Cr. This was also suggested by the presence of some regions with mild inflammation observed around both the Zn and the Zn alloy implants in the H&E sections. In contrast, the tissue formation around the Fe implants was significantly less than that around the Co-Cr implants, with even some regions where no reendothelialization occurred, as observed both in the CECT images and in the classical 2D histology sections. This might have significant consequences, such as ISR and ST. The presence of acellular regions around all the biodegradable implants, as observed in the classical 2D sections, might also suggest impaired healing. Additionally, a significant amount of corrosion products were visible around the Zn and Zn alloy explants, with a much higher volume for the Zn alloy. This implies again a faster degradation rate for the Zn alloy relative to Zn and for Zn relative to Fe. Additionally, this might also point to differences in biocompatibility between the materials or to a dependence of biocompatibility on the rate of implant biodegradation. The varying volumes of corrosion products could influence tissue response and the healing process, as the by-products of corrosion can interact differently with biological tissues.

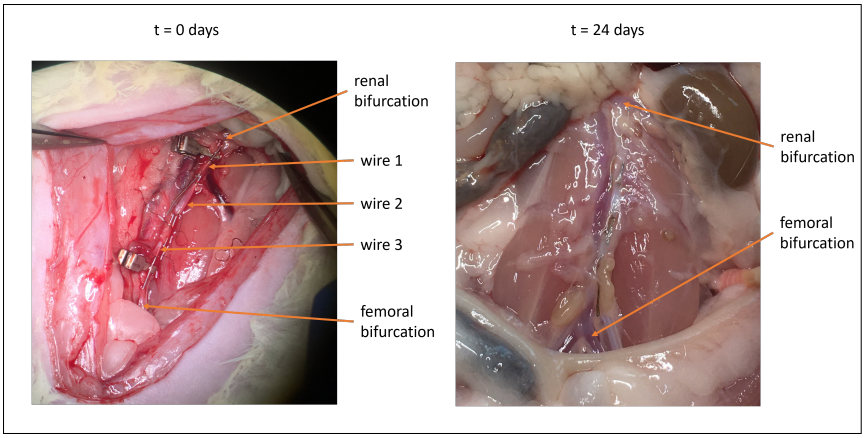
This study allowed us to successfully validate the use of microCT and CECT imaging for assessing candidate stent materials in an *in vivo* setting. However, several limitations were identified. The first major limitation is the use of metallic wires, which cannot entirely replicate all aspects of

a stent, particularly mechanical properties such as strength and ductility. Additionally, unlike a real stent, the wires are not always fully in contact with the endothelial wall, requiring the assessment of different regions of the wires. MicroCT and CECT need to be validated for the imaging of full stents with different geometries. Another limitation of this study is that it relies on a healthy animal model. Future research could benefit from using an atherogenic animal model, such as the well-established apoE-/- transgenic mouse model of atherogenesis. It would be necessary to confirm that the diseased tissue, such as atherosclerotic lesions, can be distinguished with microCT or CECT. Moreover, while our study employed a rat model, exploring stent deployment and implantation in larger animal models, such as pigs, which are more anatomically similar to humans, would be valuable. Finally, our study focused on microCT and CECT imaging as non-destructive techniques, which opens the possibility of combining them with other techniques in future research. For instance, investigating the inflammatory properties of explants using immunofluorescence staining or histopathology, or evaluating the nature of the corrosion products using SEM, could provide a more comprehensive understanding of the biocompatibility and degradation behavior of the materials.

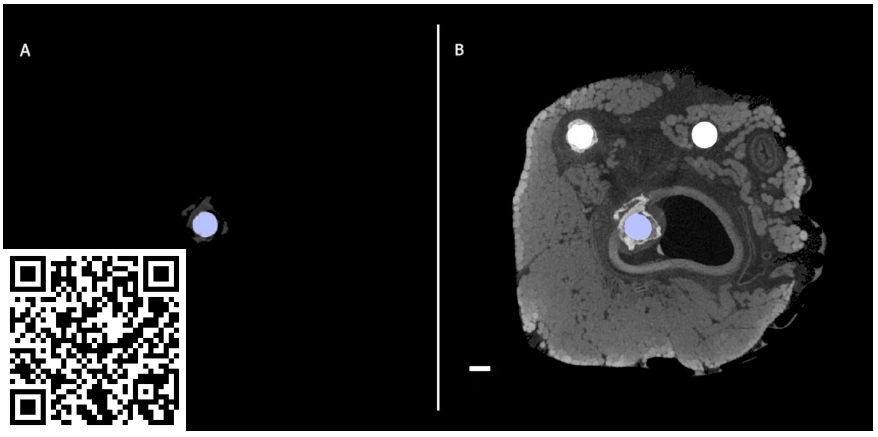
7.5 Conclusion

This study demonstrates the potential of microCT and contrast-enhanced microCT imaging to study the *in vivo* degradation behavior and the biocompatibility of candidate biodegradable intravascular stent materials non-destructively in 3D by using wires implanted in an aortic rat model. In the future, this imaging technique has the potential to provide crucial information for the development of new stent materials for improved biodegradable implants.

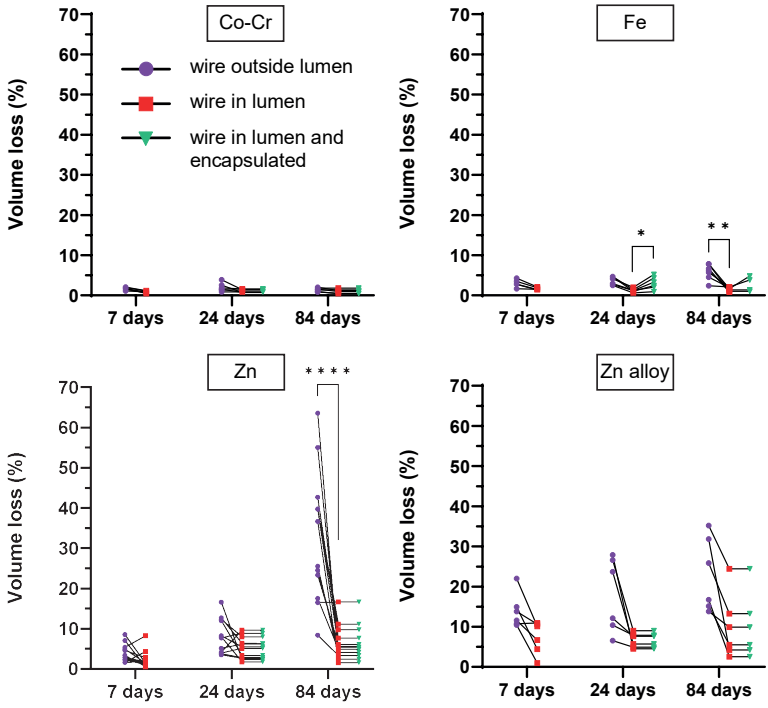
7.6 Supplementary materials



Suppl. Fig. 7.1: Pictures of the surgery. Implantation of three different wires in the rat abdominal aorta between the renal and femoral bifurcations at time point 0 (left) and just before sample collection at 24 days (right).



Suppl. Video 7.1: MicroCT and CECT-based images of a Zn alloy explant after 84 days of implantation. (A) MicroCT slices showing the wire and the corrosion products and (B) CECT slices of the same explant after staining with Lugol's iodine for 17 hours, showing the wire, the corrosion products, and the surrounding soft tissue. Light blue: original, non-degraded parts of the wire. Scalebars = 200 µm.



Suppl. Fig. 7.2: Comparison of the percentage volume loss for different locations of the wires for all time points and all metal types. Comparison of the percentage volume loss for the portion of the wire outside the lumen (circle), the portion inside the lumen (square), and the portion inside the lumen that is encapsulated by neointima (triangle) for time points 7, 24, and 84 days and for all metal types (Co-Cr, Fe, Zn, and Zn alloy), * $p \leq 0.05$, ** $p \leq 0.01$, *** ≤ 0.001, **** ≤ 0.0001.

PART IV
Discussion and conclusion

8

Overview, general discussion, and future perspectives

8.1 Thesis overview, limitations, and potential improvements for each part

This thesis manuscript describes the optimization and application of high-resolution X-ray microfocus computed tomography (microCT) and contrast-enhanced microCT (CECT) to study the 3D microstructure of healthy vascular tissues and to investigate two different treatment options for cardiovascular occlusive diseases: synthetic vascular grafts and biodegradable intravascular stent materials. The synthetic materials (vascular grafts and metallic stent materials) were investigated using microCT while the soft biological tissues (native blood vessels and blood vessels implanted with stent materials) were studied using microCT combined with contrast-enhancing staining agents (CESAs), referred to as CECT.

8.1.1 Part I

This part started by providing background information on the cardiovascular system, related cardiovascular occlusive diseases, and their treat-

ments. It then gave the general problem statement and objectives of this thesis. The main body of this manuscript was divided in two parts (Part II and Part III).

8.1.2 Part II

Part II was related to microCT-based imaging of the native blood vessels and synthetic grafts. This started with a published review of the literature on the application of X-ray-based imaging techniques (mainly microCT, CECT, and PCCT) to study the cardiovascular system. This review highlighted the importance of better describing the 3D microstructural properties of cardiovascular tissues to better understand cardiovascular diseases and their development and treatments. The part of this review related to the vasculature underlined the potential of microCT-based techniques to visualize the complex microstructure of the native blood vessel wall. However, it also emphasized some important shortcomings in terms of resolution, quantitative data, and currently used contrasting methods. Indeed, the description of the microstructural tissue constituents and their 3D arrangement is often limited by the spatial resolution or restricted to small regions of interest and lacks in quantitative characterization of the different microstructural constituents. For obtaining contrast between different soft tissues, two main options exist: the use of CESAs for contrast enhancement for CECT or the use of PCCT. For the first one, CESAs have started to emerge quickly, but they are often destructive or harmful to the native tissue and their staining mechanisms are not well understood. For the second one, the equipment required is expensive and often not readily available.

Based on this review of the literature, the second chapter of Part II, aimed at optimizing CECT to study the vessel wall microstructure of different types of blood vessels (aorta, femoral artery, and vena cava) in different species (rat, porcine, and human) at high resolution and in a non-destructive way. After an optimization study of the penetration rate and the contrast enhancement, 1:2 Hf-WD POM was identified as the optimal CESA for visualizing the blood vessel wall microstructure thanks to its non-destructive character and optimal contrast enhancement of the different vessel wall layers and the elastin component. The latter is one of the main constituents contributing to the function of a blood vessel. Moreover, the 3D information shows that elastin forms not only fibers, as might be interpreted from 2D cross-sectional images, but a complex network of in-

terconnected sheets. To investigate this complex branching between sheets, 3D information is crucial. The importance of carefully choosing an animal model when studying a disease was highlighted through our finding that the aorta and femoral artery of the rat, pig, and human are structurally different, especially in terms of spatial arrangement, shape of the elastic lamellae, and arrangement of the external elastic lamina. In the femoral artery, differences in thickness ratio between the media and adventitia layers were highlighted. There were also large differences detected between types of blood vessels, even though the same disease treatments are often applied to different types of blood vessels (*e.g.*, the same synthetic grafts with only a difference in diameter are used to treat different types of diseased blood vessels). Synthetic vascular grafts, which create a bypass for blood flow, are one of the main treatment options currently used to treat blood vessel calcification and occlusion. Using microCT imaging, the microstructural properties, such as fiber thickness, fiber separation, fiber volume fraction of different currently used synthetic grafts (Dacron, Gore-Tex, and Vectra) were compared to show the large differences in microstructure between healthy native tissue and synthetic grafts. This also explained the large gap in functional behavior between both. In the future, using the microCT images, it is possible to further investigate the structural parameters of the fibers of the grafts. Indeed, using a fiber correlation tool, their orientation, diameter, and length can be determined. This is turn allows for the customization of grafts with specific desired characteristics, tailoring them to meet specific functional requirements.

This study provides important knowledge to further improve current diseases treatments, such as the design of superior synthetic vascular grafts. However, some limitations were identified. The first one is related to the amount of samples used for the assessment of the different blood vessel types. Biological tissues are not always easy to collect and because we were analyzing several tissue types coming from multiple species, we only investigated n=3 samples per blood vessel type. In the future, it would be interesting to use more samples and to verify the reproducibility of the imaging. Based on the data from this study, a power analysis would allow determining the number of samples needed. It is also important to note that the staining and scanning protocol need to be optimized and adapted for each new type of tissue to obtain the best image quality. Finally, the focus remained on imaging the elastin component of the vessel wall. We were not able to visualize the collagen fibers, for which spatial resolution

should be further increased. To achieve a higher resolution of the same region of interest, multi-scans (multiple datasets at higher resolution with a smaller field of view that can be reconstructed into one single dataset to visualize an entire sample) could be done in the future. The tissue microstructure visualization could also be improved by using cryogenic CECT (cryo-CECT), a technique in which the sample is kept frozen during acquisition, allowing to reveal the individual soft tissue constituents thanks to segregation between the CESA and the water contained in the tissue upon ice crystallization [199]. Further research into CESAs that are collagen- or elastin-specific would also allow their distinction and visualization.

8.1.3 Part III

Part III of this manuscript focused on X-ray-based imaging of metallic implants for biodegradable intravascular stents, another important treatment option for blood vessel narrowing or blockage. It was divided in three chapters. The first one was a review of the literature on the advancements and development of intravascular stents including the different generations of permanent and biodegradable stents that have been developed, the requirements a stent should fulfill, the different materials that have been investigated, and the different possible clinical outcomes of stent implantation and how they are evaluated. This chapter underlined the further need to investigate different metallic alloys with better corrosion properties and subsequently improved biocompatibility to improve current clinical outcomes.

The two subsequent chapters of Part III focused on microCT-based technical advancements for investigating candidate materials to be used as intravascular stents. The first study involved the application of microCT and the optimization of image processing methods to investigate the degradation behavior and surface properties of different biodegradable metal types after *in vitro* immersion tests in physiological conditions. The different metals were investigated in the form of wires, a simplified stent model, that represents a single stent strut. The aim of this study was to establish a method to evaluate the corrosion behavior and the surface properties in 3D of candidate materials in a more detailed and accurate manner than has currently been done. By optimizing microCT-based imaging and data processing tools, the corrosion rate through the volume loss, the corrosion behavior and surface properties, through the assessment of the surface

roughness, and the corrosion products of three biodegradable metal types (pure iron, pure zinc, a quinary zinc alloy) were investigated and compared to a reference biostable cobalt-chromium alloy. This study showed that iron (Fe) had a suitable corrosion mode, with homogeneous, surface corrosion and very low values of surface roughness but a very low corrosion rate. Pure zinc (Zn) had a higher corrosion rate but exhibited pitting and non-uniform corrosion. The quinary Zn alloy (Zn-Ag-Cu-Mn-Zr), which was developed to improve the inflammation resistant properties of pure Zn, had improved corrosion properties, the corrosion behavior being more homogeneous and showing less pitting. However, the formation of deep internal dendrites was observed. Thanks to further analysis with SEM, it was found that this was due to a deficiency in the alloying process, which led to preferential corrosion in some regions.

This work provides insights into the evaluation of candidate stent materials using microCT, allowing to obtain 3D information in a non-invasive way from *in vitro* immersion tests. However, when imaging the metallic wires, we focused on a smaller region of interest of each wire in order to obtain high-resolution images (1 µm voxel size). Here again it would be interesting to do multi-scans to obtain a high-resolution image of the entire wire. Another limitation is the computation of the surface roughness based on the microCT images. Indeed, accuracy of the roughness measurements depends on the image quality, such as spatial resolution, noise, and contrast resolution. *Kerckhofs et al.* have shown that for higher roughness (at the micro-scale), the microCT-based measurements can be used with comparable or even better accuracy than standard profile measuring methods. However, for low roughness (submicron-scale), the spatial image resolution and the noise level in the images limit the use of microCT-based roughness measurements [299]. Finally, different wires were used to assess the degradation at each time point. However, the same study could be done over time. This means that wires could be imaged with microCT at a certain time point and placed back in the solution to continue the experiment over time.

In the final chapter of Part III, the same materials (Co-Cr, Fe, Zn, and Zn-Ag-Cu-Mn-Zr) were investigated in an *in vivo* study. The wires were implanted in the rat abdominal aorta and the animals were sacrificed at different time points to collect the explants. MicroCT was first used in the same way as in the previous chapter to obtain the *in vivo* corrosion

behavior and rate of the different metal types, and to visualize the corrosion products. CECT was then optimized, by finding the optimal CESA for this application. A buffered Lugol's iodine solution was identified as ideal because it allowed a strong contrast enhancement of the soft tissue surrounding the implanted wires, while minimizing further degradation of the wires during the staining process. Combining microCT with CECT allowed to identify different regions of the wires (regions outside the lumen, inside the lumen, and inside the lumen and encapsulated) thanks to the visualization of the soft tissue and to assess the regional volume losses. It also allowed to segment and quantify the volume, surface area, and 3D thickness of the neointimal tissue around the wires. This chapter demonstrated the advantage of combining microCT and CECT to assess the degradation behavior and the biocompatibility of candidate biodegradable stent materials in 3D.

This study provides a better understanding of the biological integration of different metallic implants than has been possible to obtain before by providing information on the explants as a whole as opposed to small ROIs or 2D sections. Nevertheless, some limitations have been identified. The wires were implanted in the rat abdominal aorta. However, as discussed in chapter 4 of this manuscript, blood vessel microstructure varies according to the vessel type and the species. The rat aorta, for example, is different from the human aorta, not only in size but also in terms of structural properties, such as the arrangement of the elastic lamellae in the medial layer. Outcomes of this study could be different with other animal models or in human patients. Moreover, in humans, stents are often placed in other blood vessels, different from the aorta, such as the coronary or the femoral arteries. Therefore, it is important to consider doing the same study on other animal models that more closely replicate the conditions of the human body and in other blood vessels that are more often affected by narrowing or blockage. As we already showed the potential of CECT to image different blood vessel types in different species, imaging protocols used for the rat aorta explants could be adapted to other blood vessel types. Moreover, wires were implanted in the animals as a cheaper and easier model of a stent. However, a single wire cannot replicate all aspects of a stent. Full stents also involve the deployment step, and they should provide sufficient mechanical support to the vessel wall. These characteristics cannot be studied with wires. Therefore, it is important to repeat these experiments with full stents. As long as streaking artefacts due to the pres-

ence of the strongly attenuating metal in the soft tissue can be minimized, microCT and CECT imaging can be adapted to other implant geometries. Additionally, this study was done on healthy animals. In the future, it would be interesting to first validate our imaging techniques on the blood vessels of diseased animal models, such as the well-known apoE-/- transgenic mouse model of atherogenesis or an atherogenic pig model. Then, the same surgery can be carried out on these animals and imaging of the explants would allow assessing the behavior of these metals in diseased animals. Finally, it was not possible to do a longitudinal study, evaluating the corrosion behavior of the same implant over time, because this would require *in vivo* imaging, which would be too limited in terms of resolution to visualize the same level of detail.

A precise comparison of the degradation rate and behavior found in the *in vitro* and *in vivo* studies was challenging. Earlier time points had to be evaluated *in vitro* compared to *in vivo* because of the faster degradation *in vitro*. However, the *in vitro* study allowed to gain an initial understanding of the degradation rate and the degradation behavior of the different metals without the need for animal experiments. The last time point of the *in vitro* study corresponded to the first time point of the *in vivo* study (7 days). For this time point, both studies showed that the degradation rate was highest for the Zn alloy, followed by Zn, and then Fe. In both studies, Fe exhibited the most favorable degradation behavior, characterized by homogeneous and uniform degradation, ideal for stent applications. However, its degradation rate is too low and needs to be improved. Development and testing of new Fe alloys are necessary, and it is yet to be established whether these alloys will maintain the same level of degradation behavior and biocompatibility as pure Fe. The Zn alloy presented a more appropriate corrosion rate than Fe, and exhibited the same biocompatiblity properties as pure Zn (similar neointima morphometrics) but should be further investigated to check its biocompatibility at the cellular level. Table 8.1 lists the pros and cons of performing *in vitro* versus *in vivo* experiments.

It is important to understand that the degradation rate and behavior of the metals are closely related to their microstructure, including aspects such as grain size, grain orientation, and the presence and distribution of precipitates, inclusions, and impurities. Investigating these microstructural aspects could provide more information on the reasons for pitting ver-

sus uniform corrosion. The latter can be attributed to various phenomena, including micro-galvanic coupling within metallic alloys, homogeneous versus non-homogeneous dissolution of some particles inside the matrix, damage to the protective layer from mechanical or chemical damage, and grain boundaries acting as pitting initiation sites or complicating the microstructure enough to alter uniform corrosion pathways. Therefore, future studies should also focus on evaluating the microstructure of the metals to draw informed conclusions about their degradation behavior. This can be done using techniques, such as optical microscopy, SEM in combination with EDX or EBSD, transmission electron microscopy (TEM), or X-ray diffraction (XRD).

Table 8.1 Pros and cons of the *in vitro* and the *in vivo* studies

In vitro	*In vivo*
+ no need to sacrifice animals	+ closer to reality of the physiological environment
+ data can be acquired over shorter time period	+ allows to investigate biocompatibility with the tissue
+ less costly and time consuming	- data acquisition takes more time because it is necessary to look at late time points
+ it is possible to do a longitudinal study, investigating the same sample over time	- need to sacrifice animals
- very different from what happens in physiological conditions	- the animal model used is not fully representative of reality (wire instead of stent, rat instead of animal that is closer to human, implantation in the aorta instead of in the coronary or femoral arteries, healthy animal model used instead of diseased one)
- not possible to investigate the biocompatibility with the tissue in our study	- longitudinal study with *in vivo* imaging is not be possible at the same resolution

8.2 General discussion and future challenges

8.2.1 Comparison of microCT-based imaging with other imaging techniques

Table 8.2 presents a comparison of various structural imaging methods, both preclinical and clinical, alongside microCT. This comparison focuses on their characteristics in terms of 2D versus 3D imaging, acquisition time, and spatial resolution.

It should be noted that the non-destructive nature of microCT-based imaging allows for its combination with other imaging methods, an approach known as correlative imaging. For example, CECT can be used to obtain a representation of the overall 3D volume of a structure and then regions of interest can be selected to obtain a higher-resolution image with a complementary imaging technique. In this thesis, we combined CECT with classical 2D histology, widely recognized as the standard technique for high-resolution imaging of biological tissues. Classical 2D histology is often used for validation of CECT images, owing to its ability to provide information at the cellular level through well-established tissue component-specific stains in the form of 2D sections. We have shown that for visual qualitative validation, it was advantageous to do this. On the other hand, we have proved that it could not be used for quantitative structural analysis due to a substantial shrinkage (43% volume reduction for the porcine aorta) because of paraffinization. Additionally, the sectioning and colorimetric staining after paraffin embedding caused additional damage or changes to the microstructure of the tissue. We also showed the potential of combining microCT imaging with SEM for the characterization of the degradation products of the metallic wires.

Table 8.2 Comparison of different structural imaging techniques with regards to the 2D versus 3D character, acquisition time, and spatial resolution

	Imaging technique	2D versus 3D	Working principle	Acquisition time	Resolution
Optical microscopy	Bright-field microscopy	2D	Image is formed due to the differential absorption, reflection, or refraction of the light by various structures in the specimen	Few minutes	0.25 µm
	Confocal microscopy	2D and 3D	Uses a laser as light source to illuminate specimen and a pinhole aperture in front of the detector to eliminate out-of-focus light, creating more precise images	Minutes to hours depending on resolution and sample size	0.25 µm
	Multiphoton microscopy	2D and 3D	Uses near-infrared light; two or more photons of lower energy are absorbed simultaneously by a fluorophore in the specimen, emitted light from the excited fluorophores is collected to form an image	Minutes to hours depending on resolution and sample size	0.25 µm
	Lightsheet microscopy	2D and 3D	Illumination of the specimen with a sheet of light perpendicular to the direction of observation, fluorescent molecules in the illuminated plane absorb the light sheet and emit light at a longer wavelength	Few minutes	0.25 µm
	Optical coherence tomography	2D and 3D	Uses low-coherence, near-infrared light. Employs interferometry, where light is split into a sample and reference beam creating an interference pattern when recombined at the detector	Few minutes	1-10 µm
Electron microscopy	Scanning electron microscopy	2D	Surface of specimen is scanned using a focused beam of electrons which interact with the atoms in the sample, producing secondary electrons detected to form a high-resolution image	Few minutes	nm-scale

X-ray-based imaging	Absorption mode microCT	3D	Polychromatic X-ray source penetrates an object and captures the differential absorption rates of the X-rays by different materials within the object. Through rotation and computer reconstruction, detailed three-dimensional images of the internal structure of the object are generated.	20 min to several hours	1 µm
	Synchrotron-based microCT	3D	Same principle as absorption mode microCT but synchrotron X-ray beam has large spatial coherence, high-photon flux, and monochromatic radiation. Can exploit phase contrast imaging which computes the phase shift due to the interaction of the beam with electrons in the material	5 min to several hours	nm-scale
	Clinical CT	3D	Same principle as absorption mode microCT, but with rotating X-ray source going around the patient, with lower resolution, lower dose, and lower acquisition times	Few seconds or minutes	0.5-1 mm
Magnetic resonance imaging	MicroMRI	3D	Specimen placed in a strong uniform magnetic field, which causes paramagnetic atoms such as hydrogen, gadolinium, and manganese to align themselves in a magnetic dipole along the magnetic fields. Relaxation of the atoms is captured from the sample.	Several hours	25-100 µm
	Clinical MRI	3D	Sample principle as microMRI with lower magnetic field, lower resolution, and shorter imaging times	10-60 min	1 mm

8.2.2 Optimization of microCT and CECT to improve treatments for cadiovascular diseases

Finding the appropriate microCT or CECT imaging protocol for each application is not trivial. It is crucial to carefully optimize all aspects of sample preparation and image acquisition. The sample preparation and sample positioning in the device should be reproducible. These steps should be carefully considered because any movement of the sample during acquisition will have direct impact on the image quality, inducing motion artefacts. At the same time, the sample should maintain its original/native shape (especially in the case of a blood vessel) and cannot be squeezed in a sample holder. Finally, the acquisition parameters need to be optimized and chosen in function of the sample and the components that need to be visualized. All these aspects should be adapted to each type of sample and to the final goal of the scan (what should be visualized and at which resolution). A list of the acquisition parameters that can be adapted with the Phoenix Nanotom M, the device used in the frame of this thesis, is available in Appendix A. In the next part of this section, we will highlight the particular applications for which microCT was useful, together with its limitations. We will then discuss the context in which CECT was used and how it was optimized for our particular applications.

MicroCT

We emphasized the need for advanced 3D imaging tools and quantitative analysis of cardiovascular tissues to better understand disease development and enhance treatments for cardiovascular occlusive diseases. MicroCT emerges as a valuable imaging tool, particularly for characterizing synthetic materials like vascular grafts and metallic alloys used in intravascular stents. It allowed high-resolution 3D visualization and comparison of different synthetic grafts and extraction of their structural parameters. Additionally, microCT enabled the examination of various metals pre- and post-degradation from *in vitro* and *in vivo* experiments, allowing the computation of the degradation rate and characterization of the degradation behavior. MicroCT does not allow the visualization of biological soft tissues due to their low X-ray attenuating properties.

CECT

We have investigated several CESAs, solutions containing heavy atom elements, which passively diffuse into the soft tissues to render their constituents X-ray attenuating. However, as CECT is not a standard technique

yet, it required optimization of the tissue staining. Indeed, a current challenge of CECT imaging is that the choice of CESA, the staining time, and the CESA volume and concentration need to optimized for every tissue type and every CESA. These parameters are largely influenced by tissue size, tissue composition, tissue type, and the specific chemical interactions between the tissue and the CESA.

For the visualization and characterization of the different constituents of the blood vessel wall, we identified 1:2 Hf-WD POM as the most valuable CESA. It was non-destructive to the tissue and allowed contrast enhancement of the vessel wall layers and the elastic lamellae. It also allowed the assessment of various quantitative parameters, such as thickness of the vessel wall layers of different types of blood vessels and thickness, separation, tortuosity factor, volume fraction, and connectivity of the elastic lamellae in different regions of the media of the rat and porcine aorta.

1:2 Hf-WD POM was not appropriate for the second application, in which the goal was to visualize blood vessels implanted with metallic wires. Indeed, 1:2 Hf-WD POM is composed of metals in its highest oxidation state, therefore it was engaging in strong redox reactions with the wires, causing fast degradation during staining. To avoid this, Lugol's iodine solution was identified as a valuable CESA owing to its effective contrast enhancement of the vessel wall. However, as mentioned in our review of the literature (chapter 3), Lugol is known to cause acidification of the CESA solution during staining and, hence, causes tissue shrinkage. Therefore, we decided to use a buffered Lugol's iodine variant with a stronger buffer as solvent, preventing tissue shrinkage. This allowed to perform CECT on the explants and to visualize the interactions between the metal and the surrounding tissue and to assess its morphometric parameters, characterizing the biocompatibility.

The explants contained both low (biological soft tissue) and very strongly (metallic wires) attenuating structures. However, the presence of the strongly attenuating metal in the soft tissue is often known to cause streaking artifacts in the reconstructed images, mainly due to beam hardening and Compton scatter. Beam hardening occurs when a polychromatic X-ray passes through an object, resulting in selective attenuation of lower energy photons. As only higher energy photons are left to contribute to the X-ray beam, the mean beam energy is increased or hardened. Scanning at

higher voltages results in a harder X-ray beam and helps to reduce beam hardening artifacts but often with a reduction in soft tissue contrast. We also used a copper filter to harden the beam before it went through the samples to partly overcome beam hardening. Finally, a beam hardening correction (BHC) was applied during reconstruction of the images. Scatter leads to a change in direction and energy of the X-rays, resulting in inaccuracies when scattered photons reach a detector that would otherwise have very few photons. As beam hardening and scatter cause more photons to be detected than expected for highly-attenuated beams, it results in dark streaks along the lines of greatest attenuation. Bright streaks are seen next to the dark streaks because the high-pass filter used in the image reconstruction algorithm (filtered backprojection) exaggerates differences between adjacent detector elements [323]. It is important to note that we were able to reduce the streaking artifacts so that they did not impair the image segmentation in our study. However, with a different metallic alloy or a different implant geometry, acquisition and reconstruction parameters need to be optimized again to minimize these artifacts.

8.2.3 Future challenges of microCT-based techniques

MicroCT and CECT imaging have proven to be valuable techniques for 3D X-ray based histology and have become popular over the past decade. The field is still quite young, but it is evolving rapidly. Ongoing research involves the development of new and improved instruments (*e.g.*, higher-powered sources and faster detectors) but also the development of new CESAs which are less destructive to the tissues and diffuse faster, allowing for shorter staining times.

Recent advancements have focused on developing *in situ* imaging or 4D-microCT, which means that microCT-based imaging is performed while simultaneously applying a stimulus to the sample, such as mechanical loading or a temperature change. For now, with lab-based microCT, *in situ* imaging is often limited to time-lapse testing where, for example, loading is performed step-wise and imaging is done while there is no change in loading. However, with improved scan speeds, the goal is to push towards dynamic imaging [324]. When combined with digital volume correlation, 4D-microCT allows to quantify the local strain gradient at various loading stages, based on the volumetric images of the reference and deformed states of the sample during the deformation process. 4D-microCT could

be used in the future to assess the mechanical responses during stent expansion by performing stepwise inflation of a balloon within a stent while imaging. When combined with CESAs, 4D-CECT allows real-time visualization of blood vessel deformation under mechanical loading, such as inflation, offering a great opportunity to investigate the structure-function relationship of these complex tissues as already shown by *Brunet et al.* [111]. This technique also offers the possibility of assessing the mechanical properties of diseased vessels. In the future, 4D-CECT has the potential to assess the mechanical response of a vessel during stent expansion. However, steps are still required to a more in-depth evaluation of the impact of CESAs on the mechanical properties of biological samples.

In terms of image analysis and processing, many efforts still need to be made to obtain more standardized and automated image analysis protocols. Indeed, we have seen in this PhD project that a lot of manual segmentation is still required during image analysis. However, this is time-consuming and often user-biased. For example, convolutional neural networks could be trained with a limited number of manually segmented samples and then used to automatically predict image segmentation.

Finally, in the future, microCT-based techniques can provide input for more robust 3D computational models. Microstructural information of the blood vessel wall obtained via microscopy has already helped to create macroscopic, tissue-scale, constitutive models to predict the mechanical behavior of vascular tissues. These models are fast and efficient, however, a significant limitation arises from the non-physiological nature of the parameters of their equations, which makes it challenging to accurately depict the behavior of diseased vascular tissues. More recently, research has focused on representative volume element (RVE) modeling. RVE models, informed by microstructural analysis, offer insights into how microstructural alterations influence vascular tissue mechanical behavior, to better understand disease dynamics. In the process of creating an RVE model, it is important to capture a volume of the tissue that is sufficiently small to be computationally manageable, yet large enough to encompass the essential microstructural features. This process begins with selecting material models that accurately represent the microstructural elements of arterial tissue. Then, periodic boundary conditions are applied to the model boundaries to simulate physiological conditions, allowing to consider the mechanical properties of the entire tissue. An RVE model should account for non-

linear material behavior, typical of arterial tissue. For an RVE model to optimally predict arterial behavior, especially under diseased conditions, it must be based on precise microstructural data. RVE models for arterial tissue already exist, such as in [325], which models two families of collagen fibers with embedded truss elements within a solid matrix to capture their orientation and dispersion. However, this model lacks the inclusion of elastin, a critical arterial wall component, highlighting the necessity for better models that include all significant microstructural elements and therefore, highlighting the need for imaging techniques that provide detailed 3D microstructural information on native and diseased tissues.

Computational models represent a powerful tool in the study of blood vessels and their diseases, offering a way to simulate and analyze complex physiological and pathological processes in detail. Models can significantly improve our understanding of disease mechanisms, predict disease progression, and assess the potential efficacy of various treatments. By incorporating anatomical, physiological, and biomechanical data, computational models can provide insights into the interactions between blood flow dynamics, vessel wall mechanics, and treatment interventions in a way that is often not feasible through experimental methods alone. They have the power to predict the outcomes of a disease or disease treatment and the potential to be personalized to individual patients. However, they still present some limitations that highlight the need to continue experimental research. First, they require experimental validation to ensure their accuracy. Additionally, some biological processes and interactions might still be too complex to model. Finally, accurate modeling requires having detailed information of the mechanical and microstructural properties of the blood vessels, which vary across species, diseases, blood vessel types, and disease states, highlighting the need for continued experimental measurements.

PART V
Appendices

A

Overview of the acquisition parameters of the Phoenix Nanotom M

The different acquisition parameters that can be adapted with the Phoenix Nanotom M used in the frame of this thesis are the following:

- Geometry: the distance between the detector and the source (focus-detector distance or FDD) and the distance between the sample and the source (focus-object distance or FOD). Adjusting these parameters allows to select the magnification or the voxel size. The choice of geometry is a trade-off between field of view and X-ray flux.

- Tube voltage: the potential difference between the cathode and the anode or the speed of the electrons emitted, allowing to produce X-ray radiations with different energy spectra. The voltage has an impact on the material penetration capabilities. A higher voltage is used for denser materials.

- Tube current: the amount of electrons generated at the cathode defining the intensity of the X-ray spectrum or the X-ray flux.

- Exposure time: total time of exposition of the detector to the X-ray radiation. Higher exposure time increases the number of photons captured by the detector and increases the signal-to-noise ratio but also increases the acquisition time.
- Number of projections: determines how many projections are saved for each acquisition. It determines the sharpness of the images but when increased it also increases the acquisition time.
- Averaging: the number of images averaged at each position. It increases the total signal and reduces the noise on the images.
- Skip: the number of images that will be ignored after each sample rotation to allow sample stabilization.
- Fast scan mode: acquisition mode that allows continuous rotation of the sample and simultaneous image acquisition (averaging = 1 and skip = 0) allowing for very short acquisition times.

Bibliography

[1] Anatomy and Physiology (Boundless). *Chapter 17.2D: Systemic and Pulmonary Circulation*. Jan. 2023. URL: https://med.libretexts.org/Bookshelves/Anatomy_and_Physiology/Anatomy_and_Physiology_(Boundless)/17%3A_Cardiovascular_System%3A_The_Heart/17.2%3A_Circulation_and_Heart_Valves/17.2D%3A_Systemic_and_Pulmonary_Circulation.

[2] Christopher Ross Ethier and Craig A. Simmons. *Introductory biomechanics: from cells to organisms*. Cambridge University Press, 2013.

[3] *Creative Commons - Attribution 3.0 Unported - CC BY 3.0*. URL: https://creativecommons.org/licenses/by/3.0/.

[4] T. Christian Gasser, Ray W. Ogden, and Gerhard A. Holzapfel. "Hyperelastic modelling of arterial layers with distributed collagen fibre orientations". In: *Journal of the Royal Society Interface* 3 (6 Feb. 2006), pp. 15–35. ISSN: 17425662. DOI: 10.1098/rsif.2005.0073.

[5] Alkiviadis Tsamis, Jeffrey T. Krawiec, and David A. Vorp. "Elastin and collagen fibre microstructure of the human aorta in ageing and disease: A review". In: *Journal of the Royal Society Interface* 10 (83 2013). ISSN: 17425662. DOI: 10.1098/rsif.2012.1004.

[6] Johannes AG Rhodin. "Architecture of the vessel wall". In: *The cardiovascular system* (1980). URL: https://api.semanticscholar.org/CorpusID:83418505.

[7] Gerhard A Holzapfel et al. "Determination of layer-specific mechanical properties of human coronary arteries with nonatherosclerotic intimal thickening and related constitutive modeling Determination of layer-specific mechanical prop-erties of human coronary arteries with nonatherosclerotic intimal thickening and related con-

stitutive modeling". In: *Am J Physiol Heart Circ Physiol* 289 (2005), pp. 2048–2058. DOI: 10.1152/ajpheart.00934.2004.

[8] Ghassan Bkaily and Danielle Jacques. "Morphological and functional remodeling of vascular endothelium in cardiovascular diseases". In: *International Journal of Molecular Sciences* 24.3 (2023), p. 1998. DOI: 10.3390/ijms24031998.

[9] Ernesto Martínez-Martínez et al. "Oxidative stress and vascular damage in the context of obesity: The hidden guest". In: *Antioxidants* 10.3 (2021), p. 406. DOI: 10.3390/antiox10030406.

[10] *Creative Commons - Attribution 4.0 International - CC BY 4.0.* URL: https://creativecommons.org/licenses/by/4.0/.

[11] William D. Tucker; Yingyot Arora; Kunal Mahajan. *Anatomy, Blood Vessels*. StatPearls Publishing, 2021, pp. 1–23. ISBN: 2013206534. URL: https://www.ncbi.nlm.nih.gov/books/NBK470401/.

[12] World Healthy Organization. *Cardiovascular diseases (cvds)*. June 2021. URL: https://www.who.int/news-room/fact-sheets/detail/cardiovascular-diseases-(cvds).

[13] Jialal I. Pahwa R. *Atherosclerosis*. Jan. 2023. URL: https://www.ncbi.nlm.nih.gov/books/NBK507799/.

[14] Christopher McCormick. "Overview of cardiovascular stent designs". In: *Functionalised cardiovascular stents*. Elsevier, 2018, pp. 3–26. DOI: 10.1016/B978-0-08-100496-8.00001-9.

[15] Rupert Bauersachs et al. "Burden of Coronary Artery Disease and Peripheral Artery Disease: A Literature Review". In: *Cardiovascular Therapeutics* 2019 (2019). ISSN: 17555922. DOI: 10.1155/2019/8295054.

[16] Salim S Virani et al. "Heart disease and stroke statistics—2020 update: a report from the American Heart Association". In: *Circulation* 141.9 (2020), e139–e596. DOI: 10.1161/CIR.0000000000000757.

[17] Encyclopaedia Britannica. *Atherosclerosis*. URL: https://www.britannica.com/science/atherosclerosis.

[18] Hahn C. and Schwartz M. A. "Mechanotransduction in vascular physiology and atherogenesis". In: *Nature Reviews Molecular Cell Biology* 10 (1 Jan. 2009), pp. 53–62. ISSN: 14710072. DOI: 10.1038/nrm2596.

[19] Aldons J. Lusis. "Atherosclerosis". In: *Nature* 407 (6801 Sept. 2000), pp. 233–241. ISSN: 00280836. DOI: 10.1038/35025203.

[20] Linda L Demer and Yin Tintut. "Vascular calcification: pathobiology of a multifaceted disease". In: *Circulation* 117.22 (2008), pp. 2938–2948. DOI: 10.1161/CIRCULATIONAHA.107.743161.

[21] Hiroyuki Jinnouchi et al. "Fully bioresorbable vascular scaffolds: lessons learned and future directions". In: *Nature Reviews Cardiology* 16 (5 May 2019), pp. 286–304. ISSN: 17595010. DOI: 10.1038/s41569-018-0124-7.

[22] Peter Libby et al. "Atherosclerosis". In: *Nature Reviews Disease Primers* 5 (1 Dec. 2019). ISSN: 2056676X. DOI: 10.1038/s41572-019-0106-z.

[23] E.A.V. Rocha. "Fifty years of coronary artery bypass graft surgery". In: *Brazilian journal of cardiovascular surgery* 32 (2017), pp. II–III. DOI: 10.21470/1678-9741-2017-0104.

[24] Joao S. Soares et al. "Engineered tissue vascular grafts: Are we there yet?" In: *Applications in Engineering Science* 12 (Dec. 2022). ISSN: 26664968. DOI: 10.1016/j.apples.2022.100114.

[25] David Durán-Rey et al. "Systematic review of tissue-engineered vascular grafts". In: *Frontiers in bioengineering and biotechnology* 9 (2021), p. 771400. DOI: 10.3389/fbioe.2021.771400.

[26] A. Tiwari et al. "Improving the patency of vascular bypass grafts: The role of suture materials and surgical techniques on reducing anastomotic compliance mismatch". In: *European Journal of Vascular and Endovascular Surgery* 25 (4 2003), pp. 287–295. ISSN: 10785884. DOI: 10.1053/ejvs.2002.1810.

[27] Torrey Schmidt and J Dawn Abbott. "Coronary stents: history, design, and construction". In: *Journal of clinical medicine* 7.6 (2018), p. 126. DOI: 10.3390/jcm7060126.

[28] Natalia Beshchasna et al. "Surface evaluation of titanium oxynitride coatings used for developing layered cardiovascular stents". In: *Materials Science and Engineering: C* 99 (2019), pp. 405–416. DOI: 10.1016/j.msec.2019.01.131.

[29] Setareh Borhani et al. "Cardiovascular stents: overview, evolution, and next generation". In: *Progress in biomaterials* 7 (2018), pp. 175–205. DOI: 10.1007/s40204-018-0097-y.

[30] Crispin B Weinberg and Eugene Bell. "A blood vessel model constructed from collagen and cultured vascular cells". In: *Science* 231.4736 (1986), pp. 397–400. DOI: 10.1126/science.2934816.

[31] William G. Chang and Laura E. Niklason. "A short discourse on vascular tissue engineering". In: *npj Regenerative Medicine* 2 (1 Mar. 2017). DOI: 10.1038/s41536-017-0011-6.

[32] Liesbet Geris et al. *Computational modeling in tissue engineering*. Springer, 2013. DOI: 10.1007/978-3-642-32563-2. URL: https://link.springer.com/10.1007/978-3-642-32563-2.

[33] Shelley D Rawson et al. "X-ray computed tomography in life sciences". In: *BMC Biol.* 18.1 (2020), p. 21. ISSN: 1741-7007. DOI: 10.1186/s12915-020-0753-2.

[34] Brian D Metscher. "MicroCT for comparative morphology: simple staining methods allow high-contrast 3D imaging of diverse non-mineralized animal tissues". In: *BMC Physiol.* 9.1 (2009), p. 11. ISSN: 1472-6793. DOI: 10.1186/1472-6793-9-11. URL: https://doi.org/10.1186/1472-6793-9-11.

[35] Laurene Quenot, Sylvain Bohic, and Emmanuel Brun. "X-ray Phase Contrast Imaging from Synchrotron to Conventional Sources: A Review of the Existing Techniques for Biological Applications". In: *Appl. Sci.* 12.19 (2022). ISSN: 20763417. DOI: 10.3390/app12199539.

[36] Horst Detlef Litzlbauer et al. "Three-dimensional imaging and morphometric analysis of alveolar tissue from microfocal X-ray-computed tomography". In: *Am. J. Physiol. Cell. Mol. Physiol.* 291.3 (2006), pp. L535–L545. DOI: 10.1152/ajplung.00088.2005. URL: https://doi.org/10.1152/ajplung.00088.2005.

[37] John T Johnson et al. "Virtual Histology of Transgenic Mouse Embryos for High-Throughput Phenotyping". In: *PLOS Genet.* 2.4 (2006), pp. 1–7. DOI: 10.1371/journal.pgen.0020061. URL: https://doi.org/10.1371/journal.pgen.0020061.

[38] Sébastien De Bournonville, Sarah Vangrunderbeeck, and Greet Kerckhofs. "Contrast-enhanced microCT for virtual 3D anatomical pathology of biological tissues: A literature review". In: *Contrast Media Mol. Imaging* 2019 (2019). ISSN: 15554317. DOI: 10.1155/2019/8617406.

[39] *Eurostat, Cardiovascular diseases statistics*. 2022. URL: https://ec.europa.eu/eurostat/statistics-explained/index.php?title=Cardiovascular_diseases_statistics (visited on 05/16/2023).

[40] Helen Dolk, Maria Loane, and Ester Garne. "Congenital heart defects in Europe: Prevalence and perinatal mortality, 2000 to 2005". In: *Circulation* 123.8 (2011), pp. 841–849. ISSN: 00097322. DOI: 10.1161/CIRCULATIONAHA.110.958405.

[41] Geoffrey Huntley, Jeremy Thaden, and Vuyisile Nkomo. "Epidemiology of heart valve disease". In: *Princ. Hear. Valve Eng.* Jan. 2019, pp. 41–62. ISBN: 9780128146613. DOI: 10.1016/B978-0-12-814661-3.00003-4.

[42] Júlia López-Guimet et al. "MicroCT imaging reveals differential 3D micro-scale remodelling of the murine aorta in ageing and marfan syndrome". In: *Theranostics* 8.21 (2018), pp. 6038–6052. ISSN: 18387640. DOI: 10.7150/thno.26598.

[43] Josef Ehling et al. "Quantitative micro-computed tomography imaging of vascular dysfunction in progressive kidney diseases". In: *J. Am. Soc. Nephrol.* 27.2 (2016), pp. 520–532. ISSN: 15333450. DOI: 10.1681/ASN.2015020204.

[44] M. Clara Ortiz et al. "Microcomputed tomography of kidneys following chronic bile duct ligation". In: *Kidney Int.* 58.4 (2000), pp. 1632–1640. ISSN: 00852538. DOI: 10.1111/j.1523-1755.2000.00324.x.

[45] Michael D Bentley et al. "The Use of Microcomputed Tomography to Study Microvasculature in Small Rodents". In: *Am. J. Physiol. Regul. Integr. Comp. Physiol.* (2002). DOI: 10.1152/ajpregu.00560.2001.

[46] Daniel S. Perrien et al. "Novel methods for microCT-based analyses of vasculature in the renal cortex reveal a loss of perfusable arterioles and glomeruli in eNOS-/- mice". In: *BMC Nephrol.* 17.1 (2016), pp. 1–10. ISSN: 14712369. DOI: 10.1186/s12882-016-0235-5.

[47] Rajkumar Savai et al. "Evaluation of angiogenesis using micro-computed tomography in a xenograft mouse model of lung cancer". In: *Neoplasia* 11.1 (2009), pp. 48–56. ISSN: 14765586. DOI: 10.1593/neo.81036.

[48] Hervé Nyangoga et al. "Three-dimensional characterization of the vascular bed in bone metastasis of the rat by microcomputed tomography (MicroCT)". In: *PLoS One* 6.3 (2011), pp. 1–8. ISSN: 19326203. DOI: 10.1371/journal.pone.0017336.

[49] Rosalind Pratt et al. "Imaging the human placental microcirculation with micro-focus computed tomography: Optimisation of tissue preparation and image acquisition". In: *Placenta* 60 (2017), pp. 36–39. ISSN: 15323102. DOI: 10.1016/j.placenta.2017.09.013. URL: https://doi.org/10.1016/j.placenta.2017.09.013.

[50] Rameez Rehman, Varun S Yelamanchili, and Amgad N Makaryus. *Cardiac Imaging*. StatPearls Publishing, Treasure Island (FL), 2019. URL: http://europepmc.org/books/NBK448128.

[51] Guido Pieles et al. "μMRI-HREM pipeline for high-throughput, high-resolution phenotyping of murine embryos". In: *J. Anat.* 211.1 (2007), pp. 132–137. ISSN: 00218782. DOI: 10.1111/j.1469-7580.2007.00746.x.

[52] Ko Chin Chen et al. "High-Definition Heart Visualization Using Micro-CT Scanning on Experimental Rats". In: *J. Clin. Exp. Cardiolog.* 09.09 (2018). DOI: 10.4172/2155-9880.1000606.

[53] Pawel Kleczek, Joanna Jaworek-Korjakowska, and Marek Gorgon. "A novel method for tissue segmentation in high-resolution H&E-stained histopathological whole-slide images". In: *Comput. Med. Imaging Graph.* 79 (2020), p. 101686. ISSN: 18790771. DOI: 10.1016/j.compmedimag.2019.101686. URL: https://doi.org/10.1016/j.compmedimag.2019.101686.

[54] Maria Victoria Gómez-Gaviro et al. "Biomedical Applications of Tissue Clearing and Three-Dimensional Imaging in Health and Disease". In: *iScience* 23.8 (2020), p. 101432. ISSN: 2589-0042. DOI: https://doi.org/10.1016/j.isci.2020.101432. URL: https://www.sciencedirect.com/science/article/pii/S2589004220306222.

[55] Shailja Chatterjee. "Artefacts in histopathology". eng. In: *J. Oral Maxillofac. Pathol.* 18.Suppl 1 (Sept. 2014), S111–S116. ISSN: 0973-029X. DOI: 10.4103/0973-029X.141346. URL: https://pubmed.ncbi.nlm.nih.gov/25364159%20https://www.ncbi.nlm.nih.gov/pmc/articles/PMC4211218/.

[56] Syed Ahmed Taqi et al. "A review of artifacts in histopathology." eng. In: *J. Oral Maxillofac. Pathol.* 22.2 (2018), p. 279. ISSN: 0973-029X (Print). DOI: 10.4103/jomfp.JOMFP_125_15.

[57] Stefan H Geyer and Wolfgang J Weninger. "High-Resolution Episcopic Microscopy (HREM): Looking Back on 13 Years of Successful Generation of Digital Volume Data of Organic Material for 3D Visualisation and 3D Display". In: *Appl. Sci.* 9.18 (2019). ISSN: 2076-3417. DOI: 10.3390/app9183826. URL: https://www.mdpi.com/2076-3417/9/18/3826.

[58] Claudio Vinegoni et al. "Fluorescence microscopy tensor imaging representations for large-scale dataset analysis". In: *Sci. Rep.* 10.1 (2020), pp. 1–15. ISSN: 20452322. DOI: 10.1038/s41598-020-62233-2.

[59] Craig J. Goergen et al. "Microstructural characterization of myocardial infarction with optical coherence tractography and two-photon microscopy". In: *Physiol. Rep.* 4.18 (2016), pp. 1–10. ISSN: 2051817X. DOI: 10.14814/phy2.12894.

[60] Yu Wei Chiu et al. "Applying harmonic optical microscopy for spatial alignment of atrial collagen fibers". In: *PLoS One* 5.11 (2010), pp. 1–9. ISSN: 19326203. DOI: 10.1371/journal.pone.0013917.

[61] G. Allan Johnson et al. "Magnetic resonance histology for morphologic phenotyping". In: *J. Magn. Reson. Imaging* 16.4 (2002), pp. 423–429. ISSN: 10531807. DOI: 10.1002/jmri.10175.

[62] J. Michael Tyszka, Scott E. Fraser, and Russell E. Jacobs. "Magnetic resonance microscopy: Recent advances and applications". In: *Curr. Opin. Biotechnol.* 16 (2005), pp. 93–99. ISSN: 09581669. DOI: 10.1016/j.copbio.2004.11.004.

[63] Bastiaan Driehuys et al. "Small animal imaging with magnetic resonance microscopy". In: *ILAR J.* 53.1 (2008), pp. 35–53. ISSN: 10842020. DOI: 10.1093/ilar.49.1.35.

[64] Sonia Nielles-Vallespin et al. "Assessment of Myocardial Microstructural Dynamics by In Vivo Diffusion Tensor Cardiac Magnetic Resonance". In: *J. Am. Coll. Cardiol.* 69.6 (2017), pp. 661–676. ISSN: 15583597. DOI: 10.1016/j.jacc.2016.11.051.

[65] Olivier Bernus et al. “Comparison of diffusion tensor imaging by cardiovascular magnetic resonance and gadolinium enhanced 3D image intensity approaches to investigation of structural anisotropy in explanted rat hearts”. In: *J. Cardiovasc. Magn. Reson.* 17.1 (2015), pp. 1–27. ISSN: 1532429X. DOI: 10.1186/s12968-015-0129-x.

[66] Wen Li et al. “Ex vivo diffusion tensor MRI reflects microscopic structural remodeling associated with aging and disease progression in normal and cardiomyopathic Syrian hamsters”. eng. In: *NMR Biomed.* 22.8 (Oct. 2009), pp. 819–825. ISSN: 1099-1492. DOI: 10.1002/nbm.1394. URL: https://pubmed.ncbi.nlm.nih.gov/19434665%20https://www.ncbi.nlm.nih.gov/pmc/articles/PMC2849973/.

[67] Ioannis Papantoniou et al. “Three-dimensional characterization of tissue-engineered constructs by contrast-enhanced nanofocus computed tomography”. In: *Tissue Eng. - Part C Methods* 20.3 (Mar. 2014), pp. 177–187. ISSN: 19373392. DOI: 10.1089/ten.tec.2013.0041.

[68] Hector Dejea et al. “Comprehensive Analysis of Animal Models of Cardiovascular Disease using Multiscale X-Ray Phase Contrast Tomography”. In: *Sci. Rep.* 9.1 (2019), pp. 1–12. ISSN: 20452322. DOI: 10.1038/s41598-019-43407-z.

[69] Gerlinde Logghe et al. “Propagation-based phase-contrast synchrotron imaging of aortic dissection in mice: From individual elastic lamella to 3D analysis”. In: *Sci. Rep.* 8.1 (2018), pp. 1–11. ISSN: 20452322. DOI: 10.1038/s41598-018-20673-x. URL: http://dx.doi.org/10.1038/s41598-018-20673-x.

[70] P. Cloetens et al. “Observation of microstructure and damage in materials by phase sensitive radiography and tomography”. In: *J. Appl. Phys.* 81.9 (1997), pp. 5878–5886. ISSN: 00218979. DOI: 10.1063/1.364374.

[71] Peter Cloetens et al. “Quantitative phase tomography of Arabidopsis seeds reveals intercellular void network”. In: *Proc. Natl. Acad. Sci. U. S. A.* 103.39 (2006), pp. 14626–14630. ISSN: 00278424. DOI: 10.1073/pnas.0603490103.

[72] J Baruchel, J Y Buffiere, and E Maire. *X-ray tomography in material science*. Paris (France): Hermes science publications, 2000. ISBN: 2-7462-0115-1. URL: https://inis.iaea.org/search/search.aspx?orig_q=RN:31031064.

[73] A. C. Langheinrich et al. "Quantitative 3D Micro-CT Imaging of the Human Feto-placental Vasculature in Intrauterine Growth Restriction". In: *Placenta* 29.11 (2008), pp. 937–941. ISSN: 01434004. DOI: 10.1016/j.placenta.2008.08.017.

[74] S. Cortell. "Silicone rubber for renal tubular injection." In: *J. Appl. Physiol.* 26.1 (1969), pp. 158–159. ISSN: 00218987. DOI: 10.1152/jappl.1969.26.1.158.

[75] Craig L. Duvall et al. "Quantitative microcomputed tomography analysis of collateral vessel development after ischemic injury". In: *Am. J. Physiol. - Hear. Circ. Physiol.* 287.1 56-1 (2004). ISSN: 03636135. DOI: 10.1152/ajpheart.00928.2003.

[76] Bailiang Chen et al. "Ex vivo magnetic resonance angiography to explore placental vascular anatomy". In: *Placenta* 58 (2017), pp. 40–45. ISSN: 15323102. DOI: 10.1016/j.placenta.2017.08.002. URL: https://doi.org/10.1016/j.placenta.2017.08.002.

[77] Karl Degenhardt et al. "Rapid 3D phenotyping of cardiovascular development in mouse embryos by micro-CT with iodine staining". In: *Circ. Cardiovasc. Imaging* 3.3 (2010), pp. 314–322. ISSN: 19419651. DOI: 10.1161/CIRCIMAGING.109.918482.

[78] Mario Gössl, Mair Zamir, and Erik L. Ritman. "Vasa vasorum growth in the coronary arteries of newborn pigs". In: *Anat. Embryol. (Berl).* 208.5 (2004), pp. 351–357. ISSN: 03402061. DOI: 10.1007/s00429-004-0400-7.

[79] M. Y. Rennie et al. "3D Visualisation and Quantification by Microcomputed Tomography of Late Gestational Changes in the Arterial and Venous Feto-Placental Vasculature of the Mouse". In: *Placenta* 28.8-9 (2007), pp. 833–840. ISSN: 01434004. DOI: 10.1016/j.placenta.2006.12.005.

[80] Bernard Roche et al. "Structure and quantification of microvascularisation within mouse long bones: What and how should we measure?" In: *Bone* 50.1 (2012), pp. 390–399. ISSN: 87563282. DOI: 10.1016/j.bone.2011.09.051. URL: http://dx.doi.org/10.1016/j.bone.2011.09.051.

[81] Sergio X. Vasquez et al. "Optimization of microCT imaging and blood vessel diameter quantitation of preclinical specimen vasculature with radiopaque polymer injection medium". In: *PLoS One* 6.4 (2011), pp. 2–7. ISSN: 19326203. DOI: 10.1371/journal.pone.0019099.

[82] Sahar Ghanavati et al. "A perfusion procedure for imaging of the mouse cerebral vasculature by X-ray micro-CT". In: *J. Neurosci. Methods* 221 (2014), pp. 70–77. ISSN: 1872678X. DOI: 10.1016/j.jneumeth.2013.09.002. URL: http://dx.doi.org/10.1016/j.jneumeth.2013.09.002.

[83] S Jeson Sangaralingham et al. "Cardiac Micro–Computed Tomography Imaging of the Aging Coronary Vasculature". In: *Circ. Cardiovasc. Imaging* 5.4 (2012), pp. 518–524. DOI: 10.1161/CIRCIMAGING.112.973057. URL: https://www.ahajournals.org/doi/abs/10.1161/CIRCIMAGING.112.973057.

[84] Jonathan T Butcher et al. "Quantitative volumetric analysis of cardiac morphogenesis assessed through micro-computed tomography". In: *Dev. Dyn.* 236.3 (2007), pp. 802–809. DOI: https://doi.org/10.1002/dvdy.20962. URL: https://anatomypubs.onlinelibrary.wiley.com/doi/abs/10.1002/dvdy.20962.

[85] Ruslan Hlushchuk, David Haberthür, and Valentin Djonov. "Ex vivo microangioCT: Advances in microvascular imaging". In: *Vascul. Pharmacol.* 112 (2019), pp. 2–7. ISSN: 18793649. DOI: 10.1016/j.vph.2018.09.003.

[86] Laura Schaad et al. "Correlative Imaging of the Murine Hind Limb Vasculature and Muscle Tissue by MicroCT and Light Microscopy". In: *Sci. Rep.* 7.October 2016 (2017), pp. 1–12. ISSN: 20452322. DOI: 10.1038/srep41842. URL: http://dx.doi.org/10.1038/srep41842.

[87] Ruslan Hlushchuk et al. "Innovative high-resolution microCT imaging of animal brain vasculature". In: *Brain Struct. Funct.* 225.9 (2020), pp. 2885–2895. ISSN: 18632661. DOI: 10.1007/s00429-020-02158-8. URL: https://doi.org/10.1007/s00429-020-02158-8.

[88] P. Blery et al. "Vascular imaging with contrast agent in hard and soft tissues using microcomputed-tomography". In: *J. Microsc.* 262.1 (2016), pp. 40–49. ISSN: 13652818. DOI: 10.1111/jmi.12339.

[89] Yupu Deng et al. "Optimizing imaging of the rat pulmonary microvasculature by micro-computed tomography". In: *Pulm. Circ.* 9.4 (2019). ISSN: 20458940. DOI: 10.1177/2045894019883613.

[90] Xing Qiu et al. "A method to quantify and visualize femoral head intraosseous arteries by micro-CT". In: *J. Anat.* 229.2 (2016), pp. 326–333. ISSN: 14697580. DOI: 10.1111/joa.12475.

[91] Oleg V Aslanidi et al. "Application of Micro-Computed Tomography With Iodine Staining to Cardiac Imaging, Segmentation, and Computational Model Development". In: *IEEE Trans. Med. Imaging* 32.1 (2013), pp. 8–17. DOI: 10.1109/TMI.2012.2209183.

[92] Robert S Stephenson et al. "Contrast enhanced micro-computed tomography resolves the 3-dimensional morphology of the cardiac conduction system in mammalian hearts." eng. In: *PLoS One* 7.4 (2012), e35299. ISSN: 1932-6203 (Electronic). DOI: 10.1371/journal.pone.0035299.

[93] Robert S. Stephenson et al. "High resolution 3-Dimensional imaging of the human cardiac conduction system from microanatomy to mathematical modeling". In: *Sci. Rep.* 7.1 (2017), pp. 1–13. ISSN: 20452322. DOI: 10.1038/s41598-017-07694-8.

[94] Robert S. Stephenson et al. "Morphological substrates for atrial arrhythmogenesis in a heart with atrioventricular septal defect". In: *Front. Physiol.* 9.AUG (2018), pp. 1–12. ISSN: 1664042X. DOI: 10.3389/fphys.2018.01071.

[95] Ian C Simcock et al. "Investigation of optimal sample preparation conditions with potassium triiodide and optimal imaging settings for microfocus computed tomography of excised cat hearts". In: *Am. J. Vet. Res.* 81.4 (2020), pp. 326–333. DOI: 10.2460/ajvr.81.4.326. URL: https://avmajournals.avma.org/view/journals/ajvr/81/4/ajvr.81.4.326.xml.

[96] Camilla Sandrini et al. "Accuracy of Micro-Computed Tomography in Post-mortem Evaluation of Fetal Congenital Heart Disease. Comparison Between Post-mortem Micro-CT and Conventional Autopsy." In: *Front. Pediatr.* 7 (2019). ISSN: 2296-2360. DOI: 10.3389/fped.2019.00092. URL: https://www.frontiersin.org/articles/10.3389/fped.2019.00092.

[97] Madeline Midgett, Kent Thornburg, and Sandra Rugonyi. "Blood flow patterns underlie developmental heart defects". In: *Am. J. Physiol. Circ. Physiol.* 312.3 (2017), H632–H642. DOI: 10.1152/ajpheart.00641.2016. URL: https://doi.org/10.1152/ajpheart.00641.2016.

[98] Samer S Merchant et al. "Micro-Computed Tomography for the Quantitative 3-Dimensional Assessment of the Compact Myocardium in the Mouse Embryo." eng. In: *Circ. J.* 80.8 (July 2016), pp. 1795–1803. ISSN: 1347-4820 (Electronic). DOI: 10.1253/circj.CJ-16-0180.

[99] Mathieu Nierenberger et al. "Assessing the three-dimensional collagen network in soft tissues using contrast agents and high resolution micro-CT: Application to porcine iliac veins". In: *Comptes Rendus - Biol.* 338.7 (2015), pp. 425–433. ISSN: 17683238. DOI: 10.1016/j.crvi.2015.04.009.

[100] Paula Vickerton, Jonathan Jarvis, and Nathan Jeffery. "Concentration-dependent specimen shrinkage in iodine-enhanced microCT". In: *J. Anat.* 223.2 (2013), pp. 185–193. DOI: https://doi.org/10.1111/joa.12068. URL: https://onlinelibrary.wiley.com/doi/abs/10.1111/joa.12068.

[101] Jose Novo Matos et al. "Micro-computed tomography (micro-CT) for the assessment of myocardial disarray, fibrosis and ventricular mass in a feline model of hypertrophic cardiomyopathy." eng. In: *Sci. Rep.* 10.1 (Nov. 2020), p. 20169. ISSN: 2045-2322 (Electronic). DOI: 10.1038/s41598-020-76809-5.

[102] C M Lombardi et al. "Postmortem microcomputed tomography (micro-CT) of small fetuses and hearts". In: *Ultrasound Obstet. Gynecol.* 44.5 (2014), pp. 600–609. DOI: https://doi.org/10.1002/uog.13330. URL: https://obgyn.onlinelibrary.wiley.com/doi/abs/10.1002/uog.13330.

[103] Andrew J Kim et al. "Microcomputed tomography provides high accuracy congenital heart disease diagnosis in neonatal and fetal mice". eng. In: *Circ. Cardiovasc. Imaging* 6.4 (July 2013), pp. 551–559. ISSN: 1942-0080. DOI: 10.1161/CIRCIMAGING.113.000279. URL: https://pubmed.ncbi.nlm.nih.gov/23759365%20https://www.ncbi.nlm.nih.gov/pmc/articles/PMC3908688/.

[104] J C Hutchinson et al. “Clinical utility of postmortem microcomputed tomography of the fetal heart: diagnostic imaging vs macroscopic dissection”. In: *Ultrasound Obstet. Gynecol.* 47.1 (2016), pp. 58–64. DOI: https://doi.org/10.1002/uog.15764. URL: https://obgyn.onlinelibrary.wiley.com/doi/abs/10.1002/uog.15764.

[105] P Joy Dunmore-Buyze et al. “Three-dimensional imaging of the mouse heart and vasculature using micro-CT and whole-body perfusion of iodine or phosphotungstic acid”. In: *Contrast Media Mol. Imaging* 9.5 (2014), pp. 383–390. DOI: https://doi.org/10.1002/cmmi.1588. URL: https://onlinelibrary.wiley.com/doi/abs/10.1002/cmmi.1588.

[106] Ata Doost et al. “Micro-CT scan with virtual dissection of left ventricle is a non-destructive, reproducible alternative to dissection and weighing for left ventricular size.” eng. In: *Sci. Rep.* 10.1 (Aug. 2020), p. 13853. ISSN: 2045-2322 (Electronic). DOI: 10.1038/s41598-020-70734-3.

[107] Timothy D Butters et al. “Optimal Iodine Staining of Cardiac Tissue for X-Ray Computed Tomography”. In: *PLoS One* 9.8 (2014), pp. 1–6. DOI: 10.1371/journal.pone.0105552. URL: https://doi.org/10.1371/journal.pone.0105552.

[108] Graham Rykiel et al. “Multiscale cardiac imaging spanning the whole heart and its internal cellular architecture in a small animal model”. In: *Elife* 9 (Oct. 2020). Ed. by Didier Y R Stainier, Brad Keller, and Karthik Kodigepalli, e58138. ISSN: 2050-084X. DOI: 10.7554/eLife.58138. URL: https://doi.org/10.7554/eLife.58138.

[109] Vinay M. Pai et al. “Coronary artery wall imaging in mice using osmium tetroxide and micro-computed tomography (micro-CT)”. In: *J. Anat.* 220.5 (2012), pp. 514–524. ISSN: 00218782. DOI: 10.1111/j.1469-7580.2012.01483.x.

[110] Clémentine Helfenstein-Didier et al. “Tensile rupture of medial arterial tissue studied by X-ray micro-tomography on stained samples”. In: *J. Mech. Behav. Biomed. Mater.* 78.July 2017 (2018), pp. 362–368. ISSN: 18780180. DOI: 10.1016/j.jmbbm.2017.11.032.

[111] J Brunet et al. “A Novel Method for In Vitro 3D Imaging of Dissecting Pressurized Arterial Segments Using X-Ray Microtomography”. In: *Exp. Mech.* 61.1 (2021), pp. 147–157. ISSN: 1741-2765. DOI:

10.1007/s11340-020-00645-x. URL: https://doi.org/10.1007/s11340-020-00645-x.

[112] P. Joy Dunmore-Buyze et al. "3D vessel-wall virtual histology of whole-body perfused mice using a novel heavy element stain". In: *Sci. Rep.* 9.1 (2019), pp. 1–10. ISSN: 20452322. DOI: 10.1038/s41598-018-36905-z. URL: http://dx.doi.org/10.1038/s41598-018-36905-z.

[113] Christian Dullin et al. "μCT of ex-vivo stained mouse hearts and embryos enables a precise match between 3D virtual histology, classical histology and immunochemistry". In: *PLoS One* 12.2 (2017). ISSN: 19326203. DOI: 10.1371/journal.pone.0170597.

[114] Katrien De Clercq et al. "High-resolution contrast-enhanced microCT reveals the true three-dimensional morphology of the murine placenta". In: *Proc. Natl. Acad. Sci.* 116.28 (2019), pp. 13927–13936. DOI: 10.1073/pnas.1902688116. URL: https://www.pnas.org/doi/abs/10.1073/pnas.1902688116.

[115] Greet Kerckhofs et al. "Simultaneous three-dimensional visualization of mineralized and soft skeletal tissues by a novel microCT contrast agent with polyoxometalate structure". In: *Biomaterials* 159 (2018), pp. 1–12. ISSN: 18785905. DOI: 10.1016/j.biomaterials.2017.12.016.

[116] Sébastien de Bournonville et al. "Exploring polyoxometalates as non-destructive staining agents for contrast-enhanced microfocus computed tomography of biological tissues". In: *Acta Biomater.* 105 (2020), pp. 253–262. ISSN: 18787568. DOI: 10.1016/j.actbio.2020.01.038. URL: https://doi.org/10.1016/j.actbio.2020.01.038.

[117] Anna Gonzalez-Tendero et al. "Whole heart detailed and quantitative anatomy, myofibre structure and vasculature from X-ray phase-contrast synchrotron radiation-based micro computed tomography." eng. In: *Eur. Heart J. Cardiovasc. Imaging* 18.7 (July 2017), pp. 732–741. ISSN: 2047-2412 (Electronic). DOI: 10.1093/ehjci/jew314.

[118] Gen Shinohara et al. "Three Dimensional Visualization of Human Cardiac Conduction Tissue in Whole Heart Specimens by High-Resolution Phase-Contrast CT Imaging Using Synchrotron Radiation". In: *World J. Pediatr. Congenit. Heart Surg.* 7.6 (2016), pp. 700–705. ISSN: 2150136X. DOI: 10.1177/2150135116675844.

[119] Yukihiro Kaneko et al. "Intact Imaging of Human Heart Structure Using X-ray Phase-Contrast Tomography." eng. In: *Pediatr. Cardiol.* 38.2 (Feb. 2017), pp. 390–393. ISSN: 1432-1971 (Electronic). DOI: 10.1007/s00246-016-1527-z.

[120] Patricia Garcia-Canadilla et al. "Complex Congenital Heart Disease Associated With Disordered Myocardial Architecture in a Midtrimester Human Fetus". In: *Circ. Cardiovasc. Imaging* 11.10 (2018), e007753. ISSN: 19420080. DOI: 10.1161/CIRCIMAGING.118.007753.

[121] Y Dawood et al. "Reducing soft-tissue shrinkage artefacts caused by staining with Lugol's solution". In: *Sci. Rep.* 11.1 (2021), p. 19781. ISSN: 2045-2322. DOI: 10.1038/s41598-021-99202-2. URL: https://doi.org/10.1038/s41598-021-99202-2.

[122] Hector Dejea et al. "Cardiac multi-scale investigation of the right and left ventricle ex vivo: a review". In: *Cardiovasc. Diagn. Ther.* 10.5 (2020), pp. 1701–1717. ISSN: 22233660. DOI: 10.21037/cdt-20-269.

[123] Bernhard Zach et al. "Automated texture analysis and determination of fibre orientation of heart tissue: A morphometric study". In: *PLoS One* 11.8 (2016), pp. 1–17. ISSN: 19326203. DOI: 10.1371/journal.pone.0160735.

[124] Iulia Mirea et al. *Very High-Resolution Imaging of Post-Mortem Human Cardiac Tissue Using X-Ray Phase Contrast Tomography*. June 2015. DOI: 10.1007/978-3-319-20309-6_20.

[125] Marius Reichardt et al. "Fiber orientation in a whole mouse heart reconstructed by laboratory phase-contrast micro-CT". In: *J. Med. Imaging* 7.2 (2020), p. 23501. DOI: 10.1117/1.JMI.7.2.023501. URL: https://doi.org/10.1117/1.JMI.7.2.023501.

[126] Marius Reichardt et al. "Multi-scale X-ray phase-contrast tomography of murine heart tissue". In: *Biomed. Opt. Express* 11.5 (2020), pp. 2633–2651. DOI: 10.1364/BOE.386576. URL: https://opg.optica.org/boe/abstract.cfm?URI=boe-11-5-2633.

[127] Françoi Varray et al. "High Resolution Extraction of Local Human Cardiac Fibre Orientations". In: *Funct. Imaging Model. Hear. Vol. 7945*. Ed. by Ourselin, S. and Rueckert, D. and N. Smith. Springer, Berlin, Heidelberg, June 2013, pp. 150–157. ISBN: 978-3-642-38898-9. DOI: 10.1007/978-3-642-38899-6_18.

[128] François Varray et al. “Extraction of the 3D local orientation of myocytes in human cardiac tissue using X-ray phase-contrast microtomography and multi-scale analysis”. In: *Med. Image Anal.* 38 (2017), pp. 117–132. ISSN: 1361-8415. DOI: https://doi.org/10.1016/j.media.2017.02.006. URL: https://www.sciencedirect.com/science/article/pii/S1361841517300245.

[129] Shunli Wang et al. “Investigating the 3D Local Myocytes Arrangement in the Human LV Mid-Wall with the Transverse Angle”. In: *Funct. Imaging Model. Hear.* Ed. by Yves Coudière et al. Cham: Springer International Publishing, 2019, pp. 208–216. ISBN: 978-3-030-21949-9. DOI: 10.1007/978-3-030-21949-9_23.

[130] V Baličević et al. “Assessment of Myofiber Orientation in High Resolution Phase-Contrast CT Images”. In: *Funct. Imaging Model. Hear.* Ed. by Hans van Assen, Peter Bovendeerd, and Tammo Delhaas. Cham: Springer International Publishing, 2015, pp. 111–119. ISBN: 978-3-319-20309-6. DOI: 10.1007/978-3-319-20309-6_13.

[131] Natalia A Trayanova and Raimond Winslow. “Whole-Heart Modeling”. In: *Circ. Res.* 108.1 (2011), pp. 113–128. DOI: 10.1161/CIRCRESAHA.110.223610. URL: https://www.ahajournals.org/doi/abs/10.1161/CIRCRESAHA.110.223610.

[132] Fijoy Vadakkumpadan et al. “Image-based models of cardiac structure in health and disease”. In: *WIREs Syst. Biol. Med.* 2.4 (July 2010), pp. 489–506. ISSN: 1939-5094. DOI: https://doi.org/10.1002/wsbm.76. URL: https://doi.org/10.1002/wsbm.76.

[133] Nancy Coté et al. “Inflammation Is Associated with the Remodeling of Calcific Aortic Valve Disease”. In: *Inflammation* 36.3 (2013), pp. 573–581. ISSN: 1573-2576. DOI: 10.1007/s10753-012-9579-6. URL: https://doi.org/10.1007/s10753-012-9579-6.

[134] Sam Chitsaz et al. “Correlation of calcification on excised aortic valves by micro-computed tomography with severity of aortic stenosis”. In: *J. Heart Valve Dis.* 21.3 (2012), pp. 320–327. ISSN: 09668519.

[135] Sylwia Orzechowska et al. “Physicochemical and micro-tomographic characterization of inorganic deposits associated with aortic stenosis.” In: *J. Heart Valve Dis.* 23.1 (2014), pp. 40–47. ISSN: 09668519.

[136] Piotr Mazur et al. "Stenotic bicuspid and tricuspid aortic valves: Micro-computed tomography and biological indices of calcification". In: *Circ. J.* 81.7 (2017), pp. 1043–1050. ISSN: 13474820. DOI: 10.1253/circj.CJ-16-1166.

[137] Guillermo Solache-Berrocal et al. "Correlation of Micro-Computed Tomography Assessment of Valvular Mineralisation with Histopathological and Immunohistochemical Features of Calcific Aortic Valve Disease". In: *J. Clin. Med.* 9.1 (2019), p. 29. ISSN: 2077-0383. DOI: 10.3390/jcm9010029.

[138] Jamila Boulif et al. "Assessment of aortic valve calcium load by multidetector computed tomography. Anatomical validation, impact of scanner settings and incremental diagnostic value". In: *J. Cardiovasc. Comput. Tomogr.* 11.5 (2017), pp. 360–366. ISSN: 1934-5925. DOI: https://doi.org/10.1016/j.jcct.2017.07.004. URL: https://www.sciencedirect.com/science/article/pii/S1934592517301685.

[139] Eric L Pierce et al. "Novel Method to Track Soft Tissue Deformation by Micro-Computed Tomography: Application to the Mitral Valve". In: *Ann. Biomed. Eng.* 44.7 (2016), pp. 2273–2281. ISSN: 1573-9686. DOI: 10.1007/s10439-015-1499-9. URL: https://doi.org/10.1007/s10439-015-1499-9.

[140] Milan Toma et al. "High-resolution subject-specific mitral valve imaging and modeling: experimental and computational methods". In: *Biomech. Model. Mechanobiol.* 15.6 (2016), pp. 1619–1630. ISSN: 1617-7940. DOI: 10.1007/s10237-016-0786-1. URL: https://doi.org/10.1007/s10237-016-0786-1.

[141] Charles H Bloodworth et al. "Ex Vivo Methods for Informing Computational Models of the Mitral Valve". In: *Ann. Biomed. Eng.* 45.2 (2017), pp. 496–507. ISSN: 1573-9686. DOI: 10.1007/s10439-016-1734-z. URL: https://doi.org/10.1007/s10439-016-1734-z.

[142] S M Jorgensen, O Demirkaya, and E L Ritman. "Three-dimensional imaging of vasculature and parenchyma in intact rodent organs with X-ray micro-CT." eng. In: *Am. J. Physiol.* 275.3 (Sept. 1998), H1103–14. ISSN: 0002-9513 (Print). DOI: 10.1152/ajpheart.1998.275.3.H1103.

[143] Jeroen P.H.M. van den Wijngaard et al. "3D Imaging of vascular networks for biophysical modeling of perfusion distribution within the heart". In: *J. Biomech.* 46.2 (2013), pp. 229–239. ISSN: 00219290. DOI: 10.1016/j.jbiomech.2012.11.027. URL: http://dx.doi.org/10.1016/j.jbiomech.2012.11.027.

[144] Stefan Heinzer et al. "Hierarchical microimaging for multiscale analysis of large vascular networks". In: *NeuroImage* 32.2 (2006), pp. 626–636. ISSN: 1053-8119. DOI: https://doi.org/10.1016/j.neuroimage.2006.03.043. URL: https://www.sciencedirect.com/science/article/pii/S1053811906002345.

[145] Espen J. Walker et al. "Cerebrovascular casting of the adult mouse for 3D imaging and morphological analysis". In: *J. Vis. Exp.* 57 (2011). ISSN: 1940087X. DOI: 10.3791/2958.

[146] Yong Cao et al. "Three-dimensional imaging of microvasculature in the rat spinal cord following injury". In: *Sci. Rep.* 5 (2015), pp. 1–11. ISSN: 20452322. DOI: 10.1038/srep12643.

[147] Toluwalope O. Junaid et al. "Whole organ vascular casting and microCT examination of the human placental vascular tree reveals novel alterations associated with pregnancy disease". In: *Sci. Rep.* 7.1 (2017), pp. 1–10. ISSN: 20452322. DOI: 10.1038/s41598-017-04379-0.

[148] Ileana Giuvărăşteanu. "Scanning electron microscopy of vascular corrosion casts–standard method for studying microvessels." eng. In: *Rom. J. Morphol. Embryol. = Rev. Roum. Morphol. Embryol.* 48.3 (2007), pp. 257–261. ISSN: 1220-0522 (Print).

[149] Camilla Olianti et al. "3D imaging and morphometry of the heart capillary system in spontaneously hypertensive rats and normotensive controls". In: *Sci. Rep.* 10.1 (2020), pp. 1–9. ISSN: 20452322. DOI: 10.1038/s41598-020-71174-9. URL: https://doi.org/10.1038/s41598-020-71174-9.

[150] Lucy A. Walton et al. "Morphological characterisation of unstained and intact tissue micro-architecture by X-ray computed micro- and nano-tomography". In: *Sci. Rep.* 5.May (2015), pp. 1–14. ISSN: 20452322. DOI: 10.1038/srep10074.

[151] Donald Lloyd-Jones et al. "Heart Disease and Stroke Statistics—2010 Update". In: *Circulation* 121.7 (2010), e46–e215. DOI: 10.1161/CIRCULATIONAHA.109.192667. URL: https://www.ahajournals.org/doi/abs/10.1161/CIRCULATIONAHA.109.192667.

[152] Andrei A. Postnov et al. "Possibilities and limits of X-ray microtomography for in vivo and ex vivo detection of vascular calcifications". In: *Int. J. Cardiovasc. Imaging* 25.6 (2009), pp. 615–624. ISSN: 15695794. DOI: 10.1007/s10554-009-9459-9.

[153] Margaret N. Holme et al. "Complementary X-ray tomography techniques for histology-validated 3D imaging of soft and hard tissues using plaque-containing blood vessels as examples". In: *Nat. Protoc.* 9.6 (2014), pp. 1401–1415. ISSN: 17502799. DOI: 10.1038/nprot.2014.091.

[154] Hilary E. Barrett et al. "Characterising human atherosclerotic carotid plaque tissue composition and morphology using combined spectroscopic and imaging modalities". In: *Biomed. Eng. Online* 14.Suppl 1 (2015), S5. ISSN: 1475925X. DOI: 10.1186/1475-925X-14-S1-S5.

[155] Trevor S. Self et al. "Iodine-enhanced micro-computed tomography of atherosclerotic plaque morphology complements conventional histology". In: *Atherosclerosis* 313.September (2020), pp. 43–49. ISSN: 18791484. DOI: 10.1016/j.atherosclerosis.2020.09.012. URL: https://doi.org/10.1016/j.atherosclerosis.2020.09.012.

[156] Samantha J. Borland et al. "X-ray micro-computed tomography: An emerging technology to analyze vascular calcification in animal models". In: *Int. J. Mol. Sci.* 21.12 (2020), pp. 1–27. ISSN: 14220067. DOI: 10.3390/ijms21124538.

[157] Yukihiko Momiyama et al. "The LDL-cholesterol to HDL-cholesterol ratio and the severity of coronary and aortic atherosclerosis". In: *Atherosclerosis* 222 (2 2012), pp. 577–580. ISSN: 00219150. DOI: 10.1016/j.atherosclerosis.2012.03.023.

[158] Guillaume Jondeau and Catherine Boileau. "Genetics of thoracic aortic aneurysms". In: *Current Atherosclerosis Reports* 14 (3 2012), pp. 219–226. ISSN: 15233804. DOI: 10.1007/s11883-012-0241-4.

[159] Masateru Takigawa et al. "Prevalence and predictors of coexistent silent atherosclerotic cardiovascular disease in patients with abdominal aortic aneurysm without previous symptomatic cardiovascular diseases". In: *Angiology* 63 (5 2012), pp. 380–385. ISSN: 00033197. DOI: 10.1177/0003319711419359.

[160] Akira Sekikawa et al. "Aortic stiffness and calcification in men in a population-based international study". In: *Atherosclerosis* 222 (2 2012), pp. 473–477. ISSN: 00219150. DOI: 10.1016/j.atherosclerosis.2012.03.027. URL: http://dx.doi.org/10.1016/j.atherosclerosis.2012.03.027.

[161] Alkiviadis Tsamis, Alexander Rachev, and Nikos Stergiopulos. "A constituent-based model of age-related changes in conduit arteries". In: *American Journal of Physiology - Heart and Circulatory Physiology* 301 (4 2011), pp. 1286–1301. ISSN: 03636135. DOI: 10.1152/ajpheart.00570.2010.

[162] Yann Orcel, Élise Camilleri, and Aurélie Dehaene. "Dissection aortique". In: *La Revue du praticien* 68 (7 2018), p. 752. ISSN: 00352640. DOI: 10.1016/b978-2-294-76093-8.00007-x.

[163] Akihito Matsushita et al. "Efficacy and pitfalls of transapical cannulation for the repair of acute type A aortic dissection". In: *Annals of Thoracic Surgery* 93 (6 2012), pp. 1905–1909. ISSN: 00034975. DOI: 10.1016/j.athoracsur.2012.02.036. URL: http://dx.doi.org/10.1016/j.athoracsur.2012.02.036.

[164] Shuyang Lu et al. "Bilateral versus unilateral antegrade cerebral perfusion in arch reconstruction for aortic dissection". In: *Annals of Thoracic Surgery* 93 (6 2012), pp. 1917–1920. ISSN: 00034975. DOI: 10.1016/j.athoracsur.2012.02.090.

[165] Alun H. Davies. "The Seriousness of Chronic Venous Disease: A Review of Real-World Evidence". In: *Advances in Therapy* 36 (s1 2019), pp. 5–12. ISSN: 18658652. DOI: 10.1007/s12325-019-0881-7. URL: https://doi.org/10.1007/s12325-019-0881-7.

[166] Young Jin Youn and Juyong Lee. "Chronic venous insufficiency and varicose veins of the lower extremities". In: *Korean Journal of Internal Medicine* 34 (2 2019), pp. 269–283. ISSN: 20056648. DOI: 10.3904/kjim.2018.230.

[167] Armando Mansilha and Joel Sousa. "Pathophysiological mechanisms of chronic venous disease and implications for venoactive drug therapy". In: *International Journal of Molecular Sciences* 19 (6 2018), pp. 1–21. ISSN: 14220067. DOI: 10.3390/ijms19061669.

[168] Richard A. Jonas et al. "Biological Sealants and Knitted Dacron: Porosity and Histological Comparisons of Vascular Graft Materials with and without Collagen and Fibrin Glue Pretreatments". In: *Annals of Thoracic Surgery* 41 (6 1986), pp. 657–663. ISSN: 00034975. DOI: 10.1016/S0003-4975(10)63083-4. URL: http://dx.doi.org/10.1016/S0003-4975(10)63083-4.

[169] Richard A. Jonas et al. "A new sealant for knitted dacron prostheses: Minimally cross-linked gelatin". In: *Journal of Vascular Surgery* 7 (3 1988), pp. 414–419. ISSN: 07415214. DOI: 10.1016/0741-5214(88)90437-5.

[170] Claudio A. Bustos, Claudio M. García-Herrera, and Diego J. Celentano. "Mechanical characterisation of Dacron graft: Experiments and numerical simulation". In: *Journal of Biomechanics* 49 (1 2016), pp. 13–18. ISSN: 18732380. DOI: 10.1016/j.jbiomech.2015.11.014. URL: http://dx.doi.org/10.1016/j.jbiomech.2015.11.014.

[171] Marco Amabili et al. "Viscoelastic characterization of woven Dacron for aortic grafts by using direction-dependent quasi-linear viscoelasticity". In: *Journal of the Mechanical Behavior of Biomedical Materials* 82 (2018), pp. 282–290. ISSN: 1751-6161. DOI: https://doi.org/10.1016/j.jmbbm.2018.03.038. URL: https://www.sciencedirect.com/science/article/pii/S1751616118301437.

[172] Gemma Penford et al. "Stenting and overdilating small Gore-Tex vascular grafts in complex congenital heart disease". In: *Catheterization and Cardiovascular Interventions* 91 (1 2018), pp. 71–80. ISSN: 1522726X. DOI: 10.1002/ccd.27310.

[173] J. Chlupác, E. Filová, and Lucie Bačáková. "Blood vessel replacement: 50 years of development and tissue engineering paradigms in vascular surgery". In: *Physiological Research* 58 (SUPPL.2 2009), pp. 119–140. ISSN: 08628408. DOI: 10.33549/physiolres.931918.

[174] Lian Xue and Howard P. Greisler. "Biomaterials in the development and future of vascular grafts". In: *Journal of Vascular Surgery* 37 (2 2003), pp. 472–480. ISSN: 07415214. DOI: 10.1067/mva.2003.88.

[175] Cristiano Spadaccio et al. “The long-term follow-up of large-diameter Dacron® vascular grafts in surgical practice: A review”. In: *Journal of Cardiovascular Surgery* 60 (4 2019), pp. 501–513. ISSN: 1827191X. DOI: 10.23736/S0021-9509.16.08061-7.

[176] Marco Amabili et al. “Identification of viscoelastic properties of Dacron aortic grafts subjected to physiological pulsatile flow”. In: *Journal of the Mechanical Behavior of Biomedical Materials* 110 (February 2020), p. 103804. ISSN: 18780180. DOI: 10.1016/j.jmbbm.2020.103804. URL: https://doi.org/10.1016/j.jmbbm.2020.103804.

[177] F. W. LoGerfo et al. “Downstream anastomotic hyperplasia. A mechanism of failure in Dacron® arterial grafts”. In: *Annals of Surgery* 197 (4 1983), pp. 479–483. ISSN: 00034932. DOI: 10.1097/00000658-198304000-00018.

[178] Chee Ho Chew et al. “Tissue-engineered vascular graft with co-culture of smooth muscle cells and human endothelial vein cells on an electrospun poly(Lactic-co-glycolic acid) microtube array membrane”. In: *Membranes* 11 (10 2021). ISSN: 20770375. DOI: 10.3390/membranes11100732.

[179] S. Sarkar et al. “The Mechanical Properties of Infrainguinal Vascular Bypass Grafts: Their Role in Influencing Patency”. In: *European Journal of Vascular and Endovascular Surgery* 31 (6 2006), pp. 627–636. ISSN: 10785884. DOI: 10.1016/j.ejvs.2006.01.006.

[180] P D Ballyk, C Walsh, and J Butany. “Compliance mismatch may promote graft–artery intimal hyperplasia by altering suture-line stresses”. In: *Journal of biomechanics* 31 (1997), pp. 229–237. DOI: 10.1016/s0197-3975(97)00111-5.

[181] Caitlin Martin, Thuy Pham, and Wei Sun. “Significant differences in the material properties between aged human and porcine aortic tissues”. In: *European Journal of Cardio-thoracic Surgery* 40 (1 2011), pp. 28–34. ISSN: 10107940. DOI: 10.1016/j.ejcts.2010.08.056.

[182] Jeffrey M. Mattson and Yanhang Zhang. “Structural and functional differences between porcine aorta and vena cava”. In: *Journal of Biomechanical Engineering* 139 (7 2017). ISSN: 15288951. DOI: 10.1115/1.4036261.

[183] Syed Salman Shahid et al. “Exploring arterial tissue microstructural organization using non-Gaussian diffusion magnetic resonance schemes”. In: *Scientific Reports* 11 (1 2021), pp. 1–13. ISSN: 20452322. DOI: 10.1038/s41598-021-01476-z. URL: https://doi.org/10.1038/s41598-021-01476-z.

[184] Dar Weiss et al. “Mechanics-driven mechanobiological mechanisms of arterial tortuosity”. In: 6 (49 2021). DOI: 10.1126/sciadv.abd3574.

[185] Om Prakash Choudhary and Priyan Ka. “Scanning Electron Microscope: Advantages and Disadvantages in Imaging Components”. In: *International Journal of Current Microbiology and Applied Sciences* 6 (5 2017), pp. 1877–1882. ISSN: 23197692. DOI: 10.20546/ijcmas.2017.605.207.

[186] Philip N. Lewis et al. “Contrast-enhanced tissue processing of fibrillin-rich elastic fibres for 3D visualization by volume scanning electron microscopy”. In: *Methods and Protocols* 4 (3 2021). ISSN: 24099279. DOI: 10.3390/mps4030056.

[187] Peter O. Bayguinov et al. “Modern Laser Scanning Confocal Microscopy”. In: *Current Protocols in Cytometry* 85 (1 2018), pp. 1–17. ISSN: 19349300. DOI: 10.1002/cpcy.39.

[188] Mary K. O’Connell et al. “The three-dimensional micro- and nanostructure of the aortic medial lamellar unit measured using 3D confocal and electron microscopy imaging”. In: *Matrix Biology* 27 (3 2008), pp. 171–181. ISSN: 0945053X. DOI: 10.1016/j.matbio.2007.10.008.

[189] Olaf Fritze et al. “Facilitated noninvasive visualization of collagen and elastin in blood vessels”. In: *Tissue Engineering - Part C: Methods* 16 (4 2010), pp. 705–710. ISSN: 19373392. DOI: 10.1089/ten.tec.2009.0309.

[190] Nicholas E. Buglak et al. “Light sheet fluorescence microscopy as a new method for unbiased three-dimensional analysis of vascular injury”. In: *Cardiovascular Research* 117 (2 2021), pp. 520–532. ISSN: 17553245. DOI: 10.1093/cvr/cvaa037.

[191] Benjamin T. Ledford et al. “Peptide Amphiphile Supramolecular Nanofibers Designed to Target Abdominal Aortic Aneurysms”. In: *ACS Nano* (2021). ISSN: 1936086X. DOI: 10.1021/acsnano.1c06258.

[192] Ana E. Cartaya et al. "Application of Machine Learning for Volumetric Analysis of Atherosclerotic Burden". In: *bioRxiv* (2022). DOI: 10.1101/2022.12.23.521811. eprint: https://www.biorxiv.org/content/early/2022/12/23/2022.12.23.521811.full.pdf. URL: https://www.biorxiv.org/content/early/2022/12/23/2022.12.23.521811.

[193] Aïcha Ben Zemzem et al. "X-ray microtomography reveals a lattice-like network within aortic elastic lamellae". In: *FASEB Journal* 35 (10 2021), pp. 1–11. ISSN: 15306860. DOI: 10.1096/fj.202100323RR.

[194] My Truong et al. "Sub-micrometer morphology of human atherosclerotic plaque revealed by synchrotron radiation-based μCT—A comparison with histology". In: *PLoS ONE* 17 (4 April 2022), pp. 1–18. ISSN: 19326203. DOI: 10.1371/journal.pone.0265598.

[195] Lisa Leyssens, Camille Pestiaux, and Greet Kerckhofs. "A review of ex vivo x-ray microfocus computed tomography-based characterization of the cardiovascular system". In: *International Journal of Molecular Sciences* 22 (6 2021). ISSN: 14220067. DOI: 10.3390/ijms22063263.

[196] Richard Balint, Tristan Lowe, and Tom Shearer. "Optimal Contrast Agent Staining of Ligaments and Tendons for X-Ray Computed Tomography". In: *PLoS One* 11.4 (2016), pp. 1–15. DOI: 10.1371/journal.pone.0153552. URL: https://doi.org/10.1371/journal.pone.0153552.

[197] Y. Dawood et al. "Novel imaging techniques to study postmortem human fetal anatomy: a systematic review on microfocus-CT and ultra-high-field MRI". In: *European Radiology* 30 (4 2020), pp. 2280–2292. ISSN: 14321084. DOI: 10.1007/s00330-019-06543-8.

[198] Jan Buytaert et al. "Volume Shrinkage of Bone, Brain and Muscle Tissue in Sample Preparation for Micro-CT and Light Sheet Fluorescence Microscopy (LSFM)". In: *Microsc. Microanal.* 20.4 (2014), pp. 1208–1217. ISSN: 1431-9276. DOI: 10.1017/S1431927614001329. URL: https://doi.org/10.1017/S1431927614001329.

[199] Arne Maes et al. "Cryogenic contrast-enhanced microCT enables nondestructive 3D quantitative histopathology of soft biological tissues". In: *Nat. Commun.* 13.1 (2022), pp. 1–14. ISSN: 20411723. DOI: 10.1038/s41467-022-34048-4.

[200] A.P. Ginsberg. "Inorganic syntheses". In: *Inorganic Syntheses* 1 (2007), pp. 1–197. DOI: 10.1002/9780470132326.

[201] Chika Nozaki Kato et al. “Syntheses and X-ray crystal structures of zirconium(IV) and hafnium(IV) complexes containing monovacant wells-Dawson and Keggin polyoxotungstates”. In: *Inorg. Chem.* 45.20 (2006), pp. 8108–8119. ISSN: 00201669. DOI: 10.1021/ic060656e.

[202] Archismita Misra et al. “Beyond Charge Balance: Counter-Cations in Polyoxometalate Chemistry”. In: *Angewandte Chemie - International Edition* 59 (2 2020), pp. 596–612. ISSN: 15213773. DOI: 10.1002/anie.201905600.

[203] Julien Al Shakarchi and Nicholas Inston. “Early cannulation grafts for haemodialysis: An updated systematic review”. In: *Journal of Vascular Access* 20 (2 2019), pp. 123–127. ISSN: 17246032. DOI: 10.1177/1129729818776571.

[204] Arne Maes. *Cryogenic Contrast-Enhanced MicroCT Enables Nondestructive 3D Quantitative Histopathology of Soft Biological Tissues*. 2022. DOI: 10.5281/zenodo.7034264.

[205] E. Remy and E. Thiel. “Medial axis for chamfer distances: Computing look-up tables and neighbourhoods in 2D or 3D”. In: *Pattern Recognition Letters* 23 (6 2002), pp. 649–661. ISSN: 01678655. DOI: 10.1016/S0167-8655(01)00141-6.

[206] A. Odgaard and H.J.G Gundersen. “Quantification of connectivity with special emphasis on 3D reconstractions”. In: *Bone* 14 (1993), pp. 173–182. DOI: 10.1016/8756-3282(93)90245-6.

[207] S. J. Cooper et al. “TauFactor: An open-source application for calculating tortuosity factors from tomographic data”. In: *SoftwareX* 5 (2016), pp. 203–210. ISSN: 23527110. DOI: 10.1016/j.softx.2016.09.002. URL: http://dx.doi.org/10.1016/j.softx.2016.09.002.

[208] Frits Hess. “History of (MICRO) vascular surgery and the development of small-caliber blood vessel prostheses (with some notes on patency rates and re-endothelialization)”. In: *Microsurgery* 6 (2 1985), pp. 59–69. ISSN: 10982752. DOI: 10.1002/micr.1920060202.

[209] Baocheng Zhang et al. “Small-diameter polyurethane vascular graft with high strength and excellent compliance”. In: *Journal of the Mechanical Behavior of Biomedical Materials* 121 (May 2021), p. 104614. ISSN: 18780180. DOI: 10.1016/j.jmbbm.2021.104614. URL: https://doi.org/10.1016/j.jmbbm.2021.104614.

[210] Roya M. Nezarati et al. “Electrospun vascular grafts with improved compliance matching to native vessels”. In: *Journal of Biomedical Materials Research - Part B Applied Biomaterials* 103 (2 2015), pp. 313–323. ISSN: 15524981. DOI: 10.1002/jbm.b.33201.

[211] Gary C Sieck. “Physiology in Perspective: Structure and Function—Anatomy and Physiology Are Integral”. In: *Physiology* 32.4 (2017), pp. 264–265. DOI: 10.1152/physiol.00014.2017. URL: https://doi.org/10.1152/physiol.00014.2017.

[212] Bruna B. J. Leal et al. “Vascular Tissue Engineering: Polymers and Methodologies for Small Caliber Vascular Grafts”. In: *Frontiers in Cardiovascular Medicine* 7 (January 2021), pp. 1–18. DOI: 10.3389/fcvm.2020.592361.

[213] Swathi Ravi, Zheng Qu, and Elliot L. Chaikof. “Polymeric materials for tissue engineering of arterial substitutes”. In: *Vascular* 17 (SUPPL. 1 2009), pp. 1–15. ISSN: 17085381. DOI: 10.2310/6670.2008.00084.

[214] Xinyu Wang and Vincent Chan. “Acellular Tissue-Engineered Vascular Grafts from Polymers: Methods, Achievements, Characterization, and Challenges”. In: *polymers* 14 (2022), p. 4825. DOI: 10.3390/polym14224825.

[215] Elizabeth H Stephens and K Jane Grande-Allen. “Age-related changes in collagen synthesis and turnover in porcine heart valves.” In: *The Journal of heart valve disease* 16 (6 Nov. 2007), pp. 672–682. ISSN: 0966-8519 (Print). URL: https://api.semanticscholar.org/CorpusID:41016988.

[216] Toshihiro Tsuruda et al. “Angiotensin II Induces Aortic Rupture and Dissection in Osteoprotegerin-Deficient Mice”. In: *Journal of the American Heart Association* 11 (8 2022). ISSN: 20479980. DOI: 10.1161/JAHA.122.025336.

[217] Arnout Mieremet et al. “Endothelial dysfunction in Marfan syndrome mice is restored by resveratrol”. In: *Scientific Reports* 12 (1 2022), pp. 1–12. ISSN: 20452322. DOI: 10.1038/s41598-022-26662-5. URL: https://doi.org/10.1038/s41598-022-26662-5.

[218] Wei Wen Lim et al. “Inhibition of IL11 Signaling Reduces Aortic Pathology in Murine Marfan Syndrome”. In: *Circulation Research* 130 (5 2022), pp. 728–740. ISSN: 15244571. DOI: 10.1161/CIRCRESAHA.121.320381.

[219] Luciano Figueiredo Borges et al. "Why do aortas cleave or dilate? Clues from an electronic scanning microscopy study in human ascending aortas". In: *Journal of Vascular Research* 51 (1 2013), pp. 50–57. ISSN: 10181172. DOI: 10.1159/000356296.

[220] Aïcha Ben Zemzem et al. "Early Alterations of Intra-Mural Elastic Lamellae Revealed by Synchrotron X-ray Micro-CT Exploration of Diabetic Aortas". In: *International Journal of Molecular Sciences* 23 (6 2022). ISSN: 14220067. DOI: 10.3390/ijms23063250.

[221] Jianglin Fan and Teruo Watanabe. "Atherosclerosis: Known and unknown". In: *Pathology International* 72 (3 2022), pp. 151–160. ISSN: 14401827. DOI: 10.1111/pin.13202.

[222] Seshi R. Sompuram et al. "A Molecular Mechanism of Formalin Fixation and Antigen Retrieval". In: *American Journal of Clinical Pathology* 121 (2 2004), pp. 190–199. ISSN: 00029173. DOI: 10.1309/BRN7CTX1E84NWWPL.

[223] Cecil H. Fox and Christobel Benton. "Formaldehyde: The fixative". In: *Journal of Histotechnology* 10 (3 1987), pp. 199–201. ISSN: 20460236. DOI: 10.1179/his.1987.10.3.199.

[224] Aidan D. Meade et al. "Studies of chemical fixation effects in human cell lines using Raman microspectroscopy". In: *Analytical and Bioanalytical Chemistry* 396 (5 2010), pp. 1781–1791. ISSN: 16182642. DOI: 10.1007/s00216-009-3411-7.

[225] I. Eltoum et al. "Introduction to the theory and practice of fixation of tissues". In: *Journal of Histotechnology* 24 (3 2001), pp. 173–190. ISSN: 01478885. DOI: 10.1179/his.2001.24.3.173.

[226] Etsuo A. Susaki et al. "Versatile whole-organ/body staining and imaging based on electrolyte-gel properties of biological tissues". In: *Nat. Commun.* 11.1 (2020). ISSN: 20411723. DOI: 10.1038/s41467-020-15906-5.

[227] Elisabeth Gasteiger et al. "The Proteomics Protocols Handbook". In: *The Proteomics Protocols Handbook* (2005), pp. 571–608. DOI: 10.1385/1592598900.

[228] Karen Stroobants et al. "Molecular origin of the hydrolytic activity and fixed regioselectivity of a ZrIV-substituted polyoxotungstate as artificial protease". In: *Chemistry - A European Journal* 20 (31 2014), pp. 9567–9577. ISSN: 15213765. DOI: 10.1002/chem.201402683.

[229] Ehsan Mostaed et al. "Towards revealing key factors in mechanical instability of bioabsorbable Zn-based alloys for intended vascular stenting". In: *Acta Biomaterialia* 105 (Mar. 2020), pp. 319–335. ISSN: 18787568. DOI: 10.1016/j.actbio.2020.01.028.

[230] Carole Verhaegen et al. "Bioreactivity of Stent Material: In vitro Impact of New Twinning-Induced Plasticity Steel on Platelet Activation". In: *Journal of Biomaterials and Nanobiotechnology* 10 (04 2019), pp. 175–189. ISSN: 2158-7027. DOI: 10.4236/jbnb.2019.104010.

[231] Eleonora Scarcello and Dominique Lison. "Are Fe-based stenting materials biocompatible? A critical review of in vitro and in vivo studies". In: *Journal of Functional Biomaterials* 11 (1 Mar. 2020). ISSN: 20794983. DOI: 10.3390/jfb11010002.

[232] Ehsan Mostaed et al. "Zinc-based alloys for degradable vascular stent applications". In: *Acta biomaterialia* 71 (2018), pp. 1–23. DOI: 10.1016/j.actbio.2018.03.005.

[233] Patrick K Bowen, Jaroslaw Drelich, and Jeremy Goldman. "Zinc exhibits ideal physiological corrosion behavior for bioabsorbable stents". In: *Advanced materials* 25.18 (2013), pp. 2577–2582. DOI: 10.1002/adma.201300226.

[234] Changhong Cai et al. "Non-destructive corrosion study on a magnesium alloy with mechanical properties tailored for biodegradable cardiovascular stent applications". In: *Journal of Materials Science and Technology* 66 (Mar. 2021), pp. 128–138. ISSN: 10050302. DOI: 10.1016/j.jmst.2020.07.006.

[235] Alexander A Oliver et al. "Recent advances and directions in the development of bioresorbable metallic cardiovascular stents: insights from recent human and in vivo studies". In: *Acta Biomaterialia* 127 (2021), pp. 1–23. DOI: 10.1016/j.actbio.2021.03.058.

[236] Jiabin Zong et al. "Advances in the development of biodegradable coronary stents: A translational perspective". In: *Materials Today Bio* (2022), p. 100368. DOI: 10.1016/j.mtbio.2022.100368.

[237] Giulia Magnani and Marco Valgimigli. "Dual antiplatelet therapy after drug-eluting stent implantation". In: *Interventional Cardiology Review* 11.1 (2016), p. 51. DOI: 10.15420/icr.2015:17:2.

[238] Tingzhang Hu et al. "Biodegradable stents for coronary artery disease treatment: Recent advances and future perspectives". In: *Materials Science and Engineering: C* 91 (2018), pp. 163–178. DOI: 10.1016/j.msec.2018.04.100.

[239] "Absorbable stent: Focus on clinical applications and benefits". In: *Vascular Health and Risk Management* 8 (1 2012), pp. 125–132. ISSN: 11766344. DOI: 10.2147/VHRM.S22551.

[240] Patrick K Bowen et al. "Biodegradable metals for cardiovascular stents: from clinical concerns to recent Zn-Alloys". In: *Advanced healthcare materials* 5.10 (2016), pp. 1121–1140. DOI: 10.1002/adhm.201501019.

[241] Jiayin Fu et al. "Evolution of metallic cardiovascular stent materials: A comparative study among stainless steel, magnesium and zinc". In: *Biomaterials* 230 (Feb. 2020). ISSN: 18785905. DOI: 10.1016/j.biomaterials.2019.119641.

[242] Y. F. Zheng, X. N. Gu, and F. Witte. "Biodegradable metals". In: *Materials Science and Engineering R: Reports* 77 (2014), pp. 1–34. ISSN: 0927796X. DOI: 10.1016/j.mser.2014.01.001.

[243] A.R. Saraf and S.P. Yadav. "2 - Fundamentals of bare-metal stents". In: *Functionalised Cardiovascular Stents*. Ed. by J. Gerard Wall, Halina Podbielska, and Magdalena Wawrzyńska. Woodhead Publishing, 2018, pp. 27–44. ISBN: 978-0-08-100496-8. DOI: https://doi.org/10.1016/B978-0-08-100496-8.00002-0. URL: https://www.sciencedirect.com/science/article/pii/B9780081004968000020.

[244] Y.F. Zheng. "6 - Bioabsorbable metallic stents". In: *Functionalised Cardiovascular Stents*. Ed. by J. Gerard Wall, Halina Podbielska, and Magdalena Wawrzyńska. Woodhead Publishing, 2018, pp. 99–134. ISBN: 978-0-08-100496-8. DOI: https://doi.org/10.1016/B978-0-08-100496-8.00006-8. URL: https://www.sciencedirect.com/science/article/pii/B9780081004968000068.

[245] Ian Johnson and Huinan Liu. "A Study on Factors Affecting the Degradation of Magnesium and a Magnesium-Yttrium Alloy for Biomedical Applications". In: *PLoS ONE* 8 (6 June 2013). ISSN: 19326203. DOI: 10.1371/journal.pone.0065603.

[246] A. Francis et al. "Iron and iron-based alloys for temporary cardiovascular applications". In: *Journal of Materials Science: Materials in Medicine* 26 (3 Mar. 2015), pp. 1–16. ISSN: 15734838. DOI: 10.1007/s10856-015-5473-8.

[247] Gabriela Gąsior, Jonasz Szczepański, and Aleksandra Radtke. "Biodegradable iron-based materials—what was done and what more can be done?" In: *Materials* 14 (12 June 2021). ISSN: 19961944. DOI: 10.3390/ma14123381.

[248] J. Dawn Abbott and Chirag Bavishi. "Next-Generation Bioresorbable Vascular Scaffolds: When to Get Our Hopes Up?" In: *JACC: Cardiovascular Interventions* 12 (3 Feb. 2019), pp. 256–258. ISSN: 18767605. DOI: 10.1016/j.jcin.2018.11.007.

[249] Run-Lin Gao et al. "First-in-human evaluation of a novel ultrathin sirolimus-eluting iron bioresorbable scaffold: 3-year outcomes of the IBS-FIM trial." In: *Eurointervention: Journal of Europcr in Collaboration with the Working Group on Interventional Cardiology of the European Society of Cardiology* (2023), EIJ–D. DOI: 10.4244/eij-d-22-00919.

[250] H. Idrissi et al. "On the mechanism of twin formation in Fe-Mn-C TWIP steels". In: *Acta Materialia* 58 (7 Apr. 2010), pp. 2464–2476. ISSN: 13596454. DOI: 10.1016/j.actamat.2009.12.032.

[251] Bruno C. De Cooman, Yuri Estrin, and Sung Kyu Kim. "Twinning-induced plasticity (TWIP) steels". In: *Acta Materialia* 142 (Jan. 2018), pp. 283–362. ISSN: 13596454. DOI: 10.1016/j.actamat.2017.06.046.

[252] Hongtao Yang et al. "Evolution of the degradation mechanism of pure zinc stent in the one-year study of rabbit abdominal aorta model". In: *Biomaterials* 145 (Nov. 2017), pp. 92–105. ISSN: 18785905. DOI: 10.1016/j.biomaterials.2017.08.022.

[253] H. F. Li et al. "Development of biodegradable Zn-1X binary alloys with nutrient alloying elements Mg, Ca and Sr". In: *Scientific Reports* 5 (May 2015). ISSN: 20452322. DOI: 10.1038/srep10719.

[254] Alexander A. Oliver et al. "Analysis of Vascular Inflammation against Bioresorbable Zn-Ag-Based Alloys". In: *ACS Applied Bio Materials* 3 (10 Oct. 2020), pp. 6779–6789. ISSN: 25766422. DOI: 10.1021/acsabm.0c00740.

[255] Lingyun Kong et al. "A Comprehensive Review of the Current Research Status of Biodegradable Zinc Alloys and Composites for Biomedical Applications". In: *Materials* 16 (13 July 2023). ISSN: 19961944. DOI: 10.3390/ma16134797.

[256] *Zinc and its uses*. Oct. 2023. URL: https://www.azom.com/properties.aspx?ArticleID=749.

[257] Salome Hagelstein et al. "Mechanical Analysis and Corrosion Analysis of Zinc Alloys for Bioabsorbable Implants for Osteosynthesis". In: *Materials* 15 (2 Jan. 2022). ISSN: 19961944. DOI: 10.3390/ma15020421.

[258] Li-Da Hou et al. "A review on biodegradable materials for cardiovascular stent application". In: *Frontiers of Materials Science* 10 (2016), pp. 238–259. DOI: 10.1007/s11706-016-0344-x.

[259] J. Eduardo Sousa, Patrick W. Serruys, and Marco A. Costa. "New frontiers in cardiology: Drug-eluting stents: Part I". In: *Circulation* 107 (17 May 2003), pp. 2274–2279. ISSN: 00097322. DOI: 10.1161/01.CIR.0000069330.41022.90.

[260] Isra Marei, Blerina Ahmetaj-Shala, and Chris R. Triggle. "Biofunctionalization of cardiovascular stents to induce endothelialization: Implications for in- stent thrombosis in diabetes". In: *Frontiers in Pharmacology* 13 (Oct. 2022). ISSN: 16639812. DOI: 10.3389/fphar.2022.982185.

[261] Marinella Patrizia Centemero and Jackson Rafael Stadler. "Stent thrombosis: An overview". In: *Expert Review of Cardiovascular Therapy* 10 (5 May 2012), pp. 599–615. ISSN: 14779072. DOI: 10.1586/erc.12.38.

[262] Ninian N. Lang and David E. Newby. "Emerging thrombotic effects of drug eluting stents". In: *Arteriosclerosis, Thrombosis, and Vascular Biology* 27 (2 Feb. 2007), pp. 261–262. ISSN: 10795642. DOI: 10.1161/01.ATV.0000255308.41576.ae.

[263] Jack P Chen et al. "Drug-eluting stent thrombosis: the Kounis hypersensitivity-associated acute coronary syndrome revisited". In: *JACC: Cardiovascular Interventions* 2.7 (2009), pp. 583–593. DOI: 10.1016/j.jcin.2009.04.017.

[264] Fumiyuki Otsuka et al. "Pathologic Etiologies of Late and Very Late Stent Thrombosis following First-Generation Drug-Eluting Stent Placement". In: *Thrombosis* 2012 (Nov. 2012), pp. 1–16. ISSN: 2090-1488. DOI: 10.1155/2012/608593.

[265] Josip Anđelo Borovac et al. “Neoatherosclerosis and Late Thrombosis After Percutaneous Coronary Intervention: Translational Cardiology and Comparative Medicine from Bench to Bedside”. In: *YALE JOURNAL OF BIOLOGY AND MEDICINE* 90 (2017), pp. 463–470.

[266] Donald E Cutlip et al. “Clinical end points in coronary stent trials: a case for standardized definitions”. In: *Circulation* 115.17 (2007), pp. 2344–2351. DOI: 10.1161/CIRCULATIONAHA.106.685313.

[267] Evan Shlofmitz; Connor C. Kerndt; Akarsh Parekh; Nauman Khalid. *Intravascular Ultrasound*. StatPearls Publishing, 2023. URL: https://www.ncbi.nlm.nih.gov/books/NBK537019/.

[268] Neiman A. Ramjattan; Vasimahmed Lala; Omar Kousa; Amgad N. Makaryus. *Coronary CT Angiography*. StatPearls Publishing, 2023. URL: https://www.ncbi.nlm.nih.gov/books/NBK470279/.

[269] M Karimzadeh Jouzdani, M Karimzadeh Jouzdani, and B Mohebbi. “The role of inflammatory biomarkers in predicting in-stent restenosis”. In: *Journal of Medicinal and Chemical Sciences* 4.6 (2021). DOI: 10.26655/JMCHEMSCI.2021.6.12.

[270] Joseph W Doucette et al. “Validation of a Doppler guide wire for intravascular measurement of coronary artery flow velocity.” In: *Circulation* 85.5 (1992), pp. 1899–1911. DOI: 10.1161/01.CIR.85.5.1899.

[271] Timothy Williams et al. “Complete revascularization optimizes patient outcomes in multivessel coronary artery disease: Data from the e-Ultimaster registry”. In: *Catheterization and Cardiovascular Interventions* 99.4 (2022), pp. 961–967. DOI: 10.1002/ccd.30042.

[272] Nevio Taglieri et al. “Target lesion failure with current drug-eluting stents: evidence from a comprehensive network meta-analysis”. In: *Cardiovascular Interventions* 13.24 (2020), pp. 2868–2878. DOI: 10.1016/j.jcin.2020.09.014.

[273] Yong Liu et al. “Bioresorbable scaffolds vs. drug-eluting stents for patients with myocardial infarction: A systematic review and meta-analysis of randomized clinical trials”. In: *Frontiers in Cardiovascular Medicine* 9 (2022), p. 974957. DOI: 10.3389/fcvm.2022.974957.

[274] Tatsuya Fujinami et al. "β-blockers reduced the target lesion revascularization after percutaneous coronary intervention using an everolimus-eluting stent". In: *in vivo* 36.1 (2022), pp. 416–423. DOI: 10.21873/invivo.12719.

[275] Megan L. Brophy et al. "Eating the Dead to Keep Atherosclerosis at Bay". In: *Frontiers in Cardiovascular Medicine* 4 (January 2017). ISSN: 2297055X. DOI: 10.3389/fcvm.2017.00002.

[276] Maryam Moravej and Diego Mantovani. "Biodegradable metals for cardiovascular stent application: Interests and new opportunities". In: *International Journal of Molecular Sciences* 12 (7 July 2011), pp. 4250–4270. ISSN: 14220067. DOI: 10.3390/ijms12074250.

[277] Emily K. Walker et al. "An in vitro model for preclinical testing of thrombogenicity of resorbable metallic stents". In: *Journal of Biomedical Materials Research - Part A* 103 (6 2015), pp. 2118–2125. ISSN: 15524965. DOI: 10.1002/jbm.a.35348.

[278] B. Liu and Y. F. Zheng. "Effects of alloying elements (Mn, Co, Al, W, Sn, B, C and S) on biodegradability and in vitro biocompatibility of pure iron". In: *Acta Biomaterialia* 7 (3 2011), pp. 1407–1420. ISSN: 17427061. DOI: 10.1016/j.actbio.2010.11.001.

[279] Yang Liu et al. "Study on the Mg-Li-Zn ternary alloy system with improved mechanical properties, good degradation performance and different responses to cells". In: *Acta Biomaterialia* 62 (2017), pp. 418–433. ISSN: 18787568. DOI: 10.1016/j.actbio.2017.08.021. URL: https://doi.org/10.1016/j.actbio.2017.08.021.

[280] Chie Yahata and Akira Mochizuki. "Platelet compatibility of magnesium alloys". In: *Materials Science and Engineering C* 78 (2017), pp. 1119–1124. ISSN: 09284931. DOI: 10.1016/j.msec.2017.04.153. URL: http://dx.doi.org/10.1016/j.msec.2017.04.153.

[281] Frank Feyerabend et al. "Blood compatibility of magnesium and its alloys". In: *Acta Biomaterialia* 25 (2015), pp. 384–394. ISSN: 18787568. DOI: 10.1016/j.actbio.2015.07.029.

[282] M. Peuster et al. "A novel approach to temporary stenting: Degradable cardiovascular stents produced from corrodible metal - Results 6-18 months after implantation into New Zealand white rabbits". In: *Heart* 86 (5 2001), pp. 563–569. ISSN: 13556037. DOI: 10.1136/heart.86.5.563.

[283] Matthias Peuster et al. “Long-term biocompatibility of a corrodible peripheral iron stent in the porcine descending aorta”. In: *Biomaterials* 27 (28 2006), pp. 4955–4962. ISSN: 01429612. DOI: 10.1016/j.biomaterials.2006.05.029.

[284] Ron Waksman et al. “Short-term effects of biocorrodible iron stents in porcine coronary arteries”. In: *Journal of Interventional Cardiology* 21 (1 2008), pp. 15–20. ISSN: 08964327. DOI: 10.1111/j.1540-8183.2007.00319.x.

[285] Deni Noviana et al. “The effect of hydrogen gas evolution of magnesium implant on the postimplantation mortality of rats”. In: *Journal of Orthopaedic Translation* 5 (2016), pp. 9–15. ISSN: 2214031X. DOI: 10.1016/j.jot.2015.08.003. URL: http://dx.doi.org/10.1016/j.jot.2015.08.003.

[286] Ma Jun et al. “Bio-Adaption between Magnesium Alloy Stent and the Blood Vessel: A Review”. In: *J Mater Sci Technol.* 32(9) (9 2017), pp. 815–826. DOI: 10.1016/j.jmst.2015.12.018.

[287] Kai Chen et al. “Fluid-induced corrosion behavior of degradable zinc for stent application”. In: *Journal of Materials Science and Technology* 91 (2021), pp. 134–147. ISSN: 10050302. DOI: 10.1016/j.jmst.2021.02.050.

[288] Rui Yue et al. “Microstructure, mechanical properties and in vitro degradation behavior of novel Zn-Cu-Fe alloys”. In: *Materials Characterization* 134 (July 2017), pp. 114–122. ISSN: 10445803. DOI: 10.1016/j.matchar.2017.10.015. URL: https://doi.org/10.1016/j.matchar.2017.10.015.

[289] N. T. Kirkland, N. Birbilis, and M. P. Staiger. “Assessing the corrosion of biodegradable magnesium implants: A critical review of current methodologies and their limitations”. In: *Acta Biomaterialia* 8 (3 2012), pp. 925–936. ISSN: 18787568. DOI: 10.1016/j.actbio.2011.11.014. URL: http://dx.doi.org/10.1016/j.actbio.2011.11.014.

[290] Hui Zhao et al. “Electrochemical polishing of 316L stainless steel slotted tube coronary stents”. In: *Journal of Materials science: materials in medicine* 13 (2002), pp. 911–916. DOI: 10.1023/A:1019831808503.

[291] Ivan De Scheerder et al. “Metallic surface treatment using electrochemical polishing decreases thrombogenicity and neointimal hyperplasia of coronary stents”. In: *Journal of Interventional Cardiology* 13 (3 2000), pp. 179–185. ISSN: 08964327. DOI: 10.1111/j.1540-8183.2000.tb00286.x.

[292] David Lee Butler. *Surface Roughness Measurement BT - Encyclopedia of Microfluidics and Nanofluidics*. Ed. by Dongqing Li. Springer US, 2008, pp. 1945–1949. ISBN: 978-0-387-48998-8. DOI: 10.1007/978-0-387-48998-8_1506.

[293] Juan Wang et al. “Ex vivo blood vessel bioreactor for analysis of the biodegradation of magnesium stent models with and without vessel wall integration”. In: *Acta Biomaterialia* 50 (2017), pp. 546–555. ISSN: 18787568. DOI: 10.1016/j.actbio.2016.12.039. URL: http://dx.doi.org/10.1016/j.actbio.2016.12.039.

[294] Chao Zhou et al. “Long-term in vivo study of biodegradable Zn-Cu stent: a 2-year implantation evaluation in porcine coronary artery”. In: *Acta biomaterialia* 97 (2019), pp. 657–670. DOI: 10.1016/j.actbio.2019.08.012.

[295] Song Lin et al. “Corrosion behavior and biocompatibility evaluation of a novel zinc-based alloy stent in rabbit carotid artery model”. In: *Journal of Biomedical Materials Research Part B: Applied Biomaterials* 107.6 (2019), pp. 1814–1823. DOI: 10.1002/jbm.b.34274.

[296] M. Bartosch et al. “New methods for in vivo degradation testing of future stent materials”. In: *Materials and Corrosion* 69 (2 2018), pp. 156–166. ISSN: 15214176. DOI: 10.1002/maco.201709521.

[297] Daniel Pierson et al. “A simplified in vivo approach for evaluating the bioabsorbable behavior of candidate stent materials”. In: *Journal of Biomedical Materials Research - Part B Applied Biomaterials* 100 B (1 2012), pp. 58–67. ISSN: 15524973. DOI: 10.1002/jbm.b.31922.

[298] ASTM G31-72 - J01 Committee. *Guide for laboratory immersion corrosion testing of metals*. Tech. rep. West Conshohocken, PA: ASTM International, 2004. DOI: 10.1520/G0031-72R04.

[299] Greet Kerckhofs et al. “High-resolution microfocus X-ray computed tomography for 3d surface roughness measurements of additive manufactured porous materials”. In: *Advanced Engineering Materials* 15 (3 2013), pp. 153–158. ISSN: 14381656. DOI: 10.1002/adem.201200156.

[300] Jin He et al. “A study of degradation behaviour and biocompatibility of Zn—Fe alloy prepared by electrodeposition”. In: *Materials Science and Engineering C* 117 (July 2020), p. 111295. ISSN: 18730191. DOI: 10.1016/j.msec.2020.111295. URL: https://doi.org/10.1016/j.msec.2020.111295.

[301] Shan Zhao et al. “Zn-Li alloy after extrusion and drawing: Structural, mechanical characterization, and biodegradation in abdominal aorta of rat”. In: *Materials Science and Engineering C* 76 (2017), pp. 301–312. ISSN: 09284931. DOI: 10.1016/j.msec.2017.02.167.

[302] Alban Dibra et al. “Influence of stent surface topography on the outcomes of patients undergoing coronary stenting: A randomized double-blind controlled trial”. In: *Catheterization and Cardiovascular Interventions* 65 (3 2005), pp. 374–380. ISSN: 15221946. DOI: 10.1002/ccd.20400.

[303] Roger J Guillory II et al. “Improved biocompatibility of Zn–Ag-based stent materials by microstructure refinement”. In: *Acta biomaterialia* 145 (2022), pp. 416–426. DOI: 10.1016/j.actbio.2022.03.047.

[304] Xiwei Liu et al. “Micro-alloying with Mn in Zn–Mg alloy for future biodegradable metals application”. In: *Materials & Design* 94 (2016), pp. 95–104. DOI: 10.1016/j.matdes.2015.12.128.

[305] T Huang, J Cheng, and YF Zheng. “In vitro degradation and biocompatibility of Fe–Pd and Fe–Pt composites fabricated by spark plasma sintering”. In: *Materials Science and Engineering: C* 35 (2014), pp. 43–53. DOI: 10.1016/j.msec.2013.10.023.

[306] J Cheng and YF Zheng. “In vitro study on newly designed biodegradable Fe-X composites (X= W, CNT) prepared by spark plasma sintering”. In: *Journal of Biomedical Materials Research Part B: Applied Biomaterials* 101.4 (2013), pp. 485–497. DOI: 10.1002/jbm.b.32783.

[307] Tao Huang, Yan Cheng, and Yufeng Zheng. “In vitro studies on silver implanted pure iron by metal vapor vacuum arc technique”. In: *Colloids and Surfaces B: Biointerfaces* 142 (2016), pp. 20–29. DOI: 10.1016/j.colsurfb.2016.01.065.

[308] Patrick K. Bowen et al. "Evaluation of wrought Zn–Al alloys (1, 3, and 5 wt % Al) through mechanical and in vivo testing for stent applications". In: *Journal of Biomedical Materials Research - Part B Applied Biomaterials* 106 (1 Jan. 2018), pp. 245–258. ISSN: 15524981. DOI: 10.1002/jbm.b.33850.

[309] Roger J. Guillory II et al. "In Vitro Corrosion and in Vivo Response to Zinc Implants with Electropolished and Anodized Surfaces". In: *ACS Applied Materials and Interfaces* 11 (22 2019), pp. 19884–19893. ISSN: 19448252. DOI: 10.1021/acsami.9b05370.

[310] Roger J Guillory II et al. "Preclinical In-Vivo Evaluation and Screening of Zinc Based Degradable Metals for Endovascular Stents". In: 71 (1989 2021), pp. 1436–1446. DOI: 10.1007/s11837-019-03371-5.

[311] Hualan Jin et al. "Novel high-strength, low-alloys Zn-Mg (< 0.1 wt% Mg) and their arterial biodegradation". In: *Materials Science and Engineering C* 84 (November 2017 2018), pp. 67–79. ISSN: 18730191. DOI: 10.1016/j.msec.2017.11.021.

[312] Adam J. Drelich et al. "Long-term surveillance of zinc implant in murine artery: Surprisingly steady biocorrosion rate". In: *Acta Biomaterialia* 58 (2017), pp. 539–549. ISSN: 18787568. DOI: 10.1016/j.actbio.2017.05.045. URL: http://dx.doi.org/10.1016/j.actbio.2017.05.045.

[313] Humayun Kabir et al. "Recent research and progress of biodegradable zinc alloys and composites for biomedical applications: Biomechanical and biocorrosion perspectives". In: *Bioactive Materials* 6 (3 2021), pp. 836–879. ISSN: 2452199X. DOI: 10.1016/j.bioactmat.2020.09.013. URL: https://doi.org/10.1016/j.bioactmat.2020.09.013.

[314] Wenjiao Lin et al. "Long-term in vivo corrosion behavior, biocompatibility and bioresorption mechanism of a bioresorbable nitrided iron scaffold". In: *Acta Biomaterialia* 54 (2017), pp. 454–468. ISSN: 18787568. DOI: 10.1016/j.actbio.2017.03.020. URL: http://dx.doi.org/10.1016/j.actbio.2017.03.020.

[315] Qimao Feng et al. "Characterization and in vivo evaluation of a bio-corrodible nitrided iron stent". In: *Journal of Materials Science: Materials in Medicine* 24 (3 2013), pp. 713–724. ISSN: 09574530. DOI: 10.1007/s10856-012-4823-z.

[316] Chao Wu et al. “Short-term safety and efficacy of the biodegradable iron stent in mini-swine coronary arteries”. In: *Chinese Medical Journal* 126 (24 2013), pp. 4752–4757. ISSN: 03666999. DOI: 10.3760/cma.j.issn.0366-6999.20131120.

[317] Andreas Drynda et al. “In vitro and in vivo corrosion properties of new iron-manganese alloys designed for cardiovascular applications”. In: *Journal of Biomedical Materials Research - Part B Applied Biomaterials* 103 (3 2015), pp. 649–660. ISSN: 15524981. DOI: 10.1002/jbm.b.33234.

[318] Matthew Simon Dargusch et al. “In Vivo Evaluation of Bioabsorbable Fe-35Mn-1Ag: First Reports on In Vivo Hydrogen Gas Evolution in Fe-Based Implants”. In: *Advanced Healthcare Materials* 10 (2 2021), pp. 1–15. ISSN: 21922659. DOI: 10.1002/adhm.202000667.

[319] Thaís Casagrande Paim et al. “Evaluation of in vitro and in vivo biocompatibility of iron produced by powder metallurgy”. In: *Materials Science and Engineering C* 115 (January 2020), p. 111129. ISSN: 18730191. DOI: 10.1016/j.msec.2020.111129. URL: https://doi.org/10.1016/j.msec.2020.111129.

[320] Lisa Leyssens et al. “Exploring the biodegradability of candidate metallic intravascular stent materials using X-ray microfocus computed tomography: an in vitro study”. In: *Under review in Journal of Biomedical Materials Reasearch Part B: Applied Biomaterials* (2024).

[321] Lisa Leyssens et al. “Non-destructive 3D characterization of the blood vessel wall microstructure in different species and blood vessel types using contrast-enhanced microCT and comparison with synthetic vascular grafts.” eng. In: *Acta Biomater.* 164 (July 2023), pp. 303–316. ISSN: 1878-7568 (Electronic). DOI: 10.1016/j.actbio.2023.04.013.

[322] Roger J Guillory II. “Degradable Zinc Material Characteristics and Its Influence on Biocompatibility in an in-vivo Murine Model”. PhD thesis. Michigan Technological University, 2019. DOI: 10.37099/mtu.dc.etdr/967.

[323] F Edward Boas and Dominik Fleischmann. “CT artifacts: causes and reduction techniques”. In: *Imaging Med* 4.2 (2012), pp. 229–240.

[324] Luke Hunter and Jan Dewanckele. “Evolution of micro-CT: Moving from 3D to 4D”. In: *Microscopy Today* 29.3 (2021), pp. 28–34. DOI: 10.1017/S1551929521000651.

[325] Misael Dalbosco et al. “Multiscale numerical analyses of arterial tissue with embedded elements in the finite strain regime”. In: *Computer Methods in Applied Mechanics and Engineering* 381 (2021), p. 113844. DOI: 10.1016/j.cma.2021.113844.